In-Depth Mechanistic Understanding of Photoinitiating Systems

Zur Erlangung des akademischen Grades einer

DOKTORIN DER NATURWISSENSCHAFTEN

(Dr. rer. nat.)

von der KIT-Fakultät für Chemie und Biowissenschaften

des Karlsruher Instituts für Technologie (KIT)

genehmigte

DISSERTATION

von

M. Sc. Andrea Lauer

aus Schwetzingen, Deutschland

Die vorliegende Arbeit wurde von Oktober 2014 bis März 2018 unter Anleitung von Prof. Dr. Christopher Barner-Kowollik am Karlsruher Institut für Technologie (KIT) – Universitätsbereich angefertigt.

Meiner Familie gewidmet.

Abstract

The present thesis provides in-depth insights into the mechanistic pathways of photoinduced polymerization reactions, as well as the propensity of the generated polymer end groups to undergo secondary photoinduced transformation processes. These processes are explored using pulsed-laser polymerization and post irradiation experiments combined with size exclusion chromatography hyphenated to high resolution electrospray ionization mass spectrometry (MS), tandem MS experiments, photochemically induced dynamic nuclear polarization experiments, as well as theoretical calculations. In the first part of the thesis, polymers resulting from photoinduced radical initiation processes are investigated towards their susceptibility to secondary photochemical cleavage at their respective chain termini as a function of the irradiation energy to which they are exposed. Specifically, it is found that the end group transformation proceeds via Norrish type I and II reactions, leading to unsaturated species. Initially, the influence of various methyl-substitutions on the benzoyl moiety of benzoin derivatives is investigated by applying monochromatic light (λ = 351 nm). The findings show that the light-induced transformation of benzoin-derived end groups is observed solely for benzoyl moieties which are not substituted at both *ortho*-positions, herein termed unstable end groups. The photochemical stability of the end groups, substituted in both *ortho*-positions, so-called stable end groups, can be traced back due to a shift of the n-π^* transition towards shorter wavelengths. Furthermore, these UV-stable end groups are investigated towards the influence of the irradiation wavelength on their photochemically stability. It is demonstrated that the substitution pattern on the benzoyl moieties dictates the polymer stability as a function of wavelength, which is in excellent agreement with quantum chemical predictions. In addition, the photochemically stability of the benzoyl end group is systematically investigated with regard to the influence of the solvent, the substitution with functional groups, the polymer backbone as well as under coating-like material conditions, which leads to the photoinduced formation of the unsaturated species for all applied conditions.

Next, the wavelength-dependent photochemistry of oxime ester photoinitiators is investigated. It is demonstrated that the absorptivity of these photoinitiators is by no means a measure for their monomer to polymer conversion, since the highest conversions are observed for wavelengths in the visible light regime, where the absorptivity shows the lowest value.

Finally, the Thorpe-Ingold effect is investigated during the photoinduced polymerization of the photoinitiator Irgacure 2959 with various methacrylate monomers. Here, the hydroxy isopropyl

polymer end group is capable to undergo a ring-closing reaction with the ester motif of the polymer backbone, leading to a lactone-derived polymer end group.

II

Zusammenfassung

Die vorliegende Arbeit bietet detaillierte Einblicke in den Mechanismus photoinduzierter Polymerisationsreaktionen sowie deren mögliche sekundäre Umwandlungsprozesse. Hierfür wurden Polymere mittels gepulster Laserpolymerisation synthetisiert und anschließend sekundär bestrahlt. Die Untersuchung der Polymere erfolgte unter Verwendung der Größenausschlusschromatographie, welche mit der hochauflösenden Elektrosprayionisations-Massenspektrometrie (MS) kombiniert wurde. Des Weiteren dienten Tandem-MS Experimente und die photochemisch induzierte dynamische Kernspinpolarisation der Strukturaufklärung. Theoretische Berechnungen wurden unterstützend zum Verständnis der experimentellen Ergebnisse herangezogen. Im ersten Teil der Arbeit werden durch photoinduzierte Polymerisationen dargestellte Polymere – basierend auf der Photoenergie der sie ausgesetzt sind – auf ihre Empfindlichkeit gegenüber Folge-reaktionen an ihren jeweiligen Kettenenden untersucht. Es wird gezeigt, dass die Endgruppe durch Norrish-Typ-I und -II Reaktionen zu ungesättigten Spezies umgewandelt wird. Hierzu wird zunächst der Einfluss verschiedener Methylsubstitutionen an der Benzoyleinheit von Benzoinderivaten mittels der Verwendung von monochromatischem Licht mit einer Wellenlänge von 351 nm untersucht. Die Ergebnisse zeigen, dass die lichtinduzierte Umwandlung von Benzoinendgruppen nur für Benzoyleinheiten beobachtet wird, welche nicht an beiden *ortho*-Positionen (instabile Endgruppen) substituiert sind. Die photochemische Stabilität der Endgruppen, welche in beiden *ortho*-Positionen (stabile Endgruppen) substituiert sind, lässt sich auf eine Verschiebung des n-π^*-Übergangs zu kürzeren Wellenlängen zurückführen. Des Weiteren werden diese UV-stabilen Endgruppen auf den Einfluss der Bestrahlungswellenlänge bezüglich ihrer photochemischen Stabilität untersucht. Es kann gezeigt werden, dass das Substitutionsmuster der Benzoyleinheiten die Polymerstabilität als Funktion der Wellenlänge bestimmt, welches sich ausgezeichnet mit quantenmechanischen Vorhersagen deckt. Zusätzlich wird die photochemische Stabilität der Benzoylendgruppe systematisch auf den Einfluss des Lösungsmittels, der Substitution mit funktionellen Gruppen, des Polymerrückgrats, sowie auch der Einfluss unter Bedingungen wie sie im Endprodukt (lackähnliches Material) zu finden sind, untersucht. Dabei führten alle verwendeten Bedingungen zur photoinduzierten Bildung der ungesättigten Spezies.

Im zweiten Teil der Arbeit wird die wellenlängenabhängige Photochemie von Oximester Photoinitiatoren untersucht. Es kann gezeigt werden, dass die Absorption dieser Photoinitiatoren keinesfalls ein Maß für ihren Polymerumsatz darstellt, da die höchsten Umsätze für Wellenlängen im sichtbaren Teil beobachtet werden, welche jedoch den niedrigsten

Absorptionswert zeigen. Im dritten Teil der Studie wird der Thorpe-Ingold-Effekt während der photoinduzierten Polymerisation des Photoinitiators Irgacure 2959 mittels verschiedener Methacrylatmonomeren untersucht. Hierbei ist die Hydroxyisopropyl-Polymerendgruppe in der Lage, eine Ringschlussreaktion mit der Estergruppe des Polymerrückgrats einzugehen, welches zu der Bildung von Lakton-Polymerendgruppen führt.

Publications and Conference Contributions

Publications Arising from this Thesis

- *Systematic Assessment of the Photochemical Stability of Photoinitiator-Derived Macromolecular Chain Termini*
  Lauer, A.*; Fast, D. E.*; Kelterer, A.-M.; Frick, E.; Neshchadin, D.; Voll, D.; Gescheidt, G.; Barner-Kowollik, C. *Macromolecules* **2015**, *48*, (23), 8451–8460.

- *Wavelength-Dependent Photochemistry of Oxime Ester Photoinitiators*
  Fast, D. E.*; Lauer, A.*; Menzel, J. P.; Kelterer, A.-M.; Gescheidt, G.; Barner Kowollik, C. *Macromolecules* **2017**, *50*, (5), 1815-1823.

- *Wavelength-Dependent Photochemical Stability of Photoinitiator-Derived Macromolecular Chain Termini*
  Lauer, A.; Fast, D. E.; Steinkoenig, J.; Kelterer, A.-M.; Gescheidt, G.; Barner-Kowollik, C. *ACS Macro Lett.* **2017**, *6*, (9), 952-958.

- *Installing Lactone Chain Termini During Photoinduced Polymerization*
  Lauer, A.*; Steinkoenig, J.*; Kelterer, A.-M.; Jöckle, P.; Unterreiner, A. N.; Barner-Kowollik, C. *Polym. Chem.* **2018**, *9*, (24), 3336-3341.

* These authors contributed equally

Additional Publications

- *Cleaning the Click: A Simple Electrochemical Avenue for Copper Removal from Strongly Coordinating Macromolecules*
  Jasinski, N.; Lauer, A.; Stals, P. J. M.; Behrens, S.; Essig, S.; Walther, A.; Goldmann, A. S.; Barner-Kowollik, C. *ACS Macro Lett.***2015,** *4*, (3), 298–301.

- *Toward a Quantitative Description of Radical Photoinitiator Structure-Reactivity Correlations*
  Frick, E.; Schweigert, C.; Noble, B. B.; Ernst, H. A.; Lauer, A.; Liang, Y.; Voll, D.; Coote, M. L.; Unterreiner, A.-N.; Barner-Kowollik, C. *Macromolecules* **2016**, *49*, (1), 80-89.

- *Bis(mesitoyl)phosphinic acid: Photo-Triggered Release of Metaphosphorous Acid in Solution*
  Fast, D. E.; Zalibera, M.; Lauer, A.; Eibel, A.; Schweigert, C.; Kelterer, A.-M.; Spichty, M.; Neshchadin, D.; Voll, D.; Ernst, H.; Liang, Y.; Dietliker, K.; Unterreiner, A.-N.; Barner-Kowollik, C.; Grützmacher, H.; Gescheidt, G. *Chem. Commun.* **2016**, *52*, (64), 9917-9920.

- *Imaging Single-Chain Nanoparticle Folding via High-Resolution Mass Spectrometry*
  Steinkoenig, J.; Rothfuss, H.; Lauer, A.; Tuten, B. T.; Barner-Kowollik, C. *J. Am. Chem. Soc.* **2017**, *139*, (1), 51-54.

- *Two-in-One: λ-Orthogonal Photochemistry on a Radical Photoinitiating System*
  Hurrle, S.; Lauer, A.; Gliemann, H.; Mutlu, H.; Wöll, C.; Goldmann, A. S.; Barner-Kowollik, C. *Macromol. Rapid Commun.* **2017,** *38*, (13), 1600598.

- *Wavelength Dependence of Light-Induced Cycloadditions*
  Menzel, J. P.; Noble, B. B.; Lauer, A.; Coote, M. L.; Blinco, J. P.; Barner-Kowollik, C. *J. Am. Chem. Soc.* **2017**, *139*, (44), 15812-15820.

Conference Contributions

- *Systematic Assessment of the Photochemical Stability of Photoinitiator-Derived Macromolecular Chain Termini*
  Poster at the European Symposium of Photopolymer Science, Leipzig, Germany
  September 11–14, **2016**

- *Wavelength-Dependent Photochemistry of Oxime Ester Photoinitiators*
  Poster at the Pacific Symposium on Radical Chemistry, Brisbane, Australia
  July 18-22, **2017**

- *Wavelength-Dependent Photochemical Stability of Photoinitiator-Derived Macromolecular Chain Termini*
  Poster at the Photopolymerization Fundamentals, Boulder, USA
  September 17-20, **2017**

Contents

1

Introduction

Light is utilized as one of the most powerful tools to control the formation, structure, and properties of polymeric materials.[1,2,11,12,3–10] The generation of synthetic polymers via photo-initiated processes by radical intermediates is of paramount importance for industrial research as well as for industrial applications. First patents for UV-curable inks and coatings were granted in the 1940s and had been commercialized in industrial production lines twenty years later. Since then, significant achievements in the development of monomers, oligomers, and photoinitiators provide efficient formulations for various applications in technology and medicine, for instance coatings, 3D-printing, microelectronics, adhesives, optics, dental composites, and food packaging.[13,14,23,24,15–22] The importance of photoinduced polymerizations stems from the fact that the polymerization can be temporally controlled with well-defined starting and end points as well as conducted at ambient temperature. The main part of the current thesis addresses a key question of photo-initiated polymerization: Can post-irradiation of photo-cured polymers be utilized to enhance the functionality of materials and by which mechanistic pathways do these transformations proceed? Secondary photochemically induced transformation processes can either occur during the photo-curing process itself (for example when high energy fluxes are used) or after the initial photo-curing process during the service time of the generated polymers via e.g. atmospheric exposure to radiation. For the precision design of polymeric materials, it is however, absolutely mandatory to possess exact knowledge of the end group structure of the

photolytically generated polymers. Such information is to date scarce, yet of critical importance when designing and applying photoinitiation systems, since the generation of the underpinning data requires the combination of a range of state-of-the-art analytical techniques and appropriate pulsed-laser equipment for the generation of well-defined polymeric materials. Thus, this information enables the construction of an encompassing mechanistic image of the fragmentation processes occurring during the irradiation of photolytically generated polymeric materials. The generated knowledge can constitute the basis for the development of innovative approaches towards the functionalization of polymers via photochemical means as well as provide guidance for the provision of photo-cured materials with a long service lifetime.

The first part of the current dissertation will close a critical gap in the fundamental understanding of such secondary photoinduced processes. Initially, the focus is placed on the influence of methyl-substitution of benzoin-type-derived polymer end groups towards secondary irradiation at 351 nm. Here, the combination of pulsed-laser polymerization and irradiation coupled with size exclusion chromatography hyphenated to electrospray ionization mass spectrometry (PLP/PLI-SEC-ESI-MS), photochemically induced dynamic nuclear polarization (photo-CIDNP) spectroscopy as well as quantum chemical calculations was used as a powerful tool to arrive at a structure reactivity correlation based on the observed photolytically induced end group transformations. In addition, these photoinitiator-derived chain termini were investigated towards their wavelength-dependent photochemical stability by employing a unique tunable pulsed-laser irradiation system with strictly monochromatic light as well as high resolution SEC-ESI-MS. Furthermore, the benzoyl polymer end group was systematically investigated towards its capability to undergo cleavage reactions. Therefore, the influence of the solvent as well as the influence of the aromatic substituents on the photoinduced cleavage process with various functional groups, such as fluorine and methoxy, was investigated. To assess the influence of the polymer backbone, monomers with longer side chains, as well as sterically hindered side chains were employed. In addition, the secondary irradiation procedure was conducted with coating-like materials, to simulate such influence in the final UV-cured product. The photoinitiator/monomer/solvent systems encompass a wide structural regime, allowing to draw general mechanistic conclusions regarding the photolytically induced end group transformations of photochemically prepared polymeric materials and to provide general guidelines for photoinduced end group transformations.

Next to the secondary cleavage processes of polymers, the second part of the thesis addresses the wavelength-dependent photochemistry of oxime ester photoinitiator, which was studied via a combination of PLP-SEC-ESI-MS, photo-CIDNP spectroscopy, and underpinned by theoretical calculations. The in-depth investigation of photoinitiator systems in terms of their light-induced

fragmentation behavior and the resulting macromolecular product spectrum is of key importance for their rational design and usage in a diverse field of applications. While many studies examine the behavior of photoinitiators in terms of the formed radical fragments (via electron spin resonance (ESR) spectroscopy) and the subsequently induced monomer to polymer conversion as a function of time, only few studies exploit the power of high resolution mass spectrometry coupled to pulsed-laser polymerization for a detailed 'post-mortem' analysis of the generated product spectrum to deduce mechanistic information. In addition, almost all studies exclusively make use of either one monochromatic wavelength (e.g. 351 or 355 nm) or employ broadly emitting lamps to induce initiator decay.

The last part of the dissertation focuses on the possibility of photoinitiator-derived polymer end groups to undergo chemical reactions during the photoinduced polymerization process, with the polymer backbone itself. Here, specific end group transformations yield lactone chain termini as evidenced by high-resolution SEC-ESI-MS, including a precision structural determination via MS/MS experiments, and as well supporting nuclear magnetic resonance (NMR) measurements. Such an in-depth analysis of the spontaneous induced polymer end group transformation allows access to lactone polymer end groups, which can be further utilized for post-modification approaches. More importantly, these observations put the typical photochemically behavior of photoinitiators into question, since the mass spectrum does not indicate the expected end groups. An overview of the projects addressed in the current dissertation is given in Figure 1.1.
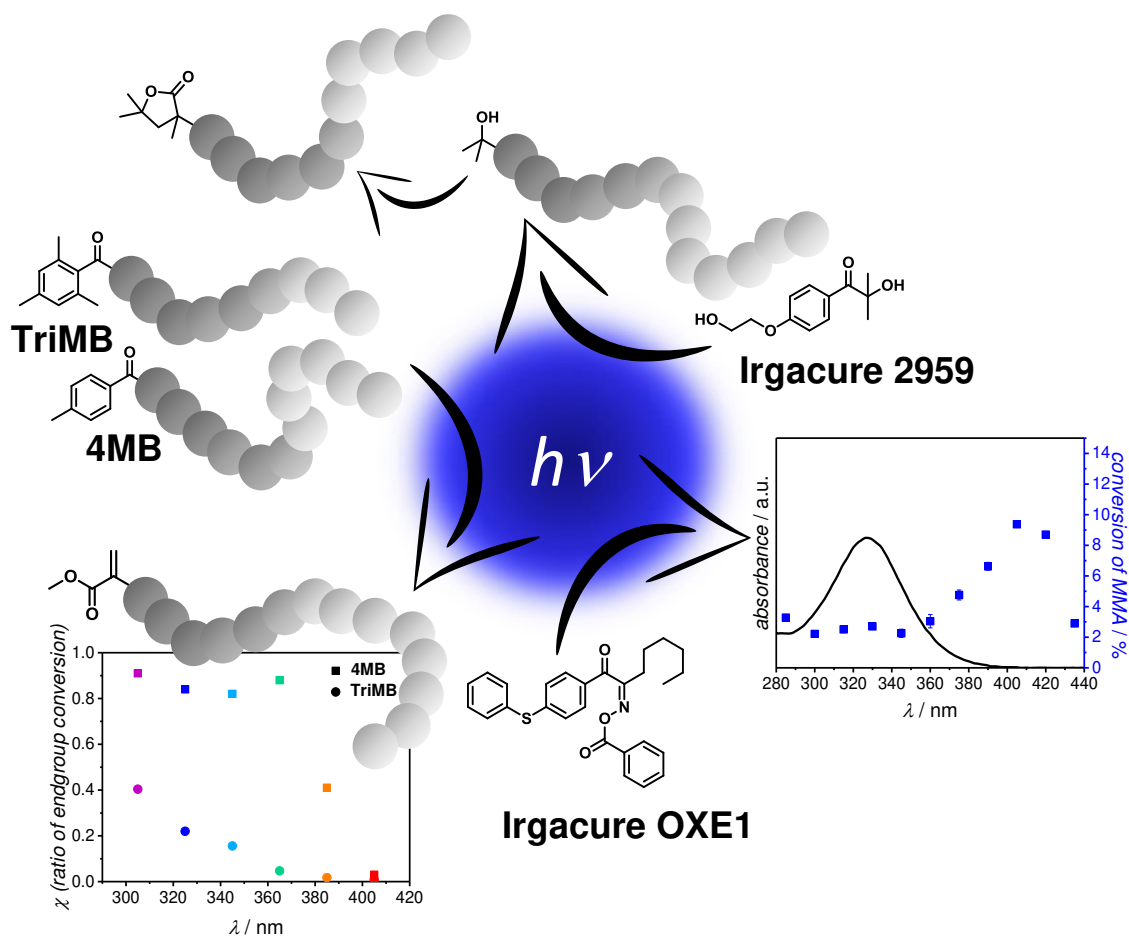
Figure 1.1.: Overview of the projects addressed in the current dissertation.

2

Theory and Background

The present Chapter provides an overview of all theoretical topics and aspects that are relevant for this dissertation. Hereby the main focus lies on photoinduced polymerization, mass spectrometry as well as photochemistry. The content of this Chapter is designed to provide the reader with all necessary information that will form the basis of the scientific output in the present thesis. Thus, the reader is able to follow the subsequent scientific discussion. The main topics (free radical polymerization, photochemistry, radical photoinitiators, lasers, chemically induced dynamic nuclear polarization (CIDNP) spectroscopy, mass spectrometry (MS), Thorpe-Ingold effect, investigation of photoinitiated polymerizations via a combination of pulsed-laser polymerization (PLP) and electrospray ionization mass spectrometry (ESI-MS)) are outlined.

2.1 Free Radical Polymerization

Free radical polymerization (FRP) is one of the most important polymerization techniques utilized for industrial production of soft matter materials. By the virtue of its mild and versatile reaction conditions, high tolerance and orthogonality toward many functionalities and a wide range of monomers that can be polymerized, a large diversity of polymers can be produced via FRP.[25] Hence, high molecular weight products can be obtained due to the high reactivity of radical species in FRP. However, due to its reaction mechanism, the conventional FRP method

comprises some significant disadvantages and limitations in its practical application.[26] For instance, the synthesized polymers display several limitations such as poor control over the molecular weight and the dispersity as well as the lack of defined end group functionality. The polymerization process for FRP is depicted in Scheme 2.1 and can be divided into four fundamental reaction steps:[27]

- Initiation
- Propagation
- Termination
- Chain Transfer
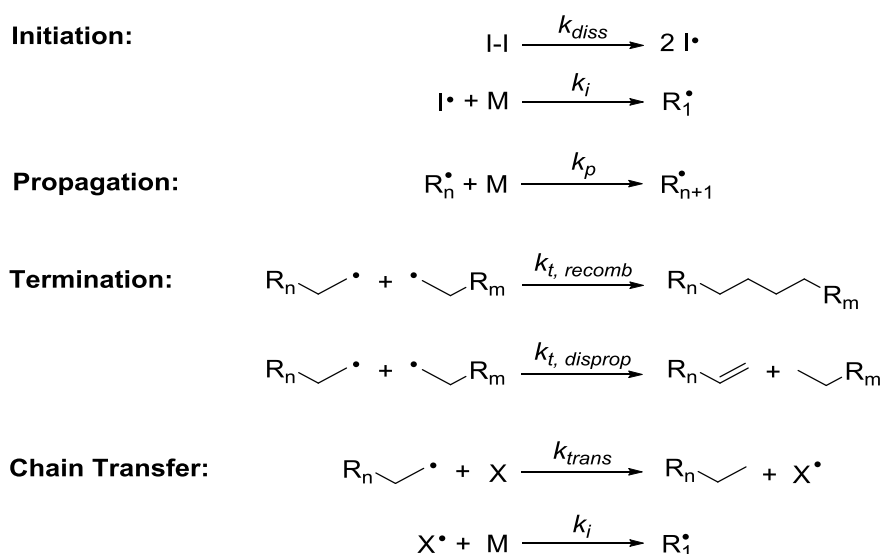
Scheme 2.1.: Four basics steps of FRP. Initiation step: dissociation of the initiator and successive addition of a generated free radical to a monomer molecule; Propagation step: addition of monomer; Termination step: recombination and disproportionation of radicals; and the chain transfer step: leading to re-initiation through newly formed radicals.

The Initiation process consists of two reaction steps (refer to Scheme 2.1). In the first step, the initiator decomposes into two radicals. The dissociation reaction can be triggered by variable approaches, including heat,[28,29] irradiation[30] or electrochemical processes,[31] depending on the type of initiator system, where the first two approaches are more frequently employed. Thus, the decomposition step is considered to be the rate determining step in the initiation process, and typical values for the rate coefficient k_{diss} of the dissociation vary between 10^{-1} and 10^{-6} s^{-1}. The decrease of the initiator concentration $[I]$ during the polymerization process can be expressed as:

$$-\frac{\mathrm{d}[I]}{\mathrm{d}t} = k_{\mathrm{diss}} \cdot [I] \tag{2.1}$$

The rate of generation of primary radicals follows general first order kinetics and can be given by:

$$\frac{d[I\cdot]}{dt} = 2 \cdot f \cdot k_{diss} \cdot [I] \tag{2.2}$$

The factor 2 captures that two radicals are formed after dissociation, and the initiator efficiency, f, is not always 100%, since the recombination and other side reactions of the generated radicals can occur during the initiation reaction. The second part of the initiation process is the radical reaction with the first monomer molecule (association step), which is a critical step in the polymerization kinetics.[9] The rate coefficient for this monomer association is k_i and the overall rate expression for the initiation process can be depicted as:

$$\frac{d[R_1\cdot]}{dt} = k_i \cdot [M] \cdot [I] \tag{2.3}$$

The propagation reaction describes the subsequent addition of monomer molecules to the radical species generated as a result of the first step (refer to Scheme 2.1). In this context, the growing macromolecule always entails a radical end group.[32,33] The rate coefficient of propagation, k_p, is dependent on the chemical properties of the monomer. The value of k_p is in the order of 10^2 L·mol^{-1}·s^{-1} for slowly polymerizing monomers, such as styrene, and 10^4 L·mol^{-1}·s^{-1} for acrylates, which are fast polymerizing monomers.[34−36] The rate of propagation can be given as:

$$-\frac{d[M]}{dt} = k_p \cdot [R\cdot] \cdot [M] \tag{2.4}$$

The rate coefficient k_p is highly depending not only on the chemical structure of the monomer, but also on the reaction temperature. For very high monomer to polymer conversions, diffusion control can be additionally observed, which originates from the high viscosity of the reaction mixture.

The termination step ends chain growth and is the result of the reaction of two radical chain ends. The termination of polymer chains can be classified in two possible reaction pathways: Combination and disproportionation. Combination occurs when two macroradicals react with each other to form a single so-called "dead polymer chain".[37] However, via disproportionation a first radical chain abstracts a hydrogen atom of a second radical chain by ß-elimination, leading to one dead polymer chain and one polymer chain carrying double bond functionality, where the latter is able to function as macromonomer during further polymerization processes.[38] Most of the typical monomers undergo both combination and disproportionation reactions. For monomers such as methyl methacrylate, the disproportionation reaction is more favorable than

the combination reaction, due to a higher steric hindrance closely located to the double bond. In contrast, styrene as a monomer – since possesses a less sterically hindered double bond – undergoes rather combination reactions.[39–41] The termination reaction of two macromolecular radicals in solution is diffusion-controlled and thus the rate determining step. In this regard, an increase in the monomer to polymer conversion increases both the chain length and the viscosity of the polymerization mixture resulting in the deceleration of the termination reaction.[42] The termination step proceeds as a statistical process, leading to polymer chains with different lengths. The governing rate coefficient k_t of the termination reaction varies between 10^6 and 10^8 L·mol^{-1}·s^{-1}. The rate of termination follows second order kinetics and can be given by:

$$-\frac{d[R\cdot]}{dt} = 2 \cdot k_t \cdot [R\cdot]^2 \tag{2.5}$$

An additional step in conventional FRP is the chain transfer reaction (refer to Scheme 2.1),[43] which leads to the limitation of the molecular weight that may be maximally obtained. However, in contrast to the termination reaction, the radical concentration remains constant. In the chain transfer step the growing macroradical $[R\cdot]$ is able to transfer the radical functionality to a transfer agent $[X]$. In this context, the hydrogen atom of the transfer agent is abstracted by the macroradical. The active radical site is transferred to the transfer agent leading to a dead polymer chain. The newly formed radical $[X\cdot]$ can reinitiate the polymerization reaction. The rate of chain transfer is given by the Equation 2.6:

$$-\frac{d[X]}{dt} = k_{tr} \cdot [R\cdot] \cdot [X] \tag{2.6}$$

Critically, transfer can potentially occur to any molecule present in the reaction media, for example the polymer or the solvent. Hence, the radical can be transferred to different molecules such as the initiator, solvents,[43] monomers,[44] polymer chains,[45] or consciously added compounds (e.g. thiols).[46] On the other hand, radical transfer towards the polymer backbone, either intra- or intermolecular, gives rise to branched polymers. [47]

2.1.1 Photoinitiated Free Radical Polymerization

Photoinitiated polymerization is usually referred to as a chain growing process which is initiated by light. The main common component of such reactions is the radical photoinitiator, and will be discussed in detail in Section 2.3. After the absorption of light, the photoinitiator decomposes into initiating radicals, which leads via the addition of monomer molecules to a growing polymer chain (refer to Figure 2.1).
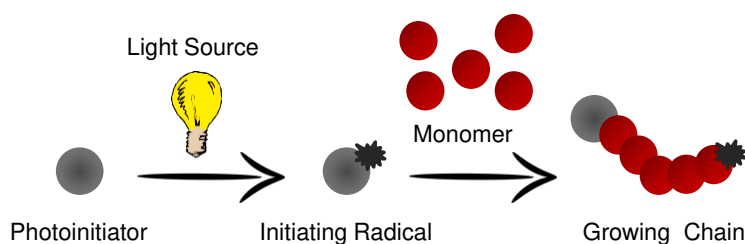
Figure 2.1.: General presentation of a photoinitiated free radical polymerization.

In addition to thermally triggered free radical polymerization, photoinitiated free radical polymerization plays an important role in industrial manufacturing as well as in fundamental research. The most striking advantage of a photoinduced polymerization in contrast to a thermally triggered one, which usually requires enhanced temperatures, is its applicability at ambient temperatures or even below. Furthermore, less side reactions such as chain transfer reactions occur when lower temperatures are applied. Another aspect is that the photoinduced polymerization can be performed with monomers possessing low ceiling temperatures. These monomers can be only polymerized at low temperatures, since high reaction temperatures will result in depolymerization dominating the polymerization process. In addition, for biochemical applications, e.g. immobilization of enzymes, employing low reaction temperature for the polymerization of the monomers is essential. A further practical advantage is the possibility of photochemically curing of large coated surfaces or fine structures, especially when the formulation (monomer and initiator) is placed in an application, such as dental fillings.[24,48] Consequently, owing to their substantial advantages, photoinduced polymerization reactions have been the basis of manifold applications in industries such as coatings, adhesives, inks, printing plates, microelectronics, optical waveguides, dental fillings and the fabrication of 3D objects amongst others.[24,49–54,55] In addition to their application capabilities, these reactions are of substantial use in fundamental research, where a plethora of studies exploit the photopolymerization processes in various media for soft matter material design. However, there is an urgent need in identifying the reactive species in photoinduced processes via spectroscopic methods, such as laser-flash photolysis,[56,57] femtosecond spectroscopy,[58,59] electron spin resonance spectroscopy,[56,60] chemically induced nuclear polarization (CIDNP) spectroscopy,[61,62] and mass spectrometry (MS).[63,64]

Pulsed-Laser Polymerization (PLP) Technique

PLP is the synthesis method of choice for the subsequent polymer end group analysis via mass spectrometry (refer to Section 2.6) within the present thesis. The mass spectrometric analysis of polymeric material requires low molecular weight polymers in the range of 150-6000 m/z (range of the employed system), which can be prepared by the PLP technique. The advantage of laser-induced initiation processes is based on the operating pulse pattern (pulse frequency in the range of 1-500 Hz for the excimer laser setup and 100 Hz for the tunable laser setup), which enables limiting the growth time and as a consequence the molecular weight of the generated macroradicals between two successive pulses. In this method, the radicals are generated through a photoinitiator, which is surrounded by monomer molecules and activated by a short laser pulse (~5-10 ns). Thus, the radical concentration increases instantaneously and the propagation step of a conventional free radical polymerization reaction starts. The macroradicals can grow in the so-called "dark-time" until the next laser pulse hits the sample. After the next laser pulse, the radical concentration is once again increased, which leads to termination processes of the generated polymeric radical. However, not every chain is terminated after the second pulse, and thus is able to persist growing. Correspondingly, new radicals are formed, and can grow to macroradicals (refer to Figure 2.2).

□ = Monomer Solution   ● = Photoinitiator   ●●●●● = Growing Chain   ●●●●● = Terminated Chain
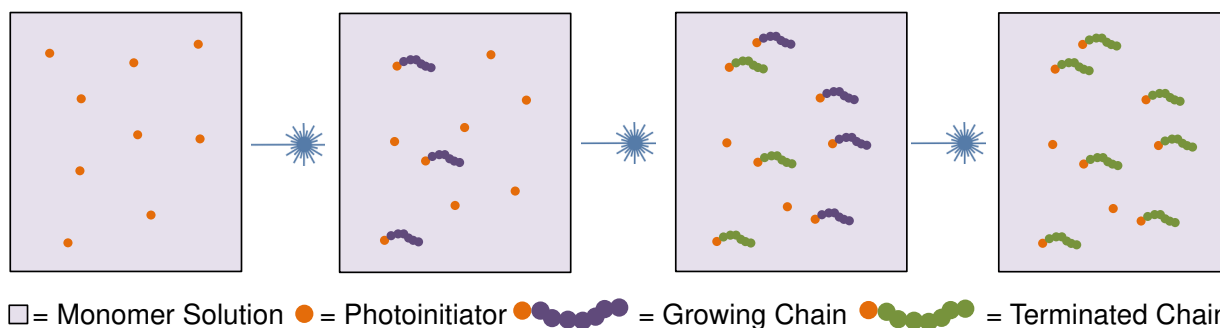
Figure 2.2.: Example of chain growth during PLP. Consecutive laser pulses start the propagation of new chains (purple circles) as well as end the propagation of previously initiated chains (green circles).

In 1977, the PLP technique was for the first time described by Sokolov[65,66] and co-workers and experimentally implemented by Olaj[67,68] and co-workers. When coupled to size exclusion chromatography (SEC), the technique is mainly applied in the field of polymerization kinetics to determine the propagation rate coefficient k_p of various monomers.[35,36,69–73] Thus, the combination of these methods takes advantage that some radicals survive a laser pulse and can further propagate in a second or third dark-time. Due to accumulation of polymer chains surviving various dark-times, the SEC traces of such photoinitiated polymers are multimodal. Their characteristic molecular weights (M_1, M_2, M_3) increases continuously ($M_i = i \cdot M_1$) after

each dark-time, a feature that can be employed – by taking the maxima of the first derivatives of the polymer distribution – to determine the propagation rate coefficients k_p according to Equation 2.7.

$$L_i = \frac{M_i}{MW_M} = i \cdot k_p \cdot c_M \cdot t_0 \quad \text{with } i = 1,2,3... \tag{2.7}$$

L_i is the degree of polymerization, M_i is the molecular weight of the respective inflection point, MW_M is the molecular weight of the monomer, i is the number of the inflection point, c_M is the monomer concentration, and t_0 is the time between two pulses (dark-time). According to the stationary state paradigm, the monomer concentration is expected to be constant during the PLP experiment and Equation 2.7 is only valid for very low monomer to polymer conversion (up to 1-3%). The experimental setup of the conducted PLP experiments, using an excimer or tunable-wavelength laser system, is shown in Figure 2.3. The assembly of the sample holder is similar for both systems, as the generated horizontal laser beam (excimer laser: mirror, tunable-wavelength laser: prism) is deflected to hit the photo vial vertically from below.

Figure 2.3.: Experimental PLP setup employed for polymer fabrication and photochemical end group transformation, utilizing an excimer laser (left side) or tunable-wavelength laser (right side).

2.2 Photochemistry

2.2.1 Beer-Lambert Law

The law of Beer-Lambert describes the reduction of the radiation intensity with the path length when passing through an absorbing substance. The concept underpinning the law was already discovered by Pierre Bouguer in the year 1729,[74] however it is attributed to Johann Heinrich Lambert, who even cited Bouguer´s "Essai d'Optique sur la Gradation de la Lumiere" in his own work "Photometria".[75] In 1852 August Beer extended the law by including the concentration of the solution in the absorption coefficient.[76] The law states:

$$A = \varepsilon_\lambda \cdot c \cdot l \tag{2.8}$$

Where, A is the measured experimental absorbance, ε_λ is a wavelength-dependent molar absorptivity coefficient with units of $M^{-1} \cdot cm^{-1}$, c is the molar concentration of the absorbing substance in $mol \cdot L^{-1}$, and l is the path length of the incident light beam through the solution in cm.

For multiple substances that absorb light, the total absorbance is the sum due to all absorbers and can be expressed as:

$$A = (\varepsilon_1 \cdot c \cdot l) + (\varepsilon_2 \cdot c \cdot l) + \cdots \tag{2.9}$$

The subscript refers to the respective molar absorptivity and concentration of the different absorbing substances. For experimental measurements the transmittance is utilized and can be defined as:

$$T = {}^I\!/\!_{I_o} \tag{2.10}$$

Where I is the intensity of the light coming out of the sample and I_o is the intensity of the incident light beam. Since transmittance and absorbance are inversely related, the relationship between transmittance (T) and absorbance (A) can be expressed as:

$$A = -\log(T) = -\log({}^I\!/\!_{I_o}) \tag{2.11}$$

2.2.2 Jablonski Diagram

Upon light absorption a molecule is excited from the ground state (S_0) into excited states (S_n). Those excited states are energetically elevated and undergo deactivation processes, which are competing with each other, within a short period of time (10^{-13}-10^{-2} s). The positions of the electronic states as well as the activation and deactivation processes are dependent on each molecule. These processes can be illustrated in a so-called Jablonski Diagram (refer to Figure 2.4). S_n represents the singlet electronic states, where v is vibrational energy level associated with the electronic states. T_1 indicates the first triplet electronic state. The arrows state the absorption and emission (non-radiative and radiative) processes as well as the non-radiative transitions (internal conversion (IC) and intersystem crossing (ISC)). By means of the Jablonski Diagram, the photophysical processes are discussed in the following: [77]
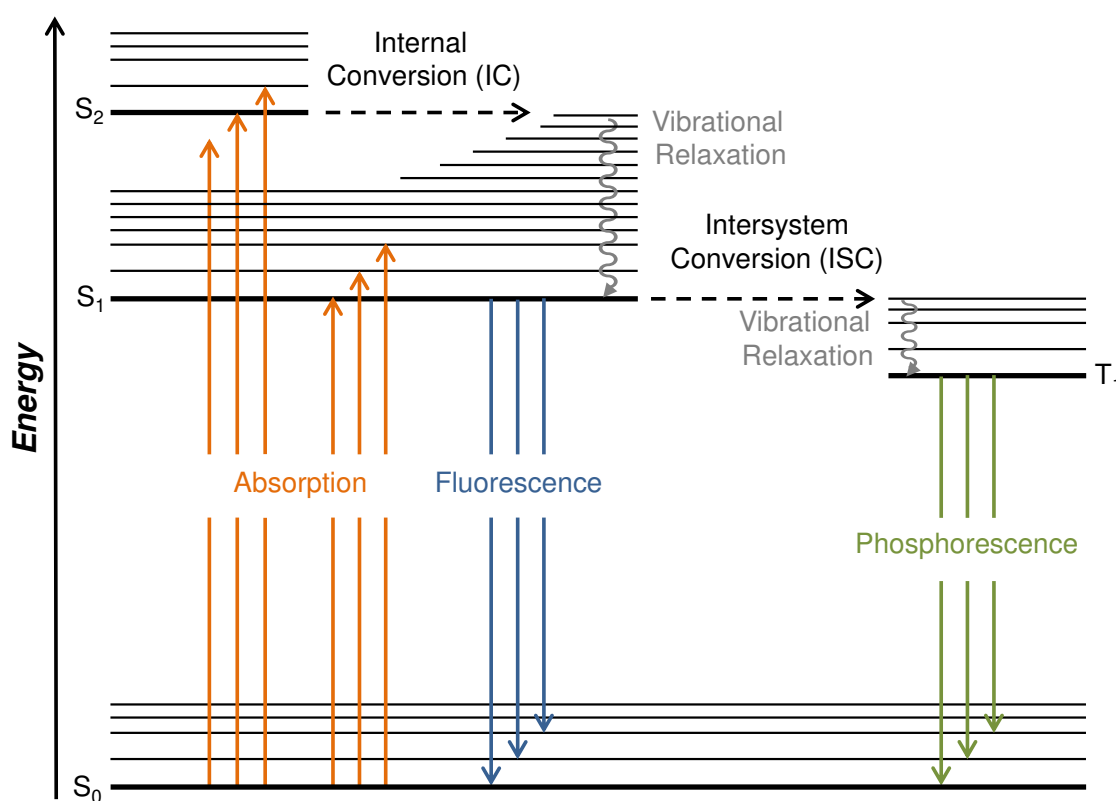
Figure 2.4.: Jablonski diagram: the energies of the ground electronic singlet state S_0, excited singlet S_1, and triplet T_1 (together with vibrational states) are depicted by *horizontal lines*. The most important radiative (fluorescence and phosphorescence) and non-radiative (vibrational transitions, internal conversion and intersystem crossing) processes are depicted by *arrows*. The position of the electronic and the vibrational levels are not drawn to scale.

- **Absorption:** Molecules are at ambient temperature in the vibrational ground state ($v = 0$) of the electronic ground state (S_0). After light absorption, the molecule performs a transition from the ground state (S_0) to an excited state (S_n: n≥1). The transition is very fast and takes place on the order of 10^{-15} s. The most probable (intensive) electronic transitions are between vibrational states, where the wave function shows the optimum overlap (Franck Condon Principle, refer to Section 2.2.3).

- **Vibrational relaxation and internal conversion:** Vibrational relaxation and internal conversion are both very fast non-radiative processes and occur between 10^{-13} and 10^{-12} s. Thus, the non-radiative transition takes place from excited states to energetic lower states by emitting energy in the form of heat to the environment. During vibrational relaxation, the reduction of vibrational energy occurs within the electronic state up to the vibrational ground state ($v = 0$). In contrast, the transition of internal conversion takes place from an excited electronic level to the subjacent level of the same spin multiplicity.

- **Fluorescence:** Fluorescence is a slow radiative process on the order of 10^{-9}-10^{-5} s. Thereby, the transition takes always place from the vibrational ground state ($v = 0$) of the first excited electronic state S_1 to one of the vibrational levels of the ground state S_0 (Kasha Rule). Here, the Franck-Condon principle must be considered: The probable (intensive) transitions occur between electronic states ($S_1 \rightarrow S_0$) with the highest overlap of the vibrational wave. The emission shape of the spectrum is independent of the excitation wavelength (the minimum energy to enable the $S_0 \rightarrow S_1$ transition must be exceeded).

- **Intersystem Crossing:** From the excited electronic state S_1 in the ground vibrational state $v = 0$, a spin forbidden transition on the time scale of 10^{-9}-10^{-6} s to the triplet state can occur. Following the rule of El-Sayed, the non-radiative transition only takes place between different exited states with different spin multiplicity.[78]

El-Sayed rule: **Allowed** processes: $^1(n\pi^*) \leftrightarrow {}^3(\pi\pi^*)$, $^3(n\pi^*) \leftrightarrow {}^1(\pi\pi^*)$

                           Forbidden processes: $^1(n\pi^*) \leftrightarrow {}^3(n\pi^*)$, $^3(\pi\pi^*) \leftrightarrow {}^1(\pi\pi^*)$

- **Phosphorescence:** From the excited electronic state T_1 a spin forbidden transition in between 10^{-5}-10^{-2} s to the electronic ground state S_0 can occur. As in the case for the transitions leading to fluorescence, the transition takes always place from the vibrational ground state ($v = 0$) of the first excited electronic state T_1 to one of the vibrational levels

of the ground state S_0 (Kasha Rule). However, this radiative process is rather unlikely due to the long lifetime.

2.2.3 Franck-Condon Principle

The Franck-Condon principle states that the most probable electronic transitions occur between states with similar nuclear configuration and similar vibrational behavior.[79,80] This is due to the fact that the electronic excitation is fast and as nuclei are more massive than electrons, the distance of the nuclei does not change during the photoinduced process. In quantum mechanics, the value of the overlapping integrals of the vibrational wave functions of both electronic states is the significant value for the probability of the vertical electronic transition (refer to Figure 2.5).
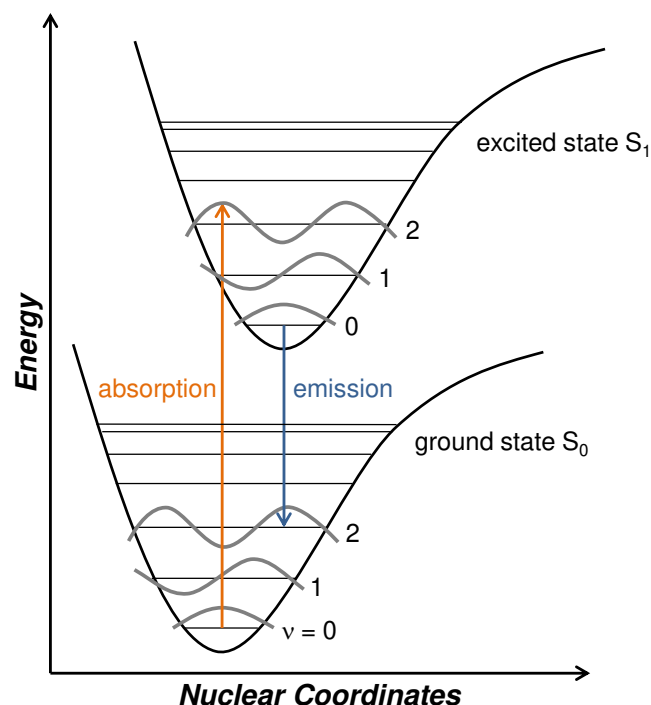
Figure 2.5.: Diagram illustrating the Franck-Condon principle. Electronic transitions appear as vertical transitions, while the nuclear coordinates remain constant. The transitions occur between electronic states with the highest overlap of the vibrational wave functions.

2.2.4 Molecular Electronic Transitions

Molecular orbitals (MO) are obtained by combining the atomic orbitals (AO) on the atoms in the molecule through the LCAO concept (linear combination of atomic orbitals). After absorption of UV or visible (UV-Vis) light, an organic molecule is promoted from the electronic ground state (S_0) to an excited state (S_1), which can be attributed to the outer electrons, mostly originating from the $2s$ and $2p$ orbitals of the carbon atoms. Thus, a jump of an electron from an occupied MO to a vacant MO causes the electronic transition. In general, the energetically favored energy

transition will be from the highest molecular orbital (HOMO) to the lowest molecular orbital (LUMO). There are three types of electronic transition which can be considered:

- Transitions involving π, σ, and n electrons
- Transitions involving charge-transfer electrons
- Transitions involving d and f electrons (not covered in this Section)

The most possible electronic transitions, involving σ, π and n electrons, are depicted in Figure 2.6 and will be discussed in the following.[77,81,82]
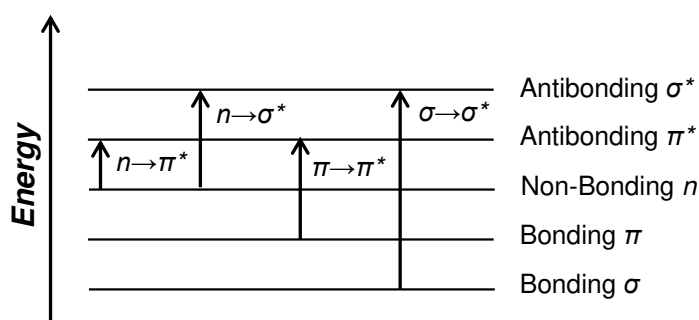

Figure 2.6.: Schematic representation of possible electronic transitions, involving σ, π, and n electrons.

σ to σ^* transitions

These transitions occur between a bonding and antibonding σ orbital. Inspection of Figure 2.6 shows that the required energy for this transition is rather high compared to the other electronic transitions. The absorption maxima based on σ-σ^* transitions are invisible in the UV-Vis region (200-800 nm).

n to σ^* transitions

In saturated compounds, which contain atoms with lone pairs (non-bonding electrons, e.g.: oxygen atom), n-σ^* transitions can occur. In this case, the transition takes place in the wavelength range between 150-250 nm. The number of organic functional groups with n-σ^* character in the UV region is quite small.

n to π^* transitions

n-π^* transitions arise between symmetry different orbitals (localized n and delocalized π orbitals) and due to the poor overlapping of those orbitals, they are symmetry forbidden. The absorption wavelengths are typically close to 300-380 nm and the molar absorption coefficients are relatively low, ranging from 10 to 100 L·mol^{-1}·cm^{-1}. The polarity of the utilized solvent, in which the organic molecule is dissolved, has an effect on the absorbance spectrum (solvatochromism).

With increasing polarity of the solvent, the absorption peaks corresponding to the n-π^* transitions are shifted towards shorter wavelengths (blue or hypsochromic shift). This effect occurs due to the increased solvation of the lone pair, which lowers the energy of the non-bonding orbital.

π to π^* transitions

π-π^* transitions occur in molecules with unsaturated groups (aromatic systems) between π orbitals and are symmetry allowed transitions. The molar absorption coefficients are higher than those in n-π^* transitions, ranging between 1000 to 10,000 L·mol^{-1}·cm^{-1}. Due to the attractive polarization forces between the solvent and the absorber, which lowers the energy levels of both, the excited and unexcited states, the absorption peaks caused by π-π^* transitions are often red shifted. The effect is more pronounced for the excited state, than for the unexcited state and the resulting energy difference is therefore slightly decreased, leading to a small red shift (bathochromic shift).

Charge - Transfer (CT) transitions

In strongly polarized molecules with delocalized molecular orbitals, charge-transfer transitions can occur. Here, the energy is delocalized upon excitation in the entire molecule. The absorption coefficients of these molecules are typically high and their transition is red shifted, in contrast to non-polarized molecules.

2.2.5 Cage Effect

In 1934, the cage effect was introduced for the first-time by Frank and Rabinowitch.[83] Their hypothesis suggested that molecules in the liquid state rather resemble an encapsulated particle than acting alone as individual particle.[84] In the gas phase, after absorption of light, a molecule which cleaves into radicals can immediately fall apart in different directions. However, the behavior of a molecule dissolved in a liquid phase (solvent or monomer) is different compared to the behavior of molecules in the gas phase. The cleavage in the liquid phase leads to two radicals that exist next to each other for a certain time surrounded by solvent or monomer molecules, the so-called cage effect. Due to the high rate coefficient for the interaction of two radicals, the radicals recombine with each other before they dissociate by diffusion (refer to Scheme 2.2).
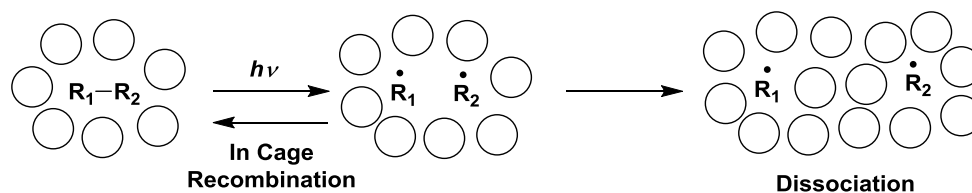
Scheme 2.2.: Cage effect for photochemical reactions under solvent or bulk conditions. Open circles represent the solvent or monomer.
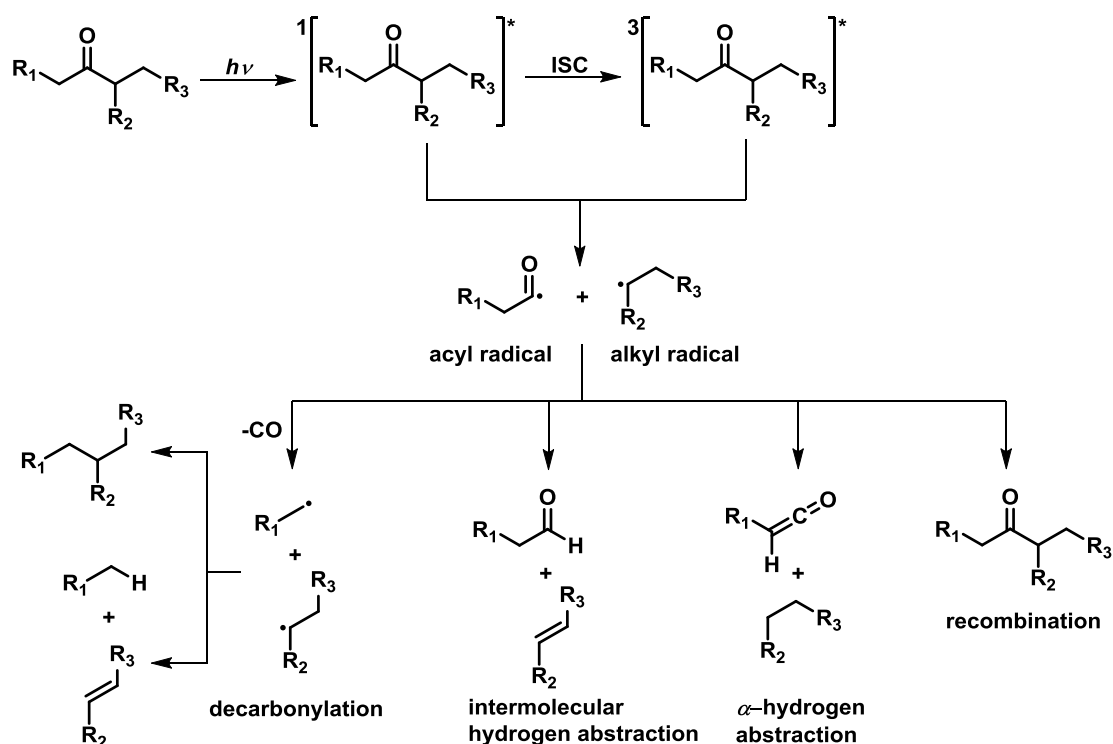
2.2.6 Norrish Type-Reactions

Norrish-type reactions are photochemical cleavage reactions, which occur in carbonyl compounds (aldehydes and ketones). In 1932, the photodecomposition of aldehydes and ketones after n-π^* excitation was for the first-time discovered and published by Norrish and coworkers.[85,86] The absorption properties of ketones and aldehydes are suitable for irradiation around 300 nm (n-π^* transition: 330-280 nm). The reactions can be mainly divided into two reaction groups: Norrish type I and II reactions.

Norrish Type I Reactions

The Norrish type I cleavage is a α–cleavage of a C-C bond, which further leads to a set of fragmentation reactions. The reaction takes place under UV light irradiation (300 nm) and the underlying mechanistic pathway of such reactions is illustrated by an example in Scheme 2.3, which will be explained in the following:

Upon light irradiation, the C-C bond cleaves into an acyl and alkyl radical, which can be formed via the excited singlet or triplet state.[87] The generated radicals can undergo several reactions, based on the movement of those radicals by diffusion and rotation. First of all, the acyl radical can undergo a decarbonylation reaction, which leads to carbon monoxide (CO) and a second alkyl radical. These alkyl radicals can further react via recombination with each other or via an intermolecular hydrogen abstraction, leading to an alkane and alkene. Secondly, the acyl and alkyl radical can undergo an intermolecular hydrogen abstraction, leading to an alkene and aldehyde. Thirdly, by presence of an α-hydrogen atom in the acyl radical, a ketene formation by hydrogen abstraction can occur. Finally, the acyl and alkyl radical can recombine inside the solvent cage.

Scheme 2.3.: The Norrish Type I reaction proceeds via α-cleavage of carbonyl functionalities such as aldehydes and ketones. The process yields highly reactive alkyl and acyl radicals, which are able to undergo various subsequent reactions.

Norrish Type II Reactions

Norrish-type II reaction occurs in molecules which possess a hydrogen atom in γ-position (three carbon positions from the carbonyl group). The underlying mechanistic pathway of such reactions is illustrated by an example in Scheme 2.4 and will be explained in the following:

Via the carbonyl functionality, the molecule is capable to undergo a light-induced intramolecular [1,5]-H shift leading to a bi-radical intermediate.[88] The presence of the latter was evidenced by photo racemization and quenching experiments.[89] Thus, the bi-radical can either be derived from an excited singlet or triplet state and is able to further undergo several reactions.[90,91] Firstly, the bi-radical can undergo an elimination reaction, leading to an alkene and enol, whereas the latter can tautomerize to a carbonyl molecule. Secondly, it can undergo a reverse [1,5]-H shift, leading to the starting molecule. Finally, a cyclisation reaction can take place which leads to cyclobutanol and is named as Yang-Cyclization.[92]
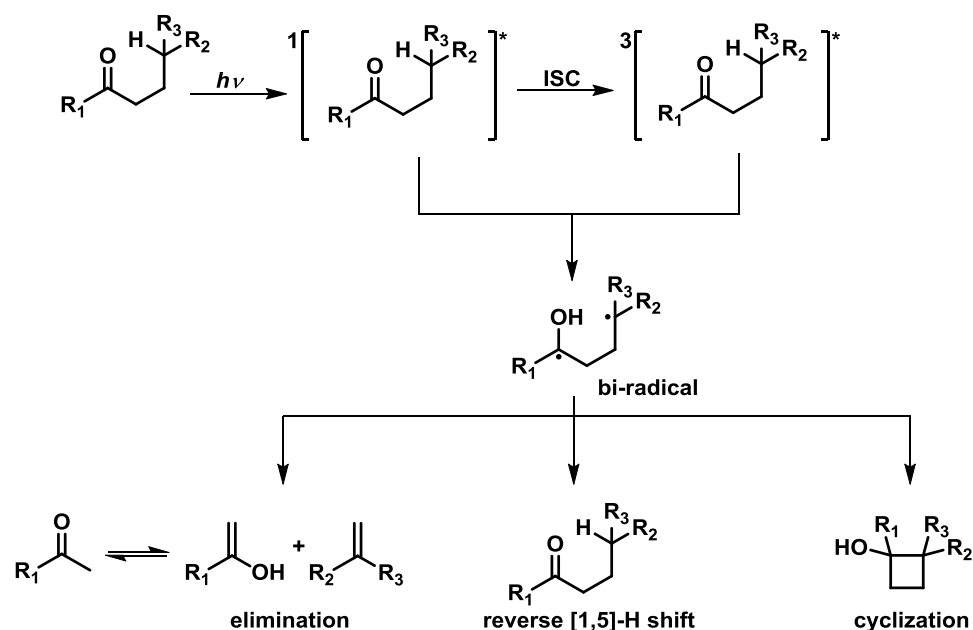
Scheme 2.4.: The Norrish-type II reaction proceeds via an intramolecular [1,5]-H shift, leading to the formation of a bi-radical molecule. The bi-radical species is able to undergo several subsequent reactions.

Norrish Type I Reactions vs. Norrish Type II Reactions

The nature of the photochemical cleavage reaction of carbonyl compounds strongly depends on the structure of the molecule itself and on the stability of the formed bi-radical. Cyclic ketones as well as lower aliphatic carbonyl compounds, in the latter possess no hydrogen atoms in γ-position, undergo Norrish-type I reactions. However, *tert*-butyl ketones also react – exceptionally and despite the presence of a hydrogen atom in γ-position – via Norrish type I reactions. Their behavior is based on the high stability of the generated *tert*-butyl radical. On the other hand, Norrish-type II reactions are observed for aliphatic ketones and long-chain alkyl phenyl ketones, which possess a hydrogen atom in γ-position. Short-chain alkyl phenyl ketones are capable of undergoing an external hydrogen abstraction, leading to pinacoles.

2.3 Radical Photoinitiators

Photoinitiators (PIs) play, next to the monomer, a major role in photoinduced polymerization reactions, since they are directly involved in the initiating step. Due to their chromophoric structure they are able to absorb light of a specific wavelength range and to convert it into reactive species, which can be radicals, cations or anions, leading to the initiation process. Radical photoinitiators can be categorized into two main classes: type I and type II PIs.

2.3.1 Type I Photoinitiators

Type I photoinitiators (PI) generate radicals in an unimolecular process, where in most cases the cleavage occurs in α-position to the carbonyl group at the CO-alkyl bond – so called α-cleavage – and is thus referred to as a Norrish type I reaction. However, the cleavage can occur at any weak bond and is not necessarily connected to the carbonyl moiety. The presence of weak bonds next to the α-carbon due to heteroatoms (C-Cl, C-S or C-N) leads to a β-cleavage or even a γ-cleavage. As an illustrative example, the alkylaminoacetophenone photoinitiator Irgacure 907 cleaves mainly upon light impact at the α-carbon atom, leading to the benzoyl and α-alkylamino radical. However, since it includes a nitrogen atom next to the α-carbon in its structure, a cleavage at the β-position can occur, which leads to the phenacyl and morpholino radical (refer to Scheme 2.5).[61]
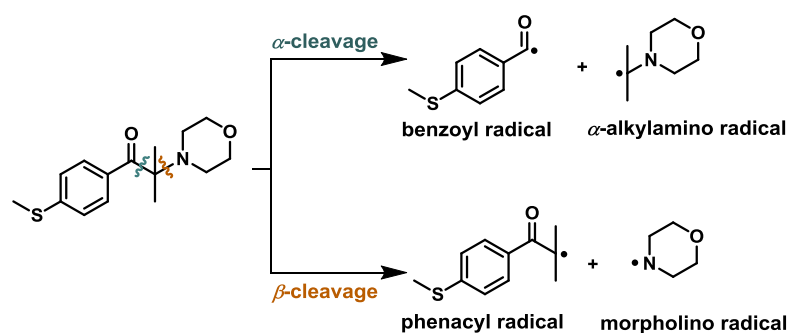
Scheme 2.5.: α- and β-cleavage of Irgacure 907.

In general, a type I initiator absorbs light of a specific wavelength which leads the molecule to an excited singlet state. Via intersystem crossing it can be transformed into a triplet state, thus leading to a α-cleavage or β-cleavage, where the first is often referred to as a Norrish type I reaction (refer to Scheme 2.6 for the mechanistic pathway). [81]


Scheme 2.6.: Photocleavage reaction from triplet state of type I photoinitiators.

The formation of radicals (R·) during such reactions follows first-order kinetics since only one species is involved in the photo-cleavage step (refer to Equation 2.12 and 2.13).

$$^{*}PI \xrightarrow{k} R_1 \cdot + R_2 \cdot \tag{2.12}$$

$$\frac{\mathrm{d}R_1 \cdot}{\mathrm{d}t} = \frac{\mathrm{d}R_2 \cdot}{\mathrm{d}t} = k \cdot {}^{*}PI \tag{2.13}$$

The advantages of type I initiators is based on their high quantum yields and reactivities. Due to the monomolecular formation of radicals, a higher radical flux can be obtained. Furthermore, when using styrene as the monomer, the PIs are particularly useful, since they show a low sensitivity to triplet quenchers.[93] However, some of these initiators feature a relatively low thermal stability. To demonstrate their structural diversity, some typical type I PIs (such as benzoin and α-hydroxy ketone) as well some specialized systems (such as sulfonyl ketone and ynone) are depicted in Scheme 2.7 and their characteristic features are described in the following:
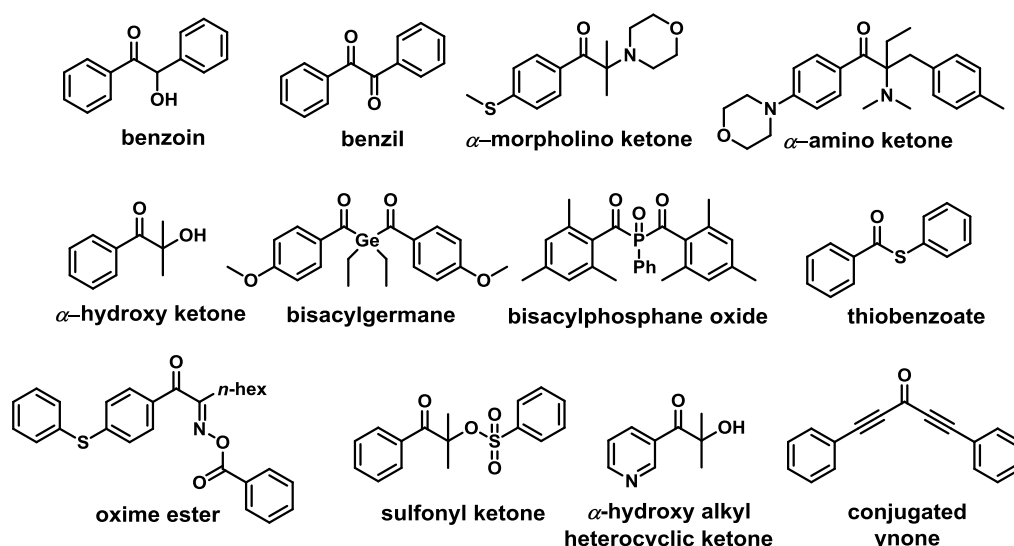
Scheme 2.7.: Various examples of type I photoinitiators.

- **Benzoin** and its derivatives are the most widely used PIs for radical polymerization of vinyl monomers.[94,95] They can be readily synthesized from benzaldehyde via benzoin condensation, which enables various modifications on the benzoyl moiety. These incorporated functional groups can have a strong influence on the initiating behavior.[96]

- **Benzil ketals** are efficient PIs based on the formation of a methyl and benzoyl radical.[97] However, the photocleavage produces also some odor and yellowing, which occurs due to the rearrangement of the first generated substituted benzyl radical. Due to the formation of the by-product methylbenzoate, which has a strong odor, benzil ketals are

not appropriate candidates for applications where aftertaste, e.g. food packaging, may be a problem.

- α-**Hydroxy ketones** are well-known, widely used and highly efficient PIs due to the high affinity of the produced hydroxy propyl radical towards the acrylate monomer. The water-soluble PI Irgacure 2959 is one of the most prominent representative of this PI class, since it can be readily modified with functional groups on the primary hydroxy group.[98,99]

- α-**Amino** and **Morpholino** based PIs are an important class of PIs due to their high efficiency and long term stability. The introduction of a morpholino group on the benzoyl group leads to a red-shifted absorption.[100]

- **Germanium** based PIs exhibit a red-shifted absorption, which is strongly pronounced for bisgermyl derivatives. Thus, the spectrum is red-shifted from approx. 360 nm to approximately 510 nm due to the contribution of the Ge d-orbitals.[101] A prominent example of such class of PIs is given by Ivocerin, which is mainly applied in dental curing and composite applications.

- **Bisacylphosphane oxides** such as Irgacure 819 are fast and efficient photoinitiators due to their ability to undergo secondary cleavage processes, leading to four active radicals. Thus, the polymer bearing a mesitoylphosphanoyl end group is capable of undergoing further cleavage processes during irradiation, which produces a mesitoyl radical plus a polymeric phosphanoyl radical.[102]

- **Oxime esters**, which undergo an α-cleavage reaction, possess a rather complex photochemistry compared to those which cleave upon irradiation at the γ-position.

- **Sulfonyl ketones** can cleave at the β-position (C-S bond) to release sulphinic acid radicals, which are inefficient catalysts for further polymerization reactions, but easily undergo hydrogen abstractions with neutral donors to produce sulphinic acid.[103]

- **Thiobenzoates** produces a benzoyl and a thiyl radical upon light impact. The latter is an attractive initiating species since it is not selective towards the addition to monomers. Furthermore, the thiyl radical shows a lower sensitivity to oxygen and is therefore highly efficient.[81]

- α-**Hydroxy alkyl heterocyclic ketones** are mostly produced to increase or decrease the electron density of the aromatic system. The rate of polymerization is higher when employing electron-poor heterocycles and reduced using electron-rich heterocycles.[81]

- **Conjugated ynones** are interesting PIs due to their extended chromophoric system.[104,105] However, the generation of radicals in the absence or presence of a co-initiator is rather complex compared to other type I PIs such as benzoin.
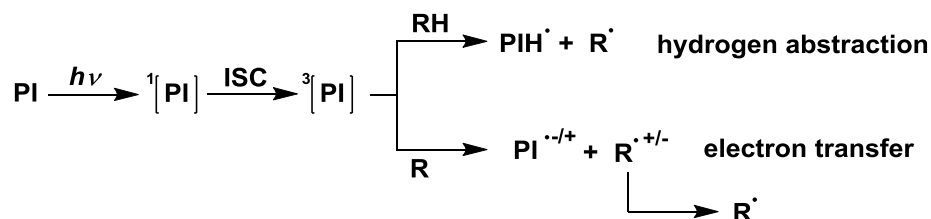
2.3.2 Type II Photoinitiators

Type II photoinitiators (PIs) produce, in contrast to type I photoinitiators, radicals via a bimolecular process. Due to their low excitation energy, which is required for fragmentation, their excited states cannot undergo type I reactions. However, they can react with a co-initiator (COI, such as amines or thiols) to generate radicals (R·). In this case, the formation of radicals follows a second-order kinetic since two species are involved (refer to Equation 2.14 and 2.15).

$$^{*}PI + COI \xrightarrow{k} R_1 \cdot + R_2 \cdot \tag{2.14}$$

$$\frac{dR_1\cdot}{dt} = \frac{dR_2\cdot}{dt} = k \cdot {}^{*}PI \cdot COI \tag{2.15}$$

The formation of initiating species occurs via two distinct pathways, illustrated in Scheme 2.8 and explained in the following: [81]

Scheme 2.8.: Hydrogen abstraction and electron transfer reactions from triplet state of type II photoinitiators.

- **Hydrogen abstraction** occurs from a suitable hydrogen donor (co-initiator) and is limited to diaryl ketones. Thus, a proton-transfer from the α-position of the co-initiator to the excited PI leads to the formation of a ketyl radical and a radical which stems from the co-initiator. Amines, thiols, alcohols, silanes and many other species can be used as co-initiators, whereby tertiary amines show the highest efficiency as hydrogen donors. However, only the radical from the co-initiator starts the initiation process, due to the resonance stabilization and steric hindrance of the formed ketyl radical. Thus, this radical can act in the termination step via combination with a growing polymer chain.

- **Electron transfer** is besides the hydrogen abstraction a further possibility of type II initiators to produce initiating species. Thus, the PI in its triplet state acts as a photosensitizer with a co-initiator, whereby after subsequent fragmentation reactions, an initiating species is formed. This species maybe a radical as well cations or anions. In this context, the photosensitizer can act either as electron donor or acceptor depending on the nature of the sensitizer and co-initiator.

Type II PIs are widely used in industry as well as fundamental research. However, these type II reactions feature some disadvantages. Firstly, the system requires highly volatile and odorous amines as hydrogen donors. Furthermore, the overall process is more sensitive to quenching of the excited PI by oxygen or monomer. Typical type II initiators as well a few possible co-initiators are depicted in Scheme 2.9 and will be described, with regard to their specific characteristics, in the following:[106]
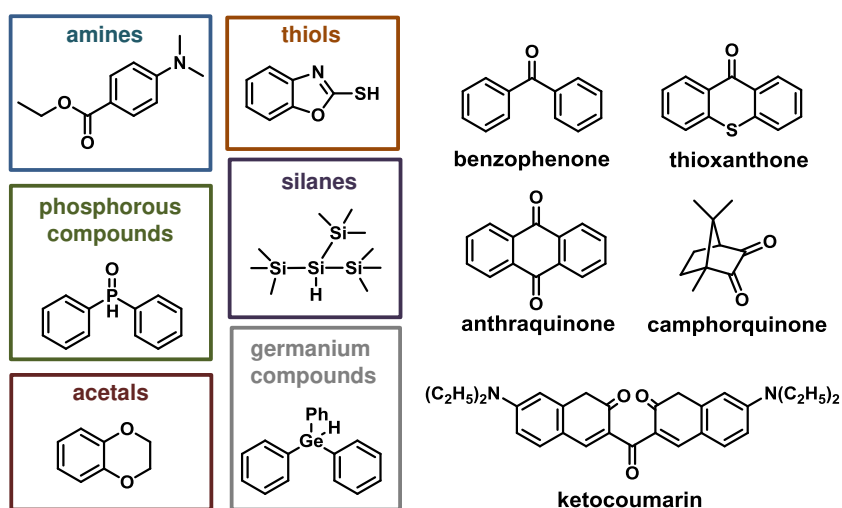
Scheme 2.9.: Examples of type II photoinitiators (right side) and co-initiators such as amines, thiols and phosphorous compounds (boxes, left side).

- **Benzophenones** are very cost-effective PIs and widely used in varnishes and inks.[107] They have a distinctive odor, which can affect the finish product, especially since due to their low molecular weight they are very prone to migration. Furthermore, benzophenone itself can lead to some long-term yellowing. Its derivative, methyl-benzophenone, is similar to benzophenone with regard to reactivity, but less volatile and less odorous.

- **Thioxanthones** feature high triplet energies and can be therefore additionally used to sensitize other PIs.[108,109] Thioxanthones possess an intrinsically yellow color, which will affect the finished product, when residue initiator remains.

- **Anthraquinones** are relatively unaffected by oxygen, since oxygen is consumed during the regeneration of anthraquinone through the oxidation of dihydroxyanthraquinone and is therefore an efficient PI. [81]

- **Camphorquinones** absorb light in the visible region (peak absorption at 468 nm), and can therefore be excited with a blue light lamp (~438 nm), which is exploited in dental composite applications.[110]

- **Ketocoumarins** can be employed as type II initiators and photosensitizer, and the latter is used in a three component system.[111]

2.4 Lasers

LASER is an abbreviation for 'Light Amplification by Stimulated Emission of Radiation'. In 1917, Einstein described the emission as an inversion of the absorption and thus laid the groundwork for the development of laser. Thirty seven years later, Townes and co-workers developed a microwave amplifier, called MASER (Microwave Amplification by Stimulated Emission of Radiation), which is based on the principle of stimulated emission of radiation.[112] In 1958, Townes[113] and co-workers extended the concept of MASER to light and two years later the first laser device was built by Maiman.[114] A laser produces a highly directional, monochromatic, coherent and polarized light beam through a process called stimulated emission of radiation which amplifies or increases the intensity of light. A laser consists of three main components (refer to Figure 2.7), i.e. lasing medium, pump source and optical resonator. The details of each component will be explained in the following:
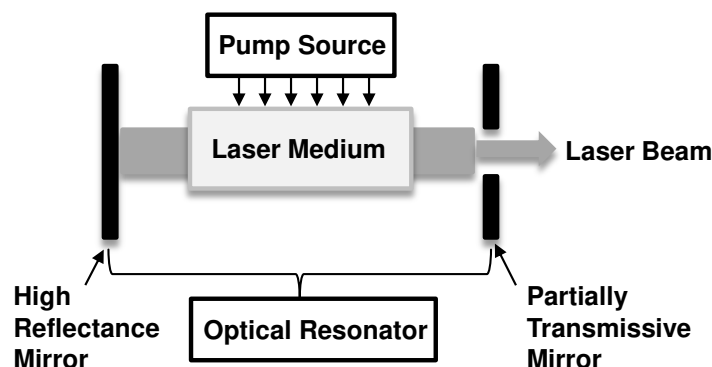
Figure 2.7.: Schematic diagram of a laser.[77]

Lasing Medium

The lasing medium can be a solid (crystals, glasses and semiconductors; e.g. ruby, Nd:YAG, Ti:sapphire), a liquid (organic dyes, e.g. rhodamine) or a gas (gas mixture, e.g. Ar, CO_2, HeNe, ArF) and usually the type of laser is named after the employed lasing medium. The medium is capable of undergoing population inversion (refer to Section **Population Inversion**), which determines the wavelength.

Pump Source

The pump source supplies the necessary energy to the laser medium, enabling light amplification. There are several types of pump sources: optical (flash lamps, continuous arc lamps, tungsten-filament lamps or even other lasers), electrical (gas discharge tubes, electric current in semiconductors), or chemical pumps.

Optical Resonator

In the simplest form, an optical resonator consists of two mirrors, which are arranged in a way that the photons pass back and forth along the length of the lasing medium being amplified each time. Typically, one mirror (output coupler) is partially transparent to allow the laser beam to exit the lasing medium.

Examples of Laser Types

There are a wide range of commercially available lasers (refer to Table 2.1.) Herein, specific attention will be paid to excimer (refer to Section 2.4.2) and tunable lasers (refer to Section 2.4.3), since these are the two types of lasers employed in the current thesis for the photoinduced synthesis and irradiation of the polymers.

Table 2.1.: Examples of laser types.[115]

Laser Medium	Type	Wavelength	Pump Source
CO_2	Gas	10600 nm	Electrical discharge
Argon	Gas	500 nm	Electrical discharge
HeNe	Gas	630 nm	Electrical discharge
Excimer (Ar:F)	Gas	193 nm	Electrical discharge
Dye	Liquid	390-640 nm	Other Laser, Flash lamp
Ruby	Solid	694 nm	Flash lamp
Nd:YAG	Solid	1064 nm	Flash lamp, Laser diode
AlGaAs	Solid (Semi-conductor)	630-900 nm	Electric current

2.4.1 Principle of Operation

Electrons can move between different energy levels (ground state energy level to excited state level and vice versa), since the atom absorbs or releases energy in form of photons. The interaction and mechanistic pathways between electrons and photons are depicted in Figure 2.8.
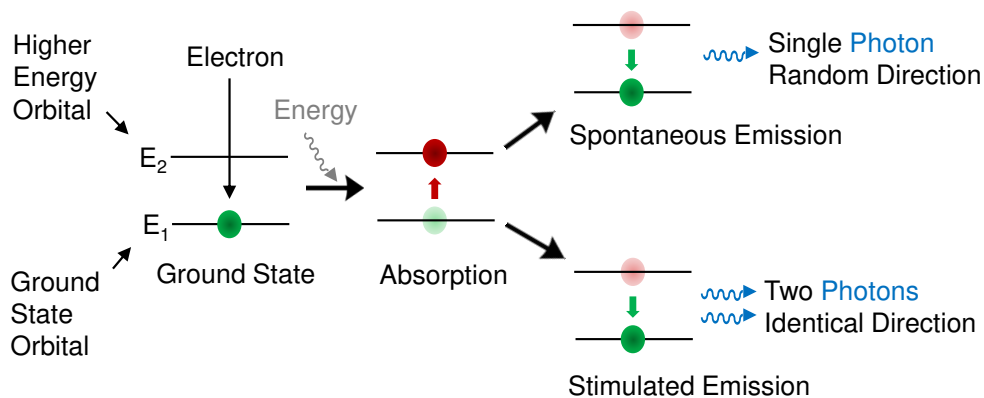

Figure 2.8.: Mechanistic pathways of the interaction between photons and electrons of an atom that generates a laser beam.[115]

The absorption of energy (from the pump source) causes the transition of an electron from the ground state energy level (E_1) to an excited level (E_2). After a certain time, an electron in a high-energy orbital (E_2) finally returns to the low energy-orbital (E_1) and the energy difference is released in form of a photon, which possesses a random phase and direction. This process is called spontaneous emission. Based on this process an incandescent bulb, neon light, fluorescent tube, cathode ray tube or heating element produces light. The energy difference (photon) is given by:

$$E_2 - E_1 = h\nu \tag{2.16}$$

where h is Planck's constant ($6.63 \cdot 10^{-34}$ Js) and ν the frequency.[116] However, when an electron collides with other excited electrons a second photon will be released, which possesses identical phase, direction, polarization and energy to the incident photon. This process is in contrast to spontaneous emission and it is called stimulated emission. Herein, the photons are reflected back and forth between the two mirrors along the axis of the lasing medium. More and more photons are stimulated, which leads to a cascade reaction and thus results in amplification or optical gain. If a majority of atoms is maintained in the excited state ("population inversion", see next Section) by the continuous energy input from the pump source, a sustained laser beam will be generated and can be released via the partially reflective mirror (output coupler). The laser beam can be pulsed or continuously, depending on the pumping is intermittent or not. The length (L) of the

optical resonator, in which the photons can populate, has a strong impact on the wavelength of the out coming laser beam and is described by

$$L = n\frac{1}{2}\lambda \tag{2.17}$$

where n is an integer.

Population Inversion

Population inversion is the process of achieving greater population in the higher energy state as compared to the lower energy state, which is required for laser operation. In a two level-system, the population of the higher energy state is negligible compared to the population of lower energy state, and is described by the Boltzmann distribution

$$\frac{N_1}{N_0} = \exp\left(\frac{-\Delta E}{k_B T}\right) \tag{2.18}$$

where N_1 and N_0 are the populations of the excited state and the ground state, ΔE the energy gap between the two states and k_B and T are Boltzmann constant and the temperature. As a result, N_1 can never become larger than N_0. In order to achieve population inversion, more energy states (three-level or four-level laser systems) are necessary, as illustrated in Figure 2.9.

In a three-level laser system, the lower energy state (1) absorbs sufficient energy and jumps into the higher energy state (2). This process is termed energy pumping. Due to the short life-time of state 2, a rapid decay through internal conversion or intersystem crossing into a third state, which is energetically lower, occurs. The life-time of state 3 is higher compared to state 2, which leads to a higher accumulation of population. Thus, population inversion between energy state 3 and 1 can be achieved. After its life-time, spontaneous emission from state 3 to state 1 triggers stimulated emission and thus light amplification. In a four-level system, the third state does not return to the ground state after stimulated emission, yet rather into a fourth state. This level is energetically higher than the ground state and barely populated, which makes a four-level laser more efficient than a three-level laser system.
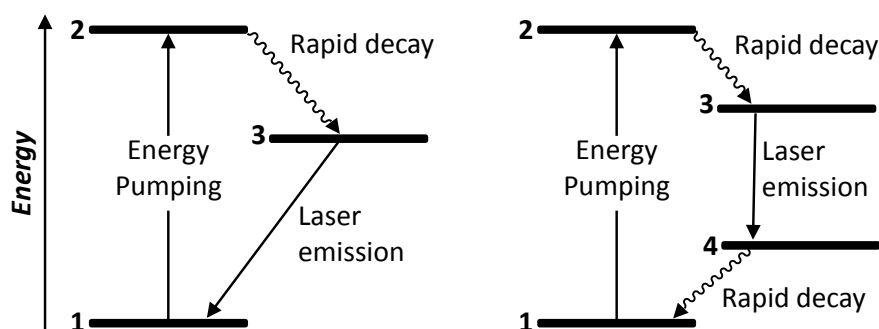
Figure 2.9.: Schematic illustration of three-level (left side) and four-level (right side) laser systems.[77]

2.4.2 Excimer Laser

In an excimer laser, the lasing material consists of gas or gas mixtures, which are capable to form an excimer (excited dimer). The lasing gaseous material is embedded in a cylindrical double-wall quartz tube (laser tube), which features electrodes on the inner and outer wall of the quartz tube. By applying high voltage with high frequency, micro discharges in the gas occur producing the laser beam. The underlying mechanism will be explained on the basis of xenon (Xe_2) as an example:

Electrons which are produced and accelerated during the micro discharge transfer their energy to xenon atoms, leading to xenon-ions (Xe^+) and excited xenon atoms (Xe^*).

$$e^- + Xe \rightarrow Xe^*, Xe^+ \tag{2.19}$$

In a second step, an excited $Xe_2{}^*$ molecule (excited dimer = excimer) is formed through the reaction of two xenon atoms in the ground state with one excited Xe^* atom.

$$Xe^* + 2Xe \rightarrow Xe_2{}^*, Xe \tag{2.20}$$

The excimer emits a photon with a wavelength at 172 nm. The resulting ground state is unstable and decomposes into two xenon atoms.

$$Xe_2{}^* \rightarrow 2Xe + h\nu \, (172 \, nm) \tag{2.21}$$
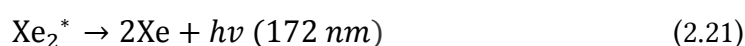
The emitting wavelength of an excimer laser depends on the employed gas or gas mixtures and an overview of some commercially available gas mixtures is listed below.

- XeCl*, λ = 308 nm

- XeF*, λ = 351 nm

- KrF*, λ = 249 nm

- ArF*, λ = 193 nm

Specifically, for the synthesis and irradiation of photoinduced polymers in the current thesis, an excimer laser with a gas mixture of XeF* was utilized, which produces monochromatic and pulsed light at a wavelength of 351 nm.

2.4.3 Tunable Laser

A tunable laser is a laser, whose output wavelength can be adjusted. Tunable laser irradiation can be achieved from one source or a combination of two sources, whereby most of the visible, near-infrared and medium-infrared spectral regions are covered. Nowadays, there are many different tunable laser systems, which are based for example on dye lasers[117] or optical parametric oscillators (OPO).[118] The first one is a primary laser and can be continuously pumped. The latter one is a secondary laser, since it requires a coherent pump source. An OPO can be used for wideband tuning in various spectral regions and was therefore applied for all the wavelength-dependent studies in the current thesis. In an OPO the optical gain is based on parametric amplification by an oscillating pump-pulse in a non-linear crystal, including a three photon process. The pump photon, in a three photon process, is converted into a so-called "signal" photon with higher energy (shorter wavelength) and an "idler" photon with lower energy (higher wavelength), depending on the phase-matching conditions. Due to conservation of energy, the relationship between the energies of the three photons can be written as:

$$E_{\text{pump}} = E_{\text{signal}} + E_{\text{idler}} \tag{2.22}$$

Thus, the main feature of an OPO is that the output photon energy can be varied in wide ranges. Figure 2.10 depicts the scheme of the laser set-up employed in the current thesis.
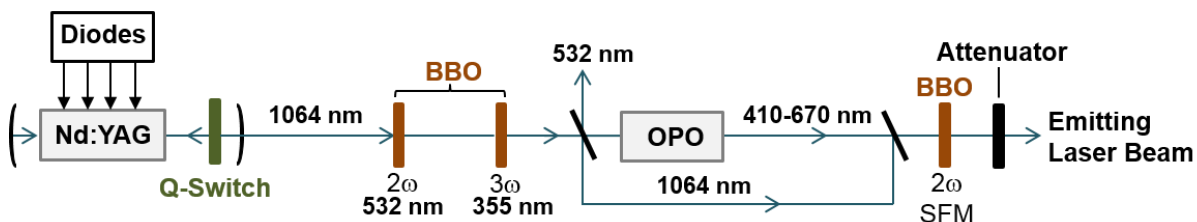

Figure 2.10.: Schematic illustration of the beam path of the applied tunable laser system.

The operating mode, the assembly and the way of the beam path of such a tunable laser, which integrates and combines a Nd:YAG laser, as well an OPO, will be explained in the following:

A Nd:YAG laser is a four-level laser and the lasing medium consists of Neodym^{3+} ions (Nd), which are embedded in a transparent $Y_3Al_5O_{12}$ crystal, called YAG (Yttrium Aluminium Granat). The Nd:YAG laser is coherently pumped with diodes. A Q-switch delays and shortens the pulses producing pulses with extremely high peak power. The laser emits then a pulsed-laser beam with a wavelength of 1064 nm, a frequency of 100 Hz and a pulse-length between 5-7 ns. By incorporating non-linear crystals (BBO = β-Barium-Borat) the laser beam is first frequency-doubled (λ = 532 nm) and then frequency-tripled (λ = 355 nm). A subsequently mirror reflects the laser beam with λ = 532 nm and λ = 1064 nm. The OPO itself is then pumped with the frequency-tripled wavelength at 355 nm. Due to non-linear processes, the output wavelengths of the OPO range from 410-670 nm. To access the wavelength ranges in the UV region, it is necessary to feed the OPO output into non-linear crystals (BBO) to perform SHG (frequency-doubling) or SFG (frequency-mixing) processes. Thus, the previously reflected laser beam with λ = 1064 nm is utilized for the SFG process. The subsequent attenuator amplifies the laser beam and separates the UV region from the Vis region. The overall possible wavelength ranges are listed below:

- 1. OPO: 410-670 nm
- 2. SFG: 295-410 nm
- 3. SHG: 270-310 nm

2.5 Chemically Induced Dynamic Nuclear Polarization (CIDNP)

The appearance of anomalous intensity patterns of nuclear magnetic resonance (NMR) lines recorded during certain chemical reactions can be described by a magnetic resonance effect called Chemically Induced Dynamic Nuclear Polarization (CIDNP). This effect can be explained by the radical pair mechanism[119,120] and is based on the interactions between unpaired electrons and nuclear spins, resulting in non-Boltzmann populations of magnetic energy levels. Thus, CIDNP spectra display so-called polarized NMR signals with enhanced absorption or emission.[121,122] CIDNP spectroscopy is utilized to study the reaction mechanism of chemical reactions involving radical pairs. The chemical shift of CIDNP spectra provides structural information on the generated products and the polarization of the signals contains information on the reaction pathway.

2.5.1 Radical Pair Mechanism

The radical pair mechanism, on which the CIDNP effect is based, was discovered by the group of Hans Fischer in 1967. It provides an explanation for the observed enhanced absorption and emission signals, which can be categorized into the net and multiplet effect and are illustrated in Figure 2.11.

- **Net effect:**

  All the signals show either enhanced emission or absorption.

- **Multiplet effect:**

  Different polarizations are observed in the same multiplet. With respect to the sequence of the emission or absorption transitions from lower field (higher chemical shift) to higher field (lower chemical shift) the patterns are defined as absorption/emission (A/E) or emission/absorption (E/A).
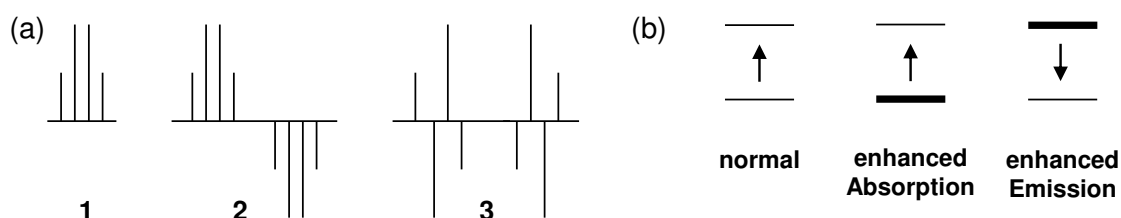

Figure 2.11.: (a) Quadruplet exhibiting CIDNP: (1) thermal equilibrium, (2) net effects, (3) multiplet effects. (b) Corresponding spin populations, under normal, enhanced absorption and emission conditions.[123]

In general, the radical pair mechanism can be explained as a three step process and is illustrated in Figure 2.12. First, a radical pair (indicated by an overline) is formed from a triplet precursor (light induced) or singlet precursor (thermally induced) by homolytic bond cleavage or electron transfer, having the same multiplicity as the precursor molecule.[124] In a second step, the radical pair can undergo nuclear spin selective singlet-triplet mixing via intersystem crossing. In the final step, subsequent reactions of singlet and triplet radical pairs occur, leading to the products which can be observed in the NMR spectrum. These products are designated as so called "cage products" (or "recombination products") and "escape products". The former is formed when the radical pair recombines and the latter is observed when the radicals escape the solvent cage. Based on the Pauli principle, recombination reactions can only occur from the singlet state and thus singlet-triplet mixing is required for the generation of escape products from triplet radical pairs.[121]
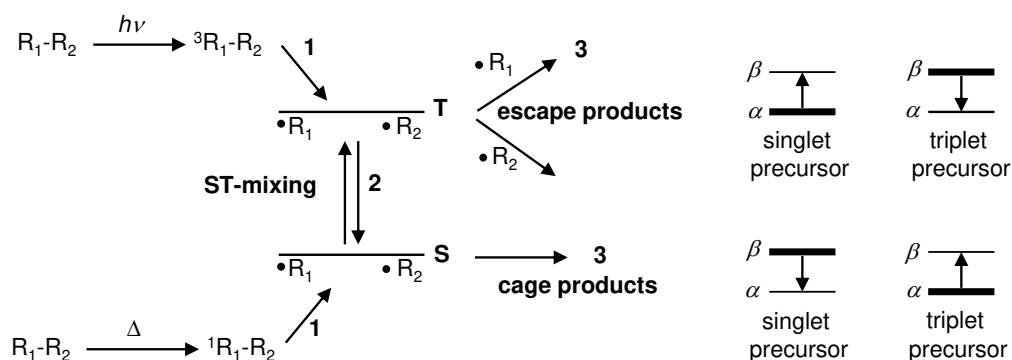
Figure 2.12.: General CIDNP reaction scheme. Step 1 is the generation of a radical pair. Step 2 involves nuclear-spin-selective intersystem crossing of the radical pair. Step 3 comprises different subsequent reactions of singlet and triplet radical pairs (cage product and escape product).[123]

The energies of singlet and triplet radical pairs are distance dependent and in the presence of an external magnetic field, the triplet state is additionally split into three sublevels (T_1, T_0 or T_2) as depicted in Figure 2.13.[123] Thus, the intersystem crossing from the singlet state to one of the three triplet states (or vice versa) is only possible at a certain radical-radical ($r > r^*$) distance r (indicated by a double-headed arrow, refer to Figure 2.13). However, the transition can only occur at distances where the exchange interaction $J(r)$ is small enough.

Figure 2.13.: Energy levels of singlet and triplet radical pairs as a function of the distance between the radicals.[121,123]

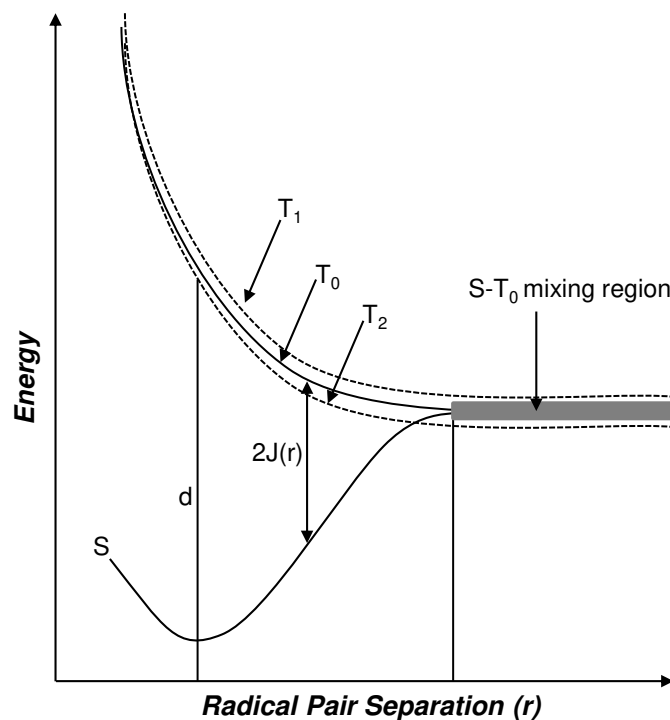The S-T_0 mixing process itself can be simply described by the vector model illustrated in Figure 2.14.[123] The mixing process of the spin states (S and T_0) is possible as a result of slight deviations in the Larmor frequency of these two spins, which is induced by small magnetic field variations.[125] Thus, the rate of S-T_0 mixing is proportional to the difference in the Larmor frequencies $\Delta\omega$ of the two electron spins and can be described by Equation 2.23.[126]

$$\Delta\omega = \omega_1 - \omega_2 = \frac{1}{2}\left[H_0\,\Delta g\,\beta_e\,h^{-1} + \sum_{i=1}^{n} a_{1\mathrm{i}}\,m_{1\mathrm{i}} - \sum_{j=1}^{k} a_{2\mathrm{j}}m_{2\mathrm{j}} \right] \qquad (2.23)$$

Where ϖ_1 and ϖ_2 are the Larmor frequencies of the unpaired electron spins of R_1 and R_2, H_0 is the strength of the magnetic field, Δg is the difference of g-factors of radical R_1 and R_2, β_e is the Bohr magneton and $a_{1\mathrm{i}}$, $m_{1\mathrm{i}}$, $a_{2\mathrm{j}}$ as well as $m_{2\mathrm{j}}$ are hyperfine coupling constant and magnetic quantum number of nuclei i and j in radical R_1 and R_2.

According to Equation 2.23, the rate of S-T_0 mixing depends on the magnetic field, the g factor difference of the two radicals, the magnitude of the hyperfine coupling constant and the nuclear spin orientation, reflected in the magnetic quantum number m. For instance, for a nucleus with a spin of ½ (like a proton), the value of m can be +½ (α) or -½ (β). Thus, the rate of S-T_0 mixing is higher in the case of a α-spin than for a β-spin, as $\Delta\varpi_+$ is larger than $\Delta\varpi_-$, which can be clearly

seen in Equation 2.24 and 2.25. Both equations are valid for a radical pair, where only one radical pair bears a magnetically active nuclear spin of ½.

$$\alpha, m_{1i} = +\frac{1}{2}, \qquad \Delta\omega_+ = \frac{1}{2}\left[H_0\,\Delta g\,\beta_e\,h^{-1} + \frac{1}{2}a_{1i}\right] \tag{2.24}$$

$$\beta, m_{1i} = -\frac{1}{2}, \qquad \Delta\omega_- = \frac{1}{2}\left[H_0\,\Delta g\,\beta_e\,h^{-1} - \frac{1}{2}a_{1i}\right] \tag{2.25}$$

Therefore, triplet radical pairs with α nuclear spins reach the singlet state faster than triplet radical pairs with β-spins. Thus, it can be explained why cage products formed from triplet precursors show enhanced absorption (α-spin levels overpopulated, refer to the right side of Figure 2.12), while the corresponding escape products show enhanced emission (β-spin levels overpopulated, refer to the right side of Figure 2.12). Enhanced absorption and emission are called CIDNP polarization, whereby polarizations from cage and escape products always have opposite signs.
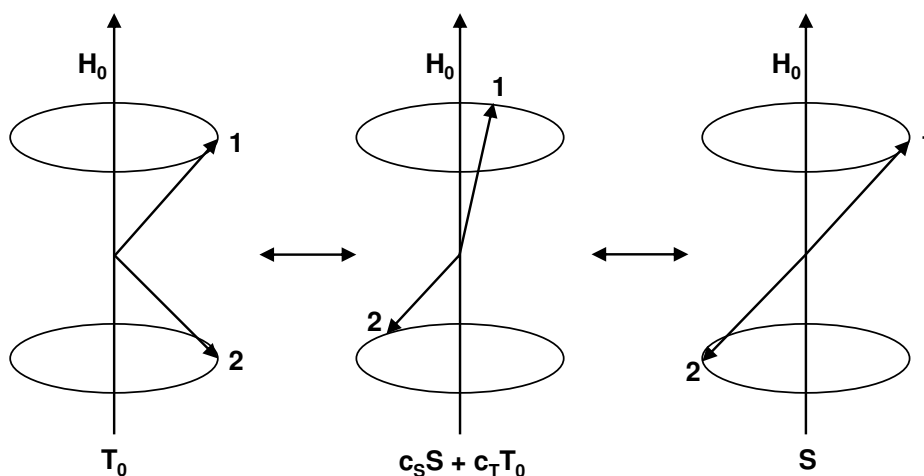
Figure 2.14.: Vector representation of S-T_0 mixing for the electron spins 1 and 2 ($c_S + c_{T0} = 1$).[121,123]

2.5.2 Kaptein´s Rule

A qualitative interpretation of CIDNP spectra can be made by applying Kaptein´s rules.[127]

- **Net effect** (Γ_{ne}):

$$\Gamma_{ne} = \mu\,\varepsilon\,\Delta g\,a_i \tag{2.26}$$

- **Multiplet effect** (Γ_{me}) of a nucleus i coupled to nucleus j:

$$\Gamma_{me} = \mu\,\varepsilon\,\Delta g\,a_i\,a_j\,J_{ij}\,\delta_{ij} \tag{2.27}$$

Where μ represents the multiplicity of the precursor (which is defined as +1 in case of a triplet precursor and as -1 for a singlet precursor) and ε states for cage (+1) and escape (-1) products, Δg takes into account the sign of the g value difference of both radicals, a is the sign of the hyperfine constant of the nucleus i and j, J is the sign of the coupling constant and δ describes whether both nuclei are on the same radical (+1) or not (-1).

Based on these rules it is possible to make predictions of the sign of the polarizations. The signals of the resulting CIDNP spectra show net effects (enhanced emission or absorption) and multiplet effects (different polarization, observed in the same multiplet), which can be analyzed by these rules.

2.5.3 Experimental Setup

In the present thesis photo-CIDNP spectroscopy was employed to investigate the photoinduced cleavage mechanism of photoinitiator-derived polymer end groups. Photo-CIDNP measurements were carried out by D. E. Fast in Graz in collaboration with the group of G. Gescheidt. The experimental setup mainly consists of a Nd:YAG laser serving as the pulsed light source (ns pulses) and a NMR spectrometer equipped with a special CIDNP probehead. The laser beam was directed via various prisms into the flat bottom of a quartz rod, transferred into the probehead and diverted by 90°, to reach the sample in the middle of the receiver coils. The experimental setup of such a photo-CIDNP experiment including a close-up of a CIDNP probehead is displayed in Figure 2.15.
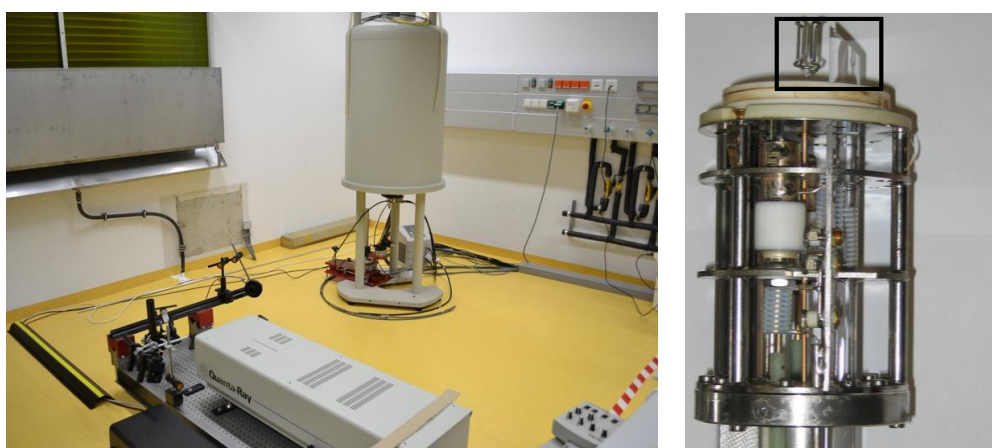

Figure 2.15.: Schematic Setup of a photo-CIDNP experiment (left side) and a special NMR probe head (right side) for photo-CIDNP experiments. The optical fiber is marked in a black box.

2.6 Mass Spectrometry (MS)

Mass spectrometry (MS) is a sensitive and versatile tool to identify the exact mass of substrates in biology and chemistry. In general, uncharged substrates are transformed to ions, since uncharged species cannot be directly detected by the mass spectrometer. Once the species are charged, the ions are subsequently separated and detected in accordance to their mass-to-charge (m/z) ratio. The obtained mass spectrum enables drawing conclusions about which ions were formed and in which relative intensities. Thus, information regarding the structure of single substances and quantitative as well qualitative compositions of mixtures can be obtained.

In principle, a mass spectrometer consists of three main components. The general scheme of a mass spectrometer is depicted in Figure 2.16. First, the sample is injected into the inlet system and the molecules are subsequently transferred into gaseous ions in an ion source. To prevent inadvertent collisions of the ionized molecules with gas molecules of the atmosphere, the ion source as well as the other two main components are kept under high vacuum. After the generation of ions, they are accelerated, focused in a beam and subsequently separated in the mass analyzer, due to their m/z ratio. In a last step, the m/z separated ions are counted by the detector and converted into an electrical signal (data processing).

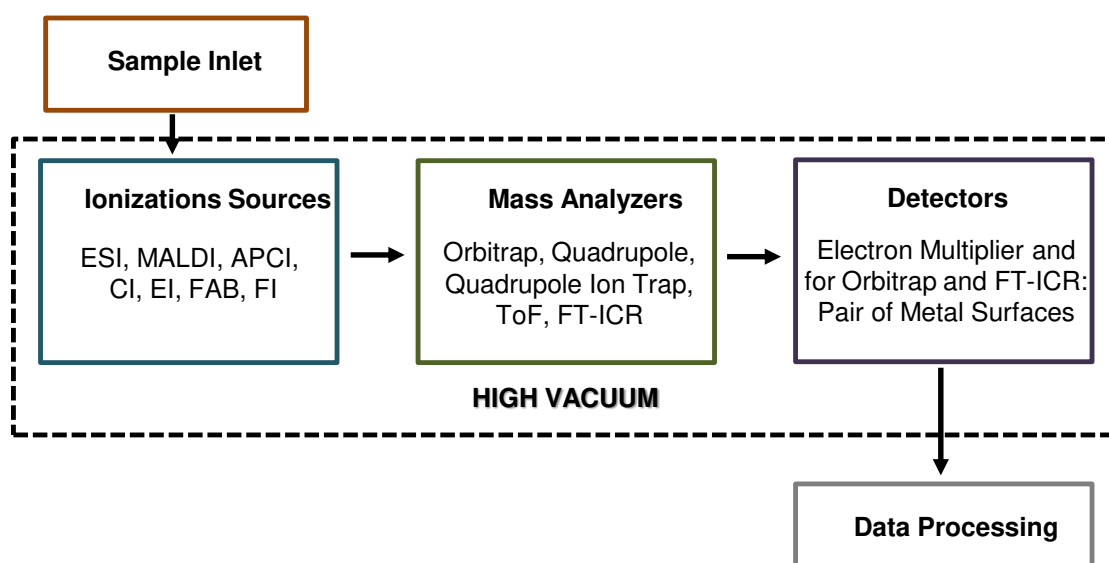**Figure 2.16.:** Three main components in a mass spectrometer: an ionization source, a mass analyzer and a detector. ESI = electrospray ionization, MALDI = matrix-assisted laser desorption ionization, APCI = atmospheric pressure chemical ionization, CI = chemical ionization, EI = electron ionization, FAB = fast atom bombardment, FI = field ionization, ToF = time-of-flight, and FT-ICR = fourier transform ion cyclotron resonance.

2.6.1 Ionization Sources

Basically, there are two principle ionization techniques, i.e. hard and soft ionization. In hard ionization techniques, such as electron ionization (EI), fast atom bombardment (FAB), and field ionization (FI), the molecules are cleaved into fragments on an atomic level. In contrast, by applying soft ionization techniques, the entirely molecular ion stays intact. Frequently, these methods are applied for biomolecules such as enzymes or peptides, but also applied in the field of synthetic macromolecule analysis. The soft ionization techniques include electrospray ionization (ESI) and matrix-assisted laser desorption ionization (MALDI) (see further details in the Sections below) as well chemical ionization (CI) and atmospheric pressure chemical ionization (APCI).

Electrospray Ionization (ESI)

The electrospray ionization (ESI) method, as alluded to before, belongs to the soft ionization techniques and was established by Yamashita and Fenn in 1984.[128,129] In 2002, Fenn was awarded the Nobel Prize in Chemistry for the development of the ESI technique in mass spectrometry. The ESI method possesses two advantages: Firstly, multiple charged ions can be obtained extending the accessible mass range and secondly, the fragmentation during ionization is reduced. Before starting the ESI process, the analyte needs to be diluted in an appropriate solvent mixture, which additionally contains a salt. In the field of polymer chemistry, a 100 micromolar (µm) solution of sodium trifluoroacetate in tetrahydrofuran (THF) and methanol (3:2) or in dichloromethane (DCM) and methanol (3:1) has been shown to be good conditions for ESI MS measurements. The addition of salt to the analyte solution and the choice of solvent can influence the ionization process, leading to super charging of the analyte.[130] Technically, the ESI process (refer to Figure 2.17) commences with the transfer of the analyte into the ion source at flow rates typically in the order of 5 microliter per minute ($\mu L \cdot min^{-1}$). The analyte solution flow is forced through an electrospray needle, where a high electronic potential (approximately 4 kilo-volt (kV)) is applied between the tip of the needle and the counter electrode. Due to the strong potential, highly charged droplets are formed into a so-called Taylor cone[131] (resulting from charge repulsion) at the tip of needle. The droplet is sprayed towards the source sampling cone and solvent evaporation occurs, which is often supported by applying elevated temperatures and an inert gas (most of the time nitrogen (N_2)) stream. The solvent evaporation leads to a shrinkage of the droplet, until the so-called Rayleigh limit[132] (critical ratio of surface charge to surface area) is reached. At that point a coulombic explosion takes place generating

smaller droplets. This shrinkage process is repeated and naked charged analyte molecules (singly or multiply charged) are obtained.
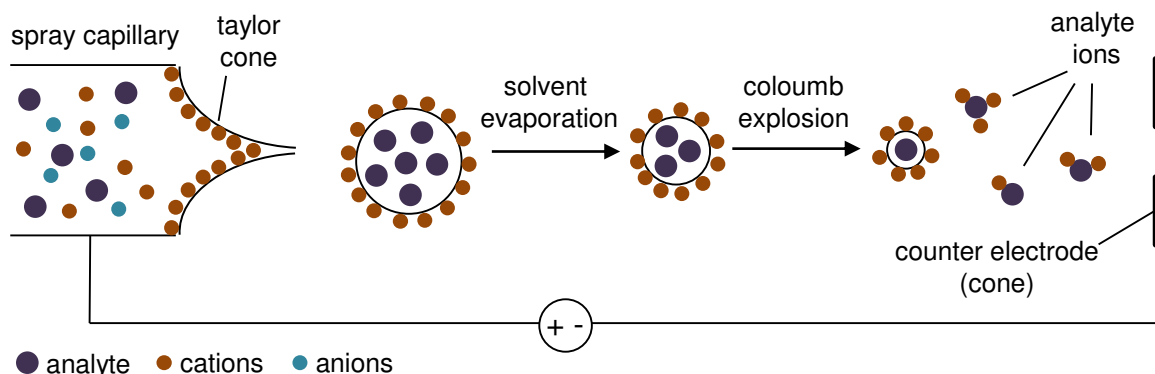

Figure 2.17.: Schematic overview of the mechanism of ion formation via ESI. Modified from reference [133] with permission from the Hindawi Publishing corporation.

Matrix Assisted Laser Desorption Ionization (MALDI)

In addition to ESI MS, MALDI is an alternative soft ionization method, which was first developed by Tanaka and Hillenkamp and is often combined with a time-of-flight (ToF) detector.[134,135] In 2002, Tanaka was awarded the Nobel Prize in Chemistry for the development of the MALDI technique in mass spectrometry. The MALDI process starts with the co-crystallization of the substrate with a MALDI matrix, where the matrix absorbs in the wavelength range of the applied laser (e.g., a N_2-Laser at λ = 337 nm can be combined with nicotinic acid or 2,5-dihydroxy benzoic acid), on a target. Laser-irradiation leads to the desorption of primarily single charged substrate ions[136] (positive or negative), due to the absorbed energy of the matrix. Compared to ESI, the MALDI process is not yet understood in detail, but it is known to primarily obtain single charged species, while ESI MS accesses multiple charged species.

2.6.2 Mass Analyzers

Various mass analyzers have been developed in order to separate ions. In this Section, the time-of-flight (TOF) analyzer, the quadrupole mass filter and the orbitrap analyzer will be discussed in detail.

Time of Flight (ToF) Analyzer

A time of flight analyzer separates ions of different *m/z* ratios via their flight time through a flight-tube.[137,138] First of all the ions, which were accelerated by an electric field, enter the ToF analyzer, which is under vacuum and contains no electrical field. The kinetic energy (E_{kin}) of an

ion achieved during the acceleration equals the potential energy (E_{el}) uptake by the electric field. Thus, the following relation holds:

$$E_{kin} = \frac{mv^2}{2} = zeU = E_{el} \tag{2.28}$$

Where v is the velocity of the ion, m is the mass of the ion, z is the charge of the ion, e is the elemental charge of an electron and U is the voltage of the applied electric field. Accordingly, the velocity of an ion can be expressed by:

$$v = \sqrt{\frac{2zeU}{m}} \tag{2.29}$$

The ions drift through the analyzer, which is an evacuated flight-tube, and due to the non-existing of an electric field, their velocity is $v = s/t$ (s is the length of the flight path and t is the time). By substituting these term into Equation 2.29, the following equation results:

$$\frac{m}{z} = \frac{2eUt^2}{s^2} \tag{2.30}$$

Thus, lighter ions reach the detector first compared to heavier ions. The advantage of such analyzer, especially useful in the field of polymers, is that the theoretically mass range in which it can operate is unlimited. The combination MALDI-ToF makes molar masses up to approximately 1 million Dalton (Da) accessible.[139]

Quadrupole Mass Filter

A quadrupole mass filter consists of four cylindrical electric rods, which are positioned in a square shape and two of them are crosswise electrically connected to each other (refer to Figure 2.18). The quadrupole operates at a direct-current (dc) voltage U which is superimposed by a radio frequency (rf) voltage V with the frequency ω. The overall potential ϕ_0 can be expressed by:

$$\phi_0 = U + V \cos \omega t \tag{2.31}$$

Due to the applied voltage, the stable or unstable trajectories of ions move centered between the four rods along the z-axis. By varying the magnitude of the voltages, only ions of a certain m/z ratio result in stable trajectories (which can be illustrated in a Mathieu diagram[140]) and can pass through the quadrupole. The quadrupole acts as a filter and is therefore called "mass filter". Quadrupole mass filters are widely employed due to their low cost and space requirements.

However, the low mass range (up to 4000 Da) and their low resolution are the main drawbacks of these analyzers.
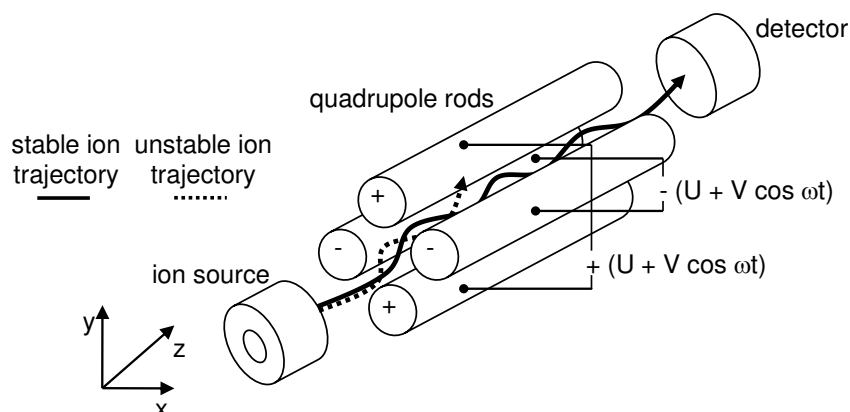
Figure 2.18.: Schematic illustration of the quadrupole mass filter and the pathway of the ions. Only stable ion trajectories (black full arrow) reach the detector. Adapted from reference [141], ©Wiley-VCH Verlag GmbH & Co. KGaA, with permission.

Orbitrap Analyzer

The orbitrap analyzer was first described in the year 2000 and represents the newest invention to analyze ion masses. The analyzer belongs, like quadrupole ion traps, to ion trapping devices. However, in contrast to the other trapping devices, the orbitrap analyzer operates without additional magnetic or radio frequency fields. It consists of an outer barrel-like electrode and an inner axial spindle, which produces a purely electrostatic field, enabling the orbitrap to act as both analyzer and detector. The accelerated ions are introduced tangentially to the electrostatic field, trapped through electrodynamic squeezing and move around the central electrode in circular orbits.[142] Due to the orbiting movements of the ions, an electric field is generated with a frequency proportional to $m/z^{0.5}$.[143] The frequencies induced by oscillating ions are measured on the outer electrode and the mass spectra are acquired through image current detection. During this process, the time-domain signals are directly converted into frequency signals via Fourier transformation, similar as in FT ICR instruments.[141] The orbitrap delivers mass resolving powers of up to 150000, mass accuracies within 2 ppm (if an internal calibration is employed) and mass ranges up to 8000 Da. Using this high-resolution accurate-mass system, a wide range of compounds, not only small molecules but also macromolecules, can be detected.

2.6.3 Mass Spectrometry on Polymers

Mass spectrometry is a powerful tool for the characterization of synthesized polymers, especially for end group analysis.[141] Thus, it enables a detailed study of the initiation process in radical polymerization, where the obtained mass spectrum of the polymer reveals an imprint of the formed radicals which are added to the monomer. This information facilitates to draw conclusions about the reaction mechanisms and initiation kinetics, which are mandatory for an in-depth understanding of the radical polymerization processes. In addition to the analysis of the structure, mass spectrometry is useful to determine the reaction progress by monitoring the peak height or the integral of the starting material peak and the final product. Compared to small molecules, the mass spectrum of a polymer is more complex. The mass spectrum of a polymer entails the distributive character of the polymer, including a plethora of peaks with mass differences associated with the monomer mass. For radical polymerizations, the mass spectrum contains most of the time both combination and disproportionation product peaks, which result from the termination processes. Chains terminated by combination reactions of two radicals show a staircase-like pattern due to the different numbers of isotopes. Furthermore, the two disproportionation peaks also show a staircase-like pattern, however, due to their mass difference of 2 Da, the peaks are superimposed and the pattern has a characteristic shape, which can be described by "high- low-high-low". In disproportionation products, one species carries a double bond and one a proton, which leads to the mass difference. Examples for both typical peak shape clusters are depicted in Figure 2.19.

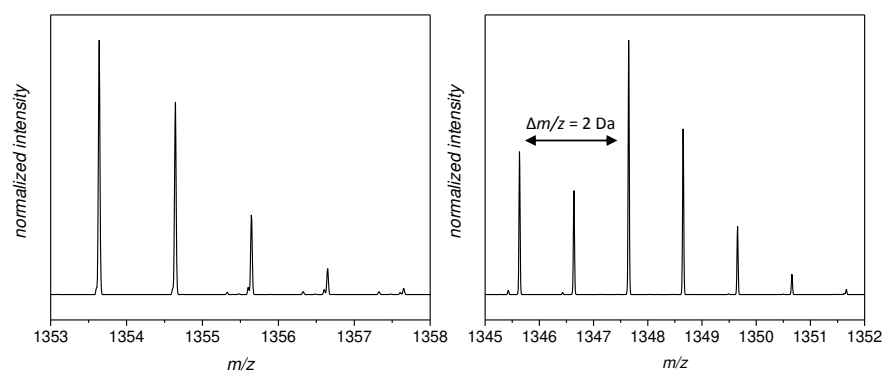**Figure 2.19.:** Characteristic peak patterns of combination products (left side) and disproportionation products (right side) of a polymer chain in a mass spectrum.

2.6.4 Higher-Energy C-Trap Dissociation (HCD)

Dissociation techniques are utilized to understand the structural composition of a molecule and induce fragmentation of a molecular ion, which results in a multitude of peaks.[144-146] These

peaks serve as the fingerprint of the molecule and are useful to confirm characteristic functional groups. Dissociation techniques are often employed in diagnostics to confirm the identity of a compound. Higher-energy C-trap Dissociation (HCD) is a variation of the conventional Collision Induced Dissociation (CID) and utilizes a higher radio frequency (rf) voltage to retain the generated fragment ions in the C-trap. The ions are first fragmented in the HCD cell, stored inside the C-trap and then injected into the orbitrap and separated due to their rational frequency differences.

2.6.5 Hyphenated Size-Exclusion Chromatography (SEC) ESI-MS

The first approach to couple liquid chromatography to ESI-MS was made by Prokai and Simonsick in 1993 and 1995.[147,148] In the field of polymer chemistry, ESI-MS is often applied for the determination of the polymer end group. However, due to the nature of the polymer backbone, ESI mass spectra display singly charged and as well multiply charged ions, resulting in superimposed peak patterns, which makes the evaluation of the mass spectra more difficult. To overcome this drawback, SEC coupled to ESI-MS as well as to refractive index (RI) detection is an ideal approach. The polymers are first separated (via SEC) with regard to their mass distributions and then in parallel injected into the ESI-MS to acquire the mass spectra, and into the RI detector to obtain the molar distribution. Based on the introduction of a second dimension into the mass spectrometric analysis, the evaluation is simplified since a certain m/z range can be selected 'slice by slice' from the chromatogram. The schematic setup of such an approach is illustrated in Figure 2.20 and was utilized in the current thesis for the polymer end group analysis.[37] In addition to the determination of the polymer end group, this coupled system allows obtaining quantitative molar mass distributions.[149] These distributions are established by employing a computational algorithm, which is based on the maximum entropy principle and able to processes the data from the two detectors. This procedure can be employed without additional calibration and exploits single oligomer profiles (SOP) and a simultaneous SEC distribution deconvolution process to obtain quantitative concentrations for each single polymer chain.[150]
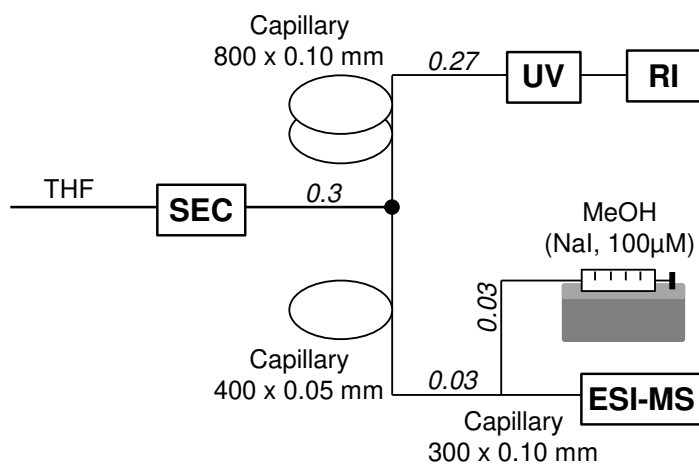
Figure 2.20.: Schematic setup employed for coupling the ESI-MS and UV/RI-detectors to the chromatographic effluent in parallel. Numbers in italic indicate flow rates in mL·min⁻¹. A 100 μM solution of sodium iodide in methanol is added post-column to increase the ionization efficiency and multiple charging. The same setup is utilized for the SEC-ESI-MS measurements in the present thesis. Adapted with permission from reference [149]. Copyright (2008) American Chemical Society (ACS).

2.7 Thorpe-Ingold Effect

The Thorpe-Ingold effect, also called gem-dialkyl effect, describes the acceleration of cyclizations based on the geminal substitution with two alkyl groups (e.g. two methyl groups). The first explanation was proposed by Beesley, Thorpe and Ingold in 1915, who discovered the effect during their investigation into the formation of spiro-compounds from cyclohexanes.[151] Accordingly, they postulated that mutual repulsion of geminal substituted dimethyl groups leads to an increase in the intramolecular angle α, which is positioned between the two dimethyl groups, and concomitantly to a decrease in the intramolecular angle β, which is located on the opposite side (refer to Scheme 2.10). By the virtue of the compression of the angle, the groups X (COOH) and Y (COOH) are closer together, which drives the cyclization reaction.

$$\alpha_3 > \alpha_2 > \alpha_1 \qquad \beta_1 > \beta_2 > \beta_3$$
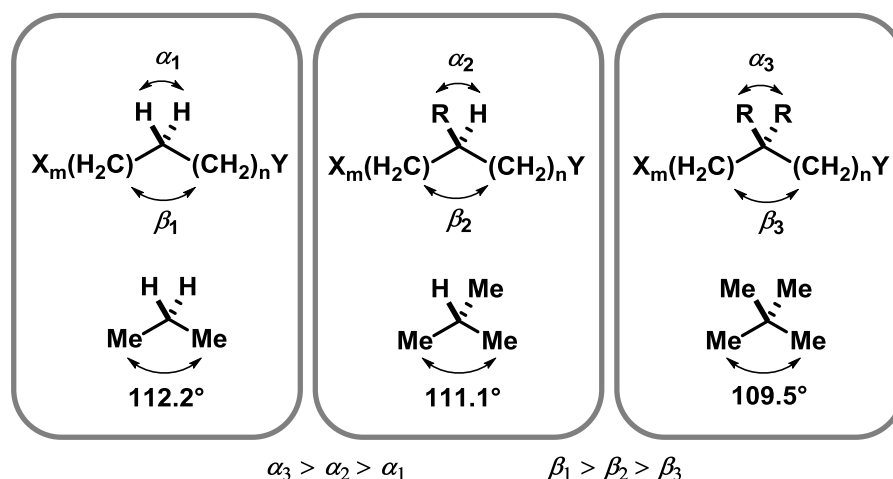
Scheme 2.10.: Illustration of the Thorpe-Ingold effect, explained by the decreasing angles from propane (112.2°) to *iso*-butane (111.1°) and *neo*-pentane (109.5°). Adapted with permission from reference [152]. Copyright (2005) American Chemical Society (ACS).

Since the discovery of the Thorpe-Ingold effect, a multitude of theoretical and experimental contributions have been made and described in the literature to understand and interpret the effect of geminal substitution with dialkyl groups. Here, only a few of them are described in the following Section and the corresponding concluding results are illustrated in Figure 2.21.

In 1960 Bruice and Pandit investigated the cyclization reactions of five and six membered rings and concluded that dialkyl substitution on the ring leads to an increase in the population of the reactive rotamers (kinetic effect), which subsequently results in a cyclization reaction, when the two residues are oriented next to each other.[153] Hence, the increase in the populations stems from an increase in the ground state energy. In the same year, Allinger and Zalkow investigated the ring formation of hexanes with various dialkly substitutions to the respective cyclohexane from a thermodynamic point of view.[154] Essentially, by increasing the gauche number of the

open-chain, the enthalpy promotes the ring formation. In addition, the branching with dimethyl groups reduces the rotation stronger in the open-chain in comparison to the closed-chain form. Thus, the entropy favors the ring formation. One year later, Ragué Schleyer found out that the angle compression has an exclusive influence on the formation of small rings, while being negligible on the formation of larger rings.[155] In 1972, Milstien and Cohen postulated that the gem-dimethyl groups along a methyl group, which is located in close proximity to these groups on the aromatic ring, are interlocked, a so-called "trimethyl lock", which explains the extraordinary cyclization rate.[156]
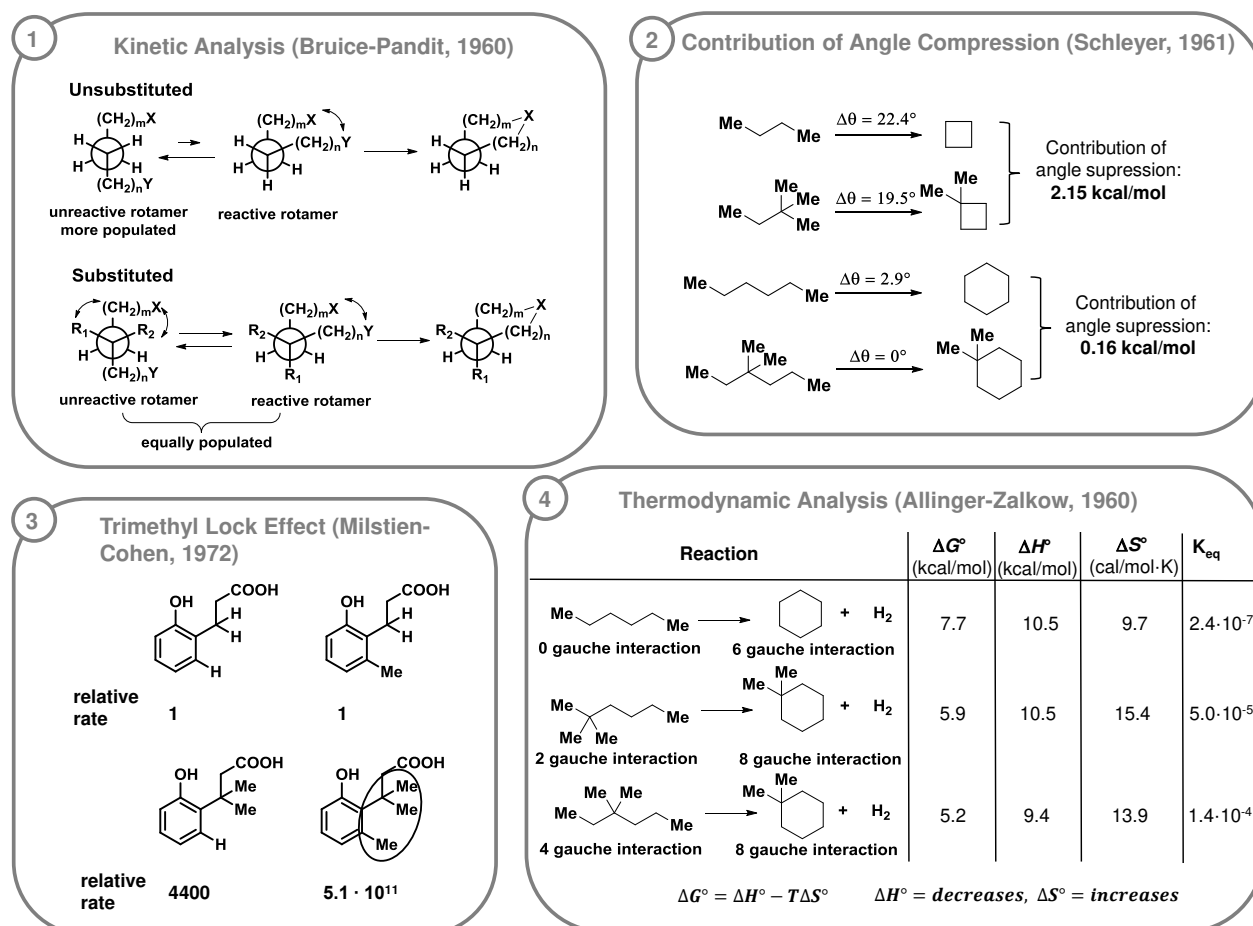

Figure 2.21.: Overview of the various factors influencing the Thorpe-Ingold effect. Figure Section 1,3 and 4 were adapted with permission from reference [152]. Copyright (2005) American Chemical Society (ACS). Figure Section 2: values taken from reference [155].

2.8 Investigation of Photoinitiated Polymerizations via the Combination of PLP and ESI-MS

The combination of PLP for the synthesis of polymeric material and ESI-MS for the latter analysis of the final polymer serves as a powerful tool to investigate polymer end groups, and thus the fate of the generated radicals on the mechanism of the photoinitiation process.

In 2007 Szablan et al.[46] investigated the effects of laser intensity, laser frequency and temperature on radical reactivities of common photoinitiators (PIs), such as benzoin, benzil, 2,2-dimethoxy-2-phenylacetophenone (DMPA), benzoin ethyl ether (BEE) and 2,2-azobisisobutylnitrile (AIBN), using MMA as monomer (refer to Scheme 2.11 for the PI structures). For benzoin, benzil and BEE, the benzoyl as well as the α-hydroxybenzyl and the ether radical act as initiating and terminating species. The photocleavage of DMPA leads to the benzoyl and acetal fragment, both able to initiate and terminate the photoinduced polymerization, where the latter is fragmented further to yield methyl radicals. These radicals act primarily as terminating moieties. When increasing the laser intensity and/or frequency, the mass spectra of the photoinitiated polymers became more complex, revealing unidentified species.
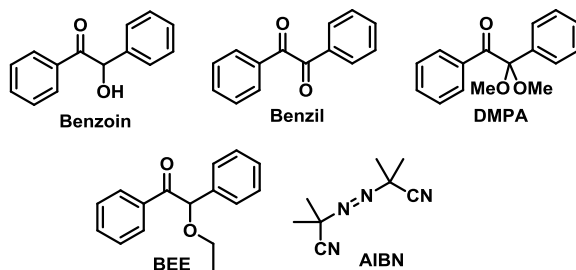
Scheme 2.11.: Photoinitiators investigated with regard to their initiation and termination behavior during PLP by varying laser intensity, laser frequency and reaction temperature.

A quantitative comparison of the initiation pathways and the effectiveness of two PI derived radicals, utilizing the PLP-ESI-MS method was for the first time employed by Günzler et al. [157] Therefore, so-called cocktail-experiments were performed with benzoin and mesitil (refer to Scheme 2.12) of varying molar compositions (1:0.3 to 1:10 benzoin vs. mesitil) in bulk polymerizations with MMA. For the quantitative comparison of the two fragments only disproportionation products were utilized. The analysis of combination products provides no information about the initiation efficiency, since both end groups are initiator fragments. The analysis revealed that the initiation efficiency of benzoyl radicals (1) is about 8.6 times higher compared to mesitil radicals (3), which is most probably due to different reactivities of benzoyl and mesitil radicals.
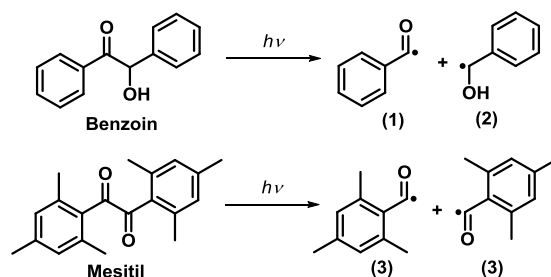
Scheme 2.12.: Comparison of benzoin and mesitil, regarding their initiation effciency.

The study of Günzler *et al.* [157] in our team laid to the groundwork of several quantitative comparisons of photoinitiator containing systems and in the following two of them are discussed. A study of Voll *et al.*,[158] investigated the initiation efficiency of various methyl-substituted benzoin-like initiators (refer to Scheme 2.13). The multi-photoinitiated free-radical pulsed-laser polymerization approach indicated that 28.2% of all disproportionation products were initiated by the benzoyl fragment of benzoin, 27% by the radical fragment of 4MB, 22% by 2,4DMB, 11% by TriMB, 4% by TetraMB, and 9% by PentaMB. Thus, the number of methyl-substituents on the benzoyl moiety leads to a decrease of the initiator efficiency.
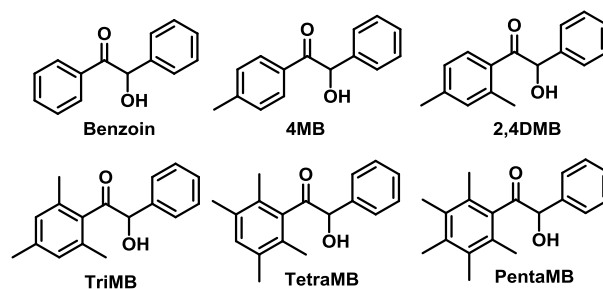
Scheme 2.13.: Methyl-substituted benzoin-type PIs that were investigated with regard to their initiation efficiency.

In a further study of Jöckle *et al.*,[159] the contribution of various substitutions on the benzoyl moiety of five monoacylgermane-based visible PI (refer to Scheme 2.14) on the overall initiation efficiency of the benzoyl fragment was investigated via a combination of PLP-ESI-MS cocktail experiments and femtosecond spectroscopy. Here, electron donating groups (assessing their +m effect), such as fluorine and methoxy, as well as electron withdrawing groups (assessing their -m effect), such as cyano and nitro, were utilized. The PLP-ESI-MS results revealed that PIs bearing nitro (NBG) and cyano (CBG) groups behave as so-called 'weak initiators', since they show only a small monomer to polymer conversion. In contrast, PIs bearing fluorine (FBG) and methoxy (MBG) groups and as well as the unsubstituted (HBG) PI were classified as 'strong initiators', where the strongest efficiency was determined for the fluorine substituted PI. In addition, femtosecond absorption spectroscopic experiments confirmed these observations, as efficient

initiators showed a fast ISC within 2-4 ps into triplet states, while weak initiators depicted mainly a fast IC in 2 ps into the ground state, leading to no radical formation.
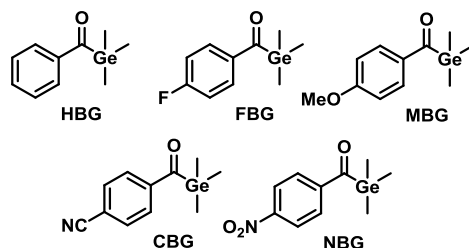
Scheme 2.14.: Monoacylgermane-based PIs with various substitutions on the benzoyl moiety, which were investigated with regard to their initiation efficiency.

Next to quantitative comparisons of PI efficiencies, PLP-ESI-MS can be utilized to investigate photoinduced reaction mechanism, which was explored in our team by Frick *et al.*[160] Here, the mechanism of the copper-mediated photoinduced reversible-deactivation radical polymerization (photoRDRP) was analyzed via the identification of the initiating species and their interaction with the reaction mixture. It was found that the photoinduced cleavage of the C-Br bond generates the initial radicals, which induce macromolecular growth and as well react with the deactivator copper species. The photoinduced electron transfer between the excited amine ligand and the deactivator copper species leads to the production of activator copper species. Free ligand species perform a quenching reaction, which produces a reduced copper complex and an amine radical anion during the excitation of the deactivator copper complex. The overall proposed mechanism of photoRDRP is illustrated in Scheme 2.15.
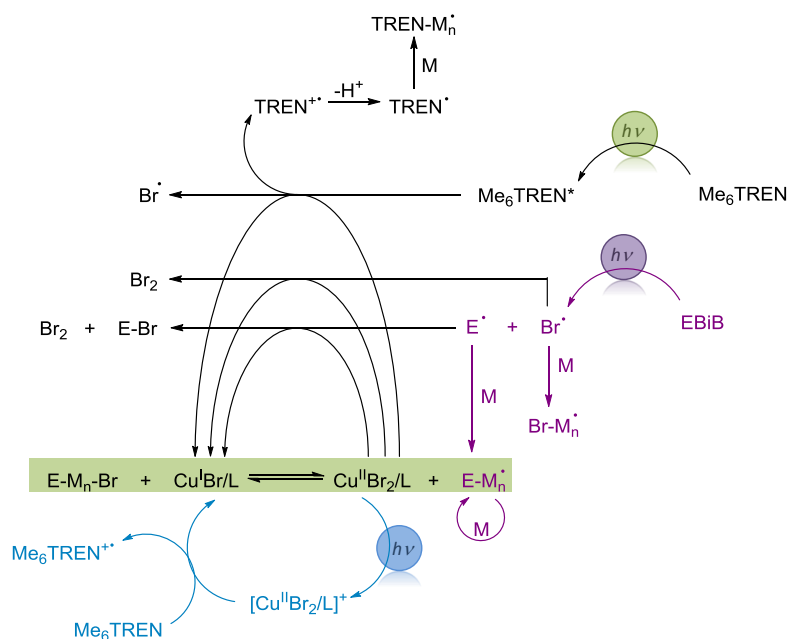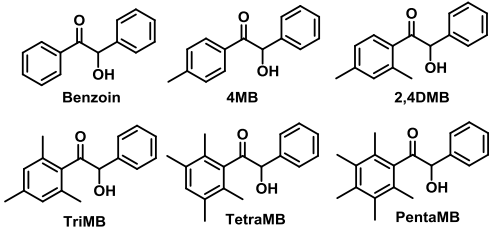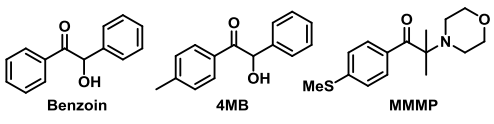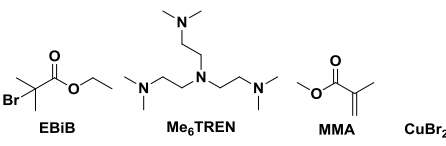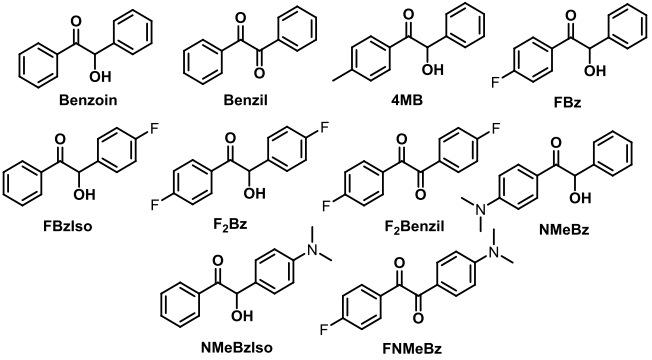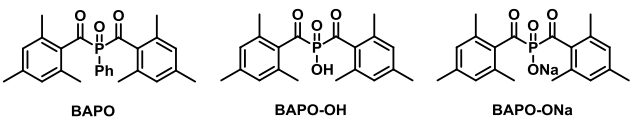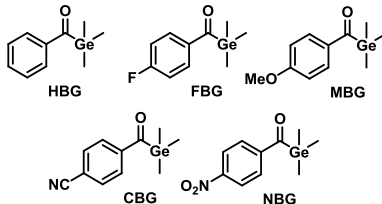
Scheme 2.15.: Proposed mechanism of photoRDRP, based on structures found in ESI-MS for varied combinations of EBiB, Me$_6$TREN, CuBr$_2$, monomer, and solvent. Adapted with permission from reference [160]. Copyright (2015) American Chemical Society (ACS).

Table 2.2: Overview of the Investigated photoinitiated polymerization reactions via the combination of PLP and ESI-MS in our team.

Applied Photoinitiating Systems	Investigation	Author and Year
	Study of photoinitiation processes	Szablan[46] *et al.*, 2007
	Quantifying the efficiency of photo-initiation processes	Guenzler[157] *et al.*, 2009
	Determination of Mark-Houwink parameters for accurate measurement of the molecular weight distribution	Gruendling[161] *et al.*, 2010
	Quantifying the efficiency of photo-initiation processes	Voll[162] *et al.*, 2011

Applied Photoinitiating Systems	Investigation	Author and Year
Benzoin, 4MB, 2,4DMB, TriMB, TetraMB, PentaMB	Quantifying the efficiency of photo-initiation processes	Voll[158] *et al.*, 2012
Benzoin	Mechanistic elucidation of photoinduced end group conversion reactions	Voll[163] *et al.*, 2012
Benzoin, 4MB, MMMP	Quantifying the efficiency of photo-initiation processes	Frick[164] *et al.*, 2014
EBiB, Me$_6$TREN, MMA, CuBr$_2$	Mechanistic elucidation of the copper-mediated photo-RDRP	Frick[160] *et al.*, 2015
Benzoin, Benzil, 4MB, FBz, FBzIso, F$_2$Bz, F$_2$Benzil, NMeBz, NMeBzIso, FNMeBz	Quantifying the efficiency of photo-initiation processes	Frick[96] *et al.*, 2016
BAPO, BAPO-OH, BAPO-ONa	Elucidation of the photoinduced reactivity	Fast[63] *et al.*, 2015
HBG, FBG, MBG, CBG, NBG	Quantifying the efficiency of photo-initiation processes	Jöckle[159] *et al.*, 2017

3

Photoinduced Polymer End Group Conversion

3.1 Introduction

In 2012, a study by Voll *et al.*[163] demonstrated for the first time that polymers, which have been prepared via photoinduced free radical polymerization technique, are prone towards secondary photoinduced reactions at their respective chain termini, based on the irradiation energy to which they are exposed. To evidence these end group transformation, which occurred via Norrish type I or II reaction (refer to Scheme 3.1), the authors employed a combination of an in-depth mass spectrometric polymer product analysis with photochemically induced dynamic nuclear polarization (photo-CIDNP) experiments. On the basis of the study by Voll *et al.*, the present Chapter will investigate in detail the photoinduced reactions of benzoyl-terminated poly(methacrylate) via a combination of pulsed-laser polymerization (PLP) and various pulsed-laser irradiation (PLI) techniques coupled to size exclusion chromatography electrospray ionization mass spectrometry (SEC-ESI-MS), photo-CIDNP experiments and quantum mechanical calculations (refer to Scheme 3.1). In particular, the influence of methyl-substitution of benzoyl-terminated end groups, yet also the influence of other functionalities (such as fluorine or methoxy groups), is examined. In addition, the study will inspect the influence of the polymer backbone and the solvent utilized for irradiation as well as the assessment of the stability under solid-state conditions to mimic real conditions of the photo-curing used in industry.
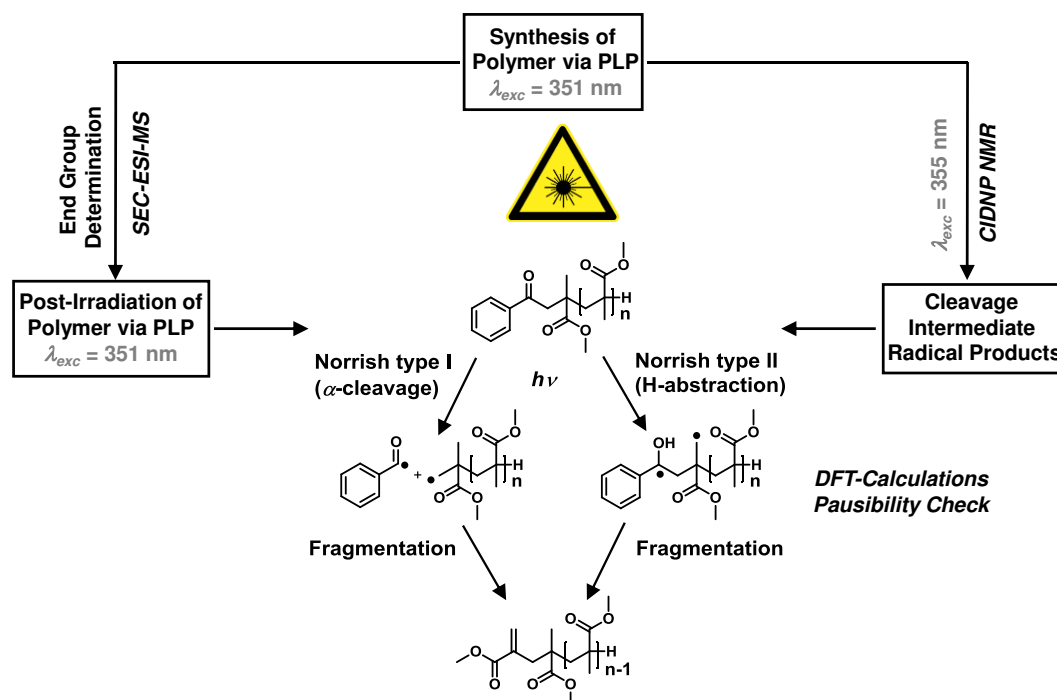
Scheme 3.1.: Research strategy, research outcomes and experimental synergies for photoinduced reactions of benzoyl-terminated poly(methyl methacrylate) via a Norrish type I and II pathway followed in the current Section. Adapted with permission from reference [165]. Copyright (2015) American Chemical Society (ACS).

3.2. Investigation of Methyl-Substituted Benzoin-Type Photoinitiators at 351 nm

In the current Section the influence of methyl-substitution on the benzoyl polymer end group towards UV light-induced end group conversion, is presented. As noted above, a previous study of Voll *et al.* demonstrated that the post-irradiation of a benzoin-initiated poly(methyl methacrylate) (pMMA) leads to a cleavage process best described as a Norrish type I or type II reaction.[163] As a first example, molecule 2,4,6-trimethylbenzoin (TriMB) was explored. Thus, TriMB-pMMA (synthesized at low laser energies, 0.35 mJ/pulse) was subjected to post-irradiation with higher laser energies (6 mJ/pulse). Surprisingly, no cleavage behavior at the polymer chain end, in contrast to the unsubstituted benzoyl chain end, could be determined, which suggests that the photoinduced end group conversion is controllable by simple methyl-substitution on the benzoyl moiety. To systematically evidence and also take control over the cleavage behavior, a library of substituted benzoins containing a variable number of methyl substituents (i.e., 2-, 3- and 4-methylbenzoin (2MB, 3MB and 4MB), 2,4- and 2,6-dimethylbenzoin (2,4DMB and 2,6DMB), and 2,3,5,6-tetra- and 2,3,4,5,6-pentamethylbenzoin (TetraMB and PentaMB), refer to Scheme 3.2) was synthesized.
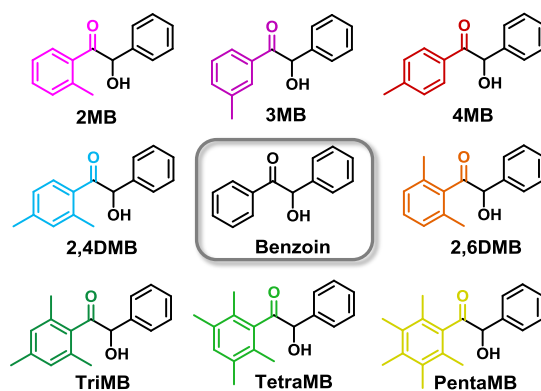
Scheme 3.2.: Photoinitiator library: Overview of the investigated benzoin-type PI with varied methyl-substitution on the benzoyl moiety. Adapted with permission from reference [165]. Copyright (2015) American Chemical Society (ACS).

The photoinitiators (PI) were polymerized by PLP with methyl methacrylate (MMA) in bulk at lower laser energies (0.35 mJ/pulse) to obtain relatively short and intact polymer chains with variable end groups, to be subjected to post PLI at higher laser energies (6 mJ/pulse). The subsequent analysis via SEC-ESI-MS generates insights regarding the potential end group transformations of the polymers and is suited to detect the cleavage products.[96,160] Photo-CIDNP experiments of the polymers provide information about possible reaction products, including small molecules and the macroradical of the post α-cleavage process.[63] Additional hydrogenation

experiments of the polymer end group transformations and their subsequent SEC-ESI-MS analysis serve both to confirm the presence of the double bonds of the unsaturated species. Density functional theory (DFT) calculations were employed for the determination of the photostability of the polymers.

3.2.1 Photoinitiator Synthesis

The benzoin derivatives illustrated in Scheme 3.2 were synthesized via two synthesis steps (refer to Scheme 3.3): Wacker oxidation and subsequent Friedel-Crafts acylation. As a first step, the respective acetophenone was oxidized with selenium dioxide to afford a phenylglyoxal. In the next step, the phenylgloxal was converted with benzene to obtain the target benzoin, which was further purified by recrystallization or column chromatography.[166]
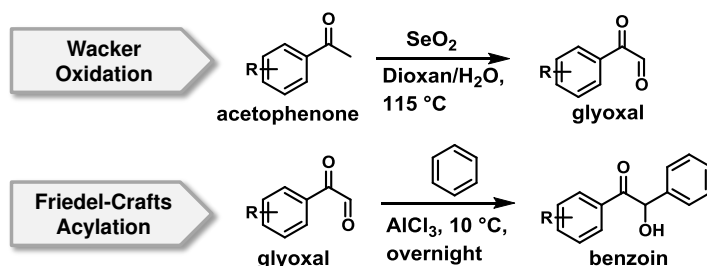
Scheme 3.3.: The benzoin derivatives were obtained by two synthesis steps: Wacker oxidation and subsequent Friedel-Crafts acylation.

3.2.2 PLP and Post-Irradiation Experiments

In the PLP study, the various PIs were compared in individual experiments. Thereby the laser beam hits the sample, containing a PI and the monomer, respectively. The excitation of the initiator leads to the formation of radicals, which start the initiation process of a free radical polymerization (FRP). Here, the termination can occur via disproportionation as well as via combination. The ratio of disproportionation products to combination products depends on the selected monomer. For MMA, mainly disproportionation products can be found. In order to determine the structure of the polymer end group, high resolution mass spectrometry is the method of choice. Thus, the polymers were first synthesized by PLP at lower laser energies (0.35 mJ/pulse), purified via precipitation, post-irradiated at higher laser energies (6 mJ/pulse) and subsequently hydrogenated. All of these synthesized, post-irradiated and hydrogenated polymer samples were carefully assessed by SEC-ESI-MS. Scheme 3.4 illustrates the synthetic procedures and the obtained structures on the example of 4MB. The reason for employing SEC-ESI-MS is the separation of the different distributions and the related simplified evaluation of the mass spectra (for further details refer to the Section 2.6.5).
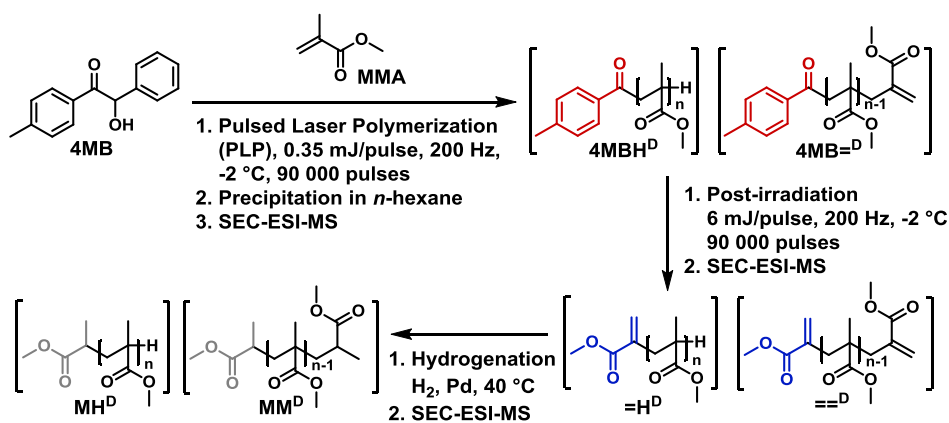
Scheme 3.4.: Synthesis of 4MB-initiated pMMA at low laser energies (0.35 mJ/pulse), post-irradiation at high laser energies (6 mJ/pulse) and subsequent hydrogenation. Adapted with permission from reference [165]. Copyright (2015) American Chemical Society (ACS).

3.2.3 Nomenclature of the Mass Spectra

The following nomenclature was adopted to label the observed mass signals in the current Chapter as well as in the following Chapters. Disproportionation peaks occur in pairs with a mass difference of 2 Da. Derived from the initiation process these peaks are labeled XH/YH or X=/Y=, where X and Y defines one of the two radical formed end groups of the polymer chain in α-position. The ω-position is defined by = or H, depending on the role of the reactive site during the H-abstraction of the disproportionation process. Post-irradiation of the polymer leads to the formation of double bonds through α-cleavage of the benzoyl end group. These resulting peaks are labeled == or =H, which defines the nature of the resulting double bond after the α-cleavage process. The respective peaks that show a shift of 2 and 4 Da after hydrogenation – indicating the disappearance of a double bond – are labeled with MM or MH. M defines the hydrogenation of the double bond during the hydrogenation process, where H describes the ω-position, depending on the role of the reactive site during the H-abstraction. The combination products are labeled X2, Y2, and XY, where 2 serves for clarity and implies that the fragment is present twice. The superscripts D and C indicate the respective disproportionation or combination products.

3.2.4 Photo-CIDNP Technique

Photo-CIDNP is a nuclear magnetic resonance (NMR) experimental technique; allowing to establish reaction mechanisms at a short time scale (μs-ns) and is specific for radical-pair based reactions. Thus, the respective photoinduced polymers were compared in individual photo-CIDNP experiments. The obtained on-line CIDNP spectra offer information regarding the

character of the reaction products, which are generated in radical reactions via the chemical shifts of their NMR resonances. The unusual signal intensities in the spectra contain information concerning the spin distribution in the intermediate radicals. With this information, the elucidation of mechanistic pathways becomes possible.

3.2.5 Photochemically Unstable Polymer End Groups

The photoinitiators 2MB, 3MB, 4MB, and 2,4DMB lead to polymer end groups, where the introduced methyl-substituted benzoyl end group allow their cleavage upon UV light irradiation. For clarity reasons, 4MB serves as an example to illustrate their cleavage behavior (the reactivity patterns for 2MB, 3MB and 2,4DMB are summarized in the appendix, Figure 8.1-8.3). Figure 3.1 shows the SEC-ESI overview mass spectra (a) and a zoom into one repeating unit (b) of 4MB initiated pMMA. The polymer synthesized at lower laser energies (0.35 mJ/pulse) is compared with the polymer that was post-irradiated at higher laser energies (6 mJ/pulse) and with the subsequently hydrogenated polymer. The structures that belong to the signals are depicted in Scheme 3.5 and the assigned signals are listed in Table 3.1. The mass spectrum of the starting polymer (0.35 mJ/pulse, in red) shows the expected disproportionation (**4MBH**, **4MB=**, **OH**, **O=**) and combination products (**O2**, **4MB2**, **4MBO**). Post-irradiation (6 mJ/pulse, in blue) of the polymer, initiated by 4MB, leads to signals at m/z = 707.3, 709.3 and 715.4 (refer to Table 3.1), which can be assigned to species containing doubled bonds (**==**, **=H**, **=OH**).

The nearly complete disappearance of the benzoyl signals (**4MB=** and **4MBH**) and the formation of the respective cleavage product signals at m/z = 707.3 and 709.3 was observed for 4MB and 3MB. Interestingly, 2MB and 2,4DMB also showed the formation of the cleavage products, but only a slight decrease in the benzoyl signals was observed. In order to evidence the formation of the double bonds, hydrogenation experiments of the post-irradiated polymers were performed. The resulting polymers were subsequently analyzed by SEC-ESI-MS. The spectrum of the hydrogenated polymer (in gray), initiated by 4MB, shows a clear shift of the disproportionation peaks at m/z = 707.3 (**==**) and 709.3 (**=H**) to m/z = 711.4 (**MM** and **MH**), as well as a shift of the combination peaks at m/z = 715.3 (**=OH**) to m/z = 717.3 (**MOH**). The strong signal at m/z = 715.4 corresponds to the combination product **O2** with H$^+$ ionization and not to the residual combination product **=OH** with Na$^+$ ionization. This phenomenon was observed for all hydrogenated samples, where particularly strong signals for the combination product [**O2** $^{H+}$] were recorded for 2MB and 2,4DMB.
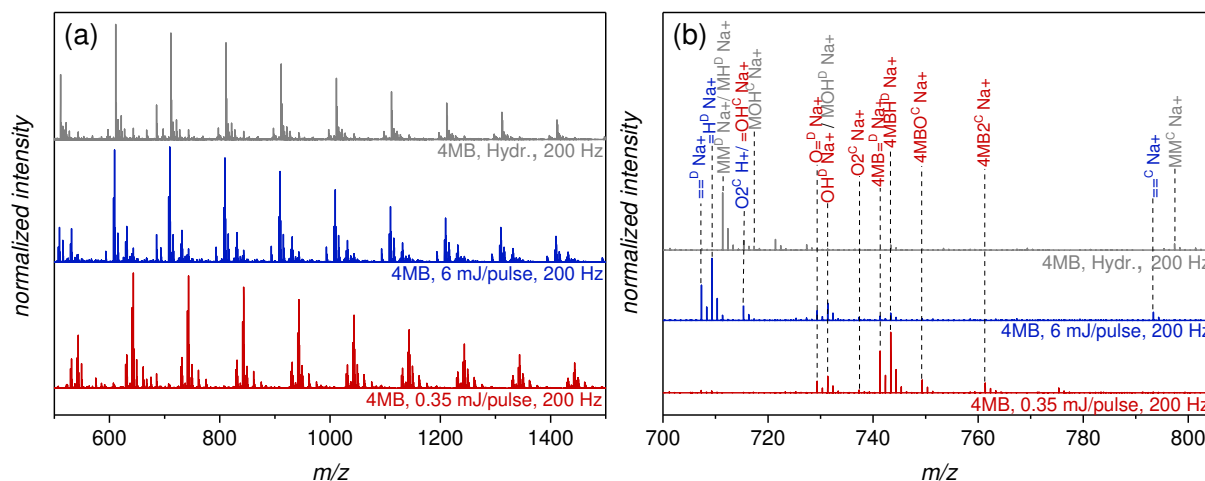
Figure 3.1.: SEC-ESI overview mass spectra (a) and zoom into one repeating unit (b) of the polymer initiated by 4MB, synthesized at low laser energies (0.35 mJ/pulse, red spectra), post-irradiated at higher laser energies (6 mJ/pulse, blue spectra), and hydrogenated (gray spectra). Adapted with permission from reference [165]. Copyright (2015) American Chemical Society (ACS).
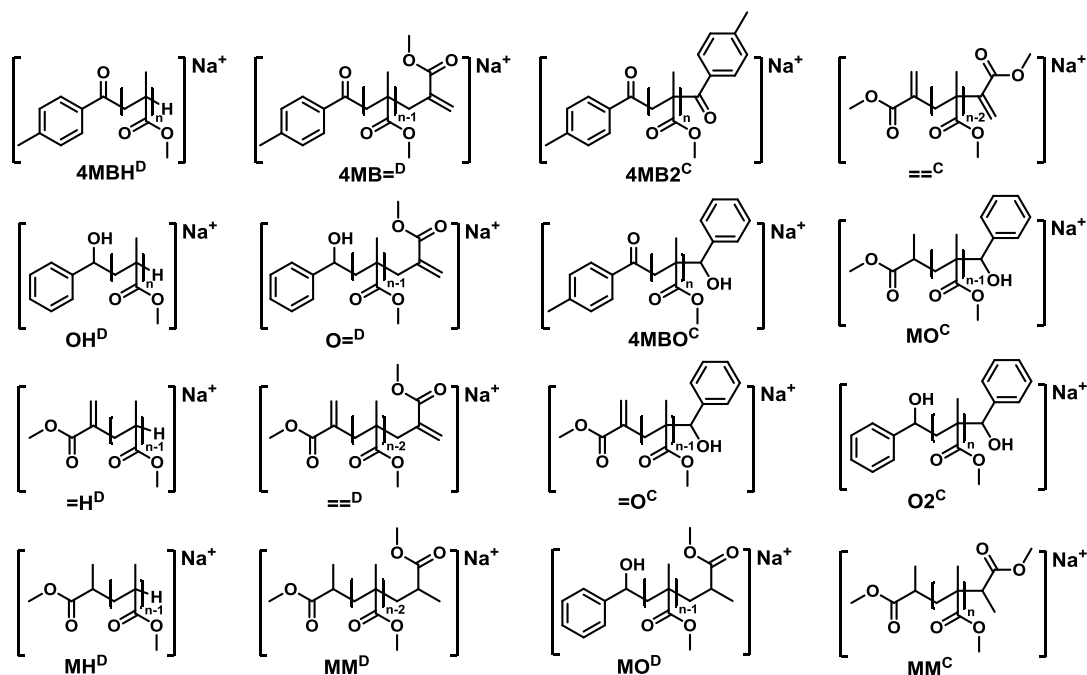
Scheme 3.5.: Disproportionation and combination products resulting from the PLP (0.35 mJ/pulse), PLI (6 mJ/pulse) and hydrogenation experiments of 4MB-pMMA, as detected by SEC-ESI-MS. Adapted with permission from reference [165]. Copyright (2015) American Chemical Society (ACS).

Table 3.1.: Overview of the signals of the PLP generated polymers (0.35 mJ/pulse), PLI (6 mJ/pulse) as well as hydrogenated polymers (4MB-initiated pMMA) as detected by SEC-ESI-MS (R = 75000). Adapted with permission from reference [165]. Copyright (2015) American Chemical Society (ACS).

Species	Ionization	$(m/z)^{\text{theo}}$/Da	$(m/z)^{\text{exp}}$/Da	$\Delta(m/z)$
4MB=[D]	Na$^+$	741.3462	741.3453	0.0009
4MBH[D]	Na$^+$	743.3618	743.3596	0.0022
O=[D]	Na$^+$	729.3462	729.3453	0.0009
OH[D]	Na$^+$	731.3618	731.3607	0.0011
4MBO[C]	Na$^+$	749.3513	749.3497	0.0016
4MB2[C]	Na$^+$	761.3513	761.3497	0.0016
O2[C]	Na$^+$	737.3513	737.3505	0.0008
==[D]	Na$^+$	707.3255	707.3248	0.0007
=H[D]	Na$^+$	709.3411	709.3395	0.0016
MM[D]	Na$^+$	711.3568	711.3583	0.0015
MH[D]	Na$^+$	711.3568	711.3583	0.0015
=OH[C]	Na$^+$	715.3306	715.3337	0.0031
O2[C]	H$^+$	715.3694	715.3678	0.0016
MO[C]	Na$^+$	717.3462	717.3473	0.0011

Based on the PLP-SEC-ESI-MS results of 4MB, it can be assumed that substitution of the benzoyl moiety with one methyl group leads to no increase of the stability against UV light irradiation at 351 nm. The same applies to 2MB, 3MB, and 2,4DMB, which is even methyl-substituted at two positions, since they all show the presence of unsaturated species after UV-irradiation.

The photo-CIDNP measurements were carried out by D. E. Fast at the University of Graz. The ^{1}H NMR and ^{1}H CIDNP spectra (λ = 355 nm) of 4MB-pMMA (synthesized at the laser energy of 0.35 mJ/pulse) are depicted in Figure 3.2. As can be seen, the presence of polarized signals in the ^{1}H CIDNP spectrum (Figure 3.2b) demonstrate that the end group conversion takes place via paramagnetic intermediates. According to Voll *et al.*, the 4-methylbenzoyl end group can react via two competing pathways (Norrish type I and II) as shown in Scheme 3.6.
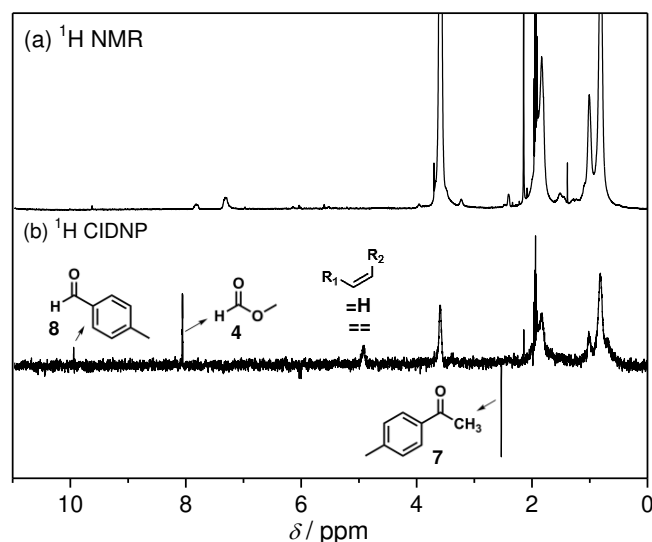
Figure 3.2.: (a) ^{1}H NMR and (b) ^{1}H CIDNP spectra of 4MB-pMMA synthesized at a laser energy of 0.35 mJ/pulse, recorded in acetonitrile-d_3 at close to 80 mJ/pulse with the assignment of the products formed from the radical reactions. Adapted with permission from reference [165]. Copyright (2015) American Chemical Society (ACS).

Direct cleavage of the ester bond of 4MBH leads to methyl formate **4**, which is associated with the quartet at $\delta = 8.06$ ppm ($J = 0.8$ Hz). Thus, the signals are derived from the single proton of methyl formate. Upon UV light 4MBH can undergo α-cleavage (Norrish type I reaction) leading via the 4-methylbenzoyl radical **5** and polymer-derived radical **6** to 4-methylacetophenone **7** and 4-methylbenzaldehyde **8**. Thus, the singlet at $\delta = 2.5$ ppm stems from the methyl-protons of 4-methylacetophenone **7** and the singlet at $\delta = 9.9$ ppm is characteristic of an aromatic aldehyde proton and can be assigned to 4-methylbenzaldehyde. Disproportionation reactions of **6** leads to the formation of methyl formate **4** and to the alkene **=H**, as well as to the formation of methane **14**. The alkene is associated with weak polarized signals at $\delta = 4.8\text{-}5.0$ ppm, indicating the formation of the double bonds (**==**, **=H**). UV-induced cleavage of 4MBH can also proceed via a Norrish type II reaction, yielding 1,4-hydroxybiradical **11**. Fragmentation of those biradical **11** result in the alkene **=H** and the enol **12**, where the latter **12** can tautomerizes to 4-methylacetophenone **7**. Due to the absence of polarized signals of methane **14** ($\delta = 0.2$ ppm), it can be assumed that the Norrish type II reaction is preferred in the case of 4MB-initiated pMMA.
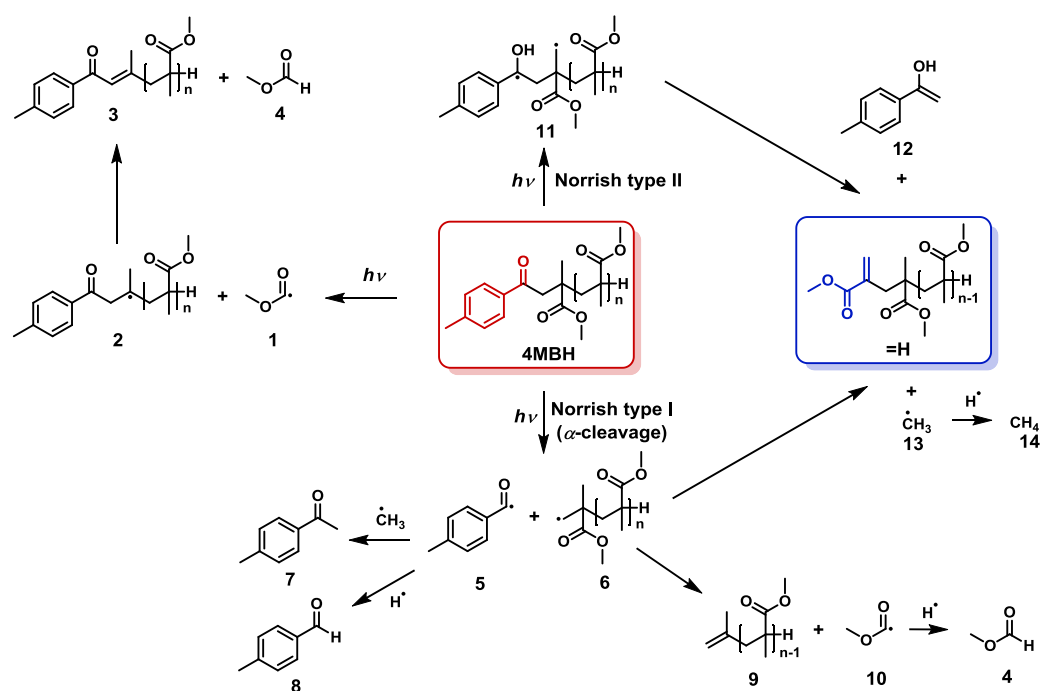
Scheme 3.6.: UV-induced reaction pathways of 4MB-initiated pMMA (synthesized at 0.35 mJ/pulse). Adapted with permission from reference [165]. Copyright (2015) American Chemical Society (ACS).

Polarized ^{1}H CIDNP signals could be also observed for 3MB-pMMA (refer to Figure 8.7) indicating end group transformation yielding radical products corresponding to those shown in Scheme 3.6. As already noted, post-irradiation and subsequent SEC-ESI-MS analysis of 2MB- and 2,4DMB-pMMA indicated only partial end group conversion. However, no polarized ^{1}H CIDNP signals could be observed for these polymers (for CIDNP spectra refer to appendix, Figure 8.7-8.8). Decisive for the partial end group conversion reaction is the difference of the sensitivity of both methods. In order to determine the method-dependent end group conversion behavior, a quantitative comparison of the cleavage product peaks with the initiation peaks for the initiators 2MB, 2,4DMB, 3MB, and 4MB was carried out. Thus, a method that evaluates the peak heights (Δh) of the polymer signals, of the obtained mass spectra, in each repeating unit was employed. Therefore, the first peaks of the respective disproportionation peak clusters (for example **2MB=** and **==**) were selected and compared with each other (refer to Figure 3.3).
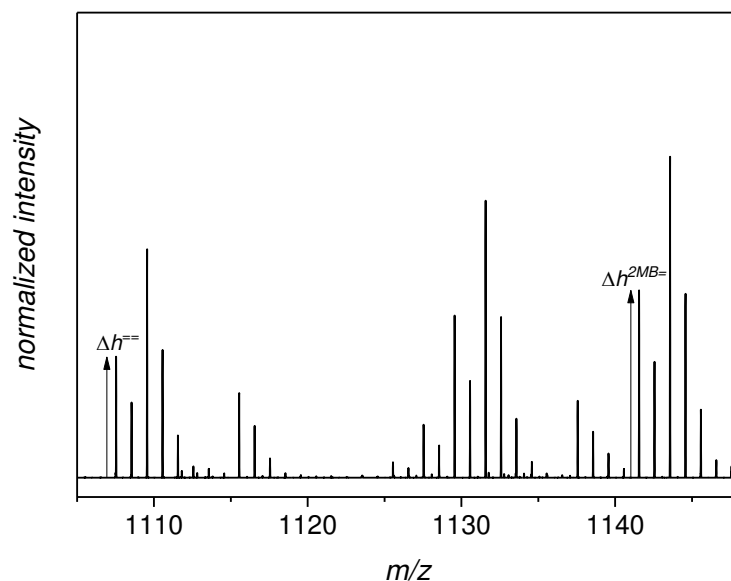
Figure 3.3.: Zoom into the SEC-ESI mass spectrum of pMMA initiated by 2MB showing the disproportionation peaks (==) and (2MB=). These peaks are used as an example for the definition of the peak height Δh. Adapted with permission from reference [165]. Copyright (2015) American Chemical Society (ACS).

The specific peak height $\Delta h^{X=}$ was employed for the calculation of the molar ratio $\chi^X(n)$, where X defines the respective end group of the intact or cleavage fragment and n defines the repeating unit (refer to Equation 3.1 and 3.2).

$$\chi^{==}(n) = \frac{\Delta h^{==}(n)}{\Delta h^{==}(n) + \Delta h^{2MB=}(n)} \tag{3.1}$$

$$\chi^{2MB=}(n) = \frac{\Delta h^{2MB=}(n)}{\Delta h^{2MB=}(n) + \Delta h^{==}(n)} \tag{3.2}$$

For the sake of simplicity, 2MB and 2,4DMB were compared with 4MB and 3MB, due to their similar cleavage behavior. Figure 3.4 depicts the plots of the $\chi^X(n)$ values for each fragment X against the degree of polymerization DP_n of 4MB (a), 2MB (b), 3MB (c) and 2,4DMB (d).

A chain length independent ESI process takes place, if a constant gradient close to zero could be observed. However, this only applies when the compared end groups are relatively similar to each other. Here, the end groups were structurally different, due to the fact that one end group is bearing an aromatic system and the other end group only small double bonds. The $\chi^X(n)$ plots of 2MB, 2,4DMB, 3MB, and 4MB (refer to Figure 3.4) show an asymptotic behavior originating from the different ionization abilities of these end groups. With increasing DP_n, the molar ratios of the intact end groups ($\chi^{X=}(n)$) increases and the cleavage end groups decreases ($\chi^{==}(n)$). The longer the chains, the less influence the end groups have on the ionization behavior and thus the

asymptotic values are most likely to be correct. Thus, a quantitative picture of the cleavage signals can most likely be obtained for long chains, i.e. high DP_n values. The results of the molar ratios of the cleavage products showed a 4-fold weaker cleavage behavior of 2MB and 2,4DMB compared to 3MB and 4MB and could be a reason for the lack of the cleavage signals in the ^{1}H CIDNP spectra for 2MB and 2,4DMB.
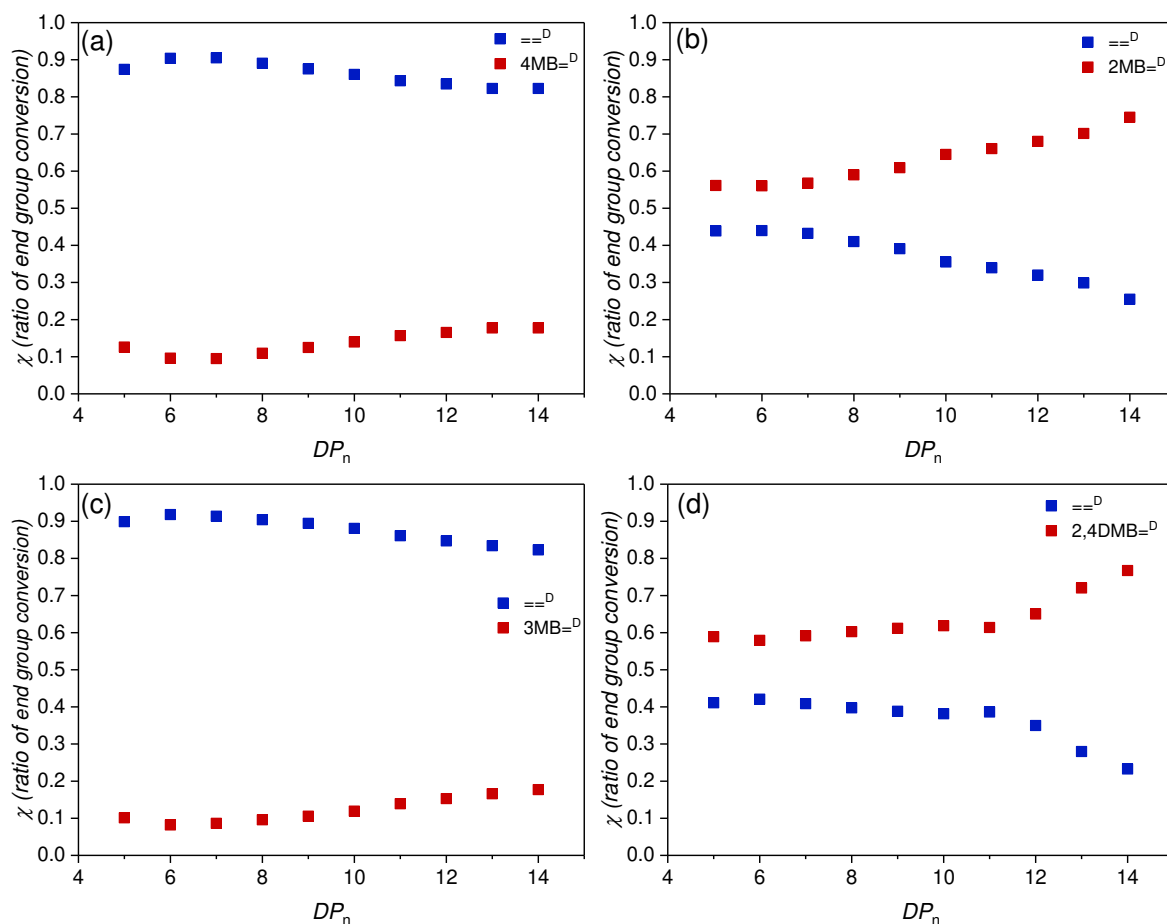
Figure 3.4.: Plot of the molar ratios χ of the peak heights (4MB=, 2MB=, 3MB=, 2,4DMB=, and ==) of 4MB (a), 2MB (b), 3MB (c) and 2,4DMB (d) vs. the DP_n. Adapted with permission from reference [165]. Copyright (2015) American Chemical Society (ACS).

3.2.6 Photochemically Stable Polymer End Groups

The PIs 2,6DMB, TriMB, TetraMB, and PentaMB are initiators forming polymer end groups that do not cleave upon UV light irradiation. Their behavior is exemplified using TriMB (the reactivity patterns for 2,6DMB, TetraMB, and PentaMB are summarized in the appendix, Figure 8.4-8.6). Figure 3.5 illustrates the SEC-ESI overview mass spectra (a) and a zoom into one repeating unit (b) of TriMB-initiated pMMA, synthesized at low laser energies (0.35 mJ/pulse, in green) and post-irradiated at high laser energies (6 mJ/pulse, in black). The assigned MS signals

are collated in Table 3.2 and the structures corresponding to the signals are depicted in Scheme 3.7.
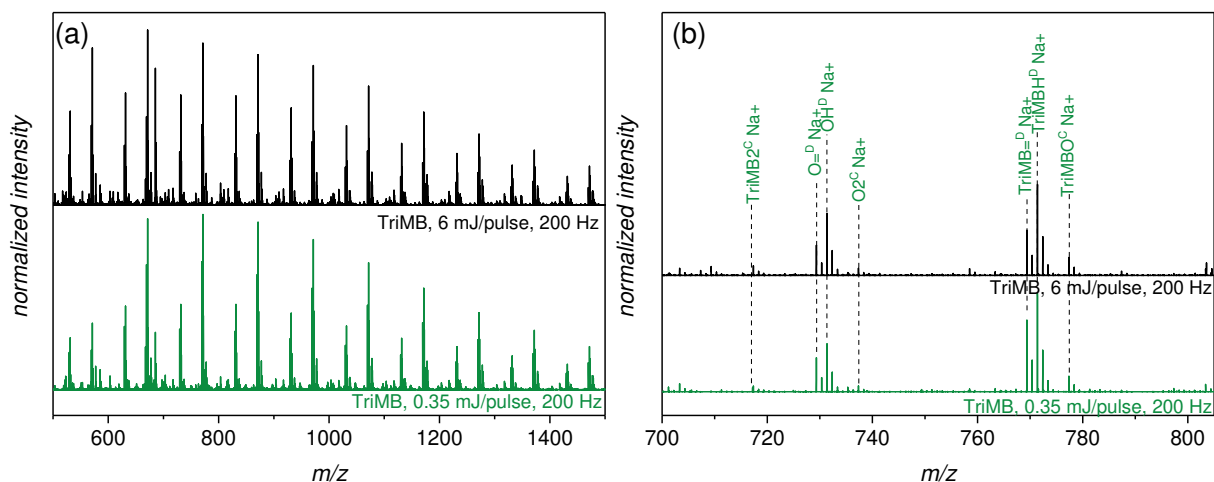
Figure 3.5.: (a) SEC-ESI overview mass spectra and (b) zoom into one repeating unit of the polymer initiated by TriMB-pMMA, at low laser energies (0.35 mJ/pulse, green spectra) and post-irradiated at higher laser energies (6 mJ/pulse, black spectra). Adapted with permission from reference [165]. Copyright (2015) American Chemical Society (ACS).

The spectrum of the starting polymer (0.35 mJ/ pulse, in green) shows the expected disproportionation (**TriMBH**, **TriMB=**, **OH**, **O=**) and the combination products (**O2**, **TriMB2**, **TriMBO**). After post-irradiation (6 mJ/pulse, in black) of the polymer, the spectrum shows – in contrast to the post-irradiation of 4MB – no signals of the cleavage products after irradiation with UV light at 351 nm. The same behavior was observed for pMMA-initiated by 2,6DMB, TetraMB, and PentaMB. Thus, it appears that multiple methyl-substitution of the benzoyl moiety causes the stability of the polymeric material against UV light irradiation. All of these so-called stable PIs have one common feature: they are substituted with methyl-groups in both *ortho*-positions on the benzoyl ring, which causes the stability against the harsh irradiation conditions.

Similarly, 2,4DMB, which is only methyl-substituted at one *ortho*-position on the benzoyl moiety, showed no stability against UV light irradiation, whereas 2,6DMB-initiated polymers remain intact, emphasizing once again the stabilizing influence of the substitution in both *ortho*-positions.
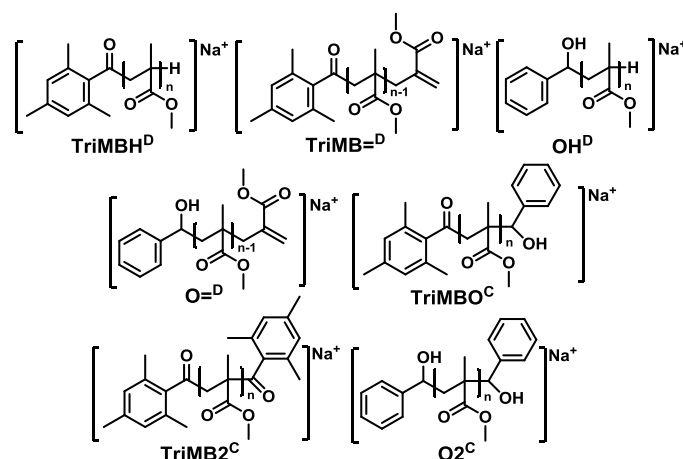
Scheme 3.7.: Disproportionation and combination products of the PLP (0.35 mJ/pulse), PLI (6 mJ/pulse) and hydrogenation experiments of TriMB-initiated pMMA, as detected by SEC-ESI-MS. Adapted with permission from reference [165]. Copyright (2015) American Chemical Society (ACS).

Table 3.2.: Overview of the polymer signals of the PLP (0.35 mJ/pulse), PLI (6 mJ/pulse) and hydrogenation experiments of TriMB-initiated pMMA, as detected by SEC-ESI-MS (R = 75000). Adapted with permission from reference [165]. Copyright (2015) American Chemical Society (ACS).

Species	Ionization	$(m/z)^{theo}$/Da	$(m/z)^{exp}$/Da	$\Delta(m/z)$
TriMBH^D	Na$^+$	771.3931	771.3915	0.0016
TriMB=^{D}	Na$^+$	769.3775	769.3763	0.0012
OH^D	Na$^+$	731.3618	731.3602	0.0016
O=^{D}	Na$^+$	729.3462	729.3449	0.0013
TriMBO^C	Na$^+$	777.3826	777.3812	0.0014
TriMB2^C	Na$^+$	717.3615	717.3598	0.0017
O2^C	Na$^+$	737.3513	737.3495	0.0018

The ^{1}H CIDNP spectrum of TriMB-pMMA (synthesized at a laser energy of 0.35 mJ/pulse, Figure 3.6) shows, in contrast to the ^{1}H CIDNP spectrum of 4MB-pMMA, no polarized signals, which is congruent with the SEC-ESI-MS results for TriMB-pMMA that also indicated no change.

As was already the case for the SEC-ESI mass spectra after post-irradiation, the ^{1}H CIDNP spectra of 2,6DMB-, TetraMB- and PentaMB-initiated pMMA displayed no changes (refer to appendix, Figure 8.8-8.9). This confirms the hypothesis that the UV stability of these end groups can be traced back to the orientation of the methyl-substitution in both *ortho*-positions of the benzoyl moiety.
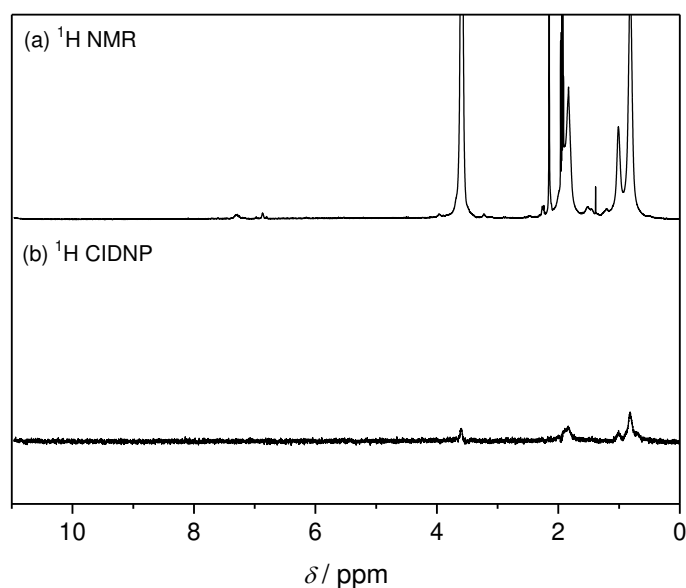
Figure 3.6.: (a) ^{1}H NMR and (b) ^{1}H CIDNP spectra of TriMB-pMMA synthesized at a laser energy of 0.35 mJ/pulse, recorded in acetonitrile-*d3* at about 80 mJ/pulse. Adapted with permission from reference [165]. Copyright (2015) American Chemical Society (ACS).

3.2.7 Comparison: PLI vs. Photo-CIDNP

As discussed in Section 3.2.5 the methods PLI, coupled to SEC-ESI-MS and photo-CIDNP spectroscopy provide different results, which can be clearly seen for 2MB- and 2,4DMB-pMMA. The cleavage products of both polymer samples after PLI experiments were determined. In the case of the photo-CIDNP experiments both samples showed absence of these cleavage products. Since the sensitivity of both methods plays an important role, the overall energy input into the polymer sample is of critical importance. For PLI experiments, the polymer is irradiated at 351 nm with 6 mJ/pulse, 90 000 pulses, 200 Hz, pulse duration of approximately 5 ns and an overall energy of 540 000 mJ. In contrast, for photo-CIDNP experiments the polymer is irradiated at 355 nm, with 80 mJ/pulse, 64 scans, 40 Hz, pulse duration of approximately 8 ns and an overall energy of 5120 mJ. Thus, the applied energy in PLI experiments is 100-fold higher than in photo-CIDNP experiments. In order to compare the effect of the employed energies of both methods, the polymers resulting after PLI and photo-CIDNP experiments were recorded via SEC-ESI-MS. Here, 4MB serves again as an example model, since the cleavage behavior could be determined via both methods. Figure 3.7 clearly shows the stronger presence of the cleavage products after PLI than after photo-CIDNP experiments. However, the energy for photo-CIDNP experiments to enhance the presence of the cleavage products could not be increased, as there is otherwise the danger that the NMR tubes can break.
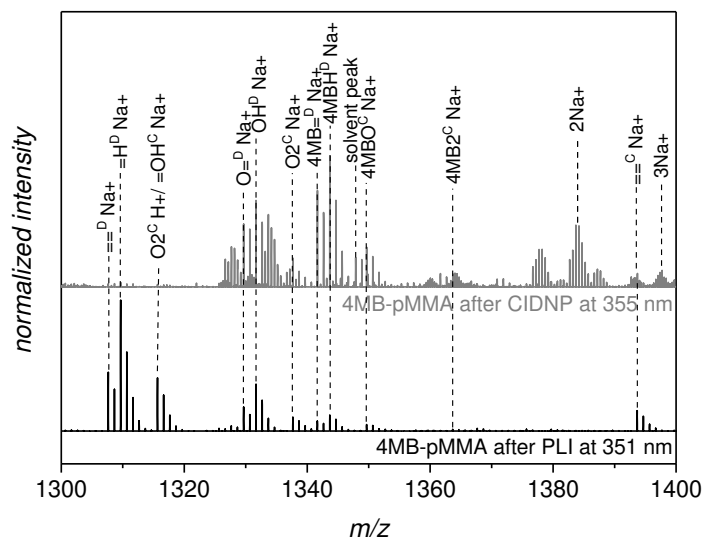
Figure 3.7.: High resolution mass spectra of 4MB-pMMA. Black spectrum: after post-irradiation with higher laser energies (6 mJ/pulse, 90 000 pulses, 200 Hz). Gray spectrum: after CIDNP experiment (80 mJ/pulse, 64 scans, 40 Hz).

3.2.8 DFT Calculations

To obtain further insights into the reactivity of the differently terminated end groups of the polymers, DFT calculations of small molecule polymer analogs were performed. The calculations were carried out by A.-M. Kelterer at the University of Graz. Since 4MB-pMMA and TriMB-pMMA were already used as example polymers in the experimental part, they were also investigated in the theoretical part as small molecule polymer analogs. To allow for inexpensive calculations, they consist of a 4MB and TriMB-substituted benzoyl moiety, connected to one methyl methacrylate (M) unit. These models should be suited for identifying the differences between the polymers entailing photochemically stable and unstable benzoyl moieties. The minimized geometries are depicted in Figure 3.8.
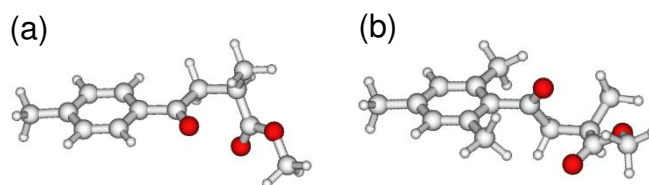
Figure 3.8.: Optimized geometries of polymer model compounds (a) 4MBM and (b) TriMBM. Optimization: DFT/B3LYP-D3/SVP.[167−172] Adapted with permission from reference [165]. Copyright (2015) American Chemical Society (ACS).

In 4MBM, the phenyl ring is coplanar with the carbonyl group, whereas in TriMBM it is twisted out of plane with a dihedral angle of ca. 70° vs. the carbonyl group. Based on the minimized geometries (Figure 3.8), (vertical) singlet excitations were computed with TD-DFT/CAM-

B3LYP/TZVP[167] and are shown in Figure 3.9 (gray), together with the experimental absorption spectra of 4MB- and TriMB-pMMA (synthesized at a laser energy of 0.35 mJ/pulse) in acetonitrile (black). The CAM-B3LYP method has been shown to overestimate vertical singlet excitations by approximately 0.5 eV.[173] Thus, the calculated S_1 transitions at 303 nm (4MBM) and 287 nm (TriMBM) correspond to excitations with 344 nm (4MBM) and 325 nm (TriMBM).
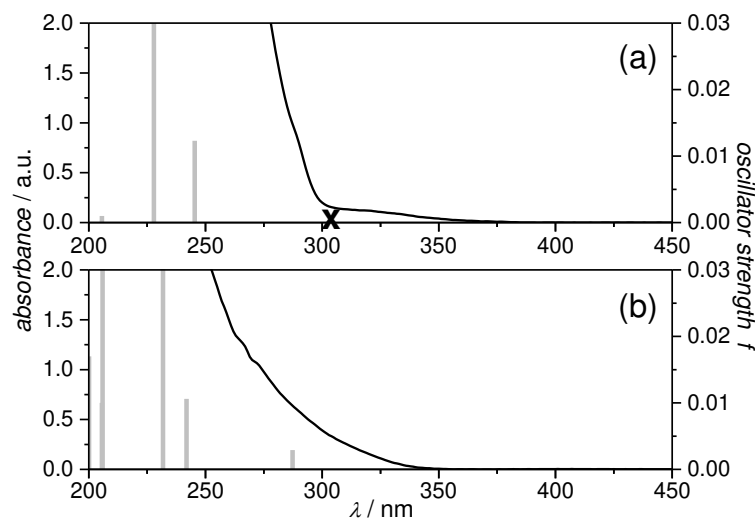
Figure 3.9.: Experimental absorption spectra of (a) 4MB-pMMA and (b) TriMB-pMMA in acetonitrile solution (black) and calculated singlet excitations (gray, S_1 of 4MBM is marked with an X). Calculated at the TDDFT/CAM-B3LYP/TZVP[174,175] level of theory. Adapted with permission from reference [165]. Copyright (2015) American Chemical Society (ACS).

On the basis of the coplanarity between the carbonyl and the phenyl moiety, the π-system is more delocalized in 4MBM than in TriMBM, leading to noticeable differences in their absorptions. For 4MBM, the S_1 singlet excitation at 303 nm (marked with 'x' in Figure 3.9a) is assigned as n-π^* transition from the C=O oxygen lone pair into the π-system. In the case of TriMBM, it is blue-shifted to 287 nm (Figure 3.9b). The oscillator strength (0.0029) of this n-π^* transition is larger than in 4MB (0.0001), due to the difference of their orbital characters. Excitations S_2 and S_3 are (in both cases) of π-π^* character and do not differ much in their intensity. A complete list of the first five vertical excitations and the relevant molecular orbitals can be found in the appendix (refer to Tables 8.7-8.8 and Figures 8.11-8.12). The triplet-triplet excitation spectra are presented in Figure 3.10. The lowest triplet excitation from T_1 was found at 1326 nm for 4MBM, while it was computed at 867 nm for TriMBM (at higher intensity). The latter is 2.25 eV higher in energy. The triplet excitation from the higher singly occupied molecular orbital (SOMO, i.e. the generated triplet) occurs at 389 nm (4MBM) and 365 nm (TriMBM), respectively. From Figure 3.10, it can be seen that in the region of the singlet absorption (marked with a "x") a number of triplet-triplet excitations are present.
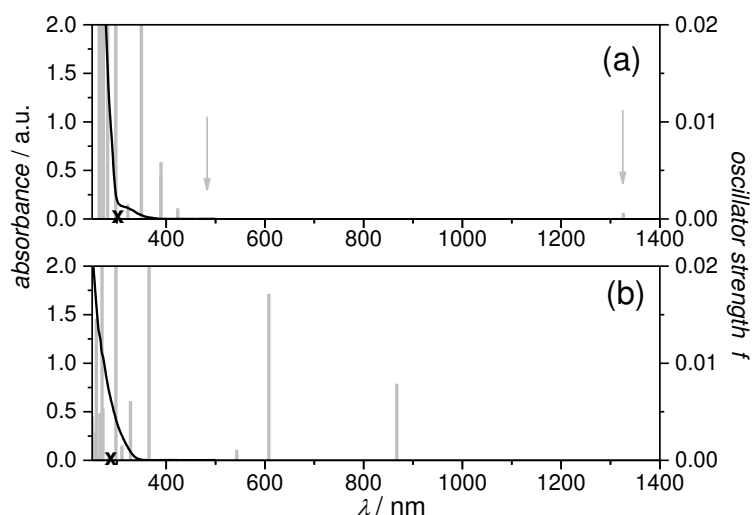
Figure 3.10.: Triplet-triplet transitions of (a) 4MBM and (b) TriMBM: the vertical lines are *T-T* excitations with their respective oscillator strengths (right axis). Vertical *T-T* transitions with small oscillator strength are marked with an arrow. The polymer singlet absorption spectrum, shifted by +0.15 eV, is shown as a black curve (left axis), and the S_1 band is marked with a 'x'.

Following El-Sayed's rule,[78] the inter system crossing (ISC) rate is high when the molecular orbital character of the singlet state is different from the triplet state, e.g. a $^3(\pi\text{-}\pi^*)$ state is achieved after ISC from a $^1(n\text{-}\pi^*)$ state (refer to Figure 3.11). From the triplet state, the molecules can undergo Norrish type I or II reactions, yielding the unsaturated species. Owing to the blue-shifted S_1 excitation of TriMBM (λ = 287 nm, $\lambda_{corrected}$ = 325 nm), only 4MBM (303 nm, $\lambda_{corrected}$ = 344 nm) can be excited into the singlet state under the given experimental conditions (photo-CIDNP: λ = 355 nm, PLI: λ = 351 nm). The calculated results of the unstable polymer end groups (2MB, 3MB and 2,4DMB) showed $n\text{-}\pi^*$ transitions in the range of 303 to 309 nm (refer to appendix, Table 8.10), able to undergo Norrish type I or II reactions. Whereas in the case of the stable polymer end groups (2,6DMB, TetraMB and PentaMB), $n\text{-}\pi^*$ transitions were identified in the range of 283 to 288 nm (refer to appendix, Table 8.10), not able to undergo Norrish type I or II reactions.
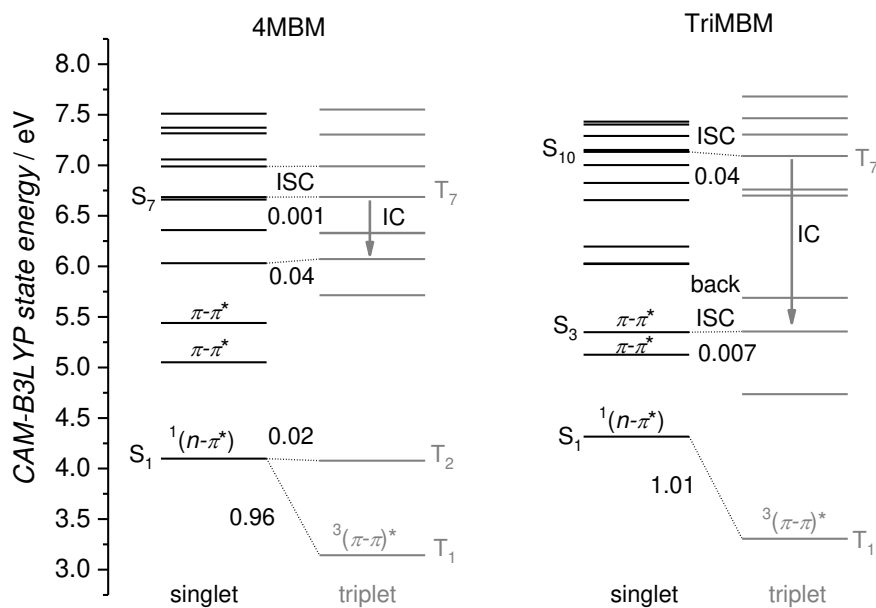
Figure 3.11.: Singlet (black) and triplet excitations (gray) of 4MBM and TriMBM, calculated at the TDDFT/CAM-B3LYP/TZVP[174,175] level of theory.

3.2.9 Summary

In summary, a library of eight photo-initiated poly(methyl methacrylate) on the basis of the benzoin structure, with various methyl-substitution on the benzoyl moiety were synthesized via PLP (at a laser energy of 0.35 mJ/pulse). The synthesized polymers were investigated towards their photochemical stability by a combination of PLI (λ = 351 nm, 6 mJ/pulse) hyphenated to SEC-ESI-MS analysis, and photo-CIDNP spectroscopy (λ = 355 nm). Critically, secondary photoinduced reactions yielding unsaturated polymeric species could be exclusively evidenced for polymers with benzoyl end groups featuring none or only one *ortho*-methyl substituent/s (2MB, 3MB, 4MB and 2,4DMB). The analysis of the post laser-irradiated polymers via SEC-ESI-MS demonstrated the conversion of the benzoyl species into unsaturated species in the polymeric material. Photo-CIDNP experiments of these photochemically unstable polymers revealed that the end group conversion occurs via Norrish type I and II reaction pathways, whereby the Norrish type II reaction is more preferred. In contrast, polymers featuring benzoyl end groups with methyl-substitution in both *ortho*-positions were stable under post laser-irradiation and photo-CIDNP conditions (2,6DMB, TriMB, TetraMB and PentaMB). DFT calculations of small molecule polymer analogs (consisting of the benzoyl end group connected to one monomer unit) were conducted to rationalize the experimental results. The calculations suggest that the disparate photochemical reactivity is likely associated with a shift of the n-π^* transitions (S_1 singlet excitations), revealing that the orientation of the phenyl moiety of photochemically unstable polymer end groups is coplanar towards the carbonyl group, which subsequently leads

to *n*-π^* transitions in the range of 303 to 307 nm (refer to Scheme 3.8). In contrast, the orientation of the phenyl moiety of photochemically stable polymer end groups is twisted out of plane towards the carbonyl group, leading to blue-shifted *n*-π^* transitions in the range of 283 to 288 nm. Based on these results, it can be concluded that the photochemical stability of benzoin-type photo-initiated polymers can be improved by simple methyl-substitution in both *ortho*-positions of the benzoyl moiety.
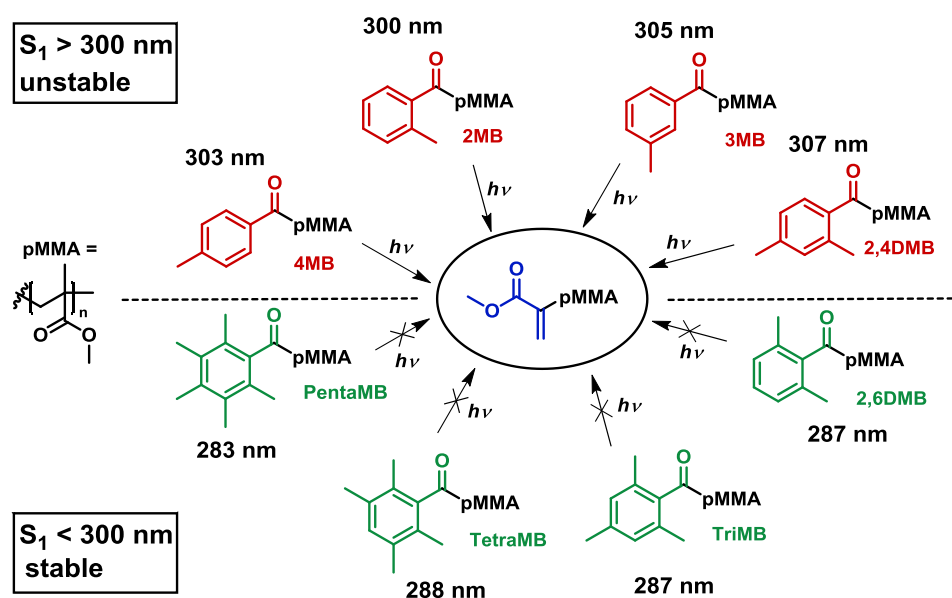
Scheme 3.8.: Overview of the investigated PIs and their respective polymer end group behavior under UV light irradiation. Initiator end groups depicted in red shows cleavage upon post-irradiation experiments, where initiators depicted in green stay intact. Adapted with permission from reference [165]. Copyright (2015) American Chemical Society (ACS).

3.3 Investigation of Methyl-Substituted Benzoin-Type Photoinitiator at Variable Wavelengths

In Section 3.2 it was demonstrated that methyl-substituted PI-derived benzoyl pMMA chain termini can undergo secondary photoinduced reactions, which occur via Norrish Type I or II pathways, leading to the formation of unsaturated species. The photochemical stability of these end groups was herby determined via a combination of PLI (6 mJ/pulse, λ = 351 nm) and subsequent high-resolution SEC-ESI-MS and photo CIDNP spectroscopy. Scheme 3.9a shows two examples (4MB: unstable end group, and TriMB: stable end group after PLI at 351 nm and 6mJ/pulse) of these investigated PI-derived polymer end groups. Interestingly, only polymers with methyl-substitution in none or one *ortho*-position were photochemically unstable at the elevated irradiation energies. In contrast, polymers with methyl-substitution in both *ortho*-positions were photochemically stable. DFT calculations suggested that the photochemical stability of the polymer end groups can be traced back to a blue shift of the n-π^* transition (S_1 singlet excitation), which occurred due to the fact that the phenyl moiety of photochemically stable end groups is twisted out of plane relative to the carbonyl group. Thus, the calculations proposed that by applying wavelengths in a range of 326 nm to 319 nm, the stable polymer end groups TetraMB, 2,6DMB, TriMB, and PentaMB (refer to Scheme 3.9b) should also cleave, which subsequently leads to the formation of the unsaturated species.
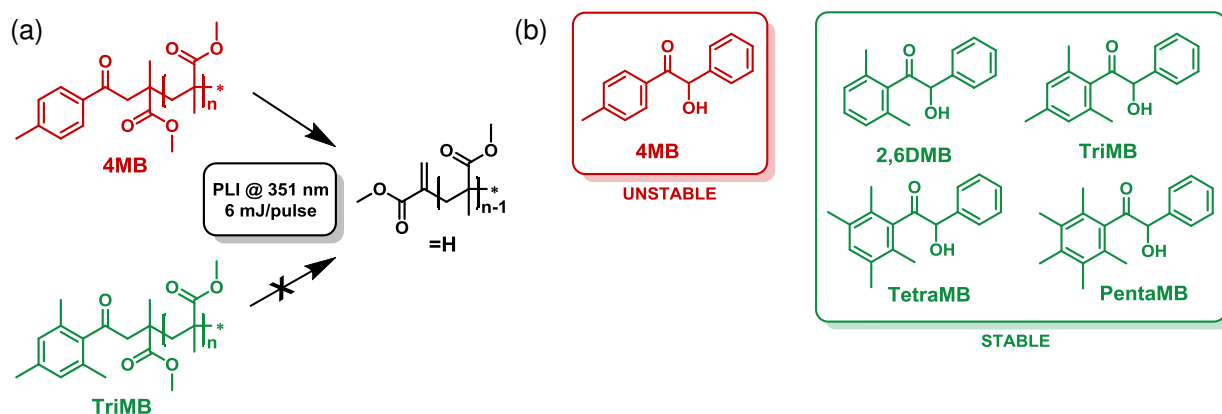
Scheme 3.9.: (a) Examples of photochemically unstable (4MB) and stable (TriMB) pMMA-chain termini under PLI at 351 nm and 6 mJ/pulse and the resulting cleavage product. (b) Overview of the investigated PI. In the red frame: PI which lead to unstable chain termini under PLI conditions at 351 nm (4MB). In the green frame: PIs which lead to stable chain termini under PLI conditions at 351 nm (2,6DMB, TriMB, TetraMB, and PentaMB). Adapted with permission from reference [176]. Copyright (2017) American Chemical Society (ACS).

Based on the results in Section 3.2, a detailed wavelength-dependent study of the influence of methyl-substitution on photochemical generated benzoyl end groups present in pMMA is presented in the following. PLP and PLI using an excimer laser and a wavelength-tunable laser combined with SEC-ESI-MS were employed for the synthesis and analysis of the polymeric materials.

3.3.1 PLP and Post-Irradiation Experiments

Five of the benzoin-type PIs described in Section 3.2, including 4MB, unstable under PLI at 351 nm, as well as four 2- and 6-substituted derivatives, stable under PLI at 351 nm (2,6DMB, TriMB, TetraMB and PentaMB, refer to Scheme 3.9b), were individually employed to polymerize MMA in bulk by PLP at low laser energy (λ = 351 nm, 0.35 mJ/pulse) and a frequency of 200 Hz to ensure intact end groups and relatively short polymer chains. The residual monomer was evaporated and the resulting polymers were precipitated in *n*-hexane to remove any residual small molecule. In the interest of simplicity, TriMB (stable end group) and 4MB (unstable end group) were employed as example polymers and subjected to pulsed-laser irradiation (PLI) in methyl isobutyrate with an overall high laser energy input (e.g.: 388000 pulses, at 345 nm) in the wavelength range of 305 to 405 nm, using the same number of photons for each wavelength. The polymer samples before and after PLI were analyzed by SEC-ESI-MS and normalized in the same retention volume region to separate the single-charged polymer species. To label the SEC-ESI-MS signals, the nomenclature introduced in Section 3.2.3 was adopted.

3.3.2 DFT Calculations

In Section 3.2.8, DFT calculations of model species consisting of the methyl-substituted benzoyl moiety linked to one monomer unit M (methyl methacrylate), have been performed. Based on the minimized geometries, vertical singlet excitations n-π^* were calculated with TD-DFT/CAM-B3LYP/TZVP.[167] The CAM-B3LYP method has been shown to overestimate vertical singlet excitations by approximately 0.5 eV.[173] Thus, the calculated relative energies and the corresponding wavelengths were corrected, considering an error of 0.5 eV for the S_1 singlet excitations. The resulting corrected relative energies and wavelengths are listed in Table 3.3. These calculations predict that the stability of the stable polymer end groups is due to a shift of the n-π^* transitions towards lower wavelengths. By applying wavelengths in the range of 326 nm to 319 nm, the stable polymer chain termini derived from the initiators 2,6DMB, TriMB, TetraMB, and PentaMB should also cleave under PLI, yielding unsaturated species.

Table 3.3.: S_1 Singlet excitations for the calculated polymer paradigms. Adapted with permission from reference [176]. Copyright (2017) American Chemical Society (ACS).

Polymer Paradigms	S_1 Singlet Excitation (n-π^* Transition)				
	E_{rel} / eV	λ / nm	E_{rel} (corrected) / eV	λ (corrected) / nm	Oscillator Strength f
4MBM	4.099	303	3.599	344	0.0001
2,6DMBM	4.315	287	3.815	325	0.0017
TriMBM	4.316	287	3.816	325	0.0029
TetraMBM	4.300	288	3.800	326	0.0006
PentaMBM	4.387	283	3.887	319	0.0006

3.3.3 Wavelength-Dependent Study of 4MB and TriMB

To obtain an overview at which wavelength the cleavage process takes place, a wavelength-dependent study (305-405 nm) of 4MB-pMMA and TriMB-pMMA (both synthesized at low laser energies at 351 nm) was carried out. In order to compare the results of the different (monochromatic) wavelengths and to concomitantly draw direct conclusions from the PLI experiments of 4MB-pMMA and TriMB-pMMA, the number of photons which hit the sample was kept constant (refer to the Experimental Section for a detailed description of how a constant photon count was achieved). The wavelength-dependent high resolution mass spectra of the PLI of 4MB-pMMA (colored spectra), as well as the parent polymer (gray spectrum) and the isotopic peak pattern simulation (black spectrum) are illustrated in Figure 3.12a. The spectrum of the parent polymer, synthesized at low laser energies (0.35 mJ/pulse, 200 Hz, 351 nm), is depicted in gray and shows the expected disproportionation (**4MB=^{D}**, **4MBH^D**, **O=^{D}**, **OH^D**) and combination products (**O2^C**, **4MB2^C**, **4MBO^C**). The results of the wavelength-dependent PLI experiments of 4MB-pMMA clearly show the disappearance of the benzoyl moiety signals and the appearance of the unsaturated species signals by screening from the highest (405 nm, red spectrum) to the lowest wavelength (305 nm, pink spectrum). The cleavage products (**==^{D}**, **=H^D**, **=O^C**, **==^{C}**) are already formed from 385 nm (orange spectrum) onwards. The appearance of the cleavage products of the polymer upon PLI at 345, 325, and 305 nm are in agreement with the results in Section 3.2, in which the PLI at 351 nm of 4MB terminated polymer chains showed the formation of unsaturated polymeric species. The assigned polymer structures before and after PLI are shown in Figure 3.12b and the experimental and theoretical *m/z*-values for each species are listed in Table 3.4.
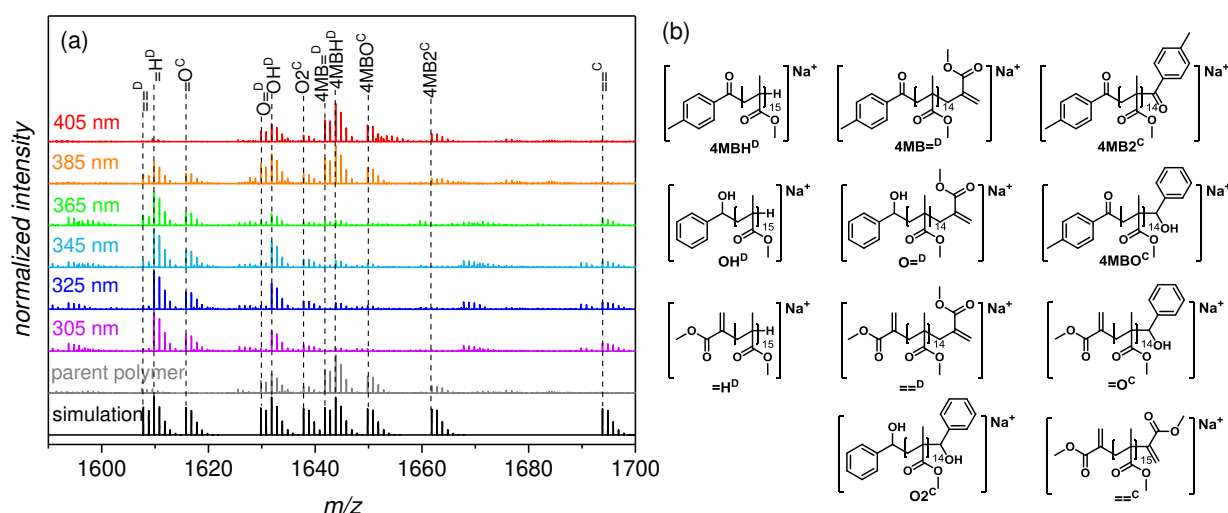
Figure 3.12: (a) High resolution SEC-ESI mass spectra of 4MB-pMMA, synthesized at low laser energies (0.35 mJ/pulse, 200 Hz, 351 nm, gray spectrum), post-irradiated at different wavelengths (305-405 nm, 100 Hz, 18 °C) at a constant photon count as well as the theoretical isotope patterns (black spectrum). (b) Disproportionation and combination products of the polymer initiated by 4MB, at low laser energies (0.35 mJ/pulse, 200 Hz, 351 nm), post-irradiated with high laser energies (100 Hz, 305-405 nm), as detected by SEC-ESI-MS. Adapted with permission from reference [176]. Copyright (2017) American Chemical Society (ACS).

Table 3.4.: Overview of the assigned signals of the polymers synthesized at low laser energies (351 nm, 0.35 mJ/pulse, 200 Hz) and post-irradiated with high laser energies (305 nm, 100 Hz) of 4MB-initiated pMMA, as detected by SEC-ESI-MS with a resolution of 50000. Adapted with permission from reference [176]. Copyright (2017) American Chemical Society (ACS).

Species	Ionization	$(m/z)^{\text{theo}}$/Da	$(m/z)^{\text{exp}}$/Da	$\Delta(m/z)$
4MBH$^{\text{D}}$	Na$^+$	1643.8332	1643.8366	0.0034
4MB=$^{\text{D}}$	Na$^+$	1641.8175	1641.8393	0.0218
4MB2$^{\text{C}}$	Na$^+$	1661.8226	1661.8483	0.0257
4MBO$^{\text{C}}$	Na$^+$	1649.8226	1649.8343	0.0117
O2$^{\text{C}}$	Na$^+$	1637.8226	1637.8243	0.0017
OH$^{\text{D}}$	Na$^+$	1631.8332	1631.8294	0.0038
O=$^{\text{D}}$	Na$^+$	1629.8175	1629.8228	0.0053
=H$^{\text{D}}$	Na$^+$	1609.8124	1609.8131	0.0007
==$^{\text{D}}$	Na$^+$	1607.7968	1607.7935	0.0033
=O$^{\text{C}}$	Na$^+$	1615.8019	1615.8026	0.0007
==$^{\text{C}}$	Na$^+$	1693.8336	1693.8350	0.0014

In Figure 3.13, the high-resolution SEC-ESI mass spectra of pMMA initiated by TriMB (0.35 mJ/pulse, gray spectrum), post-irradiated with high laser energies utilizing wavelengths in the range of 305-405 nm (colored spectra), and the isotopic peak pattern simulation (black spectrum), is depicted. The mass spectrum of the unirradiated TriMB-pMMA exhibits the expected disproportionation products (**TriMB=$^{\text{D}}$**, **TriMBH$^{\text{D}}$**, **O=$^{\text{D}}$**, **OH$^{\text{D}}$**), refer to Figure 3.13a,

gray spectrum) and combination products (**O2^C**, **TriMB2^C**, **TriMBO^C**, refer to Figure 3.13a, gray spectrum). In contrast to the wavelength-dependent PLI experiments of 4MB-pMMA, the cleavage products (==^D, =H^D, =O^C) of the irradiated TriMB-pMMA are formed from 345 nm (light blue spectrum) onwards, indicated by the appearance of the signals at $m/z = 1607.8, 1609.8, 1615.8$ (values taken from the 305 nm mass spectrum). The disappearance of the cleavage products of the chain termini after PLI at 365, 385, and 405 nm is in a good agreement with the results of Section 3.2. TriMB-pMMA was here stable upon PLI at 351 nm and should therefore be stable by applying higher wavelengths. The assigned polymer structures before and after PLI at different wavelengths are shown in Figure 3.13b and the experimental and theoretical m/z-values for each polymeric species are collated in Table 3.5.
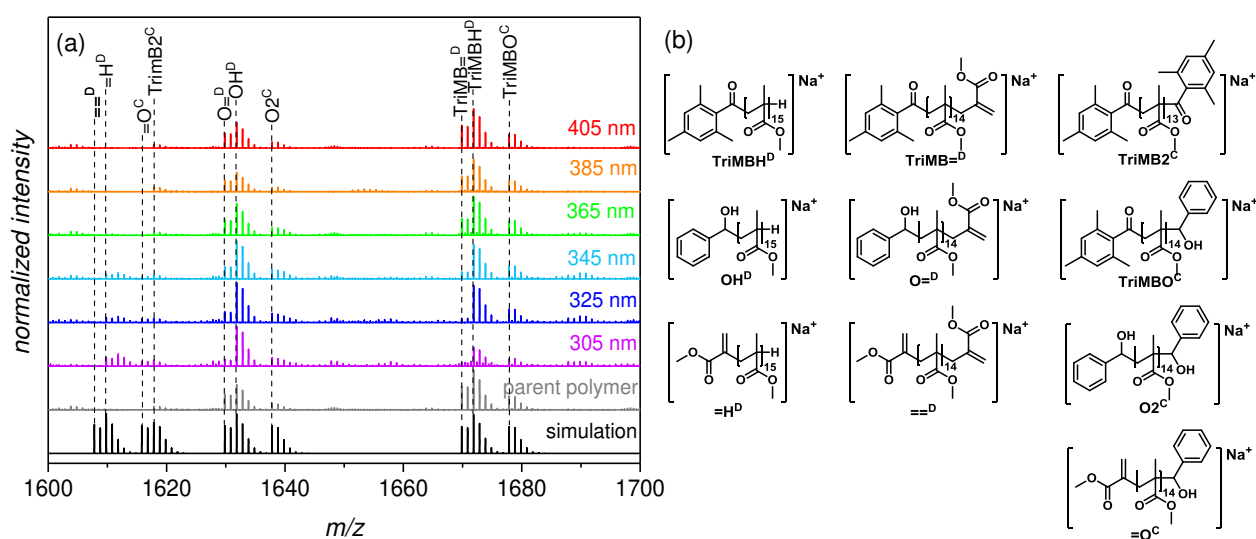
Figure 3.13: (a) High resolution SEC-ESI mass spectra of TriMB-pMMA, synthesized at low laser energies (0.35 mJ/pulse, 200 Hz, 351 nm, gray spectrum), post-irradiated at different wavelengths (305-405 nm, 100 Hz, 18 °C) at a constant photon count as well as the theoretical isotope patterns (black spectrum). (b) Disproportionation and combination products of the polymer initiated by TriMB, at low laser energies (0.35 mJ/pulse, 200 Hz, 351 nm), post-irradiated with high laser energies (100 Hz, 305-405 nm), as detected by SEC-ESI-MS. Adapted with permission from reference [176]. Copyright (2017) American Chemical Society (ACS).

Table 3.5.: Overview of the assigned signals of the polymers synthesized at low laser energies (351 nm, 0.35 mJ/pulse, 200 Hz) and post-irradiated with high laser energies (305 nm, 100 Hz) of TriMB-initiated pMMA, as detected by SEC-ESI-MS with a resolution of 50000. Adapted with permission from reference [176]. Copyright (2017) American Chemical Society (ACS).

Species	Ionization	$(m/z)^{theo}$/Da	$(m/z)^{exp}$/Da	$\Delta(m/z)$
TriMBH^D	Na$^+$	1671.8645	1671.8708	0.0063
TriMB=^{D}	Na$^+$	1669.8488	1669.8384	0.0104
TriMB2^C	Na$^+$	1617.8328	1617.8316	0.0012
TriMBO^C	Na$^+$	1677.8539	1677.8598	0.0059
O2^C	Na$^+$	1637.8226	1637.8263	0.0037
OH^D	Na$^+$	1631.8332	1631.8314	0.0018
O=^{D}	Na$^+$	1629.8175	1629.8170	0.0005
=H^D	Na$^+$	1609.8124	1609.8151	0.0027
==^{D}	Na$^+$	1607.7968	1607.7955	0.0013
=O^C	Na$^+$	1615.8019	1615.8123	0.0004

3.3.4 Quantitative Analysis of the Formation of the Unsaturated Chain Termini

For the quantitative assessment of the formation of the unsaturated species of TriMB-, 4MB-, 2,6DMB-, TetraMB-, and PentaMB-initiated pMMA, a calculation to obtain a molar ratio (χ) of these unsaturated species compared to the intact species was carried out. The quantification was conducted for TriMB and 4MB – utilized as example polymers – by applying wavelengths in the range of 305 to 405 nm. For 2,6DMB, TetraMB and PentaMB, the quantification of the unsaturated species was carried out by using the predicted wavelengths (325, 326 and 319 nm) of the DFT calculations from Section 3.2.8. In the following, the calculation to quantify the unsaturated species using TriMB as example will be explained in detail, refer to Figure 3.14.

In Section 3.2.5, the calculations to quantify these unsaturated species were performed by utilizing the peak height, Δh, of every repeating unit's respective disproportionation peak clusters and therefore the intact peaks were compared with the associated unsaturated peaks (for example: **4MB=** and **==**). Here, it is not possible to utilize the disproportionation peaks of the intact and unsaturated species (**TriMB=**, **TriMBH**, **==** and **=H**), due to non-presence of the double bonds after PLI. Thus, the non-presence of the double bonds increases with the decrease of the wavelength and occurs for every disproportionation peak pattern – for example also for **O=** and **OH** – which were not influenced by PLI, due to the non-existence of the benzoyl group.
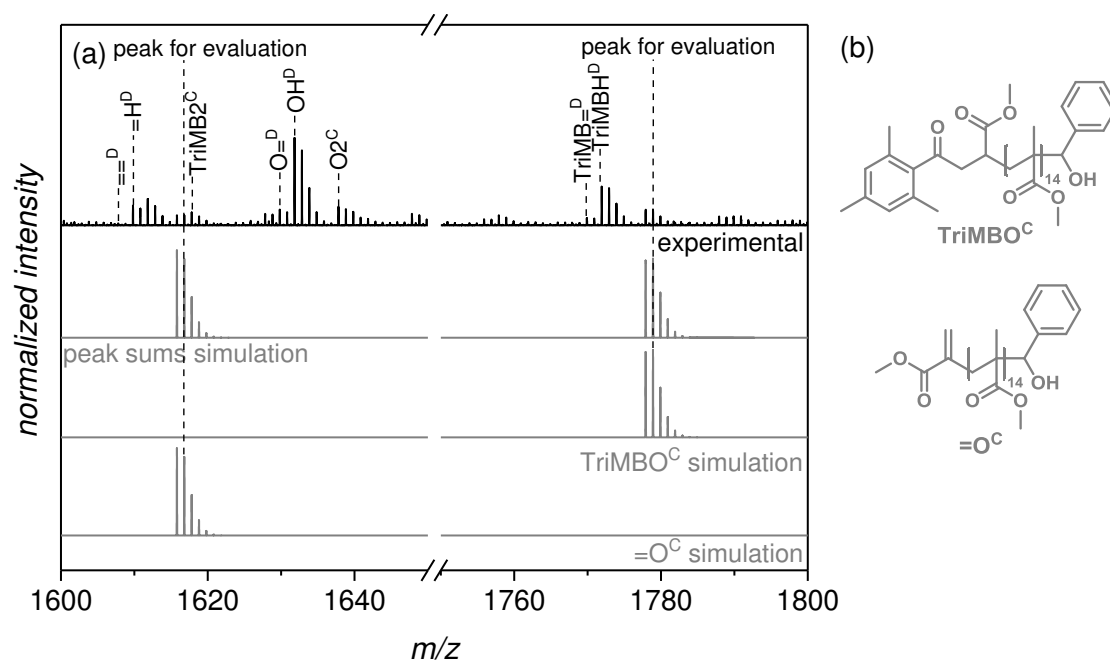
Figure 3.14.: (a) High resolution SEC-ESI mass spectrum of TriMB-pMMA, PLI with high energies (100 Hz, 305 nm, black spectrum), at a constant photon count as well as the theoretical isotopic pattern of TriMBO^C and =O^C and the sum of the simulation patterns (gray spectra); (b) Structure of the combination products (TriMBO^C and =O^C). Adapted with permission from reference [176]. Copyright (2017) American Chemical Society (ACS).

It seems that only the double bonds of the disproportionation peak pattern are affected upon PLI and it is likely that the new double bounds which are generated during the formation of the unsaturated species remain unaffected. For this reason, the combination products before and after PLI (refer to Figure 3.14b) were selected to calculate the amount of the newly formed unsaturated species, as they have no double bonds in their intact polymer structure and seem to be therefore unaffected upon PLI. In order to ensure that the assumption, regarding the non-presence of the double bonds after PLI was correct, evaluations using the mass spectra of TriMB in the wavelength range of 305 nm to 345 nm, were carried out. Therefore, the disproportionation pattern **O=** and **OH**, which is unaffected upon PLI, as well as the newly formed disproportionation pattern **==** and **=H** which occurred upon PLI, were selected. The ratios $\chi^{XH}(n)$ of every peak pattern for every wavelength were calculated, using the peak height of the signals, where X defines the respective end group of the initiation or end group converted fragment (refer to Equation 3.3 and 3.4).

$$\chi^{OH^D}(n) = \frac{\Delta h^{OH^D}(n)}{\Delta h^{O=^D}(n) + \Delta h^{OH^D}(n)} \tag{3.3}$$

$$\chi^{=H^D}(n) = \frac{\Delta h^{=H^D}(n)}{\Delta h^{==^D}(n) + \Delta h^{=H^D}(n)} \tag{3.4}$$

81

The ratios for both disproportionation patterns are similar and seem to be constant in the wavelength range of 305 to 345 nm (refer to Figure 3.15 and Table 3.6). If the newly formed double bonds of the unsaturated species (=**H**) are influenced by PLI, it could be expected that a mismatch in the ratios of both disproportionation pattern or even an increase in the ratios at lower wavelengths occurs. Thus, it can be suggested that upon PLI the double bonds of the disproportionation pattern disappear without having an influence of the newly formed unsaturated species.
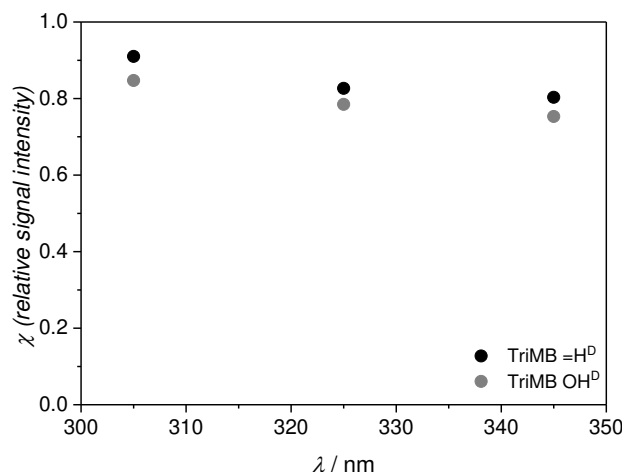
Figure 3.15.: Wavelength-dependent end group reactivity (305-345 nm) expressed by the ratios of =H^D and OH^D (refer to Equation 5.3 and 5.4) of TriMB-pMMA, determined with high resolution SEC-ESI-MS. Adapted with permission from reference [176]. Copyright (2017) American Chemical Society (ACS).

Table 3.6.: Overview of the calculated signal intensity ratios of OH^D and =H^D and the percentage deviation from =H^D to OH^D in the wavelength range of 305 to 345 nm of TriMB-pMMA, as detected by SEC-ESI-MS. Adapted with permission from reference [176]. Copyright (2017) American Chemical Society (ACS).

Species	λ / nm	Signal Intensity Ratio of XH^D	Percentage Deviation from =H^D to OH^D / %
OH^D	305	0.85	
=H^D	305	0.91	7
OH^D	325	0.78	
=H^D	325	0.83	5
OH^D	345	0.75	
=H^D	345	0.80	6

Thus, the peak height, Δh(=**O**^{C}), was utilized to calculate the amount of the newly formed unsaturated species. The ratio of the unsaturated species signal (=**O**^{C}) compared to the intact species signal (**TriMBO**^{C}) was calculated. In order to ensure that the peak height Δh(=**O**^{C}) is not influenced by the disproportionation pattern =**H**, the second peak of the combination pattern was chosen for the evaluation, as well as the second peak of the combination pattern of

TriMBO[C] (refer to Figure 3.14a). Thereby the peak height $\Delta h(=O^C (n))$ was divided by the sum of the peak height $\Delta h(=O^C (n))$ and $\Delta h(\textbf{TriMBO}^C (n+1))$ to ensure that the ratio was calculated with the corresponding end groups, respectively (refer to Equation 3.5).

$$\chi^{=O^C}(n) = \frac{\Delta h^{=O^C}(n)}{\Delta h^{TriMBO^C}(n+1) + \Delta h^{=O^C}(n)} \tag{3.5}$$

A plot of χ (λ = 305-365 nm) for each fragment of $=O^C$ vs. the degree of polymerization DP_n (refer to Figure 3.16b) shows a constant gradient close to zero, if a chain length independent ESI-MS process takes place. Figure 3.16a shows the wavelength-dependent ratio of end group conversion of 4MB- and TriMB-pMMA, derived by the height $\Delta h(=O^C)$, clearly illustrating that pMMA initiated by TriMB, starting at 345 nm, also cleaves under PLI conditions. In contrast to 4MB-pMMA, which cleaves from 385 nm and reaches the maximum of end group conversion at 365 nm. The amount of the formation of unsaturated species of TriMB-pMMA increases constantly with decreasing of the wavelength.
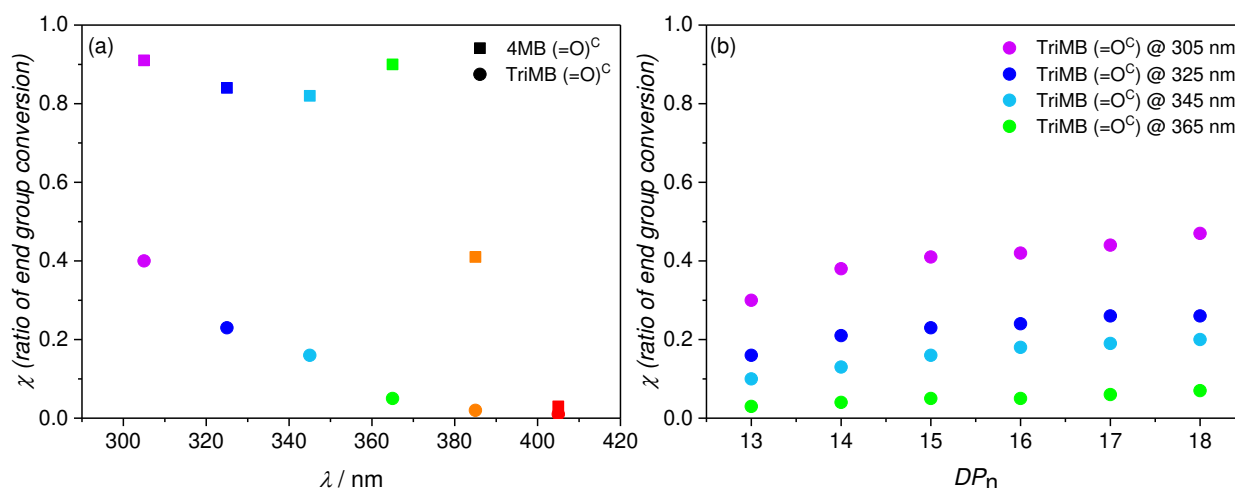
Figure 3.16.: (a) Wavelength-dependent plot from 305-405 nm of the end group conversion ratios (shown with the combination product =O) derived from the peak heights (4MBO[C] and =O[C]; TriMBO[C] and =O[C]) of 4MB-pMMA and TriMB-pMMA, determined with high resolution SEC-ESI-MS. (b) Plot of the end group conversion ratios (305-365 nm) derived from the peak heights (TriMBO[C] and =O[C]) of TriMB-pMMA vs. the DP_n. Adapted with permission from reference [176]. Copyright (2017) American Chemical Society (ACS).

As mentioned previously, the predicted wavelengths of the DFT calculations for PLI of the so-called stable polymer end groups (TriMB, 2,6DMB, TetraMB and PentaMB) are employed to evidence the end group transformation. Figure 3.17b depicts the structures of the determined polymer end groups, the theoretical calculated wavelength values and the resulting end group conversion products (for clarity, only the combination products XO are shown). In Figure 3.17a, it can be clearly seen that by applying these theoretical values (blue symbols), the end group

cleavage for all polymer end groups occurs, whereas cleavage products could be barely identified when applying 351 nm (light blue symbols, refer to Section 3.2).
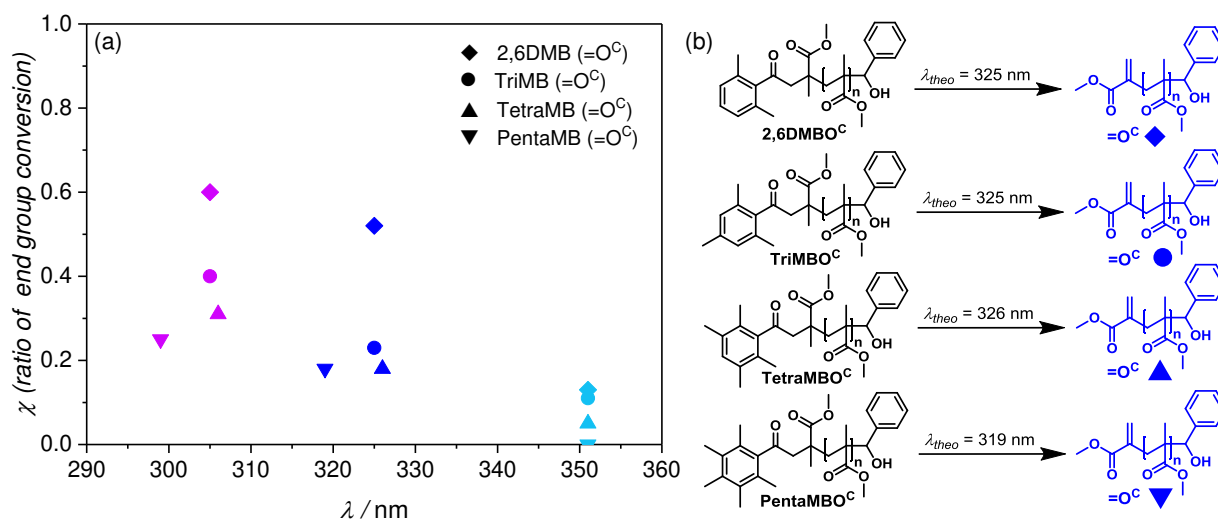
Figure 3.17.: (a) Wavelength-dependent plot of the end group conversion ratios (shown with the combination product =O) derived from the peak heights (e.g.: TriMBO^C and =O^C) of TriMB- ($\bullet$), 2,6DMB- ($\blacklozenge$), TetraMB- ($\blacktriangle$), PentaMB-pMMA ($\blacktriangledown$), determined with high resolution SEC-ESI-MS. The polymers were post-irradiated at different wavelengths (351 nm: Section 3.2, represented by light-blue symbols; predicted wavelengths, represented by blue symbols; applied delta of the wavelengths, represented by pink symbols, applying a constant photon count for each wavelength. (b) Proposed structures of the determined combination products (XO), the utilized theoretical wavelength values and the structures of the end group conversion products are shown. Adapted with permission from reference [176]. Copyright (2017) American Chemical Society (ACS).

Based on the results of the wavelength scan of TriMB-pMMA, it is evident that the end group conversion occurs most effectively at 305 nm, while DFT calculations for TriMB suggested the most effective cleavage at 325 nm. Thus, the evident wavelength delta (20 nm) of the results of TriMB was consistently applied to the theoretical values of 2,6DMB, TetraMB and PentaMB. The pink symbols in Figure 3.17a show the results obtained when employing the adjusted wavelengths. Here, it can be unambiguously seen that the amount of end group conversion for all polymer structures increases, compared to the theoretical values (blue symbols). Furthermore, a trend in end group conversions is evident, whereby 2,6DMB features the most effective end group conversion, followed by TriMB, TetraMB and finally PentaMB. The methyl-substitution on the benzoyl end group plays a crucial role here. By increasing the methyl-groups on the benzoyl moiety, the location of the *n*-orbital (HOMO) and π-C=O orbital (LUMO) also changes, which shifts the energy based on the inductive effect to lower wavelengths.

3.3.5 Investigation of the Photochemical Stability of the Polymer Backbone

In the current Section, the end group – undergoing secondary cleavage reactions upon harsh irradiation conditions (351 nm, 6mJ/pulse) – can affect the backbone of the polymer. The backbone can cleave during the formation of radicals, leading to a different polymer conformation (e.g. ring structures). In order to ensure that the polymer backbone stays intact under such UV-irradiation conditions, additional SEC-ESI-MS experiments were performed. A pMMA SEC standard (M_n = 9100 g·mol^{-1}, Đ = 1.05) was therefore used and subjected to PLI using the same conditions, i.e. the lowest wavelengths (299 nm and 305 nm). Figure 3.18a indicates that after PLI using these wavelengths the backbone remains intact, evidenced by a comparison of the non-irradiated pMMA standard. It is additionally of critical importance to inspect at the overall polymer distribution before and after irradiation. Therefore, hyphenated SEC was utilized to provide information about the polymer distribution. The SEC trace in Figure 3.18b depicts the polymer before and after irradiation at 299 and 305 nm. The results indicate that the backbone is unaffected upon UV-irradiation, since the polymer distribution does not change.
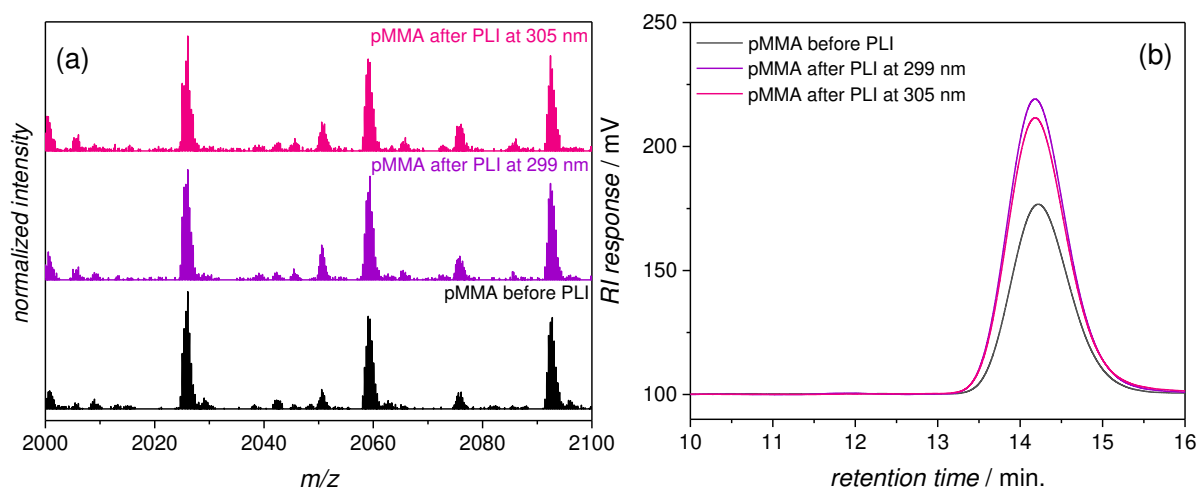
Figure 3.18.: (a) High resolution SEC-ESI mass spectra and (b) SEC trace of the pMMA SEC calibration standard obtained from Polymer Standard Service (PSS), non-irradiated (black spectrum), post-irradiated at 299 nm (purple spectrum), and post-irradiated at 305 nm (pink spectrum), at a constant photon count for each wavelength. Adapted with permission from reference [176]. Copyright (2017) American Chemical Society (ACS).

3.3.6 Summary

In summary, an in-depth wavelength-dependent study of the influence of methyl-substitution on the photochemical stability of benzoyl end groups in pMMA chain termini is presented. Five PI-derived pMMA polymers (4MB, 2,6DMB, TriMB, TetraMB, and PentaMB) were synthesized via PLP at low laser energy, and post-irradiated with high overall laser energy input, confirming the theoretically predicted stability trends: All polymer-derived end groups (2,6DMB, TriMB, TetraMB and PentaMB) except the one based on 4MB, show an increased stability against UV light irradiation. However, the stable polymer-derived end groups show different degrees of stability depending on their substitution pattern. Thus, the methyl-substitution on the benzoyl moiety dictates the photochemical end group stability as a function of the wavelength, which can be traced back to the influence of the inductive effect.

3.4 Systematic Assessment of the Role of the Benzoyl Fragment

In the Sections 3.2 and 3.3 it was shown that the benzoyl polymer end group is capable to undergo secondary cleavage reactions, depending on the substitution pattern of the phenyl ring. In the current Section a systematically investigation to assess the effect of the photoinduced end group conversion of benzoyl-derived end groups, is presented. Therefore, the influence of the solvent as well as the influence of the aromatic substituents on the cleavage behavior with various functional groups, such as fluorine and methoxy, was investigated. Furthermore, the influence of the polymer backbone, utilizing monomers with longer side chains, as well as sterically hindered side chains, was examined. In addition, the secondary irradiation procedure was conducted under solid-state conditions, simulating the effect in the final coating-like product. The photoinitiator/monomer/solvent/solid-state systems encompass a wide structural regime as well as various PLI conditions to draw general mechanistic conclusions regarding the photoinduced polymer end group transformations.

3.4.1 Influence of the Solvent

Since it is known that chemical reactions are dependent on the solvent, the post-irradiation of benzoyl-terminated end groups were performed in various solvents (methyl isobutyrate, toluene, dioxane, dichlormethane, ethylacetate, and acetonitrile, refer to Scheme 3.10), thus spanning a wide range of irradiation conditions (polar and non-polar solvents). The solvent methyl isobutyrate (MIB) was already used in Section 3.2 and 3.3 for post-irradiation experiments, since it mimics the structure of the used monomer methyl methacrylate (MMA). To keep the experiments simple focusing only on the effects of the solvents, benzoin-initiated pMMA, where the phenyl ring is not substituted with functional groups, was used for this investigation.
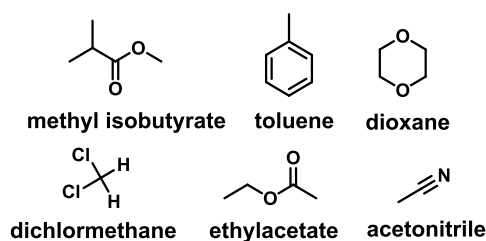
Scheme 3.10.: Various solvents (e.g. toluene, dioxane) applied for post-irradiation reactions (6 mJ/pulse, 351 nm).

The high resolution mass spectra of the PLI experiments in various solvents of precipitated benzoin-pMMA (colored spectra), the parent polymer (black spectrum) as well as the associated structures of the polymeric species are illustrated in Figure 3.19.
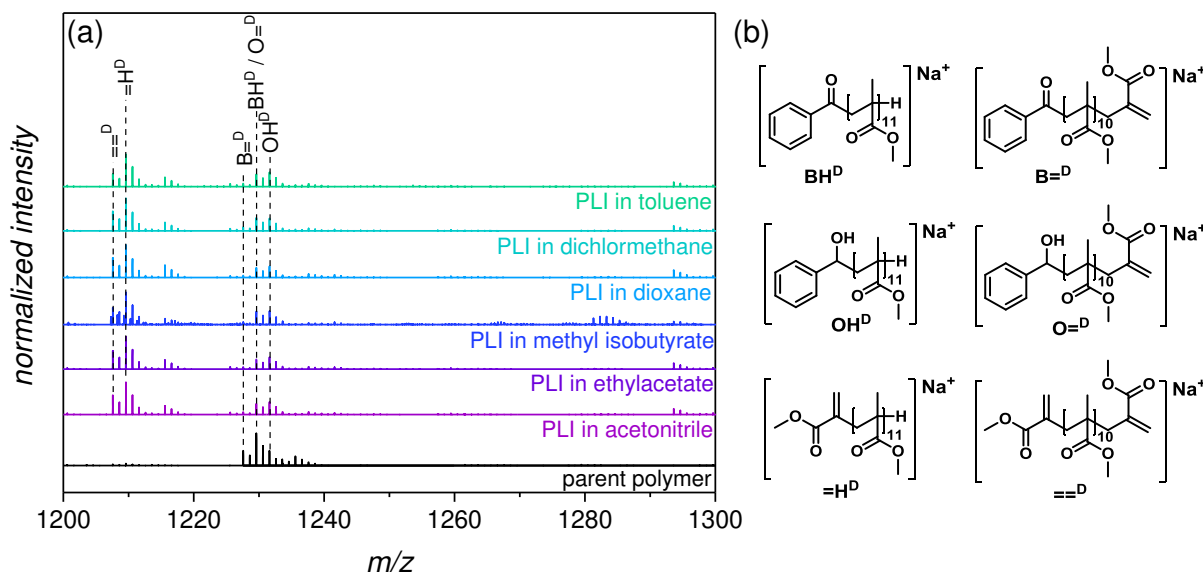
Figure 3.19.: (a) High resolution SEC-ESI mass spectra of benzoin-initiated pMMA, synthesized at low laser energies (0.35 mJ/pulse, 200 Hz, 351 nm, black spectrum) and post-irradiated in different solvents (351 nm, 200 Hz, colored spectra). (b) Disproportionation products of the polymeric material, as detected by SEC-ESI-MS.

For clarity, only the disproportionation products are assigned. The results clearly show that after PLI at 6 mJ/pulse the disproportionation pattern **B=^{D}** and **BH^D** decreases and the disproportionation pattern of the new unsaturated species **==^{D}** and **=H^D** arises, while there is no significant difference between the PLI experiments in the various solvents. Thus, the n-π^* transition is not influenced by the used solvent.

3.4.2 Influence of Various Functional Groups in *para*-Position

In Section 3.2 it was shown that methyl-substitution in *para*-position on the benzoyl moiety leads, after PLI of the respective polymer, to the formation of unsaturated species. To further investigate the cleavage behavior, a systematic investigation of the benzoyl fragment including various functional groups, such as fluorine, tertiary amines (morpholino group), thioethers, and methoxy-groups in *para*-position was carried out (refer to Scheme 3.11). Thus, the substitution with different functional groups in addition to the benzoyl moiety causes a change in the electronic structure of the molecule, having an important impact on its photochemical behavior. In this context, only fluorine belongs to the electron-withdrawing groups, since the inductive effect is more pronounced than the mesomeric effect. On the other hand, tertiary amines

(morpholino group), thioethers, and methoxy-groups, as well as the methyl-groups from Sections 3.2 and 3.3 belong to functional groups, which possess an electron-pushing character, as the mesomeric effect is more dominant.
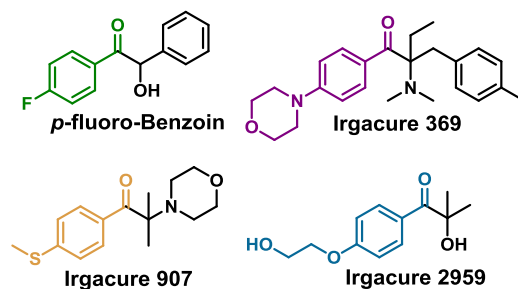
Scheme 3.11.: PIs with various substitutions (*para*-position) of the benzoyl fragment (colored).

Figure 3.20 represents the parent precipitated polymers (colored spectra) initiated by *p*-fluoro-Benzoin (FBz), Irgacure 369 (369), Irgacure 907 (907) and Irgacure 2959 (2959) as well as the PLI experiments (black spectrum) at 6 mJ/pulse, respectively.

Figure 3.20.: High resolution SEC-ESI mass spectra of pMMA before (0.35 mJ/pulse, colored spectra) and after PLI (6 mJ/pulse, black spectra), initiated by (a) FBz, (b) 369, (c) 907, and (d) 2959.

The polymer structures are presented in Scheme 3.12 in an abbreviated form due to illustration reasons. The unsaturated species are present after PLI and benzoyl fragments are hardly existent after post-irradiation for all polymer samples. Irradiation of 369-pMMA leads to unknown species with MMA as repeating unit (labeled with a question mark "?"). High energy collision dissociation (HCD) measurements to enlighten the end group structure of these species did not lead to a structural elucidation. Further investigation needs to be carried out to identify the unknown species. In the light of the results of the PLI experiments with various substitutions on the benzoyl fragment in *para*-position, no clear statement on the effect of electron-withdrawing and electron-pushing groups towards the end group conversion can be made.
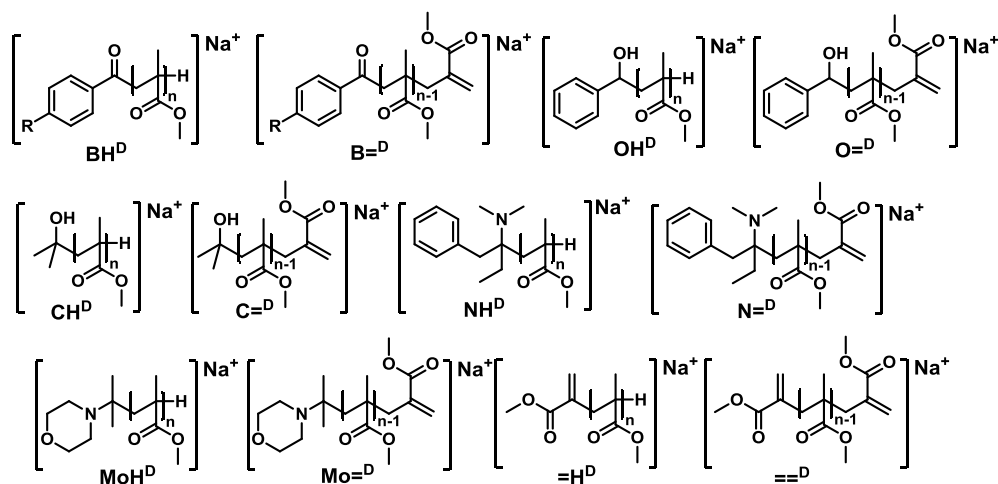
Scheme 3.12.: Disproportionation products of the PLP (0.35 mJ/pulse) and post-irradiation (6 mJ/pulse) experiments of FBz-, 369-, 907- and 2959-initiated pMMA, as detected by SEC-ESI-MS. The residue R on the benzoyl fragment serves as a simplified presentation and represents der various residues of the PIs regarding to their benzoyl fragment.

3.4.3 Influence of the Polymer Backbone

The chain conformation depends on the backbone and consequently on the choice of the monomer, but at the same time on the used solvent. Thus, the conformation refers to the structure that is associated with the rotation of molecules around the single bonds. In the present Section, the focus lies on the influence of the backbone structure towards the UV light stability of the end group. For simplicity, benzoin, which already served as example initiator in Section 3.4.1, was utilized to polymerize the monomer in bulk and the resulting polymers (precipitated in proper solvent) were subjected to PLI at 6 mJ/pulse. In the previous Sections, only MMA was used for PLI experiments. Here, the monomers *n*-butyl methacrylate (*n*-BMA), *t*-butyl methacrylate (*t*-BMA) and benzyl methacrylate (BnMA, refer to Scheme 3.13) were selected to enable a comparison with the results obtained for MMA with regard to the length

(*n*-BMA: longer ester chain than MMA), the branch (*t*-BMA) and the steric hindrance (BnMA) on the photoinduced end group conversion.
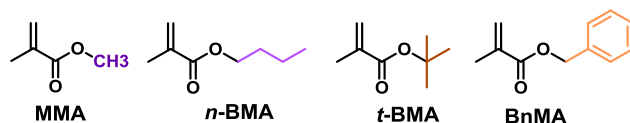
Scheme 3.13.: Employed methacrylate monomers with variations in the length, branches and sterically hindrance. The monomers were employed in the photoinduced polymerization using benzoin and subsequently applied for PLI at 6 mJ/pulse.

The high resolution mass spectra of the monomer-dependent PLI experiments (colored spectra) – using benzoin as initiator – and as well as of the parent polymer (black spectrum) are illustrated in Figure 3.21. The associated structures, focussing only on the disproportionation products and the ester residues, are illustrated with R and depicted in Scheme 3.14.
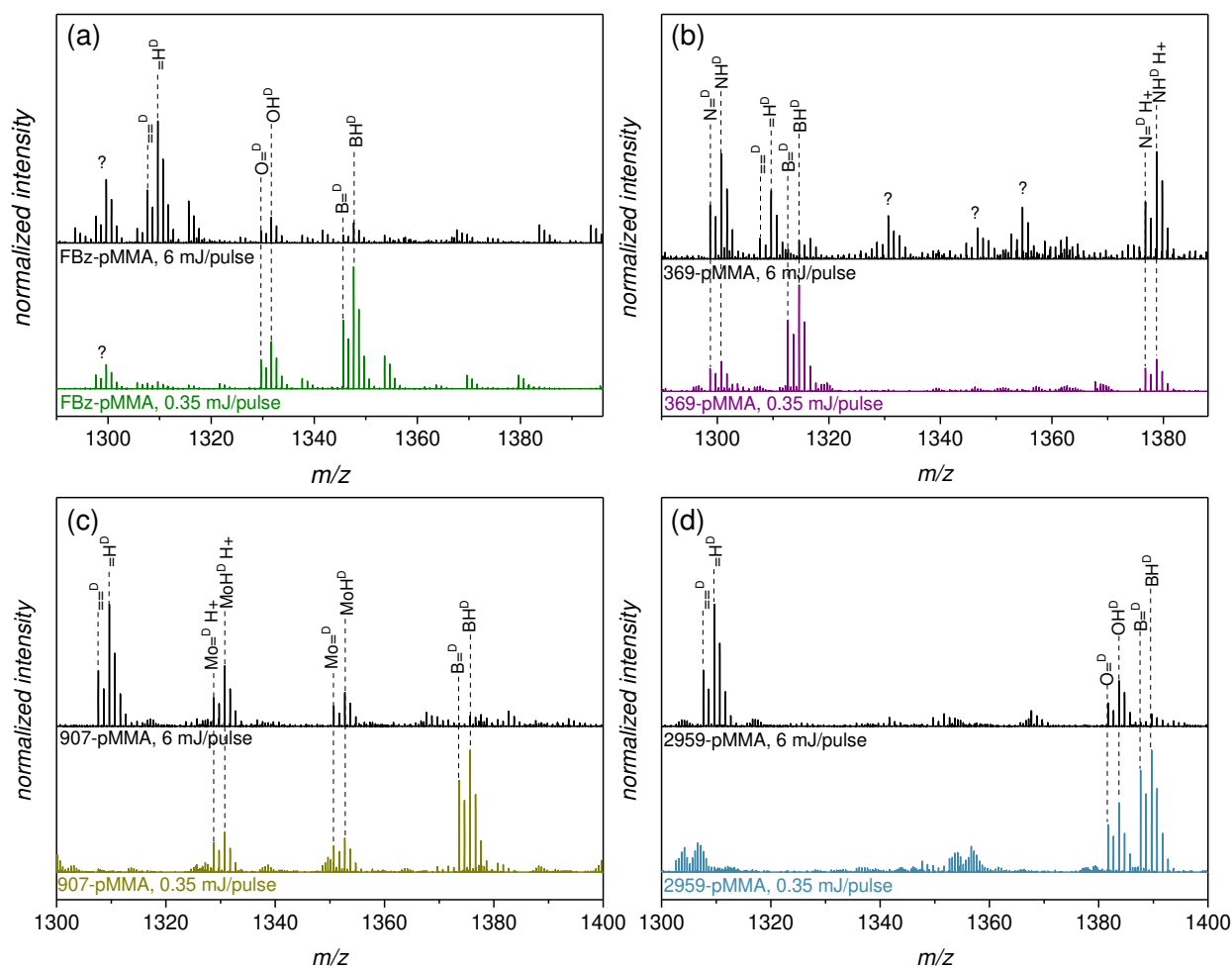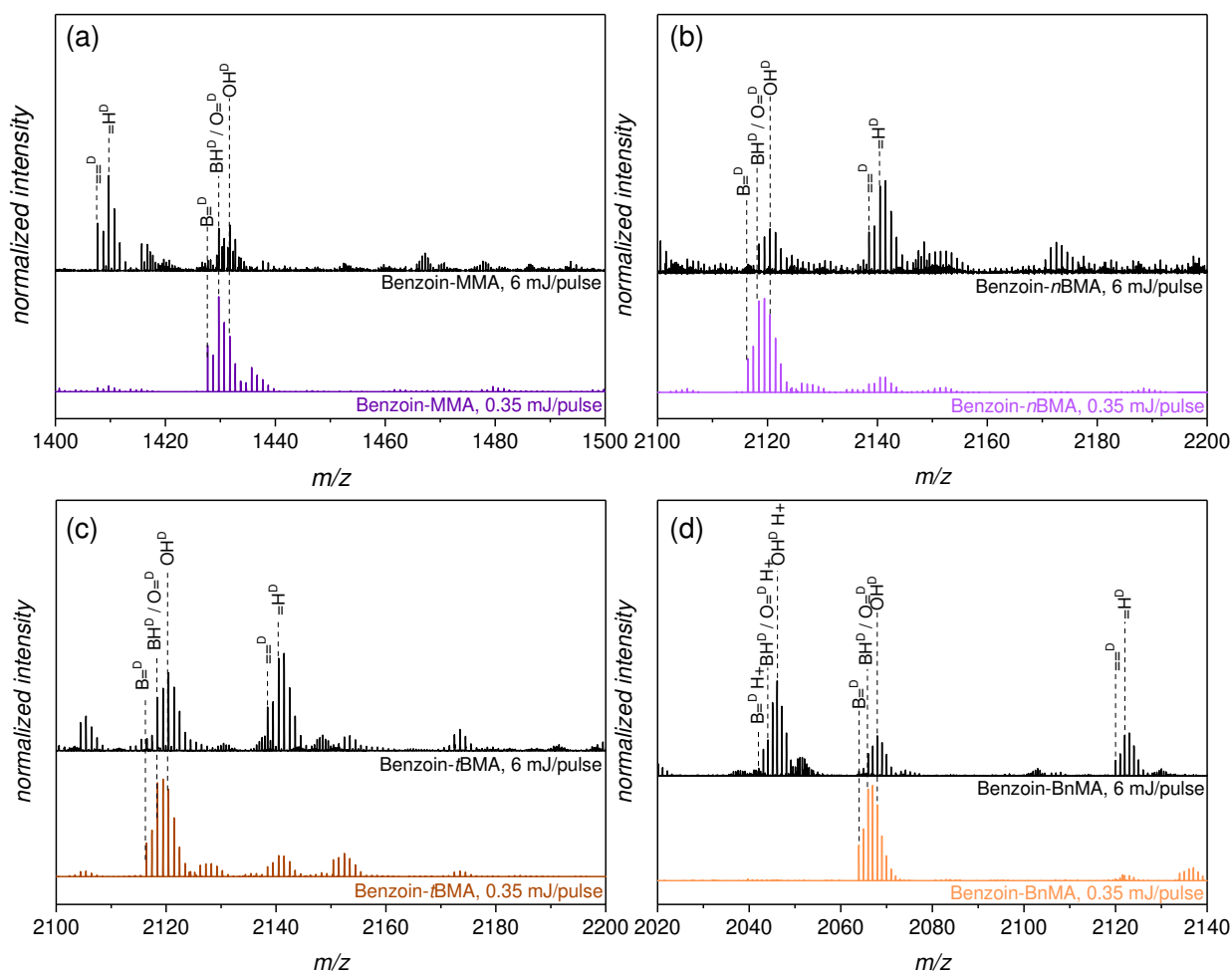

Figure 3.21.: High resolution SEC-ESI mass spectra of the polymers before (0.35 mJ/pulse, colored spectra) and after PLI (6 mJ/ pulse, black spectra) initiated by Benzoin.

Inspection of Figure 3.21 indicates that there are no significant differences, as for all different polymer backbones the unsaturated species are formed upon PLI. Neither the longer ester side chain (*n*-BMA) nor the branches (*t*-BMA) or sterically hindrances (BnMA) of the backbone seem to have an influence on the photoinduced end group conversion.
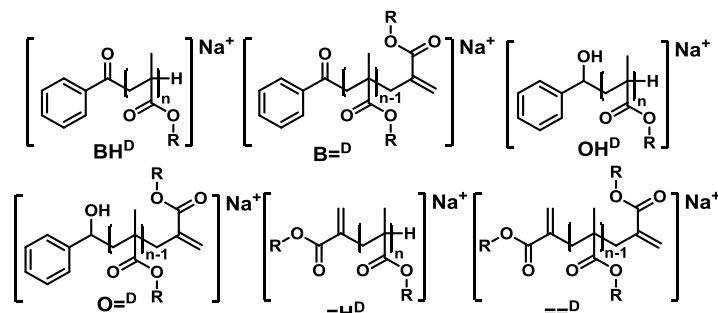
Scheme 3.14.: Disproportionation products of the PLP (0.35 mJ/pulse) and post-irradiation (6 mJ/pulse) experiments of the Benzoin-initiated poly(meth acrylates), as detected by SEC-ESI-MS.

3.4.4 Solid-State Experiments

Photoinduced polymerizations are mainly applied as coatings in the industrial field. Since the photoactive component is still present inside the polymer after the UV-induced reaction, it is of great interest to conduct the post-irradiation reaction of the end group under real-life conditions (so-called solid-state). Therefore, 3MB-pMMA was dried inside the glass vial after polymerization. The resulting polymer coating, which is located on the bottom of the glass vial, was subsequently subjected to solid-state PLI. In order to simulate the effect in the final coating-like product, the sample was not purged with nitrogen. To allow for a better comparison, 3MB-pMMA was also subjected to PLI conditions in solution (normal PLI conditions, MIB as solvent) (refer to Figure 3.22).
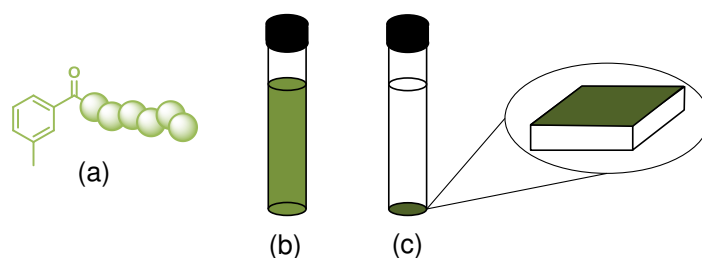
Figure 3.22.: (a) Benzoyl-terminated end group. (b) PLI conditions of 3MB-initiated pMMA in solution and (c) in solid-state.

The high resolution mass spectra of the parent polymer (0.35 mJ/pulse, light green, a), of the PLI experiment in solution (middle green, b) and under solid-state conditions (dark green, c) are depicted in Figure 3.23a. Only the disproportionation products of the polymeric material are shown in Figure 3.23b. Inspection of the data indicates that under both conditions the end group

conversion takes place, which is displayed by the presence of the unsaturated species (==$^{\mathbf{D}}$ and =$\mathbf{H}^{\mathbf{D}}$). However, it seems that the conversion is more effective after solid-state PLI, than after normal PLI conditions, indicated by the presence of the benzoyl-fragment in the mass spectra of the sample under normal PLI conditions. One reason for this observation may be associated with the penetration depth of the laser beam. For the solid-state sample, the laser beam covers the complete sample, since it only has to penetrate a thin polymer layer, whereas for the solution sample the laser beam has to penetrate the complete solution (0.5 mL) which is equivalent to a liquid level of 2 cm.
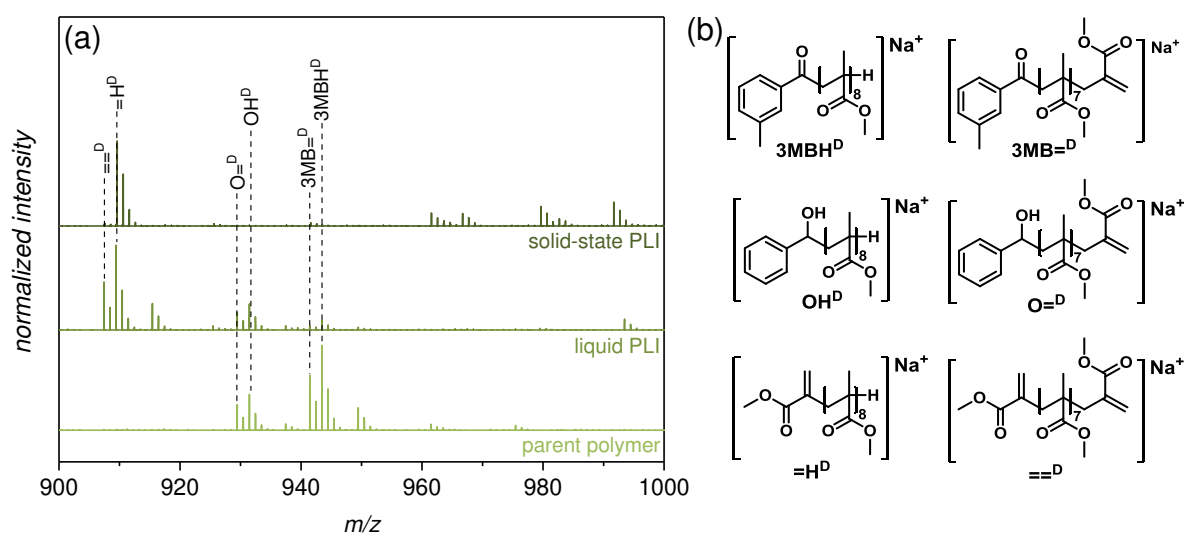
Figure 3.23.: (a) High resolution SEC-ESI mass spectra of the 3MB-initiated pMMA, synthesized at low laser energies (0.35 mJ/pulse, 200 Hz, 351 nm, light green), post-irradiated in liquid conditions (351 nm, 200 Hz, middle green) and post-irradiated under solid-state conditions (351 nm, 200 Hz, dark green). (b) Disproportionation products of the polymeric material, as detected by SEC-ESI-MS.

3.4.5 Summary

In summary, an in-depth study of the benzoyl fragment regarding its role in photoinduced end group conversion is presented. It has been found that neither the utilized solvent for post-irradiation, nor the backbone of the polymer or functional groups, which increases or decreases the electron density of the aromatic system, have a significant influence on the photoinduced end group conversion. Additional experiments to mimic the effect in the final UV-cured product, showed a slightly stronger presence of the unsaturated species compared to the normal applied PLI conditions in solution.

4

Wavelength-Dependent Photochemistry of Oxime Esters
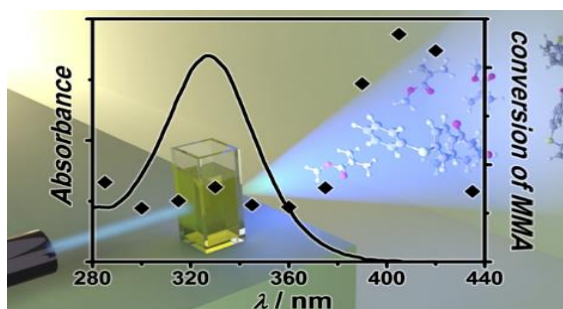
4.1 Introduction

The oxime esters OXE01 and OXE02 (refer to Scheme 4.1b) are mainly developed in the manufacturing industry for the curing of highly pigmented thick films in color filter resists.[177] In fundamental science, their photoreactivity and ability to initiate radical photopolymerizations are investigated. Upon light irradiation, the oxime ester motif of these initiators can undergo two pathways depending on their substitution (refer to Scheme 4.1a).[178,179,180] The fragmentation reaction leads to the formation of radicals[181–183] and can induce the polymerization process in presence of vinyl monomers. Via a second pathway, the oxime ester can also undergo *E/Z*-isomerization, which does not lead to the formation of radicals and consequently no polymer can be formed.
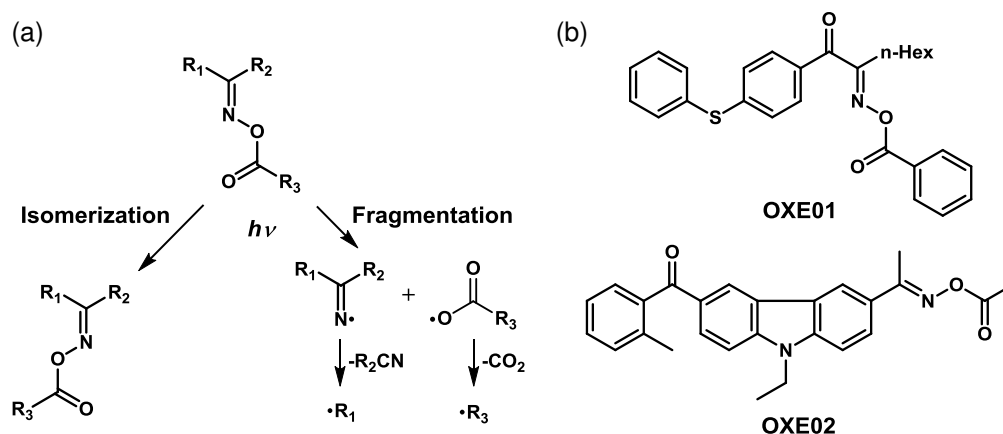
Scheme 4.1.: (a) Photoinduced reaction pathways of oxime esters and (b) structures of oxime ester photoinitiators OXE01 and OXE02. Adapted with permission from reference [184]. Copyright (2017) American Chemical Society (ACS).

In the current Chapter, an in-depth study of the wavelength-dependent photochemical and physical properties of the oxime esters OXE01 and OXE02 utilizing UV-Vis spectroscopy, density functional theory (DFT) calculations, photochemically induced dynamic nuclear polarization (photo-CIDNP) spectroscopy, and pulsed-laser polymerization using a wavelength-tunable laser with subsequent size exclusion chromatography coupled to high resolution electrospray ionization mass spectrometry (PLP-SEC-ESI-MS) is presented. UV-Vis spectroscopy and DFT calculations provide information about the absorption properties and the excited states of oxime esters OXE01 and OXE02, and both are relevant for the understanding of the photoinduced cleavage processes of the photoinitiators (PIs). Further, photo-CIDNP spectroscopy is a suitable, nuclear magnetic resonance (NMR) technique to establish the cleavage mechanism of photoactive compounds. PLP–SEC–ESI–MS is a technique which combines the generation of polymers with subsequent analysis via mass spectrometry, hyphenated to size exclusion

chromatography. This method allows the analysis of photoinitiator derived polymer end groups. Via a wavelength-tunable laser in a PLP setup, the conversion as well as the influence of the irradiation wavelength on the photochemistry of the initiation process for each wavelength can be determined. Thus, a wavelength-dependent reactivity plot utilizing an identical amount of photons for each wavelength can be obtained.

4.2 UV-Vis Measurements and DFT Calculations

To understand photoinduced processes, the first step is the analysis of the absorption spectra and the calculation of excited states. DFT calculations were carried out by A.-M. Kelterer at the Graz University. Here, Figure 4.1 illustrates the experimentally recorded UV-Vis spectra and the calculated vertical singlet excitations (S_1-S_6) of the most stable S_0 ground state geometries, which are in good agreement if the mean absolute deviation of the CAM-B3LYP method is considered. However, it must be noted that Jacquemin and coworker have found that these methods can lead to an overestimation of vertical singlet excitations of n-π^* and π-π^* transitions by 0.07 and 0.25 eV.[173] The S_1 singlet excitation of OXE01 is at 329 nm, has n-π^* character and results primarily from the HOMO-6 (localized at the lone pairs of the benzoyl group oxygen and of the nitrogen atom) into the LUMO (localized at the π-system of the benzoyloxy moiety plus large contributions at C-N). The S_2 singlet excitation is located at 312 nm, characterized as a π-π^* transition and results primarily from the HOMO (localized at the π-system of the diphenyl sulphide moiety including the sulfur lone pair) into the LUMO.
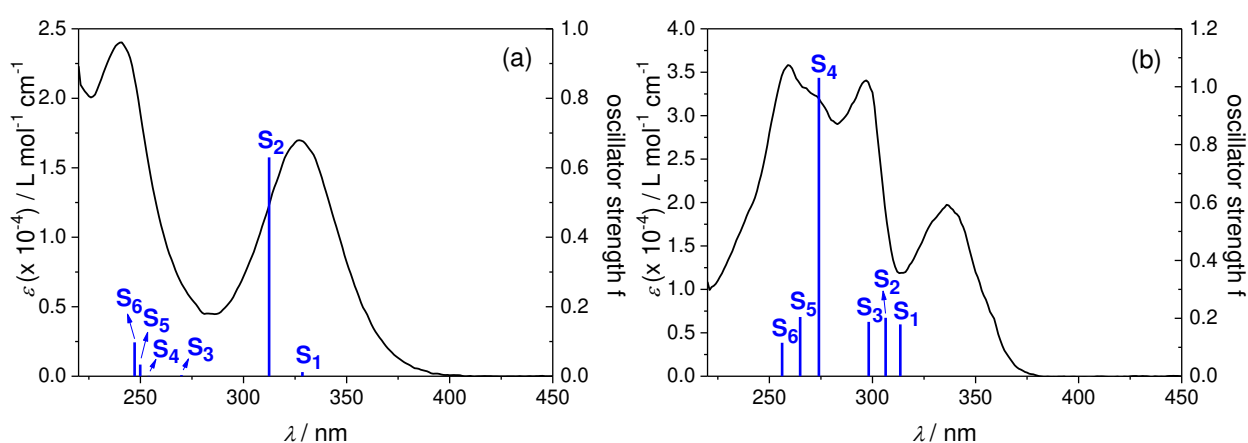
Figure 4.1.: Experimental UV-Vis spectra in acetonitrile solution (black) and calculated excited singlet states (blue) of (a) OXE01 and (b) OXE02. Calculated at the TD-DFT/CAM-B3LYP/6-311++G(2d,2p) level of theory. Adapted with permission from reference [184]. Copyright (2017) American Chemical Society (ACS).

The most stable molecular orbitals (LUMO and HOMO) are illustrated in Figure 4.2a and their corresponding first six vertical singlet excitations are listed in the appendix (refer to Table 8.29).
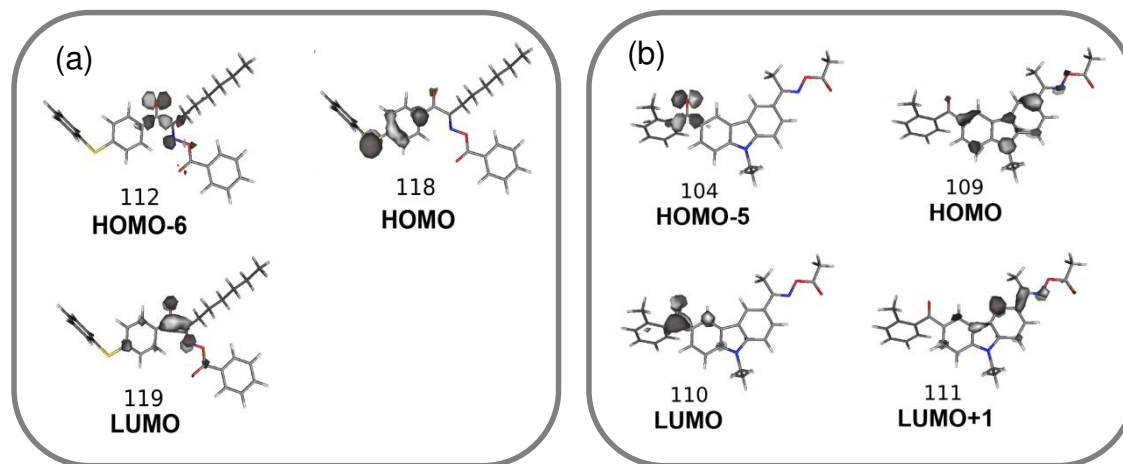
Figure 4.2.: Molecular orbitals of (a) OXE01 and (b) OXE02 in the most stable S_0 singlet ground state; contour values of 0.05 a.u. were applied. Adapted with permission from reference [184]. Copyright (2017) American Chemical Society (ACS).

For OXE02, the S_1 (314 nm) and as well the S_2 (306 nm) singlet excitations have mixed n-π^*/π-π^* character resulting primarily from the HOMO-5 (localized at the oxygen lone pairs of the benzoyl group) and the HOMO (localized at the ethyl-carbazole moiety) into the LUMO (localized at the π-system of the benzoyl moiety with large contributions at the carbonyl group). The S_3 singlet excitation, located at 298 nm results primarily from the HOMO into the LUMO+1. The most stable molecular orbitals (LUMO and HOMO) are illustrated in Figure 4.2b and their corresponding first six vertical singlet excitations are listed in the appendix (refer to Table 8.30).

The molar extinction coefficient is for both initiators relatively high compared to other initiators, such as benzoin, and its value at the wavelength maximum absorbance of the first band is for OXE01: $\varepsilon_{327} = (1.75 \pm 0.03) \cdot 10^4$ L·mol^{-1}·cm^{-1} and for OXE02: $\varepsilon_{338} = (2.01 \pm 0.02) \cdot 10^4$ L·mol^{-1}·cm^{-1}). By comparison of the absorption spectra of both initiators, the one of OXE01 extends more into the near-visible range compared to OXE02.

4.3 Photo-CIDNP Experiments

Owing to the further fragmentation reactions (see Scheme 4.1), which the initial radicals of oxime ester can undergo, the photoinduced cleavage mechanisms are more complex compared to other Norrish type I initiators such as benzoin or bisacylphosphine oxides.[166,185] In order to understand and follow these reactions, photo-CIDNP is the technique of choice. The photo-

CIDNP measurements were carried out by D. E. Fast at the University of Graz. The ^{1}H NMR and ^{1}H CIDNP spectra (excitation at λ = 355 nm) of OXE01 are depicted in Figure 4.3.
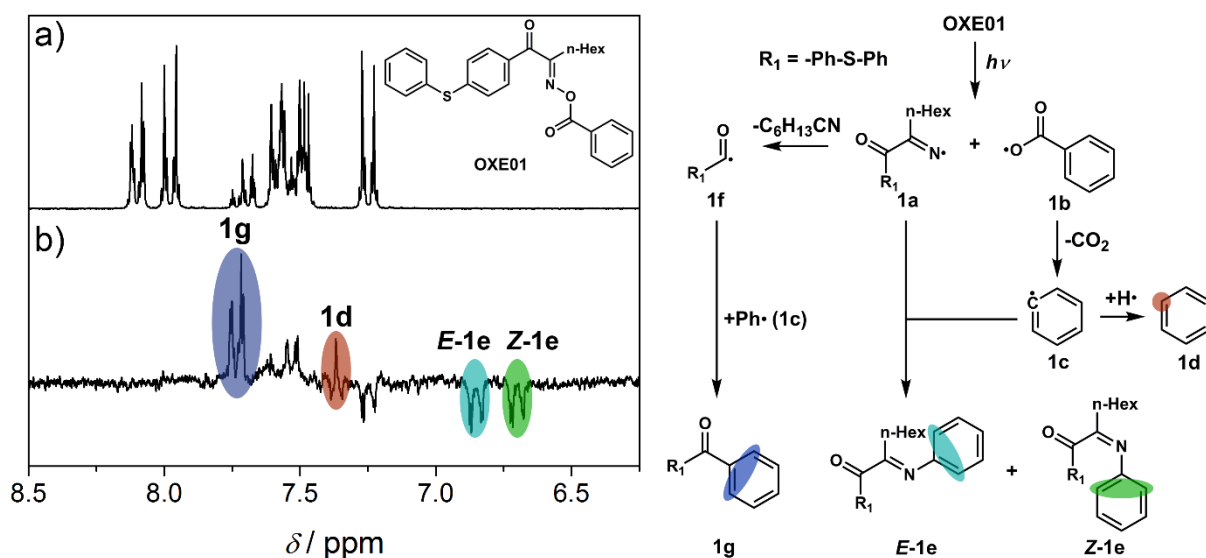
Figure 4.3.: (a) ^{1}H NMR and (b) ^{1}H CIDNP spectra of OXE01, recorded in CD$_3$CN at a laser energy of about 70 mJ/pulse (λ = 355 nm), and the corresponding photofragmentation mechanism and the resulting products. Adapted with permission from reference [184]. Copyright (2017) American Chemical Society (ACS).

Upon light irradiation, the N-O bond of the oxime ester motif of OXE 01 cleaves into the iminyl **1a** and the benzoyloxy radical **1b**. The latter can further undergo a decarboxylation reaction, leading via the radical **1c** to benzene **1d** (singlet at δ = 7.37 ppm), after hydrogen atom transfer (probably from the solvent). On the other hand, the iminyl radical can terminate with the formed phenyl radical **1c** to stereoisomeric imines **E-1e** and **Z-1e** (doublets, δ = 6.85 and 6.70 ppm, J = 8.4 Hz). Furthermore, the iminyl radical can undergo further fragmentation reactions leading to the ketone **1g** (doublet at δ = 7.73 ppm, J = 6.8 Hz) via the termination of the benzoyl radical **1f** with the phenyl radical **1c**.

The ^{1}H NMR and ^{1}H CIDNP spectra (excitation at λ = 355 nm) of OXE02 are illustrated in Figure 4.4. A similar cleavage behavior, which was already explained for OXE01, can be proposed for OXE02. First, the oxime ester motif cleaves, leading to the iminyl **2a** and the acetyloxy radical **2b**. The latter can undergo a decarboxylation reaction which leads via the termination of two methyl radicals **2c** to ethane **2d** (singlet at δ = 0.85 ppm). Termination of the methyl radical with the acetyloxy radical **2b** results in the formation of methyl acetate **2e** (methyl-protons at δ = 3.60 and 2.01 ppm). Furthermore, the singlets at δ = 3.31 and 3.05 ppm can be correlated with the imines **E-2f** and **Z-2f**, which are formed after recombination of the iminyl radical 2a with the methyl radical **2c**. The singlets at δ = 2.47 and 2.22 ppm originate from the methyl protons of

OXE02, which can be explained by the recombination of **2a** and **2b**, due to the cage effect.[84] Taking the results of the above photo-CIDNP measurements into account, the photoinduced fragmentation mechanism of OXE01 and OXE02 via the cleavage of the N-O bond is in excellent agreement with the reported mechanisms.[181–183]
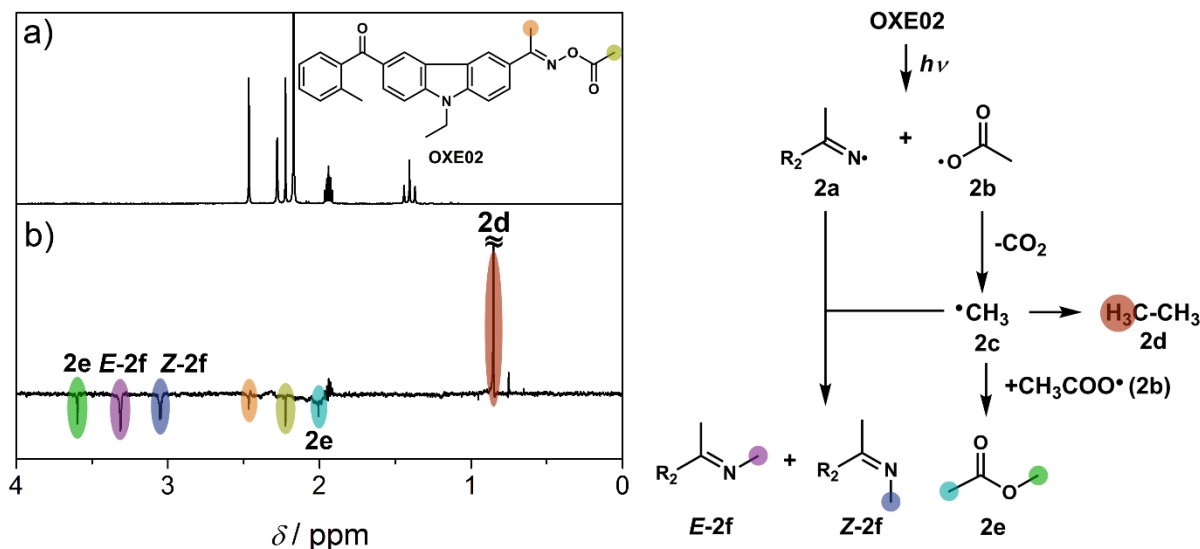
Figure 4.4.: (a) 1H NMR and (b) 1H CIDNP spectra of OXE02, recorded in CD3CN at a laser energy of close to 70 mJ/pulse (λ = 355 nm), the corresponding photofragmentation mechanism and the resulting products. Adapted with permission from reference [184]. Copyright (2017) American Chemical Society (ACS).

4.4 Variable Wavelength PLP-SEC-ESI-MS Study

PLP-SEC-ESI-MS provides detailed insights into the end group structure of the polymer and enables to draw conclusions regarding the photopolymerization process. In the current Section, both photoinitiators were individually employed to polymerize MMA under bulk conditions. In order to compare the wavelength effects on the polymerization outcome among each other, the number of photons which hit the sample was kept constant for each wavelength (refer to the Experimental Section for a detailed description of how a constant photon count was achieved). The monomer to polymer conversion for each wavelength was determined and the synthesized polymers were subsequently analyzed without further purification via SEC-ESI-MS to establish the composition of the polymer end groups. The nomenclature from Chapter 3 was adopted to label the observed SEC-ESI-MS polymer signals. Figure 4.5 depicts the high resolution SEC-ESI mass spectra of pMMA initiated by OXE01 (60 µmol photons, 285-435 nm, colored spectra) and as well as the isotopic simulation (black spectrum). Interestingly, the observed end group signals of the polymer do not differ between the employed wavelengths from 285 to 435 nm. This observation is decisive for the interpretation of the wavelength-dependent reactivity profiles discussed in the next Section. The corresponding polymer structures and assigned end group

signals are listed in Scheme 4.2 and Table 4.1. For OXE01, the mass spectrum shows the highest ion abundance for polymer end groups derived from the benzoyloxy radical **1b** (**O=$^{\text{D}}$**, **OH$^{\text{D}}$** and **O2$^{\text{C}}$**), and the benzoylradical **1f** (**S=$^{\text{D}}$**, **SH$^{\text{D}}$**, **S2$^{\text{C}}$** and **SO$^{\text{C}}$**). The first occurs from the cleavage of the N-O bond and the latter results from the fragmentation of the iminyl radical **1a**, which itself does not induce photopolymerization.[183] On the other hand, the lowest ion abundance was determined for polymer end groups initiated by the phenyl radical **1c** (**P=$^{\text{D}}$** and **PH$^{\text{D}}$**). These observations were unexpected, since the phenyl radical **1c** is the main initiating species in thermally initiated radical polymerizations with e.g. dibenzoyl peroxide.[186] However the employed low temperature during the photoinduced polymerization could explain the unexpected observations, since the decarboxylation reaction is slower compared to the initiation process. The results are consistent with the published MALDI-TOF-MS data of OXE01-initiated poly(2-phenoxyethyl acrylate).[187] The mass spectra reveals furthermore unknown signals, which are labeled with a question mark "?" and have not been assigned to a polymer structure.
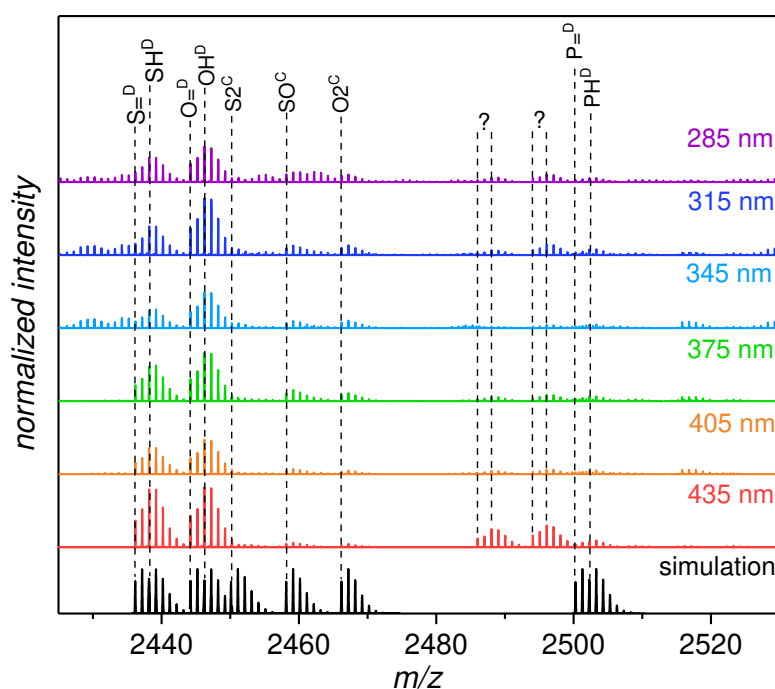
Figure 4.5.: High resolution SEC-ESI mass spectra of OXE01-initiated pMMA (zoom into one repeating unit) synthesized by variable-wavelength PLP (285–435 nm, 100 Hz, 18 °C) at a constant photon count, alongside the theoretical isotope patterns (for signals marked with "?", a polymer structure has not been assigned). Adapted with permission from reference [184]. Copyright (2017) American Chemical Society (ACS).

Table 4.1.: Overview of the assigned polymer products of OXE01-initiated pMMA, synthesized by PLP (345 nm, 0.35 mJ/pulse, 100 Hz, 18 °C), as detected by high resolution SEC-ESI-MS (R = 43000). Adapted with permission from reference [184]. Copyright (2017) American Chemical Society (ACS).

Species	Ionization	$(m/z)^{theo}$/Da	$(m/z)^{exp}$/Da	$\Delta(m/z)$
P=^{D}	Na$^+$	2500.2788	2500.2991	0.0203
PH^D	Na$^+$	2502.2945	2502.3013	0.0068
S=^{D}	Na$^+$	2436.1723	2436.1932	0.0209
SH^D	Na$^+$	2438.1879	2438.1902	0.0023
O=^{D}	Na$^+$	2444.2162	2444.2390	0.0228
OH^D	Na$^+$	2446.2319	2446.2460	0.0141
S2^C	Na$^+$	2450.1126	2450.1235	0.0109
SO^C	Na$^+$	2458.1566	2458.1663	0.0097
O2^C	Na$^+$	2466.2006	2466.2197	0.0191
?	?	-	2485.9012	-
?	?	-	2488.0866	-
?	?	-	2494.0242	-
?	?	-	2496.0858	-
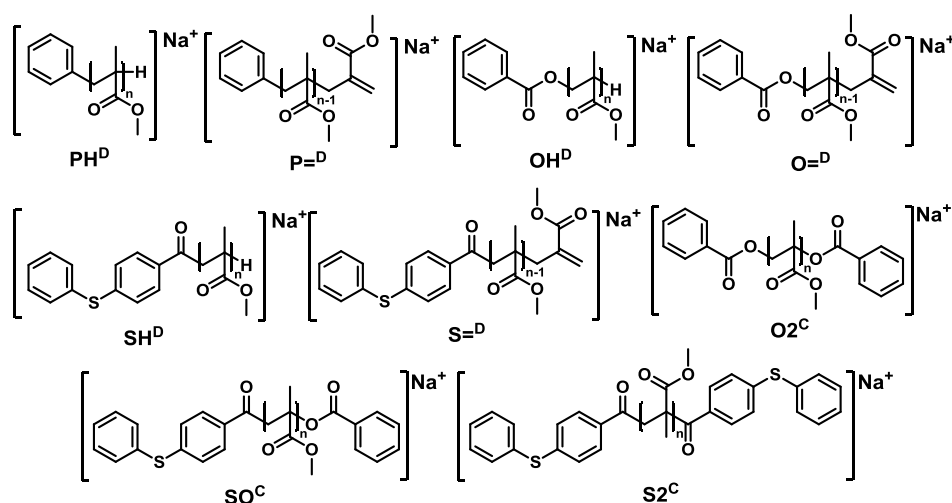
Scheme 4.2.: Structures of the disproportionation and combination products of OXE01-initiated pMMA, synthesized by PLP (345 nm, 0.35 mJ/pulse, 100 Hz, 18 °C), as detected by high resolution SEC-ESI-MS. Adapted with permission from reference [184]. Copyright (2017) American Chemical Society (ACS).

In summary, the high resolution SEC-ESI mass spectra of pMMA initiated by OXE02 (60 µmol photons, 285-405 nm, colored spectra) as well as the isotopic simulation (black spectrum) are shown in Figure 4.6. The mass spectrum of OXE02 irradiated at 435 nm is not shown due to the low obtained ion abundance. The corresponding polymer structures and assigned end group signals are listed in Scheme 4.3 and Table 4.2. As already stated for OXE01, the mass spectra of OXE02 also show that there is barely any difference in the generated polymer end group pattern

within the employed wavelength regime of 285 to 405 nm. The mass spectrum of OXE02 depicts polymer end groups derived by the methyl radical **2c** ($\mathbf{C=^D}$, $\mathbf{CH^D}$, $\mathbf{C2^C}$). Compared to OXE01, where the benzoyloxy radical **1b** is incorporated as a polymer end group, the acetyloxy radical **2b** does not initiate the photoinduced polymerization. Here, under PLP conditions, the acetyloxy radical **2b** undergoes a decarboxylation reaction to afford the methyl radical **2c**. Furthermore, the mass spectrum shows the combination product $\mathbf{CN^C}$ (methyl in α-position and imine in ω-position). Based on the low reactivity of iminyl radicals towards double bonds,[183] it may be expected that $\mathbf{CN^C}$ emerges from primary radical termination (i.e. termination of a chain radical initiated by a methyl radical with iminyl radical **2a**) and not from termination by combination of two chain radicals.
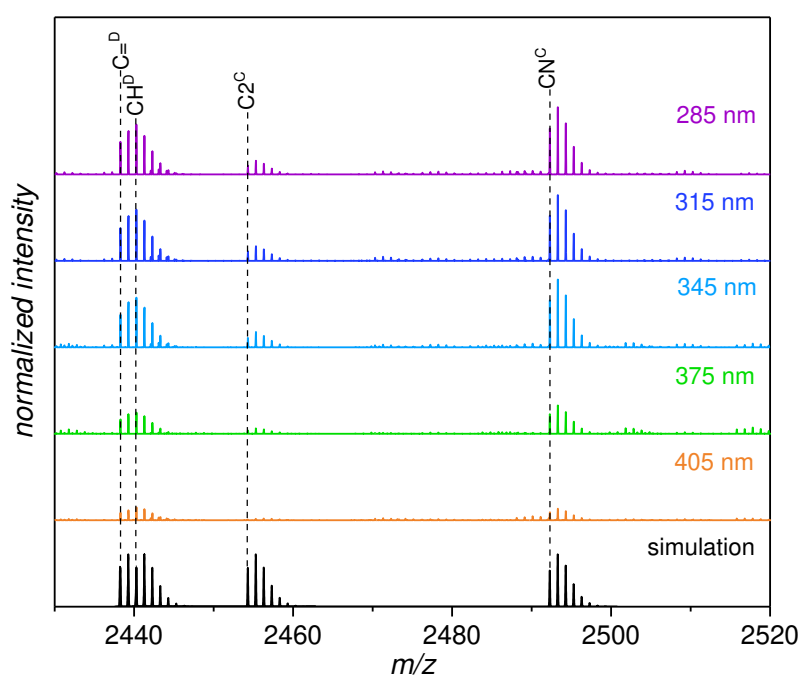
Figure 4.6.: High resolution SEC-ESI mass spectra of OXE02-initiated pMMA (zoom into one repeating unit) synthesized by variable-wavelength PLP (285-405 nm, 100 Hz, 18 ℃) at a constant photon count as well as the theoretical isotope patterns. The mass spectrum of OXE02 irradiated at 435 nm is not shown due to the low obtained ion abundance. Adapted with permission from reference [184]. Copyright (2017) American Chemical Society (ACS).
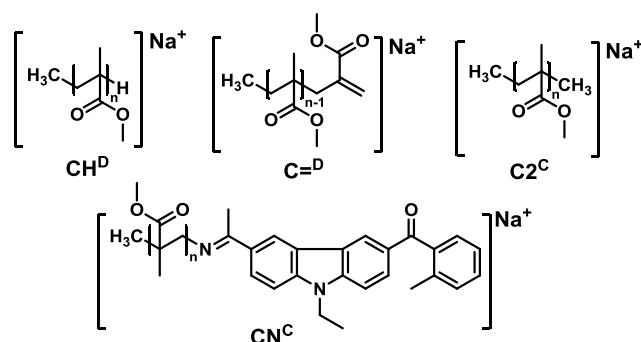
Scheme 4.3.: Structures of the disproportionation and combination products of OXE02-initiated pMMA synthesized by PLP (345 nm, 0.35 mJ/pulse, 100 Hz, 18 °C), as detected by high resolution SEC-ESI-MS. Adapted with permission from reference [184]. Copyright (2017) American Chemical Society (ACS).

Table 4.2.: Overview of the assigned polymer products of OXE02-initiated pMMA, synthesized by PLP (345 nm, 0.35 mJ/pulse, 100 Hz, 18 °C), as detected by high resolution SEC-ESI-MS (R = 43000). Adapted with permission from reference [184]. Copyright (2017) American Chemical Society (ACS).

Species	Ionization	$(m/z)^{theo}$/Da	$(m/z)^{exp}$/Da	$\Delta(m/z)$
C=^{D}	Na$^+$	2438.2632	2438.2827	0.0195
CH^D	Na$^+$	2440.2788	2440.2823	0.0035
C2^C	Na$^+$	2454.2945	2454.3198	0.0253
CN^C	Na$^+$	2492.2791	2492.2919	0.0128

4.5 Wavelength-Dependent Conversion

In the current Section, the monomer to polymer conversion under bulk conditions when initiated with monochromatic wavelength in the range of 285 to 435 nm for OXE01 and OXE02 was examined. As noted above, each sample at each applied wavelength was irradiated with the same number of photons (60 µmol, the absorption of photons by the photo vial were considered, refer to the Experimental Section for a detailed description of how a constant photon count was achieved). The measurements were performed three times per irradiation wavelength and the conversion was determined gravimetrically, refer to the appendix Tables 8.31-8.32). The obtained average conversion for each wavelength for OXE01 and OXE02, as well as the corresponding UV-Vis spectra are shown in Figure 4.7. Inspection of Figure 4.7 demonstrates that the highest conversion for both initiators were obtained by applying the wavelength of 405 nm (OXE01: 9.4% ± 0.2%; OXE02: 3.1% ± 0.2%; refer to Figure 4.7 and Table 4.3), despite the low molar extinction coefficients in this wavelength region.
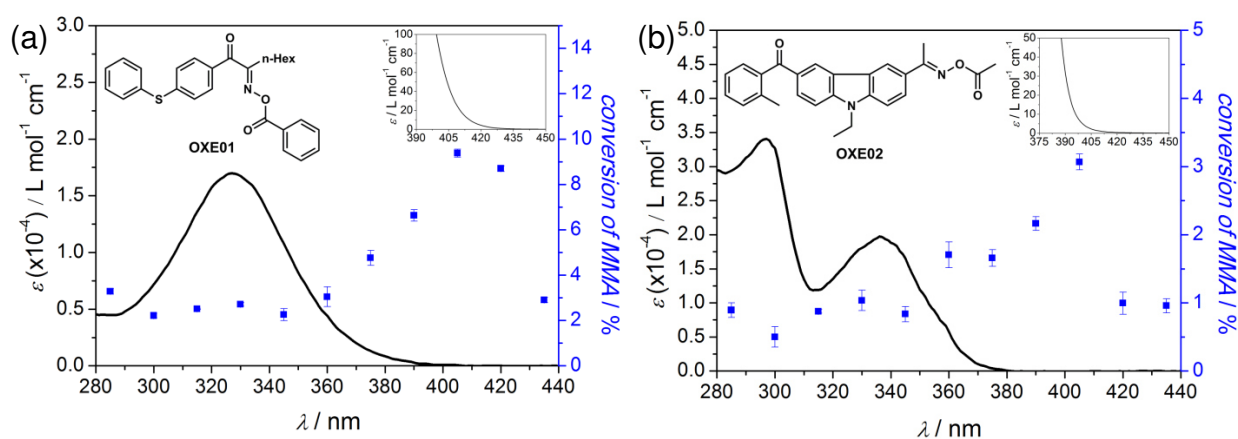
Figure 4.7.: Comparison of the UV-Vis spectra (insets: zoom into 375/390 to 450 nm) and the wavelength-dependent conversion of methyl methacrylate initiated by (a) OXE01 and (b) OXE02, synthesized by PLP at a constant photon count (60 μmol) per irradiation wavelength. Adapted with permission from reference [184]. Copyright (2017) American Chemical Society (ACS).

Table 4.3.: Wavelength-dependent conversion of MMA initiated by OXE01 and OXE02, synthesized by PLP with a constant photon count (60 μmol) per irradiation wavelength, as well as the corresponding molar extinction coefficients (ε). Adapted with permission from reference [184]. Copyright (2017) American Chemical Society (ACS).

	OXE01		OXE02	
λ / nm	*Conversion of MMA / %*	ε / L·mol⁻¹·cm⁻¹	*Conversion of MMA / %*	ε / L·mol⁻¹·cm⁻¹
435	2.9 ± 0.2	0.4 ± 0.1	1.0 ± 0.2	0.3 ± 0.1
420	8.7 ± 0.2	4.5 ± 0.1	1.0 ± 0.2	0.7 ± 0.1
405	9.4 ± 0.2	45 ± 1	3.1 ± 0.2	2.2 ± 0.1
390	6.6 ± 0.3	310 ± 5	2.2 ± 0.1	29 ± 1
375	4.8 ± 0.4	1400 ± 50	1.7 ± 0.2	630 ± 10
360	3.0 ± 0.5	4600 ± 100	1.7 ± 0.2	6200 ± 50
345	2.3 ± 0.3	11000 ± 150	0.8 ± 0.2	17500 ± 100
330	2.7 ± 0.1	17300 ± 250	1.0 ± 0.2	18700 ± 150
315	2.5 ± 0.1	14000 ± 300	0.9 ± 0.1	13100 ± 150
300	2.2 ± 0.1	7600 ± 400	0.5 ± 0.2	35400 ± 300
285	3.3 ± 0.2	5000 ± 600	0.9 ± 0.2	32100 ± 450

Further, the conversion at 405 nm (9.4% ± 0.2%) and 420 nm (8.7% ± 0.2%) of OXE01 is almost identical. However, this observation was unexpected, since the wavelength-dependent photoinitiator reactivity decisively differs from the measured absorption spectra. In order to further support these findings, additional light induced polymerizations of OXE01 and OXE02 with LEDs as light sources (385 to 450 nm) were performed. The obtained conversions of the LED irradiation experiments mirror the findings of the above laser-induced conversion results

(refer to Figure 4.8 and Table 4.4). Importantly, it can be stated that both initiators still absorb photons in the region of 405 to 435 nm under the applied PLP conditions (c_{PI} = 5·10^{-3} M), although the molar extinction coefficients are extremely low (refer to the zoom in Figure 4.7 and Table 4.3).
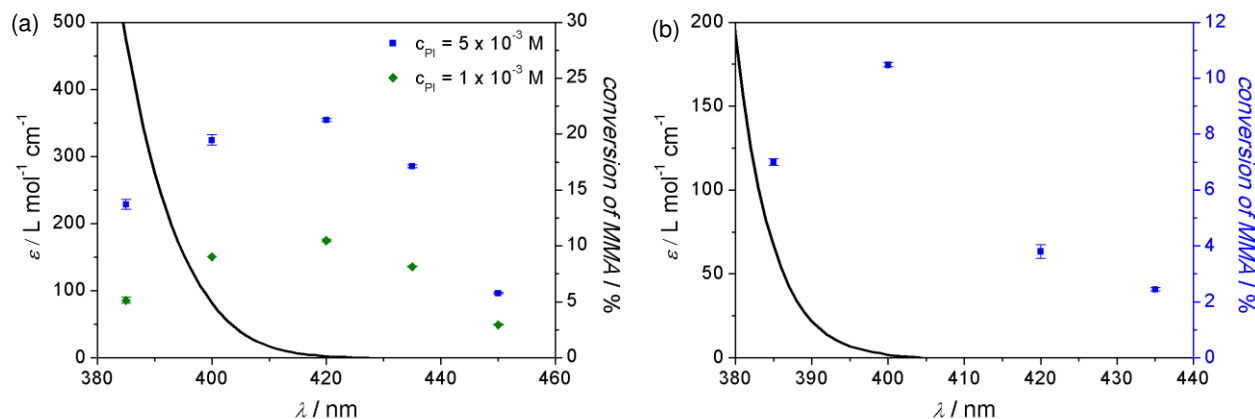
Figure 4.8.: Comparison of the UV-Vis spectra of (a) OXE01 and (b) OXE02 (c_{PI} = 5·10^{-3} M in acetonitrile) and the wavelength-dependent conversion of methyl methacrylate initiated by (a) OXE01 (c_{PI} = 5·10^{-3} M, blue; c_{PI} = 10^{-3} M, green) and (b) OXE02, synthesized under LED irradiation (1 hour). Adapted with permission from reference [184]. Copyright (2017) American Chemical Society (ACS).

Table 4.4.: Wavelength-dependent conversion of MMA initiated by OXE01 (c_{PI} = 10^{-3} and 5·10^{-3} M) and OXE02 (c_{PI} = 5·10^{-3} M), synthesized under LED irradiation, and the corresponding molar extinction coefficients (ε). Adapted with permission from reference [184]. Copyright (2017) American Chemical Society (ACS).

	OXE01			OXE02	
λ / nm	Conversion of MMA / %		ε / L·mol^{-1}·cm^{-1}	Conversion of MMA / %	ε / L·mol^{-1}·cm^{-1}
	5·10^{-3} M	10^{-3} M		5·10^{-3} M	
450	5.8 ± 0.1	3.0 ± 0.1	-	-	-
435	17.1 ± 0.2	8.2 ± 0.1	0.37 ± 0.03	2.4 ± 0.1	0.31 ± 0.02
420	21.3 ± 0.2	10.5 ± 0.2	4.5 ± 0.1	3.8 ± 0.3	0.66 ± 0.06
400	19.5 ± 0.5	9.0 ± 0.1	87 ± 2	10.5 ± 0.1	4.8 ± 0.1
385	13.7 ± 0.5	5.1 ± 0.3	530 ± 10	7.0 ± 0.2	89 ± 4

4.6 Understanding the Unusual Wavelength-Dependent Conversion Behavior

In order to find an explanation for these unexpected polymer conversions of both initiators, the Lambert-Beer law was utilized to calculate the amount of absorbed light:

$$A_\lambda = \varepsilon_\lambda \cdot c \cdot l \tag{4.1}$$

$$T_\lambda = 10^{-A_\lambda} \tag{4.2}$$

$$PAL_\lambda = (1 - T_\lambda) \cdot 100 \tag{4.3}$$

A_λ absorbance at wavelength λ

ε_λ molar extinction coefficient at wavelength λ (L·mol^{-1}·cm^{-1})

c molar concentration (mol·L^{-1})

l path length of the light through the sample (cm)

T_λ transmittance at wavelength λ

PAL_λ percentage of absorbed light at wavelength λ

Therefore, the optical path length of 2 cm, which results from the liquid level within the photo vials under PLP conditions, was employed to calculate by means of the molar concentration and the molar extinction coefficient the absorption for different wavelengths. When applying a wavelength of 405 nm, only 5% of the incoming light is absorbed by OXE02. On the other hand, for OXE01 it can be calculated that at wavelengths of 405 nm and 420 nm, 65% and 10% of the incoming light are absorbed. However, OXE01 shows despite of the different abilities of both wavelengths to absorb light (405 nm: 65%; 420 nm: 10%; refer to Table 4.5), almost similar conversions of MMA (405 nm: 9.4% ± 0.2%; 420 nm: 8.7% ± 0.2%; refer to Table 4.3).

Table 4.5.: Molar extinction coefficients (ε) and calculated values of the percentage of absorbed light (*PAL*) at 2 cm and the path length ($l_{99\%}$) at which 99% of the incident light are absorbed based on the Lambert-Beer Law for OXE01 and OXE02. Adapted with permission from reference [184]. Copyright (2017) American Chemical Society (ACS).

OXE01				OXE02			
λ / nm	ε / L·mol^{-1}·cm^{-1}	*PAL at 2 cm* / %	$l_{99\%}$ / cm	λ / nm	ε / L·mol^{-1}·cm^{-1}	*PAL at 2 cm* / %	$l_{99\%}$ / cm
435	0.37 ± 0.03	0.9 ± 0.1	1100 ± 100	435	0.31 ± 0.02	0.7 ± 0.1	1300 ± 100
420	4.5 ± 0.1	9.8 ± 0.3	90 ± 5	420	0.66 ± 0.06	1.5 ± 0.2	610 ± 60
405	45 ± 1	65 ± 1	9 ± 0.5	405	2.2 ± 0.1	5.0 ± 0.3	180 ± 10
394	200 ± 10	99 ± 0.2	2.0 ± 0.1	390	29 ± 1	50 ± 2	14 ± 0.5
-	-	-	-	381	195 ± 5	99 ± 0.2	2.1 ± 0.1

Thus, it can be stated that the monomer to polymer conversion is not absolutely correlated to the concentration of initiating radicals. Since a lower concentration of chain radicals also decreases the probability of chain termination, longer polymer chains are obtained. The obtained number average molecular weights (M_n, refer to Table 4.6) of the polymer samples synthesized with LEDs as light sources and initiated by OXE01 and OXE02, respectively, showed an increase with increasing irradiation wavelength.

Table 4.6.: Number and weight average molecular weights (M_n and M_w) and dispersities (*Đ*) of pMMA initiated by OXE01 and OXE02 (c_{PI} = 5·10^{-3} M), respectively, synthesized under LED irradiation. Adapted with permission from reference [184]. Copyright (2017) American Chemical Society (ACS).

OXE01				OXE02			
λ / nm	M_n / g·mol^{-1}	M_w / g·mol^{-1}	*Đ*	M_n / g·mol^{-1}	M_w / g·mol^{-1}	*Đ*
450	144000	337000	2.3	-	-	-
435	44500	93900	2.1	220000	540000	2.4
420	29500	71400	2.4	116000	306000	2.7
400	21700	74300	3.4	32000	72900	2.3
385	14700	150700	10.3	19400	102000	5.3

Thus, it can be assumed that an influence on the conversion in this range seems improbable. As already mentioned, the molar extinction coefficients with maxima of $\varepsilon \geq 1.75 \cdot 10^4$ L·mol^{-1}·cm^{-1} for both initiators are very high. However, a high ε can also restrict the penetration depth of the incoming light beam, which can then lead to the formation of radicals only at the boundary layer of the photo vial. This fact leads to the lowering of the polymer yield. In addition, the path length at which 99% of the incoming light is absorbed ($l_{99\%}$) under PLP conditions was calculated. However, the calculated values of $l_{99\%}$ are greater than the liquid level of the photo vial (2 cm),

for higher wavelengths starting from 394 nm for OXE01 and 381 nm for OXE02 (refer to Table 4.5). As a result, the penetration depth is not responsible for the observed disparate correlation between the absorption properties of the initiators and polymer yield. To underpin the theoretical observations, polymerizations using LEDs and a lower initiator concentration (c_{PI} = 1·10^{-3} M) were performed, where the lower concentration should increase the penetration depth. Indeed, the conversion increases for each wavelength, yet the trend of the conversion stays the same, see Figure 4.8a.

4.7 Summary

In summary, the wavelength-dependent investigation of two oxime ester based photoinitiators which are of particular interest in fundamental and applied research as well as for manufacturers, was presented. It could be shown that the obtained high resolution mass spectra of the photoinduced polymers are invariant to the applied (monochromatic) irradiation wavelengths. However, the monomer to polymer conversion shows distinct departure from the measured absorption spectra, despite of the same number of incoming photons for each wavelength. No final explanation could be identified to fully explain the unexpected polymer conversion at higher wavelengths. Such a behavior could be also observed for wavelength-dependent photoligation experiments, where the product conversion is invariant to the absorption of the starting materials.[188]

5

Photoinduced Generation of Lactone Chain Termini
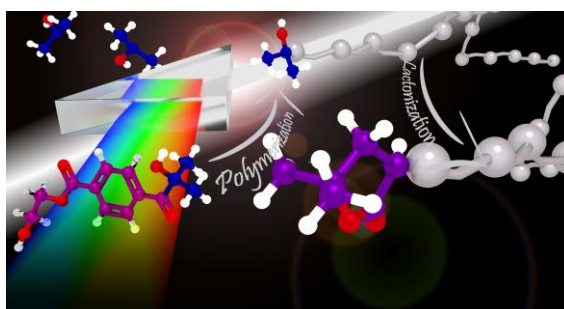
5.1 Introduction

Photoinitiators (PIs) constitute the crucial component of photoinduced radical polymerization reactions. Their properties have been thoroughly studied using a variety of experimental techniques, including chemically induced dynamic nuclear polarization (CIDNP) sepctroscopy,[189] absorption spectroscopy,[96] mass spectrometry[160] and by theoretical studies.[58] Most studies address the synthesis of new cleavable moieties,[190,191] describe the investigation of the polymerization rate and kinetics,[71,192] or elucidate kinetics.[160,163] Furthermore, the investigation of a PI can also be carried out by not only focusing on the photophysical properties, but rather on the ability to induce polymerization as a function of their structure. One example of a frequently employed, highly functional photoinitiator is Irgacure 2959 (2-hydroxy-4′-(2-hydroxyethoxy)-2-methylpropiophenone), a type I photoinitiator which cleaves upon UV light, generating two radicals. The generated fragments are structurally different, i.e. an isopropyl alcohol radical (**O·**) and a benzoyl radical (**B·**) (refer to Scheme 5.1). Both radicals are equipped with a hydroxy moiety for further functionalization.[98,99] In addition to providing an anchor for functionalization, the incorporated isopropyl alcohol polymer end group induces an angular compression of the tetrahedral end group center due to the geminal methyl groups, which results in a ring-closing reaction between the alcohol end group and the polymer backbone (e.g. with the ester motif of methacrylates). The underlying effect of this cyclization reaction is termed Thorpe-Ingold effect, which was discovered by Beesley, Thorpe and Ingold in 1915.[151] Thus, this Chapter of the current thesis will explore the Thorpe-Ingold effect induced lactonization reaction during photoinduced polymerization, initiated by Irgacure 2959. The spontaneous polymer end group transformation to yield lactone chain termini was investigated as a function of the monomer type, wavelength, temperature and irradiation energy. The presence of the lactone terminated end groups was evidenced via size exclusion chromatography hyphenated with electrospray ionization mass spectrometry (SEC-ESI-MS). The polymeric materials were synthesized utilizing pulsed-laser polymerization (PLP) induced by a wavelength-tunable monochromatic laser system and an excimer-laser system ($\lambda = 351\,\text{nm}$), which the latter provides high energies at variable sample temperatures. Furthermore, detailed density functional theory (DFT) calculations were performed to obtain insight into the lactonization mechanism, while MS/MS experiments were conducted for a precise structural characterization and nuclear magnetic resonance (NMR) measurements for detailed monitoring of polymer end groups served as a supporting secondary analytical method.

5.2 PLP Experiments

The detailed mass spectrometric investigation of the Thorpe-Ingold effect induced lactonization reaction of the photoinitiator Irgacure 2959 during PLP involved eight monomers (methyl methacrylate (MMA), ethyl methacrylate (EMA), *n*-propyl methacrylate (*n*PMA), *iso*-propyl methacrylate (*i*PMA), *n*-butyl methacrylate (*n*BMA), *tert*-butyl methacrylate (*t*BMA), dimethyl-amino-ethyl methacrylate (DMAEMA), and benzyl methacrylate (BnMA, refer to Scheme 5.1)), wavelengths spanning 275-360 nm in ~20 nm increments, energies of 0.35-2.5 mJ/pulse, and temperature-dependence studies in the regime of 0-60 °C. For the monomer-dependent study, Irgacure 2959 was utilized to polymerize the monomer in bulk via PLP at low laser energies (0.35 mJ/pulse, λ = 351 nm, 100 Hz), to ensure intact end groups and short polymer chains for the latter analysis of the polymeric material. The residual monomer was evaporated and the polymer was analyzed with SEC-ESI-MS without further purification. The nomenclature introduced in Chapter 3 was adopted to address the observed SEC-ESI-MS signals.
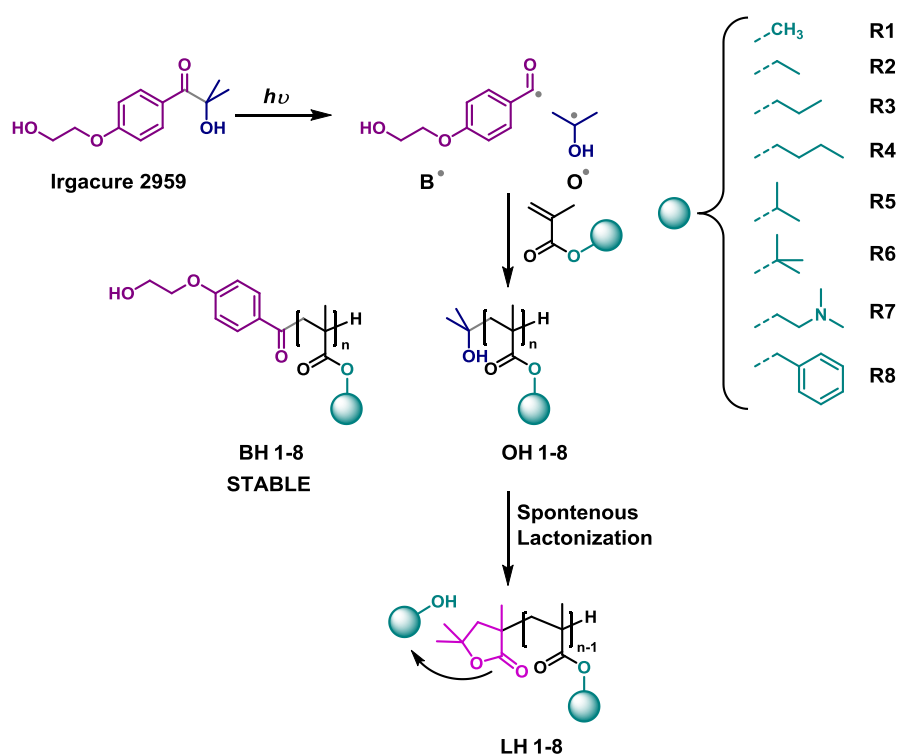
Scheme 5.1.: End group transformations of photochemically generated (Irgacure 2959) hydroxy isopropyl-terminated (OH) poly(methacrylates, R1-R8), induced by the Thorpe-Ingold effect to obtain lactone-derived end groups (LH). Adapted from reference [193] with permission from the Royal Society of Chemistry.

5.3 Investigation of the Lactone Presence and Formation via MS and NMR Spectroscopy

In the following Section, the presence and formation of the lactone species will be discussed on the example of p(nPMA) to avoid repetitive mass spectrometric evaluation. All mass spectra of p(MMA), p(EMA), p(iPMA), p(nBMA), p(tBMA), p(DMAEMA), and p(BnMA) can be found in the appendix (Figures 8.21-8.28). Figure 5.1 depicts one repeating unit from the high-resolution mass spectrum of p(nPMA) initiated by Irgacure 2959 (λ = 351 nm, 0.35 mJ/pulse, black spectrum), the associated isotopic pattern simulation (gray spectrum) and the assigned polymer structures. The associated experimental and theoretical m/z values are collated in Table 5.1.

Figure 5.1.: (a) High-resolution SEC-ESI mass spectrum of p(nPMA) initiated by Irgacure 2959, synthesized at low laser energies (0.35 mJ/pulse, 100 Hz, 351 nm, black spectrum) and the associated isotopic pattern simulation (gray spectrum). (b) Disproportionation products (XH) of the polymers initiated by Irgacure 2959 as assigned to signals found in SEC-ESI mass spectrum. Adapted from reference [193] with permission from the Royal Society of Chemistry.

The recorded mass spectrum exhibits the expected disproportionation pattern from the UV-induced cleavage process of the photoinitiator (**B=^{D}**, **BH^D**, **O=^{D}**, **OH^D**; for complete polymer structures refer to the appendix Scheme 8.9) as well a third disproportionation pattern with signals at m/z = 1558.0 and 1560.0 (values are taken from the mass spectrum at 351 nm). ESI-MS measurements can be influenced by their ionization leading to favored ionization of a species over another species. Hereby, charge competition, energy which is required to exit the solvent shell, as well as dipol interactions, belong to the primarily causes of ionization issues. To overcome such ionization influences, the ESI-MS measurements were conducted with constant settings of the orbitrap mass spectrometer, minimizing these influences to a minimum. Excluding adduct formation in positive ion mode (i.e. H$^+$ or K$^+$ attachment) of the expected Irgacure 2959-derived species, as well as ionization issues due to the mild ionization conditions during the ESI-

MS process, the third peak pattern is associated with the transformation of the hydroxy isopropyl end group to a lactone end group during PLP. Thus, species from the spontaneous lactone formation in case of p(nPMA) (labeled as **LH^D** and **L=^{D}**) have the highest ion abundance in the mass spectra in comparison to the other disproportionation pattern (**B=^{D}**, **BH^D**, **O=^{D}**, **OH^D**). The observed trend remained consistent for every repeating unit of the polymer.

Table 5.1.: Overview of the assigned signals of p(nPMA) synthesized at low laser energies (351 nm, 0.35 mJ/pulse, 100 Hz), as detected by SEC-ESI-MS with a resolution of 50000. Adapted from reference [193] with permission from the Royal Society of Chemistry.

Species	Ionization	$(m/z)^{theo}$/Da	$(m/z)^{exp}$/Da	$\Delta(m/z)$
BH^D	Na$^+$	1597.9732	1597.9718	0.0014
B=^{D}	Na$^+$	1595.9576	1595.9593	0.0017
OH^D	Na$^+$	1620.0515	1620.0460	0.0055
O=^{D}	Na$^+$	1618.0358	1618.0379	0.0021
LH^D	Na$^+$	1559.9940	1559.9948	0.0008
L=^{D}	Na$^+$	1557.9783	1557.9806	0.0023

To confirm the presence of the lactone species in the polymer, HCD as well as ^{13}C NMR measurements were carried out. The HCD measurement was performed with the species **LH^D** (m/z = 1431.9) of p(nPMA) by applying high energy of 30 eV to the molecular ion.
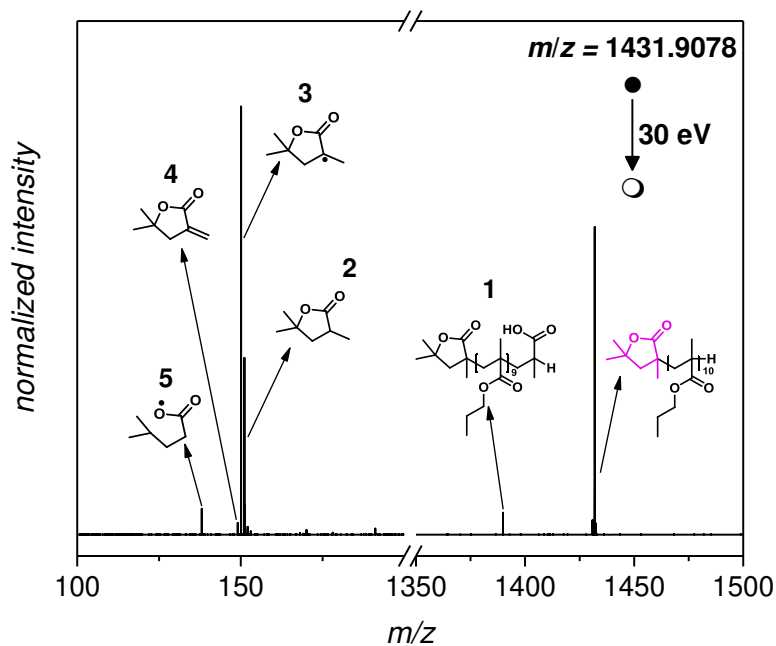
Figure 5.2.: High-resolution HCD spectrum of LH^D of p(nPMA) initiated by Irgacure 2959 at low laser energies (100 Hz, 351 nm, 0.35 mJ/pulse). Adapted from reference [193] with permission from the Royal Society of Chemistry.

The associated spectrum as well as the assigned structures of the molecular ions and the resulting fragments are illustrated in Figure 5.2. Firstly, the backbone undergoes cleavage, resulting in fragment **1**. This fragmentation is consistent throughout the polymer, yet, for sake of simplicity the spectrum only shows one cleavage. Furthermore, the end group breaks, resulting in a multitude of signals (fragments **2-4**) around 150 Da, which can be assigned to various lactone species.

Since the lactone is incorporated only as an end group in the polymer, 2D ^{13}C-^{13}C incredible natural abundance double quantum transfer experiments (INADEQUATE) to clearly determine the peak signals in the obtained ^{13}C NMR spectrum are not feasible, due to the insensitivity of such 2D experiment, as only 0.01% of the carbons are excited at natural abundance. Therefore, the ^{13}C NMR measurements served only as supporting information for the end group conversion, yielding the lactone species. Here, ^{13}C NMR measurements were conducted with two polymers, where one reveals the lactone species in the mass spectrum (p(*n*PMA)) and the other one does not (p(*n*BMA)). The obtained spectra are depicted in Figure 5.3.
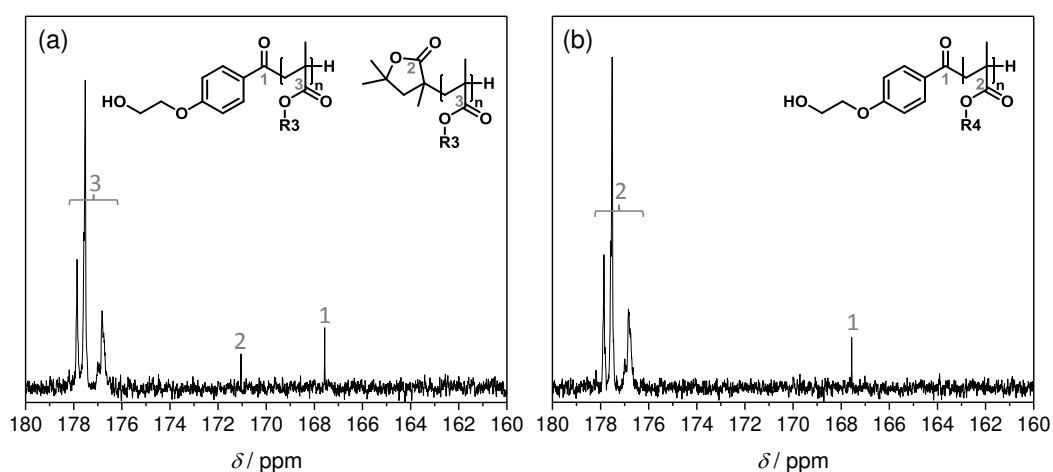
Figure 5.3.: ^{13}C NMR spectra of p(*n*PMA) (a) and p(*n*BMA) (b) initiated by Irgacure 2959. For simplicity, only the carbonyl region is shown. Adapted from reference [193] with permission from the Royal Society of Chemistry.

The evaluation of these spectra was limited to the carbonyl region, as the carbon atom of the carbonyl motif of the lactone-ring appears in this region. It can be clearly seen that the spectrum of p(*n*PMA) exhibits an additional resonance at 171 ppm compared to the p(*n*BMA) spectrum. Thus, it can be assumed that the additional resonance in the spectrum of p(*n*PMA) belongs to the carbonyl atom of the lactone species.

In addition, a photoinitiator without the hydroxy group at the isopropyl terminus was investigated, in order to confirm the mechanistic pathway of the lactonization reaction.

Irgacure 907 (2-methyl-4′-(methylthio)-2-morpholinopropiophenone) belongs to the class of the α-aminoacteophenone photoinitiators (type I PI) and cleaves into benzoyl- and α-alkylamino-radicals upon irradiation. Irgacure 907 was utilized to polymerize nPMA in bulk via PLP and further analyzed with SEC-ESI-MS, applying the same conditions as above. As can be clearly seen from the mass spectrum (refer to Figure 5.4), without the hydroxy group attached to the isopropyl moiety, the ester cannot be cleaved as no nucleophile is in direct proximity.
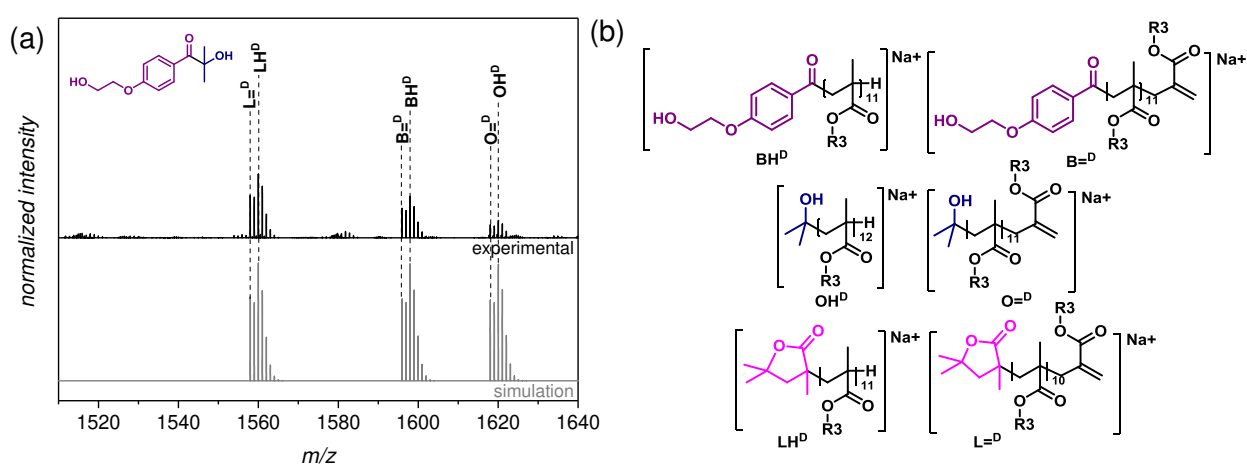

Figure 5.4.: (a) High-resolution SEC-ESI mass spectrum of p(nPMA) initiated by Irgacure 907, synthesized at low laser energies (0.35 mJ/pulse, 100 Hz, 351 nm, black spectrum) and the associated isotopic pattern simulation (gray spectrum). (b) Disproportionation products (XH) of the polymers initiated by Irgacure 907, at low laser energies (0.35 mJ/pulse, 100 Hz, 351 nm), as detected by SEC-ESI-MS. Adapted from reference [193] with permission from the Royal Society of Chemistry.

5.4 Quantitative Analysis of the Lactone Chain Termini

In addition to evidencing the lactone formation itself, a quantitative investigation for every polymer initiated by Irgacure 2959 was performed. For this, the method of Chapter 3 which evaluates the peak heights Δh of the polymer signals in each repeating unit, was applied. In order to ensure that the peak height $\Delta h(\mathbf{LH^D})$ is not influenced by other disproportionation or combination patterns, as it is the case for pMMA (refer to appendix Figure 8.21), the respective second peaks of every disproportionation peak cluster (**OH** and **LH**) were selected and compared against each other (see Figure 5.5). The individual peak height $\Delta h(X)$ was employed for the calculation of $\chi^{LH}(n)$, where X defines the respective end group of the initiation or end group converted fragment (see Equation 5.1).

$$\chi^{LH^D}(n) = \frac{\Delta h^{LH^D}(n)}{\Delta h^{LH^D}(n) + \Delta h^{OH^D}(n+1)} \tag{5.1}$$

A plot of the $\chi^{LH}(n)$ values for each fragment **LH^D** vs. the degree of polymerization DP_n (refer to appendix Figures 8.32-8.35), exhibits a constant gradient close to zero, suggesting that a chain length independent ESI-MS process takes place.
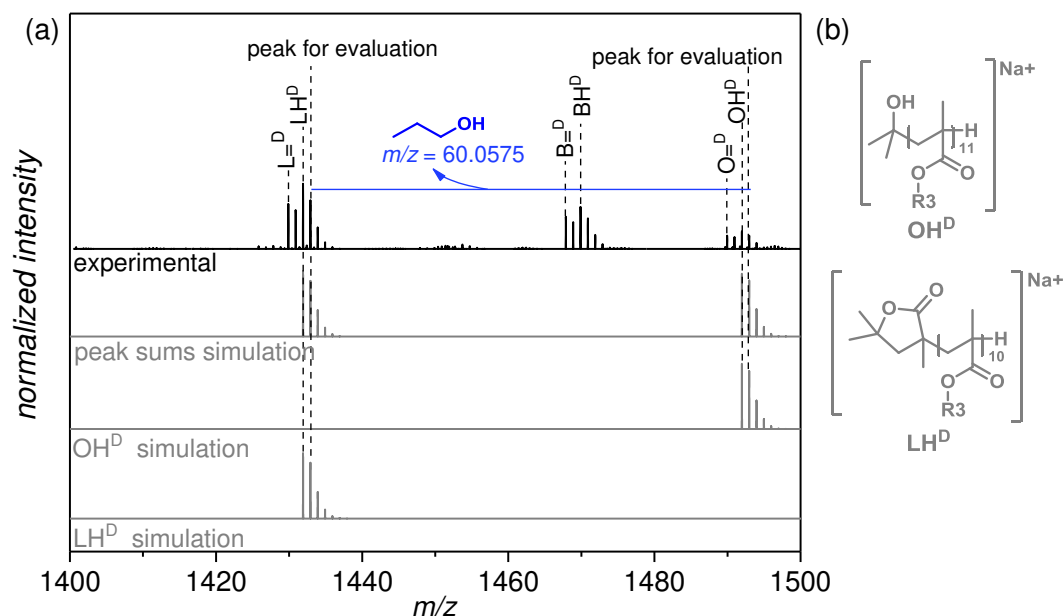
Figure 5.5.: (a) High-resolution SEC-ESI mass spectrum of p(nPMA) initiated by Irgacure 2959 at low laser energies (100 Hz, 351 nm, 0.35 mJ/pulse, black spectrum), and the theoretical isotopic pattern of OH^D and LH^D, as well as the sum of the simulation pattern (gray spectrum). (b) Structure of the disproportionation products (OH^D and LH^D). Adapted from reference [193] with permission from the Royal Society of Chemistry.

5.5 Investigation of Various Polymer Backbones

Since the ester motif of the polymer backbone plays a key role in the formation of the lactone, methacrylate monomers with different residues, including longer alkyl chains, branched chains, aromatic residues, as well as heteroatom containing residues, were employed in the PLP experiments. Each polymerization was performed under bulk conditions, utilizing Irgacure 2959 at low laser energies (351 nm, 100 Hz). The degree of end group formation in correlation to the monomer was calculated by utilizing Equation 5.1. The thereby obtained ratios of lactonization for each type of polymer are collated in Table 5.2. On the one hand it is evident that the reaction occurs rather efficiently for the polymers p(DMAEMA) (100%), p(BnMA) (close to 85%), and p(nPMA) (close to 80%). On the other hand, the polymers p(MMA), p(EMA), p(iPMA), p(BMA), and p(tBMA) exhibited lactonization products in significantly lower, yet still clearly detectable, amounts.

Table 5.2.: Overview of the averaged ratios of lactone end groups of the polymers synthesized at low laser energies (351 nm, 0.35 mJ/pulse, 100 Hz) and initiated by Irgacure 2959, as detected by SEC-ESI-MS with a resolution of 50000. Adapted from reference [193] with permission from the Royal Society of Chemistry.

Polymers	Pulses	χLH^D	χOH^D
p(MMA)	90 000	0.10	0.90
p(EMA)	90 000	0.06	0.94
p(nPMA)	90 000	0.78	0.22
p(iPMA)	90 000	0.04	0.96
p(nBMA)	90 000	0.06	0.94
p(tBMA)	90 000	0.02	0.98
p(DMAEMA)	45 000	1.00	0.00
p(BnMA)	22 500	0.83	0.17

5.6 Understanding the Lactone Mechanism via DFT Calculations

Detailed Density Functional Theory (DFT) calculations were performed by A.-M. Kelterer (TU Graz) in order to obtain further insights into the lactonization mechanism. For these studies, small molecule polymer analogs (to allow for inexpensive calculations), consisting of a hydroxy isopropyl moiety connected to two monomer units were selected. Since nPMA (**R3**) and nBMA (**R4**) were already used as example monomers in the experimental part, they were also investigated in the theoretical part as small molecule polymer analogs. These models should be suited for identifying the differences between the polymers containing lactone end groups and those not containing these end groups. Therefore, the ester motif for **R3** and **R4** were opted and the relative Free Gibb's energy of the reaction pathways was calculated. The nucleophilic attack of the isopropyl alcohol to the prochiral ester motif generates a chiral intermediate, which subsequently forms the lactone and liberates the propyl alcohol (or butyl alcohol). In Hanson's nomenclature, such an attack is referred to as a *si* face attack (generating an *S* enantiomer) or a *re* face attack (generating an *R* enantiomer) (refer to Appendix Scheme 8.16). The calculations indicate that the *si* face attack generates the thermodynamically more stable (-12 kJ·mol^{-1} (*si* face attack) vs. +8.04 kJ·mol^{-1} (*re* face attack)) conformer independent of the alcohol motif (**R3** or **R4**, refer to the Appendix Table 8.46). Figure 5.6 illustrates the computed *si* face pathway (values for *re* face pathway, refer to the Appendix Figure 8.39) of the small molecule polymer analogs (propyl (**R3**) and butyl (**R4**)). From the open polymer structure a direct ring closure leads to an intermediate structure. This ring-closing reaction is the rate limiting step and has similar barrier for both polymer structures (153.7 kJ·mol^{-1} (**R3**) and 155.4 kJ·mol^{-1} (**R4**), respectively). In the

transition state, the O-C bond length is ~1.72 Å and the proton is located between the two oxygen atoms. The alcohol is then released from this intermediate, leading to a stable lactone-alcohol adduct with a lactone-alcohol distance of approximately 3.5 Å. Here, the formed lactone structure is thermodynamically disfavored for the butyl substituent (+2.2 kJ·mol^{-1} over the open polymer end group) and favored for the propyl substituent (stabilized by -12 kJ·mol^{-1}). Thus, based on the DFT calculations, there is an evidence that the ester motifs can influence the lactonization reaction, confirming the experimental findings that the lactone is generated for propyl substituents with a high ratio, but not for butyl substituents.
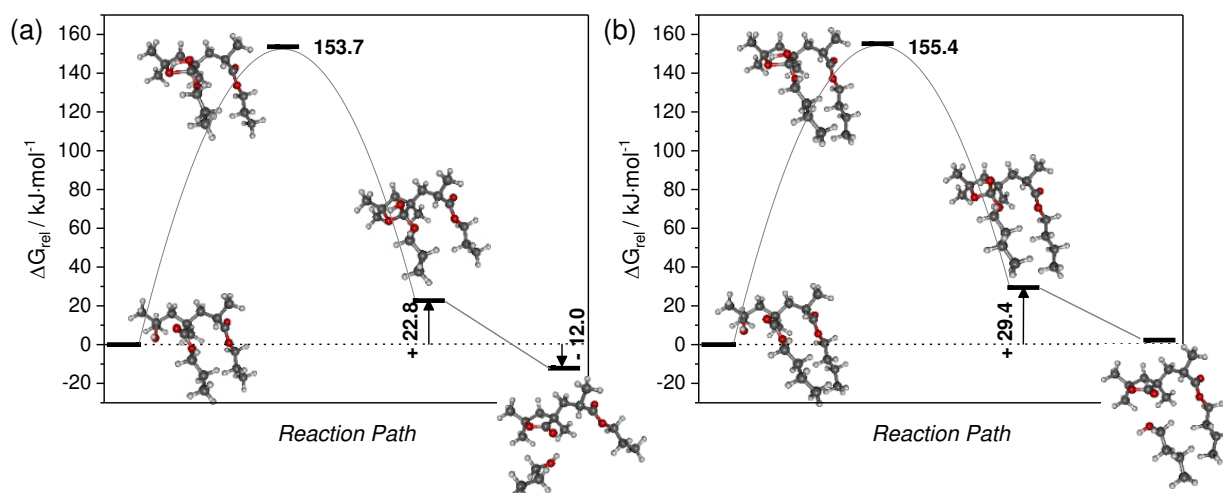
Figure 5.6.: Relative Gibbs Free energies of reaction paths after *si* face attack for propyl (a) and butyl (b) substituted molecules. The relative energy of the lowest open polymer is set to ΔG_{rel} = 0.0 kJ·mol^{-1}. Geometries of the propyl and butyl substituted molecules are provided within the graph. Adapted from reference [193] with permission from the Royal Society of Chemistry.

5.7 Investigation of Variable Wavelengths

As p(nPMA) exhibits high lactone ion abundancies, a precision wavelength screen with nPMA was performed. In order to quantify the degree of end group transformation as a function of wavelength, the calculation of Equation 5.1 was utilized. Figure 5.7 depicts the high-resolution SEC-ESI mass spectra of p(nPMA) initiated by Irgacure 2959 utilizing wavelengths in the range of 275-360 nm, employing a constant photon count per wavelength (colored spectra, refer to the Experimental Section for a detailed description of how a constant photon count was achieved) as well as the isotopic pattern simulation (black spectrum). The mass spectrum of all photo-initiated polymers employing different wavelengths display the same expected disproportionation products (**L=**, **LH**, **O=**, **OH**, **B=**, **BH**) as in the preliminary experiment at a fixed wavelength of 351 nm. The ratio of lactonization of the polymer is invariant to the wavelength as evident from Figure 5.7b. The respective plots of the χ^{LH} (n) values (wavelength) for each fragment **LH^D** against the degree of polymerization DP_n can be found in the appendix

120

(Figure 8.35). The reduced of lactonization at 275 nm (absorption maximum of Irgacure 2959) is attributed to ring-opening of the lactone end group during harsh irradiation conditions (refer to Appendix Figure 8.31, Scheme 8.15, Table 8.41).
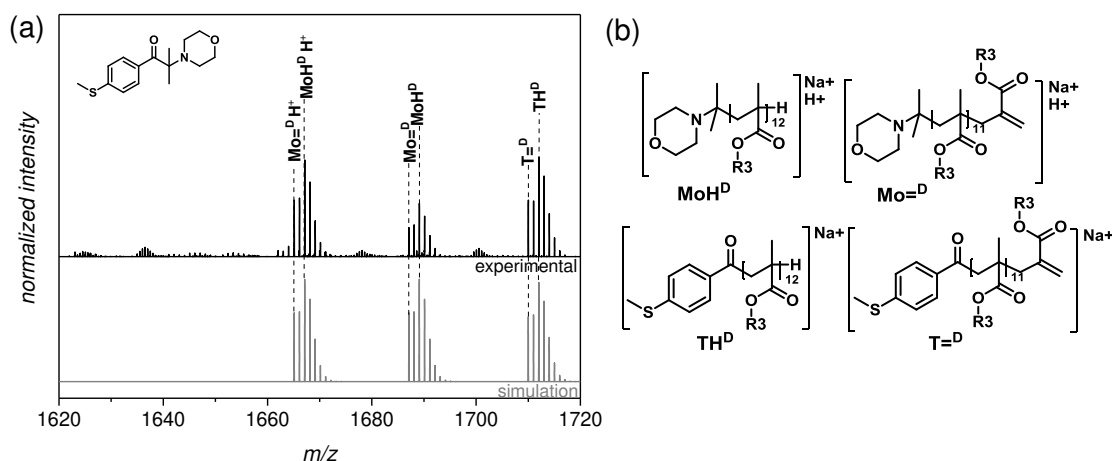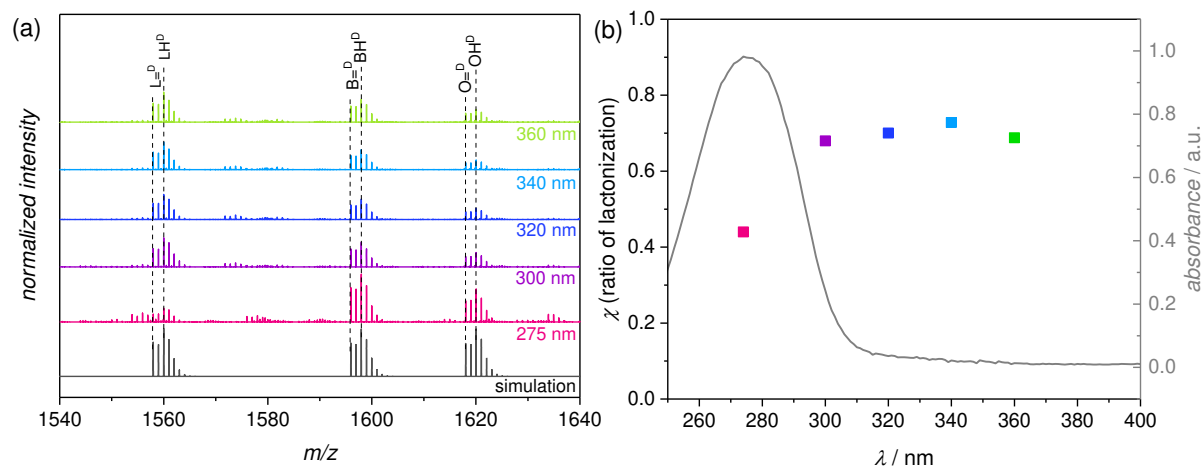

Figure 5.7.: (a) High resolution SEC-ESI mass spectra of the polymer initiated by Irgacure 2959, synthesized at low laser energies (0.35 mJ/pulse, 100 Hz, 18 °C, colored spectra) at variable monochromatic wavelengths (275-360 nm) at a constant photon count and the associated isotopic pattern simulation (black spectrum). (b) Wavelength-dependent transformation of hydroxy isopropyl to lactone end groups (275-360 nm) expressed by the lactonization ratios (shown with the disproportionation product LH^D) derived from the peak heights (OH^D and LH^C; of Irgacure 2959-pPMA (■), determined with high resolution SEC-ESI-MS as well as the UV-Vis spectrum of the photoinitiator Irgacure 2959 in MeOH ($5 \cdot 10^{-5}$ M). Adapted from reference [193] with permission from the Royal Society of Chemistry.

5.8 Investigation of the Temperature and Energy Influence

In order to investigate thermodynamic and kinetic effects, a temperature- and energy-dependent study of the spontaneous occurrence of the lactonization reaction during PLP was conducted. Here, *n*PMA served as an exemplary monomer since it was already utilized in the wavelength-dependent screening. The respective plots of the χ^{LH} (n) values (energy: 0.35-2.5 mJ/pulse, and temperature: 0-60°C) for each fragment $\mathbf{LH^D}$ against the degree of polymerization DP_n, as well as the mass spectra can be found in the appendix (Figures 8.36-8.37 and Figures 8.29-8.30). Table 5.3 depicts the energy- and temperature-dependent ratios of the lactonization reaction of Irgacure 2959-p(*n*PMA) during PLP, derived from the peak height $\Delta h(\mathbf{LH^D})$. It can be clearly seen that the formation of the lactone is not correlated with the applied energy and temperature during PLP.

Table 5.3.: Overview of the averaged ratios of lactone end groups of p(*n*PMA) synthesized at different temperatures (0-60 °C, 351 nm, 0.35 mJ/pulse, 100 Hz) and energies (18 °C, 351 nm, 0.35-2.5 mJ/pulse, 100 Hz) and initiated by Irgacure 2959, as detected by SEC-ESI-MS with a resolution of 50000. χ was calculated according to Equation 5.1. Adapted from reference [193] with permission from the Royal Society of Chemistry.

Temperature (°C)	χLH^D	Energy (mJ/pulse)	χLH^D
0	0.93	0.35	0.82
10	0.91	0.70	0.80
20	0.82	1.20	0.79
30	0.94	1.60	0.82
40	0.94	2.00	0.76
50	0.87	2.50	0.80
60	0.85	-	-

5.9 Summary

In summary, an in-depth mass spectrometric study of the monomer-, wavelength-, energy, and temperature-dependent transformation of hydroxy isopropyl polymer end groups into lactone polymer end groups was conducted. Eight photoinitiator-derived poly(methacrylates), initiated by Irgacure 2959, were synthesized via PLP at 351 nm, employing low laser energy as well a constant photon count and subsequently analyzed via SEC-ESI-MS. It emerged that the intra ring-closing reaction of the polymer end groups could only be evidenced for p(*n*PMA), p(BnMA) and p(DMAEMA). Lactonization products could hardly be detected for the polymers: p(MMA), p(EMA), p(*i*PMA), p(BMA), and p(*t*BMA). In order to confirm the experimental findings and to obtain further insight into the lactonization mechanism density functional theory (DFT) calculations of small molecule polymer analogs were conducted. These analogs consist of the hydroxy isopropyl end group connected to two monomer units (R3 and R4, respectively) with the most stable all-trans alkyl chains. Factors reducing the high ring closure barrier of the rate-limiting step were not included, e.g. steric effects such as interaction of monomers and conformational flexibility of the alkyl chains, solvent- or monomer-mediated H-transfer, tunneling of the proton through the lactonization barrier. Based on these calculations, there is a theoretical evidence that the ester motifs can influence the lactonization. Furthermore, the DFT calculations elucidated that the thermodynamically more stable lactone species is generated after *si* face attack. Wavelength-, energy- and temperature-dependent studies revealed no correlation between the tested conditions and the formation of the lactone species. Therefore, the study offers critical insights into by-product formation of photoinduced polymerizations, which are

here displayed by the monomer-dependent transformation of hydroxy isopropyl-type radical derived end groups into lactone derived end groups. The lactones are useful candidates for specific post-polymerization modification including the ring-opening of their cyclic structure.

<div style="text-align: right; font-size: 4em;">6</div>

Concluding Remarks and Outlook

In the current dissertation, the main goal was to investigate the mechanistic pathways that post-irradiated polymers undergo, which was discussed in the first part of the thesis (Chapter 3). The UV-induced transformation of polymer end groups was analyzed in-depth via a combination of pulsed-laser polymerization (PLP) and various pulsed-laser irradiation (PLI) techniques coupled to size exclusion chromatography electrospray ionization mass spectrometry (SEC-ESI-MS), photo-CIDNP spectroscopy, and theoretical calculations. PLP/PLI-SEC-ESI-MS is a powerful tool providing valuable insights into the molecular changes affecting polymer end groups, as it reveals the cleavage products of the secondary photochemically induced transformation processes. Photochemically induced dynamic nuclear polarization (photo-CIDNP) is a suitable technique to analyze such transformation processes, too, since only products formed from chemical reactions involving radical pairs are observed. Therefore, it is ideally suited to reveal structural information on the reaction products, which enables drawing conclusions about possible reaction pathways. In a study by Voll *et al.*[1] the UV light-induced transformation of benzoyl end groups, which proceeds via a Norrish Type I or II reaction, was initially explored. In the current work, however, the influence of various methyl-substitutions on the benzoyl moiety affecting their tendency for the UV-induced cleavage process was initially investigated.

Thus, eight benzoin-type derived polymer end groups were subjected to post-irradiation conditions. Hereby, only the chain termini where the *ortho*-position on the phenyl ring was not substituted with two methyl groups showed end group cleavage, leading to the loss of the aromatic functionality and the formation of unsaturated species. On the other hand, chain termini with methyl-substitution on both *ortho*-positions showed no cleavage tendency. DFT calculations suggested that the increased UV light stability of these so-called stable polymer end groups can be attributed to the inductive effect of the methyl groups, which leads to a shift of the *n-π** transitions towards lower wavelengths. Furthermore, the wavelength-dependent photochemical stability of these stable polymer end groups was studied. It was demonstrated that the substitution pattern on the phenyl moiety with methyl groups dictates the UV-stability as a function of the wavelength. Further, the influence of the solvent, the substitution with various functional groups, the polymer backbone, as well as the conduction of the post-irradiation under solid-state conditions, did not significantly affect the light induced cleavage process. The knowledge acquired from these studies enables the understanding of structure-reactivity correlations of chain termini, which are of critical importance for the application of polymeric materials, especially in coatings, where exposure to light occurs. In UV coatings, the photoinitiating species, which carries mainly a chromophoric pattern, remains as polymer end group in the final coating. In general, most formulations of coatings contain organic additives, such as hydroxy benzophenone,[194] to protect the final product from degradation caused by the UV light of the sun. Moreover, UV pigments such as titanium dioxide[195] are employed, as they protect the coating by reflecting the incident UV light. However, the application of additives also involves some drawbacks, as it might influence the properties of the coating, such as the color and it is limited in life-time. To overcome such drawbacks, the gained knowledge of the current studies can be utilized to protect the coating by improving the UV-stability of the photoactive polymer end group itself, by equipping the benzoyl moiety with methyl-substitution in both *ortho*-positions. The higher the number of methyl-groups on the benzoyl moiety, the more stable against UV light the polymer end group becomes. Therefore, the usage of additives is no longer necessary, which reduces the influence of the coating properties caused by such additives, while being more economical. Based on the findings of the present thesis, the basis for the development of innovative approaches and initiators for the photoinduced synthesis of polymers with stable end groups becomes possible, thus providing an avenue for enabling long service life-times of photo-cured materials.

In order to further improve and investigate the stability of the benzoyl end groups, the benzoyl moiety could be substituted with longer alkyl chains in both *ortho*-positions (refer to Scheme 6.1), which should cause a stronger inductive effect on the aromatic system. The

incorporation of branched alkyl groups in both *ortho*-positions should enhance the inductive effect even more than longer alkyl chains, while concomitantly effecting steric barriers so that the phenyl ring is not able to twist out of plane vs. the carbonyl group. This restriction in coplanarity in turn leads to the cleavage of the end group, leading to the unsaturated species. Furthermore, six or five membered heterocycles are able to increase (when oxygen or sulphur are included, refer to Scheme 6.1) or decrease (when nitrogen is included, refer to Scheme 6.1) the electron density of the aromatic system, thus constituting interesting candidates for the UV-induced cleavage analysis of polymer end groups. In addition, an extended aromatic system – e.g. by utilizing naphthalene, anthracene or even pyrene (refer to Scheme 6.1) instead of benzene – could, due to the red-shifted absorption character, be interesting for a wavelength-dependent screening in respect to the polymer end group conversion.
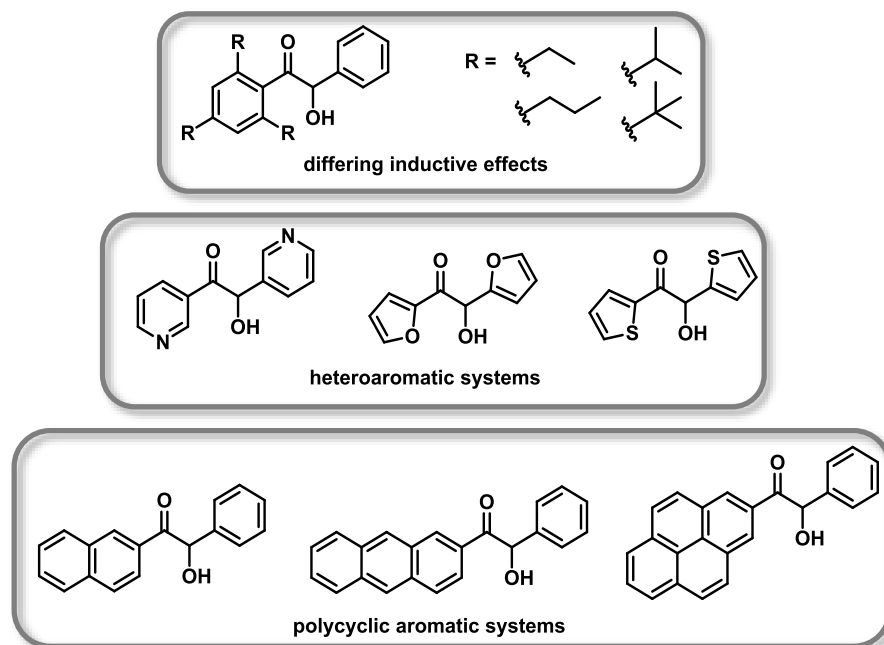
Scheme 6.1.: Further PI structures enabling investigations exploring the influence of differing inductive effects, hetero aromatic systems as well as the influence of the extension of the phenyl moiety with polycyclic aromatic systems on the post-cleavage process of photoinduced polymers.

Next, these photoinduced end group conversions yielding unsaturated species can be utilized for further post-modification reactions of the polymer, for instance via photoinduced ligation techniques. In the following, a possible approach (refer to Scheme 6.2) on the example of a benzoyl end group substituted with one methyl-group in *ortho*-position, able to perform the UV-induced end group transformation, will be discussed. Here, 2MB-pMMA is able to undergo cleavage reactions of the chain termini by applying high irradiation energy. The resulting unsaturated end group could either react via a photoreaction with a pyrene aryl tetrazole (PAT), terminated with a polyethylene glycol (PEG) chain, which even reacts with non-activated double

bonds (furan-protected maleimides[196]) or directly with a second monomer, leading in both cases to a block-copolymer. On the other hand, by applying low energy 2MB-pMMA could form a highly reactive diene – also known as *o*-quinodimethane (photoenol) – that is able to undergo an irreversible [4+2]-cycloaddition with electron-poor dienophiles such as maleimides.
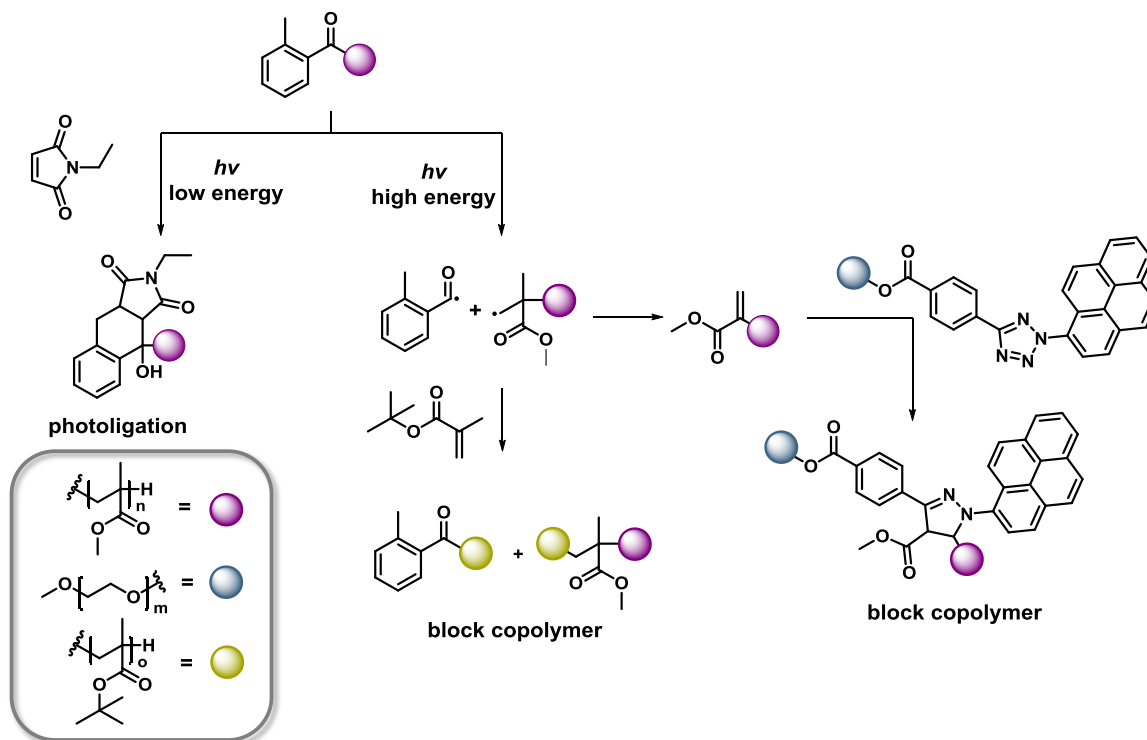
Scheme 6.2.: Overview of the light-energy induced reaction approach. The *o*-methyl-substituted benzoyl end group could undergo two reactions. Low energy: photoreaction with the maleimide. High energy: end group transformation occurs, leading to an unsaturated end group. This end group can be further exploited via two reaction paths: photoreaction with PAT-tetrazole and photoinduced polymerization with a second monomer.

In addition to the photoinduced end group conversion of polymers, the wavelength-dependent photochemistry of two oxime ester photoinitiator was investigated in the second part of the thesis (Chapter 4), utilizing a combination of PLP-SEC-ESI-MS, photo-CIDNP spectroscopy, UV-Vis spectroscopy and theoretical calculations. Once again, the PLP-SEC-ESI-MS method was employed to analyze the end group composition of the polymeric material and photo-CIDNP provides structural information regarding the reaction products, which is useful to establish the cleavage mechanism. UV-Vis spectroscopy and DFT calculations enable insights into the absorption properties and the excited states, relevant for the photocleavage of these initiators. Wavelength-dependent reactivity plots (where the monomer to polymer conversion induced at specific wavelengths by the same number of photons is mapped) were generated and revealed that both initiators lead to high monomer to polymer conversions in the visible light spectrum despite their low absorptivity beyond 400 nm. The findings highlight that the performance of a

photoinitiator system cannot be judged on the basis of its UV-Vis spectrum, but require ideally a monochromatic wavelength-dependent investigation of its photochemical and initiation behavior. The information regarding the discrepancy between the high photoinitiator reactivity and their low absorptivity disparate with their UV-Vis spectrum is of critical importance for the photoinitiator community, yet even more significant for the manufacturing industry. At present, industry is interested in highly efficient photoinitiator systems, which can be excited in the visible range, such as Ivocerin. This disparate behavior of the monomer to polymer conversion from the absorptivity of the photoinitiator needs to be further investigated. Thus, quantum mechanical calculations of possible conical intersections or photoinduced experiments, which are designed so that every sample absorbs the same amount of photons (ensuring that the optical density of each sample is kept equal per wavelength) could provide insights into these unusual photoinitiator reactivities.

In the last part of the thesis (Chapter 5), the Thorpe-Ingold effect was exploited to investigate the spontaneous UV-induced lactone end group formation during the photoinduced polymerization of the photoinitiator Irgacure 2959. Specifically, the hydroxy isopropyl polymer end group undergoes a ring-closing reaction with the ester motif of the polymer backbone leading to a lactone-derived polymer end group. The end group transformation was investigated by a combination of PLP-SEC-ESI-MS, including a precision structural determination via MS/MS experiments and additional supporting NMR measurements as well as theoretical calculations. The results demonstrated that the formation of the lactone species was not correlated to wavelength, energy or temperature, since it occurs irrespective of these parameters to the same extent. However, the analysis of the lactone formation, utilizing various monomers, revealed an unexpected behavior as not every polymer type yields the end group transformation. Additional DFT calculations were performed to give insights into these photoinduced end group processes. The calculations revealed that there is a theoretical evidence why some polymer types are able to perform the ring-closing reaction, while some other not. The findings of this study allow on one hand a convenient access to lactone end groups via photoinduced polymerization, which can be further utilized in post-modification reactions of the polymer. However, on the other hand, the unexpected end group structure for one of the most important photoinitiator comes as a surprise. These results impressively demonstrate how important in-depth mechanistic investigations of photoinitiator systems in terms of their resulting macromolecular product spectrum via high-resolution mass spectrometry are.

7

Experimental Part

7.1 Materials

Methyl methacrylate (MMA, Sigma-Aldrich, 99%, stabilized), ethyl methacrylate (EMA, TCI, 99%, stabilized), *n*-propyl methacrylate (*n*PMA, Sigma-Aldrich, 97%, stabilized), *iso*-propyl methacrylate (*i*PMA, TCI, 98%, stabilized), *n*-butyl methacrylate (*n*BMA, Sigma-Aldrich, 99%, stabilized), *tert*-butyl methacrylate (*t*BMA, Sigma-Aldrich, 98%, stabilized), benzyl methacrylate (BnMA, TCI, 98%, stabilized), and dimethyl amino-ethyl methacrylate (DMAEMA, TCI, 98.5%, stabilized), were freed from inhibitor by passing through a column of activated basic alumina (Acros). Irgacure OXE01, OXE02, 2959, 907, 369 were kindly provided by BASF and used as received. *Para*-fluoro-benzoin was kindly provided by Elena Frick. Benzoin (Sigma-Aldrich, 98%) was recrystallized twice in ethanol prior to use. 4-Methylbenzoin (4MB), 2,4-dimethylbenzoin (2,4-DMB), 2,4,6-trimethylbenzoin (TriMB), 2,3,5,6-tetramethylbenzoin (TetraMB), and 2,3,4,5,6-pentamethylbenzoin (PentaMB, 5), were synthesized according to literature procedures.[158,163] Aluminum chloride (ABCR, anhydrous), 2-methylacetophenone (Alfa Aesar, 98%), 3-methylacetophenone (Sigma-Aldrich, 98%), benzene (anhydrous, Alfa Aesar, 99.8%), dioxane (VWR, normapur), and selenium(IV) dioxide (ABCR, 99.8%) were used as received. Sodium iodide (Sigma-Aldrich, 99%), tetrahydrofuran (THF, Scharlau, multisolvent GPC grade, 250 ppm BHT), methanol (Roth, HPLC ultra gradient grade), and trifluoroacetate (Sigma-Aldrich, 99%), for SEC-ESI-MS and direct infusion ESI-MS measurements, were employed as received. For the post-

irradiation experiments, methyl isobutyrate (MIB, Acros Organics, 99%), toluene (VWR, normapur), dichloromethane (DCM, VWR, normapur), 1,4-dioxane, (HPLC grade, Carl Roth), ethyl acetate (VWR, normapur), acetonitrile (VWR, normapur), were used. Furthermore, *n*-hexane (VWR, normapur) and methanol (VWR, normapur) were used for precipitation of the synthesized polymers. Pd on activated carbon (Pd/C, Acros Organics, unreduced, 5% Pd) and a mixture of ethyl acetate (VWR, normapur) / ethanol (technical grade, 95%) in a ratio of 1:1 v/v were used for the hydrogenation experiments. Acetonitrile-*d₃* and chloroform-*d₁* for NMR and photo-CIDNP experiments were purchased from Sigma-Aldrich and used without additional treatment. Acetonitrile (Sigma-Aldrich, CHROMASOLV, for HPLC, gradient grade, >=99.9%) and methanol (VWR, normapur), for UV-Vis measurements, were used as received. For PLP and PLI experiments we used crimped photo glass vials (Lab Logistic Group GmbH (item number: 4-008202)) and crimped photo glass vials as well crimped quartz glass vials ilmasil PS (Qsil GmbH Quarzschmelze Ilmenau (item number: G540PS000000176)).

7.2 Syntheses and Preparation

7.2.1 Synthesis of 4MB, 2,4DMB, TriMB, TetraMB and PentaMB

4-methylbenzoin (4MB, 1), 2,4-dimethylbenzoin (2,4DMB, 2), 2,4,6-trimethylbenzoin (TriMB, 3), 2,3,5,6-tetramethylbenzoin (TetraMB, 4), and 2,3,4,5,6-pentamethylbenzoin (PentaMB, 5), were synthesized according to literature procedures.[158,163]

^{1}H NMR of 1 (CDCl$_3$, 400 MHz): δ = 7.75 (d, ^3J = 8.3 Hz, 2H, C$H_{arom.}$), 7.31-7.14 (m, 5H, C$H_{arom.}$), 7.12 (d, ^3J = 8.1 Hz, 2H, C$H_{arom.}$), 5.85 (d, ^3J = 5.3 Hz, 1H, CHOH), 4.52 (d, ^3J = 6.1 Hz, 1H, CHOH), 2.29 (s, 3H, CH_3)

^{1}H NMR of 2 (CDCl$_3$, 400 MHz): δ = 7.51 (d, ^3J = 7.7 Hz, 1H, C$H_{arom.}$), 7.34-7.16 (m, 5H, C$H_{arom.}$), 7.06-6.95 (m, 2H, C$H_{arom.}$), 5.89 (d, ^3J = 5.9 Hz, 1H, CHOH), 4.65 (d, ^3J = 5.9 Hz, 1H, CHOH), 2.32 (s, 3H, CH_3), 2.29 (s, 3H, CH_3).

^{1}H NMR of 3 (CDCl$_3$, 400 MHz): δ = 7.25-7.21 (m, 3H, C$H_{arom.}$), 7.12-7.11 (m, 2H, C$H_{arom.}$), 6.75 (s, 2H, C$H_{arom.}$), 5.59 (s, 1H, CHOH), 4.48 (bs, 1H, CHOH), 2.26 (s, 3H, 1 × CH_3), 1.83 (s, 6H, 2 × CH_3).

^{1}H NMR of 4 (CDCl$_3$, 400 MHz): δ= 7.25-7.13 (m, 3H, C$H_{arom.}$), 7.14-7.04 (m, 2H, C$H_{arom.}$), 6.97 (s, 1H, C$H_{arom.}$), 5.53 (d, ^3J = 5.0 Hz, 1H, CHOH), 4.51 (d, ^3J = 5.6 Hz, 1H, CHOH), 2.13-1.64 (m, 12H, 4 × CH_3).

^{1}H NMR of 5 (CDCl$_3$, 400 MHz): δ = 7.25-7.18 (m, 3H, C$H_{arom.}$), 7.11-7.08 (m, 2H, C$H_{arom.}$), 5.51 (d, ^3J = 5.6 Hz, 1H, CHOH), 4.49 (d, ^3J = 5.6 Hz, 1H, CHOH), 2.22-2.10 (m, 15H, 5 × CH_3).
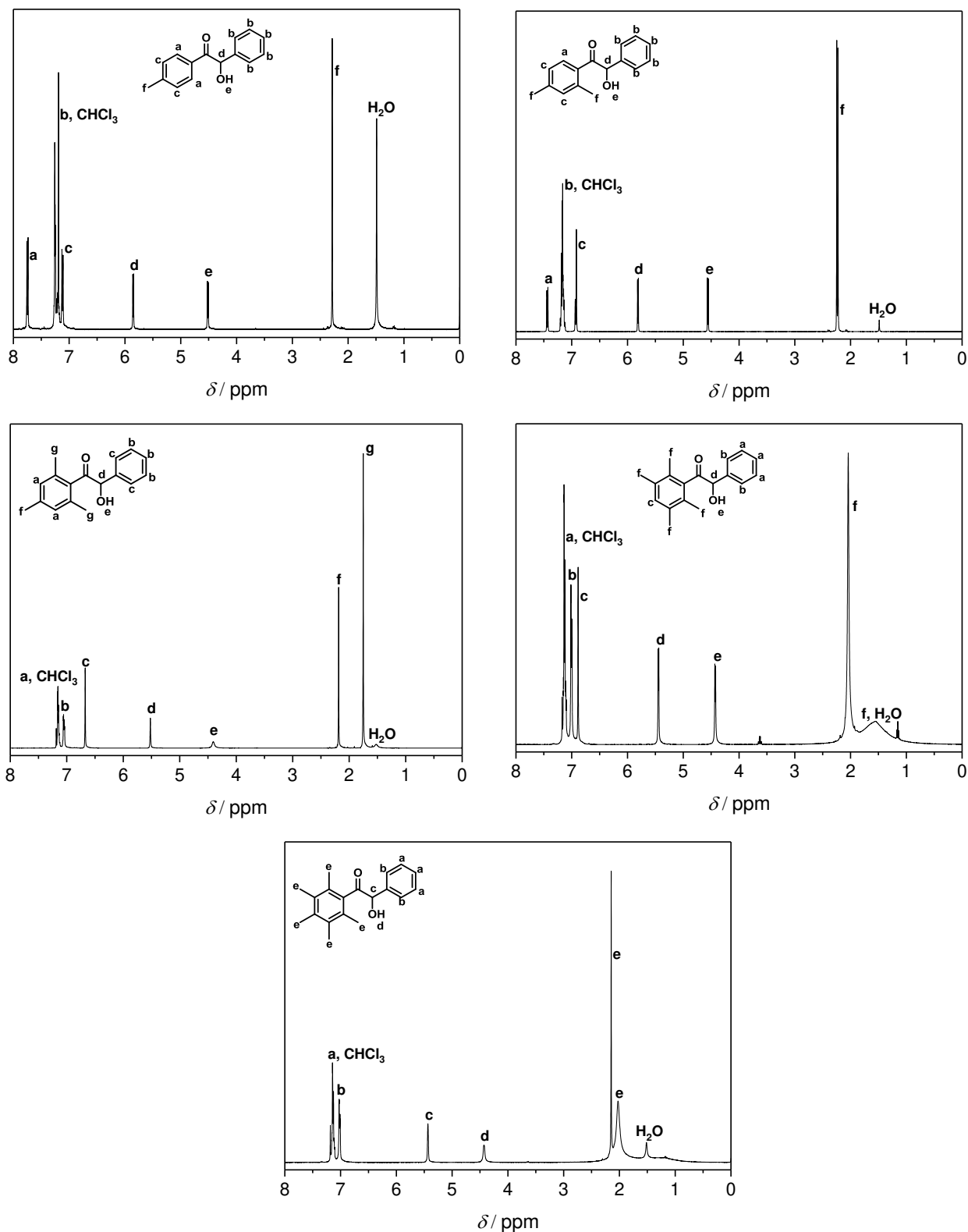
Figure 7.1.: ^{1}H NMR (400 MHz, CDCl$_3$) of 4-Methylbenzoin (4MB), 2,4-dimethylbenzoin (2,4DMB), 2,4,6-trimethylbenzoin (TriMB), 2,3,5,6-tetramethylbenzoin (TetraMB), and 2,3,4,5,6-pentamethylbenzoin (PentaMB). Adapted with permission from reference [165]. Copyright (2015) American Chemical Society (ACS).

133

7.2.2 Synthesis of 2MB, 3MB and 2,6DMB

Synthesis of 2-oxo-2-*o*-tolylacetaldehyde (6), 2-oxo-2-*m*-tolylacetaldehyde (7), and 2-(2,6-di-methylphenyl)-2-oxoacetaldehyde (8). The synthetic procedure was adapted from the literature[27] and is described exemplarily for 2-oxo-2-o-tolylacetaldehyde (6). To a solution of SeO_2 (8.28 g, 74.6 mmol, 1.00 eq) in 2.3 mL water, 2-methylacetophenone (10.0 g, 74.6 mmol, 1.00 eq) dissolved in 75 mL dioxane was added. The reaction mixture was refluxed for 6 h at 105 °C. Subsequently, the precipitated selenium was decanted and the solvent was evaporated under reduced pressure. Vacuum distillation gave 6 as a yellow oil (4.50 g, yield: 41%). (7, yield: 38%; 8, yield: 66%).

Synthesis of 2-hydroxy-2-phenyl-1-*o*-tolylethanone (2-Methylbenzoin, 2MB, 9), 2-hydroxy-2-phenyl-1-*m*-tolylethanone (3-Methylbenzoin, 3MB, 10), and 1-(2,6-dimethylphenyl)-2-hydroxy-2-phenylethan-1-one (2,6-Dimethylbenzoin, 2,6DMB, 11). The synthetic procedure was adapted from the literature[28,29] and is described exemplarily for 2-methylbenzoin (9). Anhydrous aluminum chloride (8.10 g, 60.8 mmol, 2.00 eq) was dissolved in 22 mL of anhydrous benzene. The suspension was cooled to 10 °C in an ice bath and 2-oxo-2-*o*-tolylacetaldehyde (4.50 g, 30.4 mmol, 1.00 eq.), dissolved in 22 mL of anhydrous benzene, was added dropwise to the suspension. The reaction was stirred for 2 h at 10 °C and subsequently the stirring was continued at ambient temperature overnight. The mixture was poured onto a mixture of ice/HCl$_{conc}$. The organic layer was decanted and the aqueous phase was extracted twice with a minimal amount of benzene. The organic layers were combined and the solvent was removed under reduced pressure. The crude yellow-orange solid was divided into two equal parts. One part was purified by flash chromatography (cyclohexane:ethyl acetate, 3:1 v/v) and one part was recrystallized at 90 °C from ethanol. The two purified parts were combined to give 9 as an off-white powder (1.28 g, yield: 18%). (10, yield: 9%; 11, yield: 7%).

^{1}H NMR of 9 (CDCl$_3$, 400 MHz): δ = 7.47 (d, ^3J = 7.7 Hz, 1H, C*H*$_{arom.}$), 7.24 (t, ^3J = 6.7 Hz, 1H, C*H*$_{arom.}$), 7.20-7.06 (m, 7H, C*H*$_{arom.}$), 5.81 (d, ^3J = 5.2 Hz, 1H, C*H*OH), 4.52 (d, ^3J = 5.8 Hz, 1H, CHO*H*), 2.19 (s, 3H, C*H*$_3$)

^{1}H NMR of 10 (CDCl$_3$, 400 MHz): δ = 7.67 (s, 1H, C*H*$_{arom.}$), 7.60 (d, ^3J = 7.6 Hz, 1H, C*H*$_{arom.}$), 7.25-7.16 (m, 7H, C*H*$_{arom.}$), 5.87 (s, 1H, C*H*OH), 4.49 (s, 1H, CHO*H*), 2.26 (s, 3H, C*H*$_3$)

^{1}H NMR of 11 (CDCl₃, 400 MHz): δ = 7.17-7.15 (m, 3H, C*H*arom.), 7.12-7.08 (m, 1H, C*H*arom.), 7.06-7.03 (m, 2H, C*H*arom.), 6.87 (d, ³*J* = 7.6 Hz, 2H, C*H*arom.), 5.53 (d, ³*J* = 5.3 Hz, 1H, C*H*OH), 4.40 (d, ³*J* = 5.5 Hz, 1H, CHO*H*), 1.79 (s, 6H, C*H*₃)
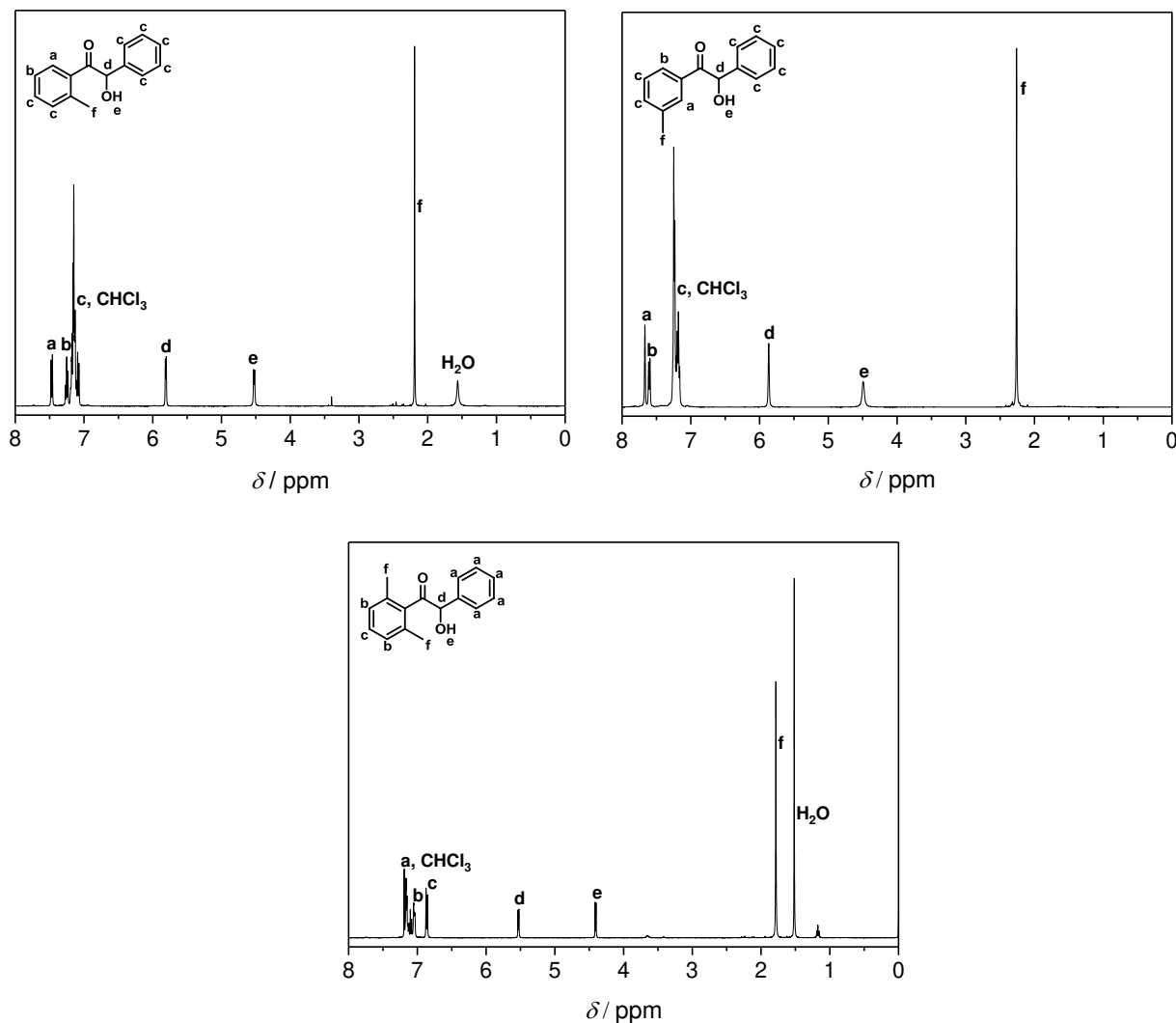
Figure 7.2.: ^{1}H NMR (400 MHz, CDCl₃) of 2-Methylbenzoin (2MB), 3-Methylbenzoin (3MB), and 2,6-dimethylbenzoin (2,6DMB). Adapted with permission from reference [165]. Copyright (2015) American Chemical Society (ACS).

7.2.3 Pulsed Laser Polymerization (PLP) and Post-Irradiation Experiments with Excimer Laser

The PLP samples were all prepared with a concentration of $c_{\text{Photoinitiator}} = 5 \cdot 10^{-3}$ mol·L^{-1} in monomer (sample volume ~ 0.5 mL), freed from oxygen by purging with nitrogen for 2 minutes and subsequently individually placed into the sample holder. The laser beam is redirected by a prism and enters the sample in a custom-made sample holder from below. The sample holder consists of a metal block with a vertical cylindrical hole (0.71 cm diameter, fixing the crimped glass vials during experiments), which was held at a constant temperature by a thermostat (model: 1196D, VWR, Darmstadt, Germany). Polymerization and post-irradiation of the polymer were carried out by an excimer laser system (Coherent XS-500, XeF, λ = 351 nm, frequency variable from 1-500 Hz). The polymerizations were performed at a low laser energy (custom-build metal filter was implemented to reduce the laser energy) and post-irradiated at high laser energy. After the polymerization, the remaining monomer was evaporated and the polymer was purified by precipitation in a proper solvent. For the post-irradiation, the respective polymer was dissolved in 0.5 mL solvent, freed from oxygen by purging with nitrogen for 2 minutes and placed into the sample holder, which was held at a constant temperature. Afterwards the post-irradiated polymer was dried under air and used without further purification for SEC-ESI-MS measurements.

Table 7.1.: Polymerization parameters.

Parameters	Section 3.2	Section 3.3	Section 3.4	Chapter 5
Monomer	MMA	MMA	various [*1]	PMA
Frequency [Hz]	200	200	200	100
Energy [mJ/pulse]	0.35	0.35	0.35	various [*3]
Pulses	90000	90000	90000	90000
Temperature [°C]	-2	-2	a.t.	various [*4]
Purification [*2]	yes	yes	yes	no

[*1] MMA, nBMA, tBMA, BnMA
[*2] pMMA: n-hexane, p(nBMA), p(tBMA): methanol:water (90:10), p(BnMA): water
[*3] temperature study: 0.35 mJ/pulse, energy study: 0.35-2.5 mJ/ pulse
[*4] temperature study: 0-60 °C, energy study: a.t.
[*5] low energy was set by the program of the laser and measured on top of the sample holder with an energy power meter Energy Max PC power meter (Coherent).

Table 7.2.: Post-Irradiation parameters.

Parameters	Section 3.2	Section 3.3	Section 3.4
Polymer amount [mg]	15	5	5
Frequency [Hz]	200	100	200
Energy [mJ/pulse]	6 [*1]	see appendix	6 [*1]
Pulses	90000	see appendix	90000
Temperature [°C]	-2	a.t.	a.t.

[*1] high energy was set by the program of the laser and not measured with an energy power meter.

7.2.4 Wavelength-Variable PLP and Post-Irradiation Experiments with Tunable Laser

The PLP samples were all prepared with a concentration of $c_{Photoinitiator}$ = 5·10^{-3} mol·L^{-1} in monomer (sample volume ~ 0.5 mL) and freed from oxygen by purging with nitrogen for 2 minutes. Subsequently, the samples were individually placed into the sample holder and irradiated at ambient temperature. The polymerization and post-irradiation of the polymers were carried out by a tunable laser system (SplitLight 600 OPO, λ = 270-650 nm) with low laser energy of 0.35 mJ/pulse for the polymerization and high energies for the post-irradiation of the polymers. Tunable UV-Vis laser light was generated by an Innolas Tunable Laser System SpitLight 600 OPO. An optical parametric oscillator (OPO) was pumped with a diode pumped Nd:YAG laser (repetition rate 100 Hz). The energy output of the laser was regulated by an attenuator (polarizer). As shown in Figure 7.3 the laser beam is redirected by a prism and enters the sample in a custom-made sample holder from below. The sample holder consists of a metal block with a vertical cylindrical hole (0.71 cm diameter), fixing the crimped glass vials during experiments. The energy of the incident laser pulses was measured via an Energy Max PC power meter (Coherent). The polymerizations were performed at low laser energies and the post-irradiation of the polymers with high laser energies (high overall energy input). For the post-irradiation, the respective polymer was dissolved in 0.5 mL solvent, freed from oxygen by purging with nitrogen for 2 minutes, placed into the sample holder and irradiated at ambient temperature. Afterwards the post-irradiated polymer was dried under air and used without further purification for SEC-ESI-MS measurements.
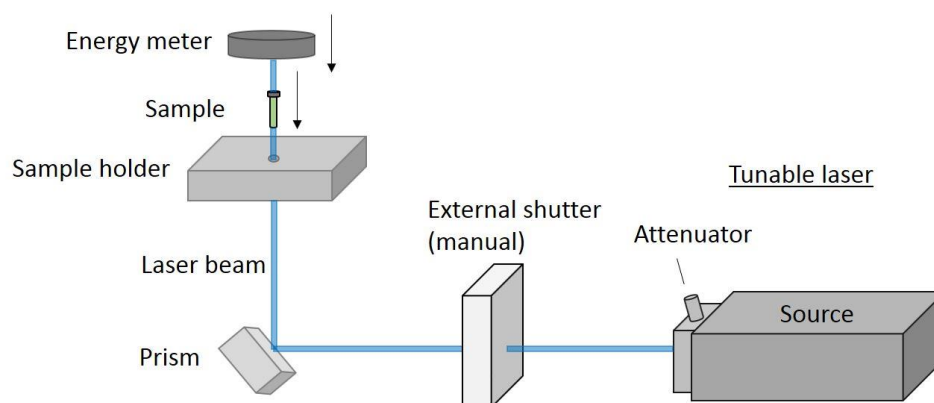
Figure 7.3.: Experimental setup for the measurement of the laser energy. Adapted with permission from reference [188].

Table 7.3.: Polymerization parameters.

Parameters	Chapter 4	Chapter 5
Monomer	MMA	various [*1]
Frequency [Hz]	100	100
Energy [mJ/pulse]	see appendix	see appendix
Pulses	see appendix	90000
Temperature [°C]	a.t.	a.t.
Purification	no	no

[*1] MMA, EMA, nPMA, iPMA, nBMA, tBMA, DMAEMA, BnMA

Table 7.4.: Post-Irradiation parameters.

Parameters	Section 3.3
Polymer amount [mg]	5
Frequency [Hz]	100
Energy [mJ/pulse]	see appendix
Pulses	see appendix
Temperature [°C]	a.t.

Calibration Procedure for Constant Photon Count

The transmittance of the crimped photo glass vials that were used for photoreactions with the tunable laser system was determined experimentally using the tunable laser setup. The transmittance of the crimped quartz glass vials was used as received from the company Qsil GmbH (refer to Table 7.5 and Figure 7.4). Measurement of the energy of laser pulses at a constant energy output was carried out directly above the sample holder, first without a crimped photo

glass vial in the sample holder and subsequently with an empty crimped photo glass vial in the sample holder. The top part of the crimped photo glass vial was removed for these measurements (Figure 7.5). Thus, only the absorbance of the bottom of the crimped photo glass vial is detected. The described procedure was performed for three individual crimped photo glass vials to account for variability between the vials. The obtained averaged values are listed in Table 7.5.

Table 7.5.: Transmittance of crimped photo glass vials and crimped quartz glass vials. Adapted with permission from reference [184]. Copyright (2017) American Chemical Society (ACS).

λ / nm	Crimped Photo Glass Vials		Crimped Quartz Glass Vials
	Mean Transmittance / %	Mean Deviation / %	Transmittance / %
270	0	0	91.8
275	0	0	91.8
280	0	0	91.9
285	13.4	0.2	92.0
290	19.7	0.6	92.1
295	30.3	0.5	92.1
300	37.7	1.0	92.2
305	45.6	0.5	92.2
310	47.5	1.0	92.3
315	51.1	0.6	92.3
320	56.3	1.2	92.3
325	58.9	0.8	92.4
330	61.0	0.9	92.4
335	62.9	0.9	92.4
340	60.4	0.9	92.4
345	64.5	1.6	92.4
350	60.4	1.1	92.5
355	62.1	0.9	92.5
360	65.1	0.3	92.5
370	65.9	1.2	92.5
380	66.3	1.2	92.5
390	70.8	0.4	92.5
400	66.9	0.9	92.5
410	68.0	1.9	-
430	75.3	0.6	-
450	76.6	0.8	-
470	77.6	0.5	-
490	79.1	0.5	-
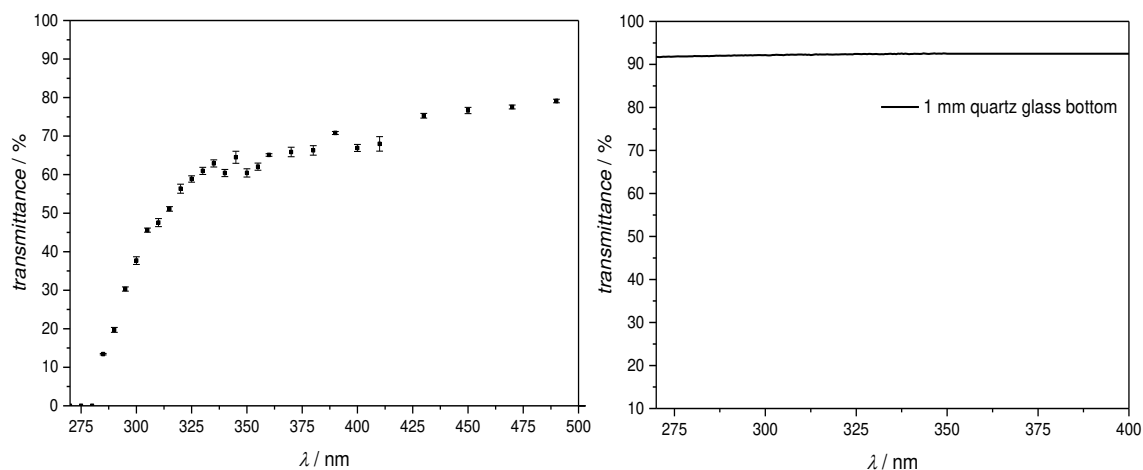
Figure 7.4.: Transmittance of crimped photo glass vials (left side) and crimped quartz glass vials (right side) dependent on irradiation wavelength. Adapted with permission from reference [184]. Copyright (2017) American Chemical Society (ACS).

Figure 7.5.: Left: vial after removal of the top part; right: crimped photo glass vial. Adapted with permission from reference [184]. Copyright (2017) American Chemical Society (ACS).

7.2.5 Polymerizations with LEDs

Polymerization samples were prepared with a photoinitiator concentration of $c_{PI} = 1 \cdot 10^{-3}$ mol·L^{-1} or $5 \cdot 10^{-3}$ mol·L^{-1} in methyl methacrylate (0.5 mL) and freed from oxygen by purging with nitrogen. Polymerizations were conducted with LEDs as light sources (λ = 385, 400, 420, 435 and 450 nm) for 1 hour. After polymerization, the remaining monomer was evaporated and the conversion was determined by gravimetry (average of 3 measurements per irradiation wavelength). The forward currents of the LEDs were adjusted, according to the specification sheets, to yield a photon flux of $4.27 \cdot 10^{16}$ s^{-1} at every wavelength.

7.2.6 Hydrogenation Experiments of the Post-Irradiated Polymers

The hydrogenation reactions of the post-irradiated polymers were performed in a high pressure laboratory reactor (Berghof, BR-100) with a maximum operating pressure of 200 bar. The samples (2MB, 3MB, 4MB and 2,4DMB) were prepared with 15 mg post-irradiated polymer and 3 mg Pd on activated carbon as the catalysts, diluted in a mixture of ethyl acetate/ethanol (1:1 v/v). The reactions were performed with a hydrogen pressure of 45 bar at ambient temperature for 4.5 h. After hydrogenation, the samples were filtered to remove the catalyst and the solvent was evaporated.

7.3 Instrumentation

7.3.1 Size Exclusion Chromatography coupled with Electrospray Ionization Mass Spectrometry (SEC-ESI-MS).

Spectra were recorded on a Q Exactive (Orbitrap) mass spectrometer (Thermo Fisher Scientific, San Jose, CA, USA) equipped with an HESI II probe. The instrument was calibrated in the m/z range 74-1822 using premixed calibration solutions (Thermo Scientific). A constant spray voltage of 4.6 kV, a dimensionless sheath gas of 8, and a dimensionless auxiliary gas flow rate of 2 were applied. The capillary temperature and the S-lens RF level were set to 320 °C and 62.0, respectively. The Q Exactive was coupled to an UltiMate 3000 UHPLC System (Dionex, Sunnyvale, CA, USA) consisting of a pump (LPG 3400SD), autosampler (WPS 3000TSL), and a thermostated column department (TCC 3000SD). Separation was performed on two mixed bed size exclusion chromatography columns (Polymer Laboratories, Mesopore 250 × 4.6 mm, particle diameter 3 μm) with precolumn (Mesopore 50 × 4.6 mm) operating at 30 °C. THF at a flow rate of 0.30 mL·min^{-1} was used as eluent. The mass spectrometer was coupled to the column in parallel to a RI-detector (RefractoMax520, ERC, Japan) in a setup described earlier. 0.27 mL·min^{-1} of the eluent were directed through the RI-detector and 30 μL·min^{-1} infused into the electrospray source after postcolumn addition of a 100 μM solution of sodium iodide in methanol at 20 μL·min^{-1} by a micro-flow HPLC syringe pump (Teledyne ISCO, Model 100DM). A 50 μL or 100 μL aliquot of a polymer solution with a concentration of 2 mg·mL^{-1} was injected into the HPLC system.

7.3.2 Electrospray Ionization Mass Spectrometry (ESI-MS)

Mass spectra were recorded on a Q Exactive (Orbitrap) mass spectrometer (Thermo Fisher Scientific, San Jose, CA, USA) equipped with an HESI II probe. The instrument was calibrated in the *m/z* range 74-1822 using premixed calibration solutions (Thermo Scientific). A constant spray voltage of 4.7 kV and a dimensionless sheath gas of 5 were applied. The capillary temperature and the S-lens RF level were set to 320 °C and 62.0, respectively. The samples were dissolved with a concentration of 0.05 mg·mL^{-1} in a mixture of THF and MeOH (3:2) containing 100 µmol of sodium trifluoroacetate and infused with a flow of 5 µL·min^{-1}.

7.3.3 Size Exclusion Chromatography (SEC)

Size exclusion chromatography (SEC) measurements were performed on a Polymer Laboratories (Varian) PL-GPC 50 Plus Integrated System, comprising an autosampler, a PLgel 5 mm bead-size guard column (50 x 7.5 mm), one PLgel 5 mm Mixed E column (300 x 7.5 mm), three PLgel 5 mm Mixed C columns (300 x 7.5 mm), and a differential refractive index detector using THF as the eluent at 35°C with a flow rate of 1 mL· min^{-1}. The SEC system was calibrated using linear poly(styrene) standards ranging from 370 g·mol^{-1} to 2.52·10^6 g·mol^{-1} and linear poly(methyl methacrylate) standards ranging from 800 g·mol^{-1} to 1.6·10^6 g·mol^{-1}.The samples were prepared with a 2 mg·mL^{-1} concentration.

7.3.4 UV-Vis Spectroscopy

Investigation of Methyl-Substituted Benzoin-Type Photoinitiators

UV-Vis spectra of the methyl-substituted photoinitiators were recorded on an Epoch 2 microplate spectrophotometer with Gen5 Data Analysis as software. All measurements were carried out in methanol in a disposable plastic UV 96-well-plate with a thickness of 5 mm at ambient temperature. UV-Vis spectra of 4MB- and TriMB-initiated poly(methyl methacrylate) for DFT calculations were recorded on a Shimadzu UV-3101PC UV-Vis-NIR scanning spectrophotometer in acetonitrile.

Wavelength-Dependent Photochemistry of Oxime Esters

UV-Vis spectra of OXE01 and OXE02 were recorded on a Shimadzu UV-2102 PC UV-vis scanning spectrophotometer in acetonitrile. LED emission spectra were recorded on a J&M Tidas (J&M, Aalen, Germany) fiber-optics, diode array spectrometer.

Photoinduced Generation of Lactone Chain Termini

UV-Vis spectrum of Irgacure 2959 was recorded on a Cary 300 Bio spectrophotometer (Varian) featuring a thermostated (298 K) sample cell holder in methanol.

7.3.5 NMR and photo-CIDNP Spectroscopy

Investigation of Methyl-Substituted Benzoin-Type Photoinitiators

Proton nuclear magnetic resonance (^{1}H NMR) spectra of the small molecules were recorded on a Bruker AM 400 (400 MHz) spectrometer. Chemical shifts (δ) are expressed in parts per million (ppm) and calibrated on characteristic solvent signals (CDCl$_3$) as internal standards. All coupling constants are absolute values and J values are expressed in Hertz (Hz). The description of signals includes: s = singlet, bs = broad singlet, d = doublet, dd = double doublet, t = triplet, q = quartet, m = multiplet.

^{1}H NMR and photochemically induced dynamic nuclear polarization (photo-CIDNP) experiments of the polymers were recorded on a 200 MHz Bruker AVANCE DPX spectrometer. Irradiation was carried out by using a frequency-tripled Quantel Brilliant B Nd:YAG laser (355 nm, 70-80 mJ/pulse, 20 Hz, pulse duration 8 ns). A pulse sequence of 'presaturation–laser flash–RF detection pulse (2 µs)–free induction decay' was used. "Dummy" CIDNP spectra without the application of a laser pulse were recorded to ensure an effective suppression of the parent NMR spectra. Chemical shifts (δ) are reported in ppm relative to tetramethylsilane (TMS) using the residual deuterated solvent signals as an internal reference (CD$_3$CN, δ_H = 1.94 ppm).

Wavelength-Dependent Photochemistry of Oxime Esters

^{1}H NMR and photo-CIDNP experiments were carried out with a 200 MHz Bruker AVANCE DPX spectrometer equipped with a custom-made CIDNP probe head. A Quantel Nd:YAG Brilliant B (355 nm, ~70 mJ/pulse, pulse length ~8-10 ns) operating at 20 Hz served as light source. A pulse sequence of 'presaturation–laser flash–RF detection pulse (2 µs)–free induction decay' was used. "Dummy" CIDNP spectra without the application of a light pulse were recorded to ensure an effective suppression of the parent NMR spectra. Chemical shifts (δ) are reported in ppm relative to tetramethylsilane (TMS) using the residual deuterated solvent signal as an internal reference (CD$_3$CN, δ_H = 1.94 ppm).

Photoinduced Generation of Lactone Chain Termini

Carbon nuclear magnetic resonance (^{13}C NMR) spectra of the polymers were recorded on a Bruker AM 400 (100 MHz) spectrometer. The samples were dissolved in CDCl$_3$ and measured with 5120 scans. Chemical shifts (δ) are expressed in parts per million (ppm) and calibrated on characteristic solvent signals (CDCl$_3$) as internal standards

7.3.6 Computational Details

Investigation of Methyl-Substituted Benzoin-Type Photoinitiators

The S_0 singlet ground state and the T_1 triplet state were computed by DFT calculations (B3LYP)[168–170,197] with inclusion of Grimme's dispersion interaction correction D3.[171] The SVP basis set was used for this purpose.[172] Standard 'tight' optimization criteria were applied. All minima were checked by frequency analysis to be true minima on the potential energy surface. Time-dependent DFT was used for the vertical excitations applying the CAM-B3LYP/TZVP[174,175] method. The optimization of the first singlet excited S_1 state was performed with TD-B3LYP-D3/SVP and the single point energies were recomputed by TD-CAM-B3LYP/TZVP for the S_0 and T_1. All computations were performed with the program *ORCA*.[198] Orbitals were depicted with *gabedit*[199] applying contour values of 0.05 a.u.

Wavelength-Dependent Photochemistry of Oxime Esters

The ground state geometries of different conformations of OXE01 and OXE02 were optimized in the gas phase with the PBE0 – D3BJ /6-31+G(d,p) method.[200–203] The hexyl group in OXE01 was kept fixed in an all-*trans* conformation. Both *E*- and *Z*-isomers were used as starting geometries. The harmonic frequencies of the compounds confirmed the minima for all conformations. Vertical excitations were calculated with the CAM-B3LYP[168,197] functional and the triple-zeta basis set 6-311++G(2d,p).[203,204] The solvent acetonitrile was included via the Polarizable Continuum Model in its integral evaluation formalism (IEF-PCM).[205] All computations were performed with the program Gaussian09.[206]

Photoinduced Generation of Lactone Chain Termini

The polymer model used for the calculations of the energetics and barriers includes two monomer units of the propyl (R3) and butyl (R4) substituents, respectively. Optimizations of the geometries were carried out by Density Functional Theory (DFT) using the M06-2X functional.[207]

Grimme's dispersion correction[171] with Becke-Johnson damping[201] (D3BJ) was applied to account the dispersion interaction of the alkyl chains. Harmonic model frequency calculations were performed to characterize the geometries as minima at the potential energy surface and to receive the Gibbs free energies at room temperature (298 K). The aug-cc-pVDZ basis set was used for optimizations and frequency calculations. To improve the energetics, the larger aug-cc-pVTZ basis set[208,209] was used for single point energies and for the correction of Gibbs free energies by adding the electronic energy difference of large and small basis set. To model the monomer surrounding, the IEF-PCM solvation model[210] in DMSO was selected. The program Gaussian09[206] was used throughout this study.

8

Appendix

8.1 Investigation of Methyl-Substituted Benzoin-Type Photoinitiators at 351 nm

8.1.1 SEC-ESI-MS Measurements

Figure 8.1.: High resolution SEC-ESI mass spectra of the polymer initiated by 3MB (zoom into one repeating unit), synthesized at low laser energies (0.35 mJ/pulse, 200 Hz, red spectrum), post-irradiated at higher laser energies (6 mJ/pulse, 200 Hz, blue spectrum), and hydrogenated (gray spectrum). Adapted with permission from reference [165]. Copyright (2015) American Chemical Society (ACS).
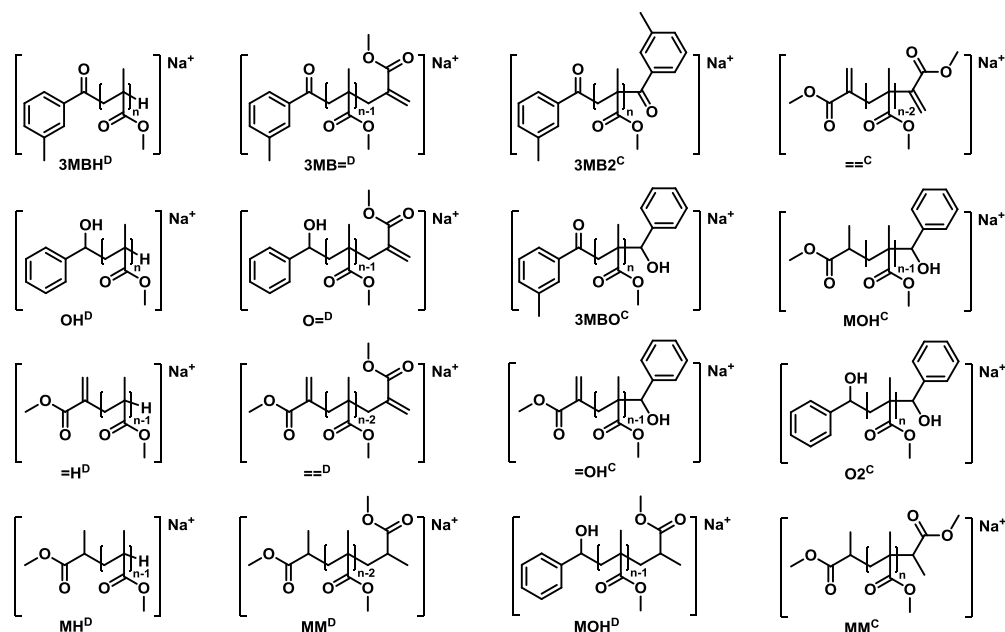
Scheme 8.1.: Disproportionation and combination products of the polymer initiated by 3MB, at low laser energies (0.35 mJ/pulse, 200 Hz), post-irradiated at higher laser energies (6 mJ/pulse, 200 Hz) and hydrogenation experiments, as detected by SEC-ESI-MS. Adapted with permission from reference [165]. Copyright (2015) American Chemical Society (ACS).

Table 8.1.: Overview of the signals of the PLP generated polymers (0.35 mJ/pulse), PLI (6 mJ/pulse) as well as hydrogenated polymers (3MB-initiated pMMA) as detected by SEC-ESI-MS (R = 55000). Adapted with permission from reference [165]. Copyright (2015) American Chemical Society (ACS).

Species	Ionization	$(m/z)^{theo}$/Da	$(m/z)^{exp}$/Da	$\Delta(m/z)$
$==^D$	Na^+	1107.53522	1107.53631	0.0011
$=H^D$	Na^+	1109.55082	1109.54921	0.0016
MM/MH^D	Na^+	1111.56652	1111.55443	0.0121
$=OH^C$	Na^+	1115.54032	1115.53702	0.0033
$O2^C$	H^+	1115.57912	1115.56289	0.0162
MOH^C	Na^+	1117.55592	1117.55786	0.0019
$O=^D$	Na^+	1129.55592	1129.55606	0.0001
OH^D	Na^+	1131.57152	1131.57065	0.0009
MOH^D	Na^+	1131.57162	1131.57443	0.0028
$3MB=^D$	Na^+	1141.55592	1141.55568	0.0002
$3MBH^D$	Na^+	1143.57152	1143.57038	0.0011
$3MBO^C$	Na^+	1149.56102	1149.55877	0.0023
$O2^C$	Na^+	1137.56102	1137.56042	0.0006
$3MB2^C$	Na^+	1161.56102	1161.56018	0.0008
$==^C$	Na^+	1193.57152	1193.57384	0.0023
MM^C	Na^+	1197.60282	1197.60696	0.0041

Figure 8.2.: High resolution SEC-ESI mass spectra of the polymer initiated by 2MB (zoom into one repeating unit), synthesized at low laser energies (0.35 mJ/pulse, 200 Hz, red spectrum), post-irradiated at higher laser energies (6 mJ/pulse, 200 Hz, blue spectrum), and hydrogenated (gray spectrum). Adapted with permission from reference [165]. Copyright (2015) American Chemical Society (ACS).
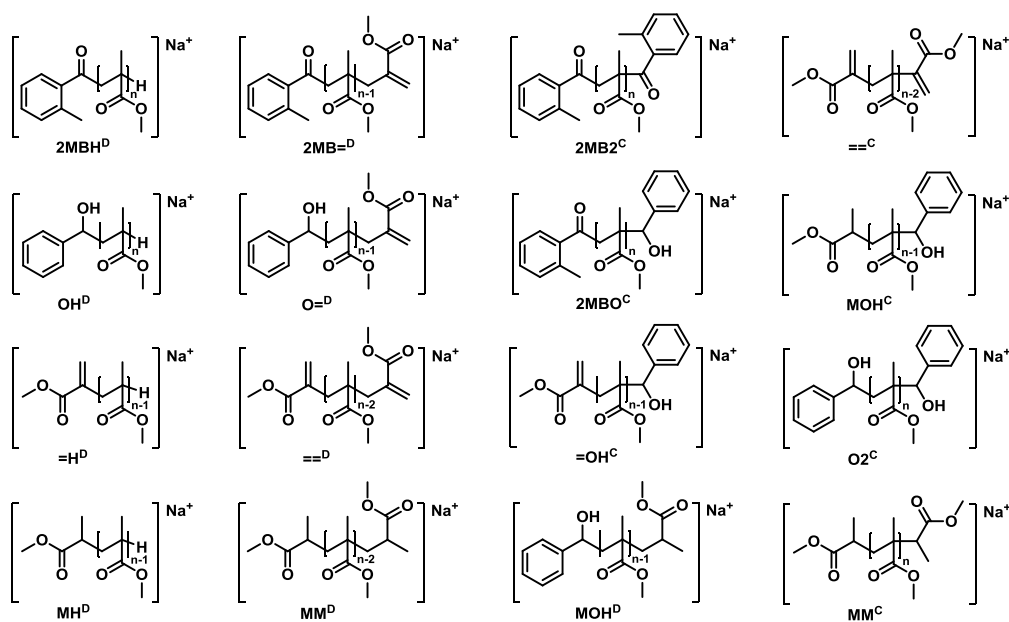
Scheme 8.2.: Disproportionation and combination products of the polymer initiated by 2MB, at low laser energies (0.35 mJ/pulse, 200 Hz), post-irradiated at higher laser energies (6 mJ/pulse, 200 Hz) and hydrogenation experiments, as detected by SEC-ESI-MS. Adapted with permission from reference [165]. Copyright (2015) American Chemical Society (ACS).

Table 8.2.: Overview of the signals of the PLP generated polymers (0.35 mJ/pulse), PLI (6 mJ/pulse) as well as hydrogenated polymers (2MB-initiated pMMA) as detected by SEC-ESI-MS (R = 75000). Adapted with permission from reference [165]. Copyright (2015) American Chemical Society (ACS).

Species	Ionization	$(m/z)^{theo}$/Da	$(m/z)^{exp}$/Da	$\Delta(m/z)$
$==^D$	Na^+	707.3255	707.3215	0.0040
$=H^D$	Na^+	709.3411	709.3420	0.0009
MM/MH^D	Na^+	711.3568	711.3561	0.0007
$=OH^C$	Na^+	711.3568	711.3561	0.0015
$O2^C$	H^+	715.3306	715.3310	0.0004
MOH^C	Na^+	715.3694	715.3679	0.0015
$O=^D$	Na^+	717.3456	717.3478	0.0022
OH^D	Na^+	729.3462	729.3476	0.0014
MOH^D	Na^+	731.3618	731.3624	0.0006
$2MB=^D$	Na^+	731.3619	731.3629	0.0010
$2MBH^D$	Na^+	741.3462	741.3475	0.0013
$2MBO^C$	Na^+	743.3618	743.3618	0.0000
$O2^C$	Na^+	749.3513	749.3513	0.0000
$2MB2^C$	Na^+	737.3513	737.3528	0.0015
$==^C$	Na^+	761.3513	761.3528	0.0015
MM^C	Na^+	793.3618	793.3668	0.0050
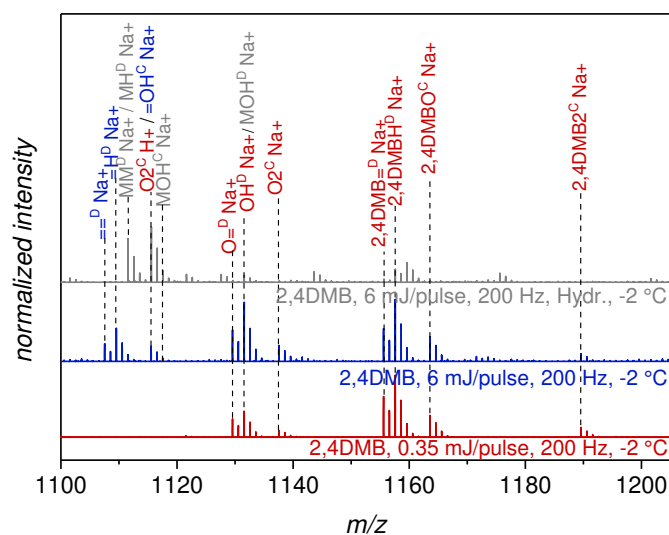
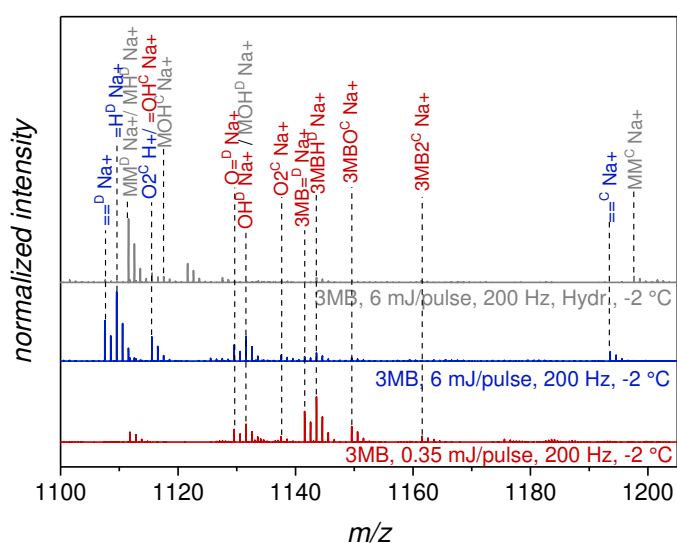**Figure 8.3.:** High resolution SEC-ESI mass spectra of the polymer initiated by 2,4DMB (zoom into one repeating unit), synthesized at low laser energies (0.35 mJ/pulse, 200 Hz, red spectrum), post-irradiated at higher laser energies (6 mJ/pulse, 200 Hz, blue spectrum), and hydrogenated (gray spectrum). Adapted with permission from reference [165]. Copyright (2015) American Chemical Society (ACS).
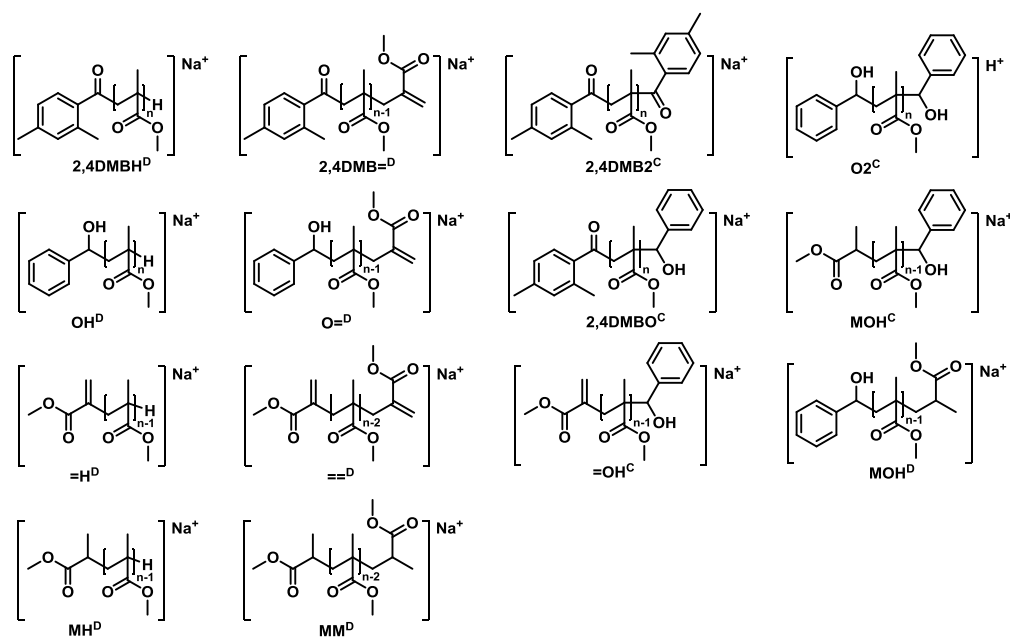
Scheme 8.3.: Disproportionation and combination products of the polymer initiated by 2,4DMB, at low laser energies (0.35 mJ/pulse, 200 Hz), post-irradiated at higher laser energies (6 mJ/pulse, 200 Hz) and hydrogenation experiments, as detected by SEC-ESI-MS. Adapted with permission from reference [165]. Copyright (2015) American Chemical Society (ACS).

Table 8.3.: Overview of the signals of the PLP generated polymers (0.35 mJ/pulse), PLI (6 mJ/pulse) as well as hydrogenated polymers (2,4DMB-initiated pMMA) as detected by SEC-ESI-MS (R = 55000). Adapted with permission from reference [165]. Copyright (2015) American Chemical Society (ACS).

Species	Ionization	$(m/z)^{theo}$/Da	$(m/z)^{exp}$/Da	$\Delta(m/z)$
$==^D$	Na$^+$	1107.5352	1107.5346	0.0006
$=H^D$	Na$^+$	1109.5508	1109.5475	0.0033
MM/MH^D	Na$^+$	1111.5665	1111.5690	0.0025
$=OH^C$	Na$^+$	1115.5403	1115.5397	0.0006
O2^C	H$^+$	1115.5791	1115.5782	0.0010
MOH^C	Na$^+$	1117.5559	1117.5599	0.0040
O=^{D}	Na$^+$	1129.5559	1129.5575	0.0016
OH^D	Na$^+$	1131.5715	1131.5678	0.0037
MOH^D	Na$^+$	1131.5716	1131.5720	0.0004
2,4DMB=^{D}	Na$^+$	1155.5716	1155.5724	0.0008
2,4DMBH^D	Na$^+$	1157.5872	1157.5869	0.0003
2,4DMBO^C	Na$^+$	1163.5767	1163.5735	0.0032
O2^C	Na$^+$	1137.5610	1137.5618	0.0008
2,4DMB2^C	Na$^+$	1189.5923	1189.5889	0.0035
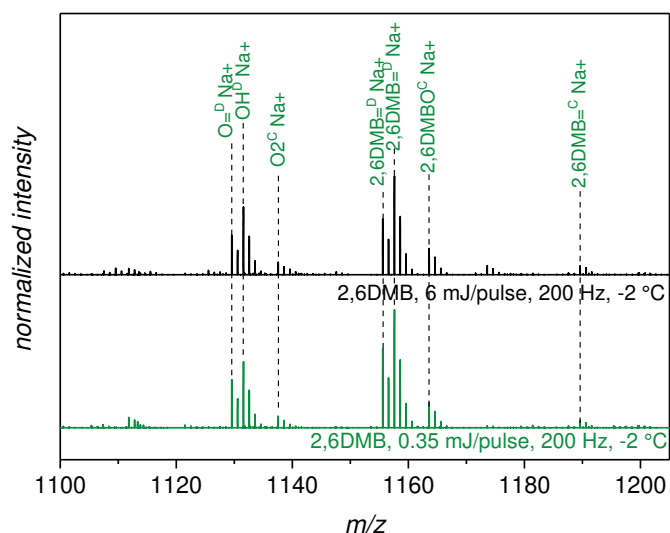
Figure 8.4.: High resolution SEC-ESI mass spectra of the polymer initiated by 2,6DMB (zoom into one repeating unit), at low laser energies (0.35 mJ/pulse, 200 Hz, green spectrum) and post-irradiated at higher laser energies (6 mJ/pulse, 200 Hz, black spectrum). Adapted with permission from reference [165]. Copyright (2015) American Chemical Society (ACS).
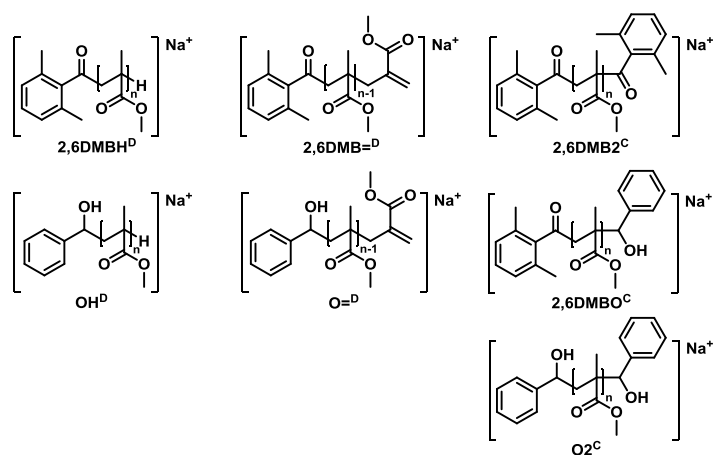
Scheme 8.4.: Disproportionation and combination products of the polymer initiated by 2,6DMB, at low laser energies (0.35 mJ/pulse, 200 Hz), and post-irradiated at higher laser energies (6 mJ/pulse, 200 Hz), as detected by SEC-ESI-MS. Adapted with permission from reference [165]. Copyright (2015) American Chemical Society (ACS).

Table 8.4.: Overview of the signals of the PLP generated polymers (0.35 mJ/pulse) and PLI polymers (6 mJ/pulse) (2,6DMB-initiated pMMA), as detected by SEC-ESI-MS (R = 55000). Adapted with permission from reference [165]. Copyright (2015) American Chemical Society (ACS).

Species	Ionization	$(m/z)^{theo}$/Da	$(m/z)^{exp}$/Da	$\Delta(m/z)$
O=^{D}	Na$^+$	1129.5559	1129.5588	0.0029
OH^D	Na$^+$	1131.5715	1131.5734	0.0019
O2^C	Na$^+$	1137.5610	1137.5633	0.0022
2,6DMB=^{D}	Na$^+$	1155.5716	1155.5739	0.0023
2,6DMBH^D	Na$^+$	1157.5872	1157.5885	0.0013
2,6DMBO^C	Na$^+$	1163.5767	1163.5793	0.0026
2,6DMB2^C	Na$^+$	1189.5923	1189.5928	0.0005
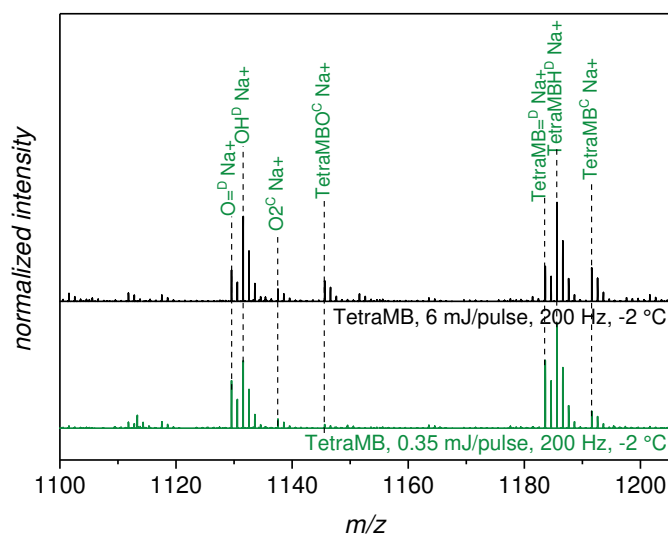
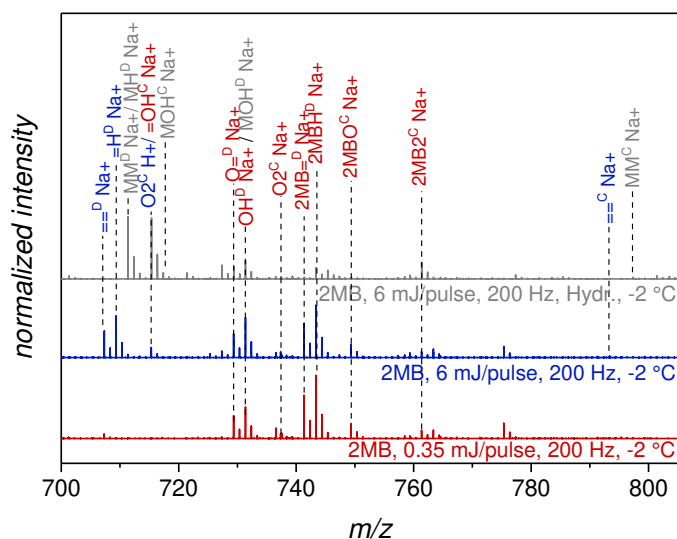**Figure 8.5.:** High resolution SEC-ESI mass spectra of the polymer initiated by TetraMB (zoom into one repeating unit), at low laser energies (0.35 mJ/pulse, 200 Hz, green spectrum) and post-irradiated at higher laser energies (6 mJ/pulse, 200 Hz, black spectrum). Adapted with permission from reference [165]. Copyright (2015) American Chemical Society (ACS).
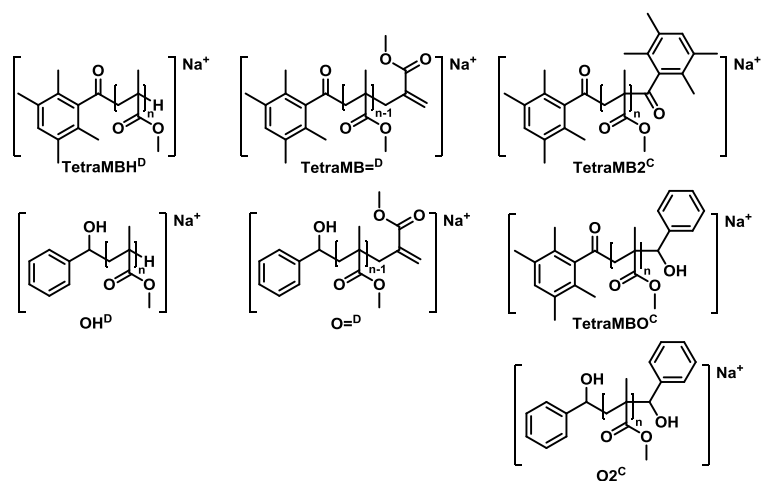
Scheme 8.5.: Disproportionation and combination products of the polymer initiated by TetraMB, at low laser energies (0.35 mJ/pulse, 200 Hz) and post-irradiated at higher laser energies (6 mJ/pulse, 200 Hz), as detected by SEC-ESI-MS. Adapted with permission from reference [165]. Copyright (2015) American Chemical Society (ACS).

Table 8.5.: Overview of the signals of the PLP generated polymers (0.35 mJ/pulse) and PLI polymers (6 mJ/pulse) (TetraMB-initiated pMMA) as detected by SEC-ESI-MS (R = 55000). Adapted with permission from reference [165]. Copyright (2015) American Chemical Society (ACS).

| Species	Ionization	$(m/z)^{theo}$/Da	$(m/z)^{exp}$/Da	$\Delta(m/z)$
O=^{D}	Na$^+$	1129.5559	1129.5557	0.0002
OH^D	Na$^+$	1131.5715	1131.5703	0.0012
O2^C	Na$^+$	1137.5610	1137.5598	0.0012
TetraMB2^C	Na$^+$	1145.6025	1145.5993	0.0032
TetraMB=^{D}	Na$^+$	1183.6029	1183.6093	0.0064
TetraMBH^D	Na$^+$	1185.6185	1185.6105	0.0080
TetraMBO^C	Na$^+$	1191.6080	1191.6058	0.0022

Figure 8.6.: High resolution SEC-ESI mass spectra of the polymer initiated by PentaMB (zoom into one repeating unit), at low laser energies (0.35 mJ/pulse, 200 Hz, green spectrum) and post-irradiated at higher laser energies (6 mJ/pulse, 200 Hz, black spectrum). Adapted with permission from reference [165]. Copyright (2015) American Chemical Society (ACS).
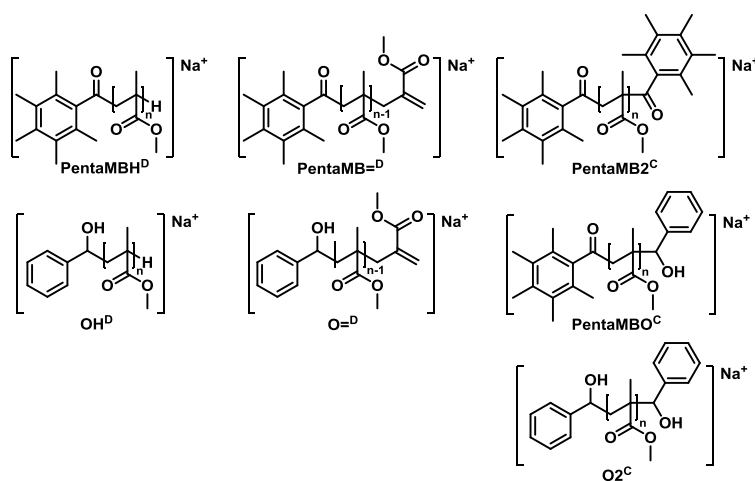
Scheme 8.6.: Disproportionation and combination products of the polymer initiated by PentaMB, at low laser energies (0.35 mJ/pulse, 200 Hz), and post-irradiated at higher laser energies (6 mJ/pulse, 200 Hz), as detected by SEC-ESI-MS. Adapted with permission from reference [165]. Copyright (2015) American Chemical Society (ACS).

Table 8.6.: Overview of the signals of the PLP generated polymers (0.35 mJ/pulse) and PLI polymers (6 mJ/pulse) (PentaMB-initiated pMMA), as detected by SEC-ESI-MS (R = 55000). Adapted with permission from reference [165]. Copyright (2015) American Chemical Society (ACS).

Species	Ionization	$(m/z)^{theo}$/Da	$(m/z)^{exp}$/Da	$\Delta(m/z)$
PentaMBO^C	Na$^+$	1105.5707	1105.5709	0.0003
O=^{D}	Na$^+$	1129.5559	1129.5542	0.0017
OH^D	Na$^+$	1131.5715	1131.5687	0.0028
O2^C	Na$^+$	1137.5610	1137.5585	0.0026
PentaMB2^C	Na$^+$	1173.6333	1173.6346	0.0014
PentaMB=^{D}	Na$^+$	1197.6180	1197.6153	0.0027
PentaMBH^D	Na$^+$	1199.6337	1199.6323	0.0013

8.1.2 NMR and photo-CIDNP Experiments
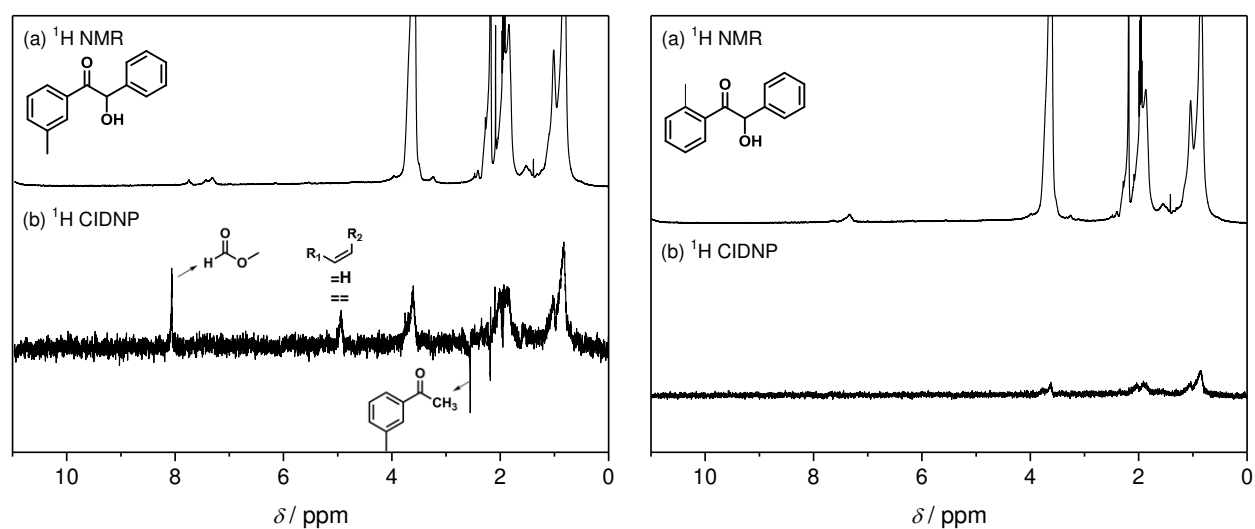
Figure 8.7.: (a) ^{1}H NMR and (b) ^{1}H CIDNP spectra of the polymers initiated by 3MB and 2MB (at a laser energy of 0.35 mJ/pulse), recorded in CD$_3$CN at about 80 mJ/pulse. Adapted with permission from reference [165]. Copyright (2015) American Chemical Society (ACS).
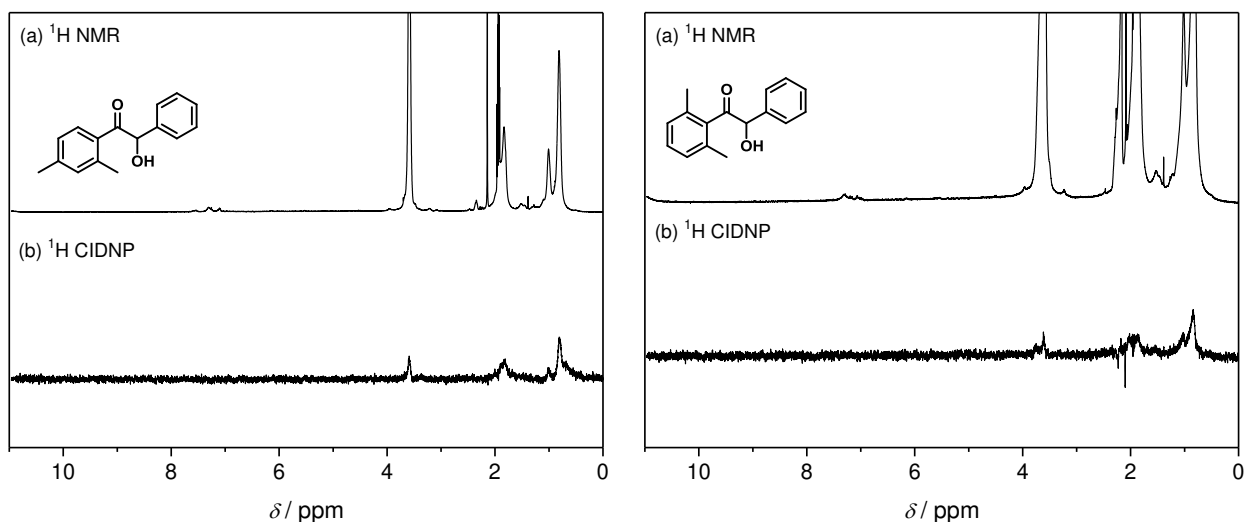
Figure 8.8.: (a) ^{1}H NMR and (b) ^{1}H CIDNP spectra of the polymers initiated by 2,4DMB and 2,6DMB (at a laser energy of 0.35 mJ/pulse), recorded in CD$_3$CN at about 80 mJ/pulse. Adapted with permission from reference [165]. Copyright (2015) American Chemical Society (ACS).
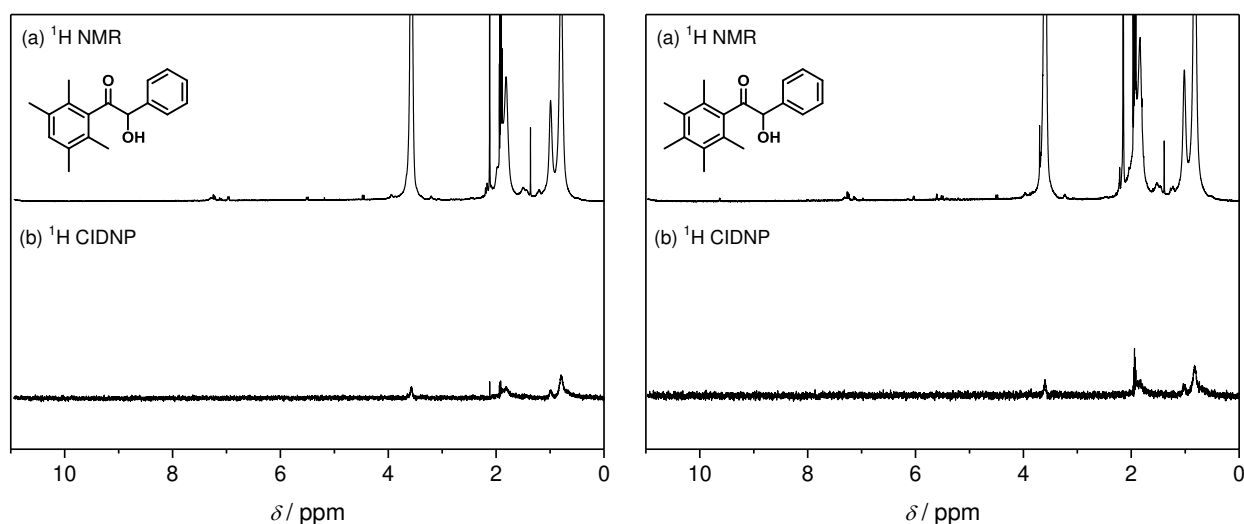
Figure 8.9.: (a) ^{1}H NMR and (b) ^{1}H CIDNP spectra of the polymer initiated by TetraMB and PentaMB (at a laser energy of 0.35 mJ/pulse), recorded in CD$_3$CN at about 80 mJ/pulse. Adapted with permission from reference [165]. Copyright (2015) American Chemical Society (ACS).

8.1.3 UV-Vis Measurements
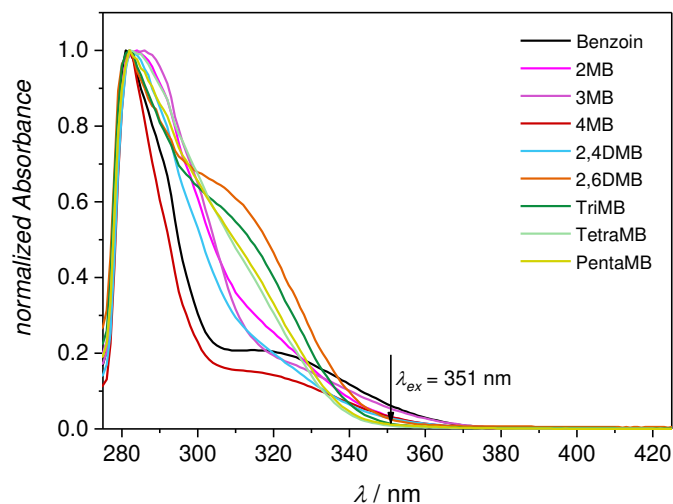
Figure 8.10. UV-Vis spectrum of the investigated photoinitiators in MeOH (c_{PI} = 1·10^{-3} M). Adapted with permission from reference [165]. Copyright (2015) American Chemical Society (ACS).

8.1.4 DFT Calculations

Table 8.7.: CAM-B3LYP vertical singlet excitations of 4MBM. Adapted with permission from reference [165]. Copyright (2015) American Chemical Society (ACS).

	S_1	S_2	S_3	S_4	S_5
λ / nm	302.5	245.4	227.9	205.6	195.0
Oscillator Strength f	0.0001	0.0123	0.4414	0.0010	0.0001
E_{rel} / eV	4.099	5.052	5.440	6.032	6.359
MOs	56a → 59a	57a → 59a	58a -> 59a	55a → 61a	55a → 59a
%	0.84	0.62	0.86	0.63	0.93
MOs		58a → 60a		55a → 64a	
%		0.31		0.19	
Main Contribution	lp($O_{C=O}$) → (C=O+π)*	π1 → (C=O+π)*	π2 → (C=O+ π)*	lp(O_{ester}) → (C=O_{ester})*	lp(O_{ester}) → (C=O+ π)*
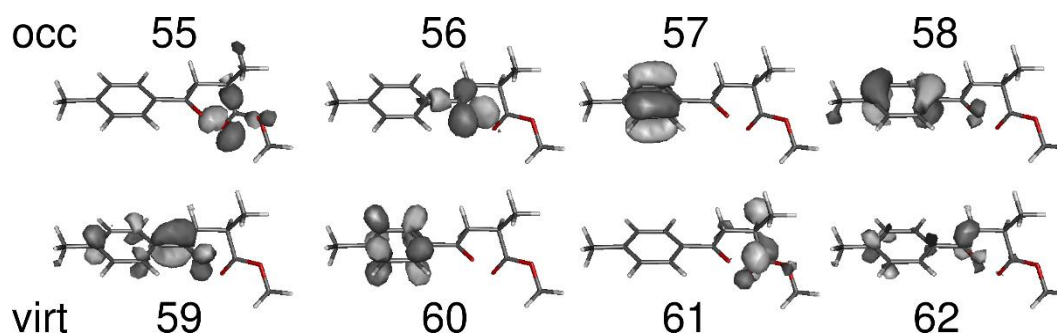
Figure 8.11.: Molecular orbitals of 4MBM in the S_0 singlet ground state. Adapted with permission from reference [165]. Copyright (2015) American Chemical Society (ACS).

Table 8.8.: CAM-B3LYP vertical singlet excitations of TriMBM. Adapted with permission from reference [165]. Copyright (2015) American Chemical Society (ACS).

	S_1	S_2	S_3	S_4	S_5
λ / nm	287.3	241.9	231.8	205.9	205.6
Oscillator Strength f	0.0029	0.0106	0.0550	0.0303	0.0100
E_{rel} / eV	4.316	5.126	5.349	6.023	6.029
MOs	64a → 67a	66a → 67a	66a → 67a	65a → 67a	63a → 70a
%	0.69	0.33	0.423	0.273	0.52
MOs	64a → 69a	65a → 67a	65a → 67a	66a → 69a	63a → 71a
%	0.17	0.23	0.30	0.17	0.15
MOs		66a → 68a		63a → 70a	
%		0.20		0.17	
Main Contribution	lp(O$_{C=O}$) → (C=O)*	$\pi 2$ → (C=O)*	$\pi 2$ → (C=O)*	$\pi 1$ → (C=O)*	lp(O$_{ester}$) → (C=O)*
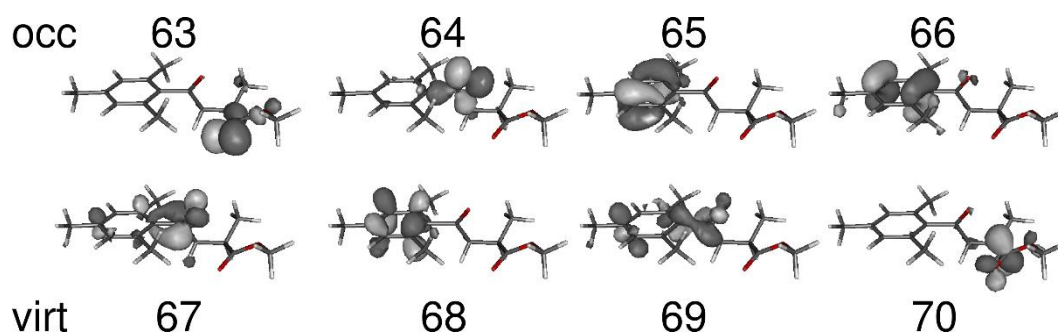
Figure 8.12.: Molecular orbitals of TriMBM in the S_0 singlet ground state. Adapted with permission from reference [165]. Copyright (2015) American Chemical Society (ACS).

Table 8.9.: Molecular orbitals of the S_1 singlet state (top) and the T_1 triplet state (bottom) of model compounds 4MBM and TriMBM. Adapted with permission from reference [165]. Copyright (2015) American Chemical Society (ACS).
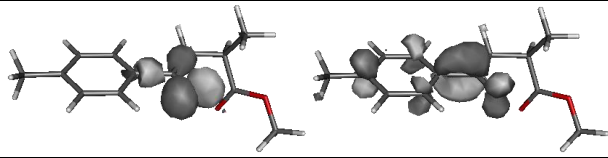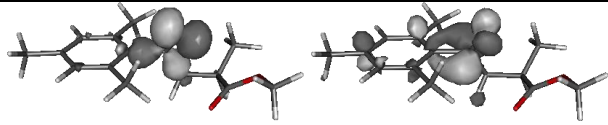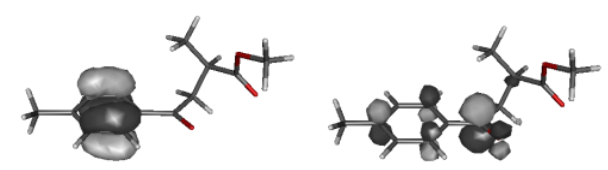
Model Compound	S_1 State	Assignment
4MBM		$^1(n\text{-}\pi^*)$
TriMBM		$^1(n\text{-}\pi^*)$
	HOMO-2 (left) – LUMO (right)	
Model Compound	**T_1 State**	**Assignment**
4MBM		$^3(\pi\text{-}\pi^*)$
TriMBM		$^3(\pi\text{-}\pi^*)$
	lower SOMO (left) – higher SOMO (right)	

Table 8.10.: S_1 Singlet excitations for all calculated polymer model compounds. Adapted with permission from reference [165]. Copyright (2015) American Chemical Society (ACS).

Polymer Model Compound	S_1 Singlet Excitation ($n\text{-}\pi^*$ Transition)		
	λ / nm	E_{rel} / eV	Oscillator Strength f
2MBM	309	4.007	0.0001
3MBM	305	4.070	0.0001
4MBM	303	4.099	0.0001
2,4DMBM	307	4.038	0.0001
2,6DMBM	287	4.315	0.0017
TriMBM	287	4.316	0.0029
TetraMBM	288	4.300	0.0006
PentaMBM	283	4.387	0.0006

8.2 Investigation of Methyl-Substituted Benzoin-Type Photoinitiators at Variable Wavelengths
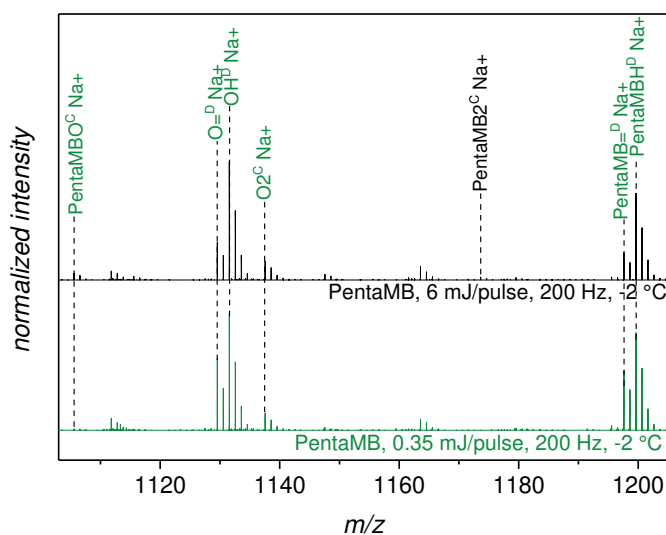
8.2.1 SEC-ESI-MS Measurements
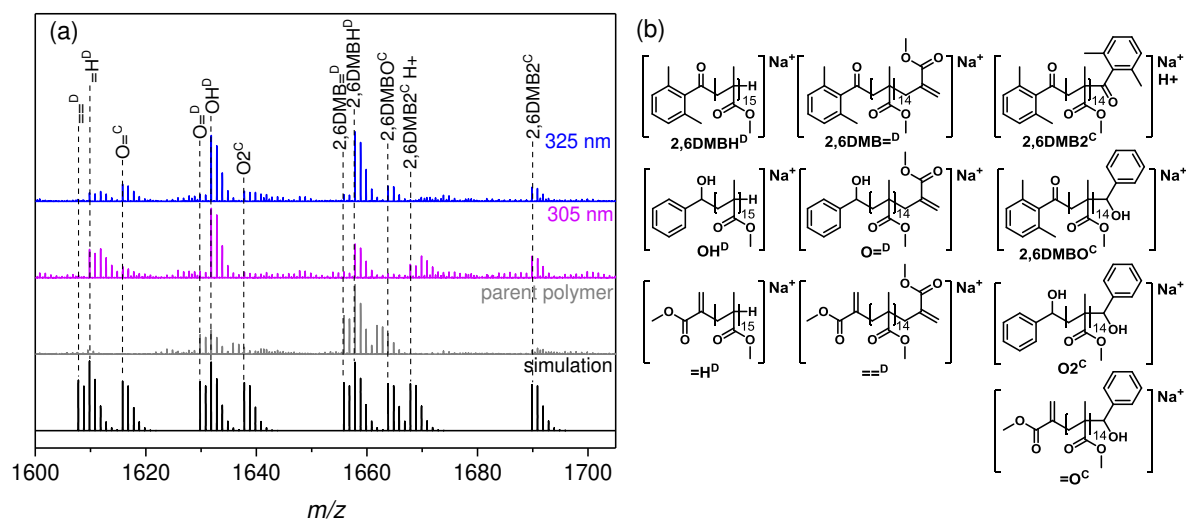
Figure 8.13: (a) High resolution SEC-ESI mass spectra of the polymer initiated by 2,6DMB (zoom into one repeating unit), synthesized at low laser energies (0.35 mJ/pulse, 200 Hz, 351 nm, gray spectrum), post-irradiated at 305 and 325 nm (100 Hz, 18 °C) at a constant photon count as well as the theoretical isotope patterns (black spectrum). (b) Disproportionation and combination products of the polymer initiated by 2,6DMB, at low laser energies (0.35 mJ/pulse, 200 Hz, 351 nm), post-irradiated with high laser energies (100 Hz, 305 and 325 nm), as detected by SEC-ESI-MS. Adapted with permission from reference [176]. Copyright (2017) American Chemical Society (ACS).

Table 8.11: Overview of the assigned signals of the polymers synthesized at low laser energies (351 nm, 0.35 mJ/pulse, 200 Hz) and post-irradiated with high laser energies (305 nm, 100 Hz) of 2,6DMB-initiated pMMA, as detected by SEC-ESI-MS with a resolution of 50000. Adapted with permission from reference [176]. Copyright (2017) American Chemical Society (ACS).

Species	Ionization	$(m/z)^{theo}$/Da	$(m/z)^{exp}$/Da	$\Delta(m/z)$
2,6DMBH[D]	Na$^+$	1657.8488	1657.8569	0.0081
2,6DMB=[D]	Na$^+$	1655.8332	1655.8500	0.0168
2,6DMB2[C]	Na$^+$	1689.8539	1689.8844	0.0305
2,6DMBO[C]	Na$^+$	1663.8383	1663.8431	0.0048
O2[C]	Na$^+$	1637.8226	1637.8410	0.0184
OH[D]	Na$^+$	1631.8332	1631.8382	0.0050
O=[D]	Na$^+$	1629.8175	1629.8160	0.0015
=H[D]	Na$^+$	1609.8124	1609.8141	0.0015
==[D]	Na$^+$	1607.7968	1607.8021	0.0053
=O[C]	Na$^+$	1615.8019	1615.8036	0.0017
2,6DMB2[C]	H$^+$	1667.8720	1667.8573	0.0147
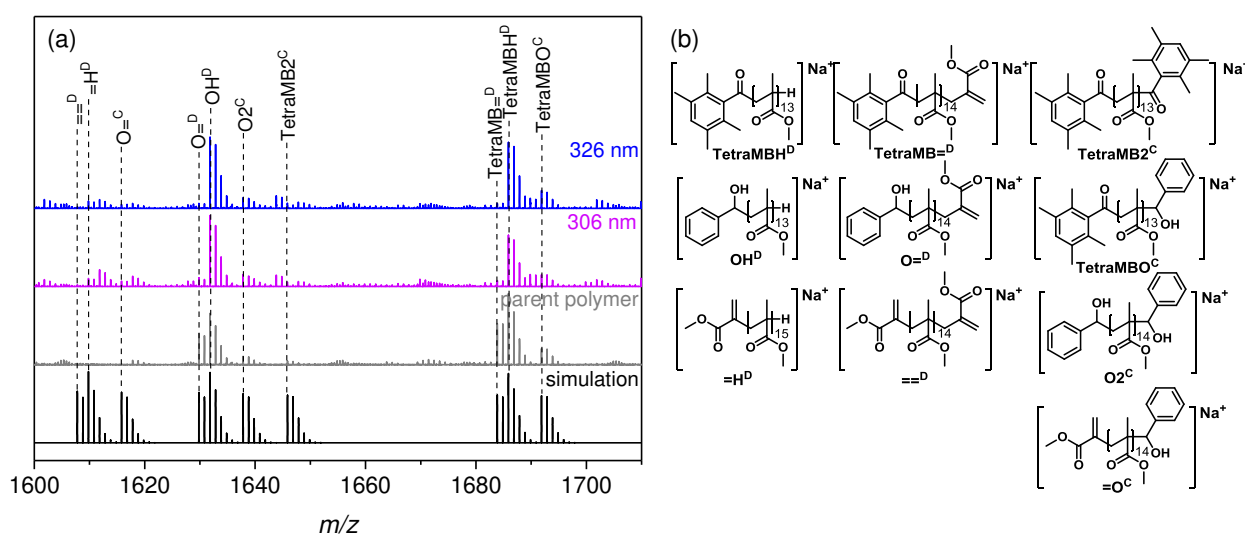
Figure 8.14.: (a) High resolution SEC-ESI mass spectra of the polymer initiated by TetraMB (zoom into one repeating unit), synthesized at low laser energies (0.35 mJ/pulse, 200 Hz, 351 nm, gray spectrum), post-irradiated at 306 and 326 nm (100 Hz, 18 °C) at a constant photon count as well as the theoretical isotope patterns (black spectrum). (b) Disproportionation and combination products of the polymer initiated by TetraMB, at low laser energies (0.35 mJ/pulse, 200 Hz, 351 nm), post-irradiated with high laser energies (100 Hz, 306 and 326 nm), as detected by SEC-ESI-MS. Adapted with permission from reference [176]. Copyright (2017) American Chemical Society (ACS).

Table 8.12.: Overview of the assigned signals of the polymers synthesized at low laser energies (351 nm, 0.35 mJ/pulse, 200 Hz) and post-irradiated with high laser energies (306 nm, 100 Hz) of TetraMB-initiated pMMA, as detected by SEC-ESI-MS with a resolution of 50000. Adapted with permission from reference [176]. Copyright (2017) American Chemical Society (ACS).

Species	Ionization	$(m/z)^{theo}$/Da	$(m/z)^{exp}$/Da	$\Delta(m/z)$
TetraMBH^D	Na$^+$	1685.8801	1685.8836	0.0035
TetraMB=^{D}	Na$^+$	1683.8645	1683.8666	0.0021
TetraMB2^C	Na$^+$	1645.8641	1645.8412	0.0229
TetraMBO^C	Na$^+$	1691.8696	1691.8739	0.0043
O2^C	Na$^+$	1637.8226	1637.8201	0.0025
OH^D	Na$^+$	1631.8332	1631.8330	0.0002
O=^{D}	Na$^+$	1629.8175	1629.8185	0.0010
=H^D	Na$^+$	1609.8124	1609.8089	0.0035
==^{D}	Na$^+$	1607.7968	1607.8046	0.0078
=O^C	Na$^+$	1615.8019	1615.7984	0.0035
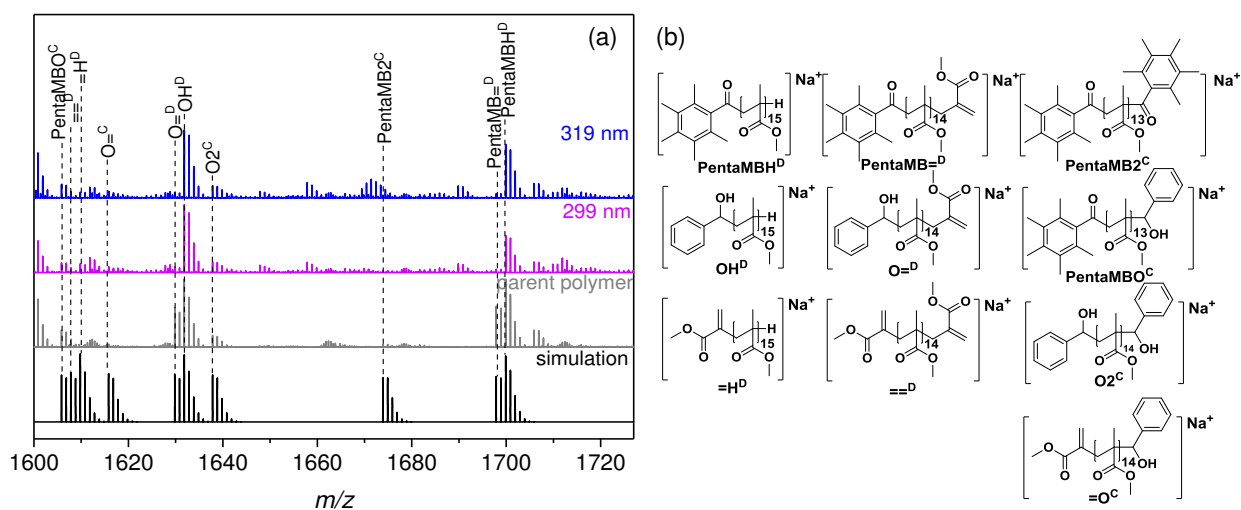
Figure 8.15.: (a) High resolution SEC-ESI mass spectra of the polymer initiated by PentaMB (zoom into one repeating unit), synthesized at low laser energies (0.35 mJ/pulse, 200 Hz, 351 nm, gray spectrum), post-irradiated at 299 and 319 nm (100 Hz, 18 °C) at a constant photon count as well as the theoretical isotope patterns (black spectrum). (b) Disproportionation and combination products of the polymer initiated by PentaMB, at low laser energies (0.35 mJ/pulse, 200 Hz, 351 nm), post-irradiated with high laser energies (100 Hz, 299 and 319 nm), as detected by SEC-ESI-MS. Adapted with permission from reference [176]. Copyright (2017) American Chemical Society (ACS).

Table 8.13.: Overview of the assigned signals of the polymers synthesized at low laser energies (351 nm, 0.35 mJ/pulse, 200 Hz) and post-irradiated with high laser energies (299 nm, 100 Hz) of PentaMB-initiated pMMA, as detected by SEC-ESI-MS with a resolution of 50000. Adapted with permission from reference [176]. Copyright (2017) American Chemical Society (ACS).

Species	Ionization	$(m/z)^{theo}$/Da	$(m/z)^{exp}$/Da	$\Delta(m/z)$
PentaMBH^D	Na$^+$	1699.8958	1699.9000	0.0042
PentaMB=^{D}	Na$^+$	1697.8801	1697.8827	0.0026
PentaMB2^C	Na$^+$	1673.8954	1673.8957	0.0003
PentaMBO^C	Na$^+$	1605.8328	1605.8380	0.0052
O2^C	Na$^+$	1637.8226	1637.8235	0.0009
OH^D	Na$^+$	1631.8332	1631.8364	0.0032
O=^{D}	Na$^+$	1629.8175	1629.8220	0.0045
=H^D	Na$^+$	1609.8124	1609.8124	0.0000
==^{D}	Na$^+$	1607.7968	1607.8386	0.0418
=O^C	Na$^+$	1615.8019	1615.8018	0.0001

8.2.2 Signal Intensity Ratio

Table 8.14.: Irradiation parameters and the amount of end group conversion of the polymer initiated by 4MB, given by the signal intensity ratio of =O^C. Adapted with permission from reference [176]. Copyright (2017) American Chemical Society (ACS).
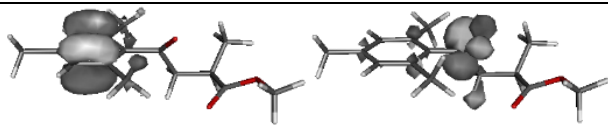
Irradiation Wave-length	Target Energy per Pulse	Number of Pulses	Glass Transmis-sion	Total Energy [2]	Number of incident Photons	Signal Intensity Ratio of =O^C
λ / nm	E / mJ	n_p	%	E / J	n_{ph} / µmol	
305	1.00	434200	92.2 [1]	400	1021	0.91
325	1.20	531500	58.9	376	1021	0.84
345	1.50	388000	60.8	354	1021	0.82
365	1.35	376500	65.8	335	1021	0.85
385	1.25	381500	66.5	317	1021	0.39
405	0.95	457300	69.4	301	1021	0.03

[1] crimped quartz glass vials were used instead of crimped photo glass vials

[2] after deduction of the glass transmission

Table 8.15.: Irradiation parameters and the amount of end group conversion of the polymer initiated by TriMB, given by the signal intensity ratio of $=O^C$. Adapted with permission from reference [176]. Copyright (2017) American Chemical Society (ACS).

Irradiation Wavelength	Target Energy per Pulse	Number of Pulses	Glass Transmission	Total Energy [2]	Number of incident Photons	Signal Intensity Ratio of $=O^C$
λ / nm	E / mJ	n_p	%	E / J	n_{ph} / μmol	
305	1.00	434200	92.2 [1]	400	1021	0.38
325	1.20	531500	58.9	376	1021	0.21
345	1.50	388000	60.8	354	1021	0.15
365	1.35	376500	65.8	335	1021	0.04
385	1.25	381500	66.5	317	1021	0.02
405	0.95	457300	69.4	301	1021	0.01

[1] crimped quartz glass vials were used instead of crimped photo glass vials
[2] after deduction of the glass transmission

Table 8.16.: Irradiation parameters and the amount of end group conversion of the polymer initiated by 2,6DMB, TetraMB, and PentaMB, given by the signal intensity ratio of $=O^C$. Adapted with permission from reference [176]. Copyright (2017) American Chemical Society (ACS).

Sample	Irradiation Wavelength	Target Energy per Pulse	Number of Pulses	Glass Transmission	Total Energy [2]	Number of incident Photons	Signal Intensity Ratio of $=O^C$
	λ / nm	E / mJ	n_p	%	E / J	n_{ph} / μmol	
2,6DMB	325	1.50	425200	58.9	376	1021	0.51
2,6DMB	305	1.00	434200	92.2 [1]	400	1021	0.61
TetraMB	326	1.50	423900	58.9	376	1021	0.18
TetraMB	306	1.00	434200	92.2 [1]	400	1021	0.30
PentaMB	319	1.50	453200	56.3	383	1021	0.18
PentaMB	299	0.75	591100	92.1 [1]	408	1021	0.25

[1] crimped quartz glass vials were used instead of crimped photo glass vials
[2] after deduction of the glass transmission

4MB-pMMA
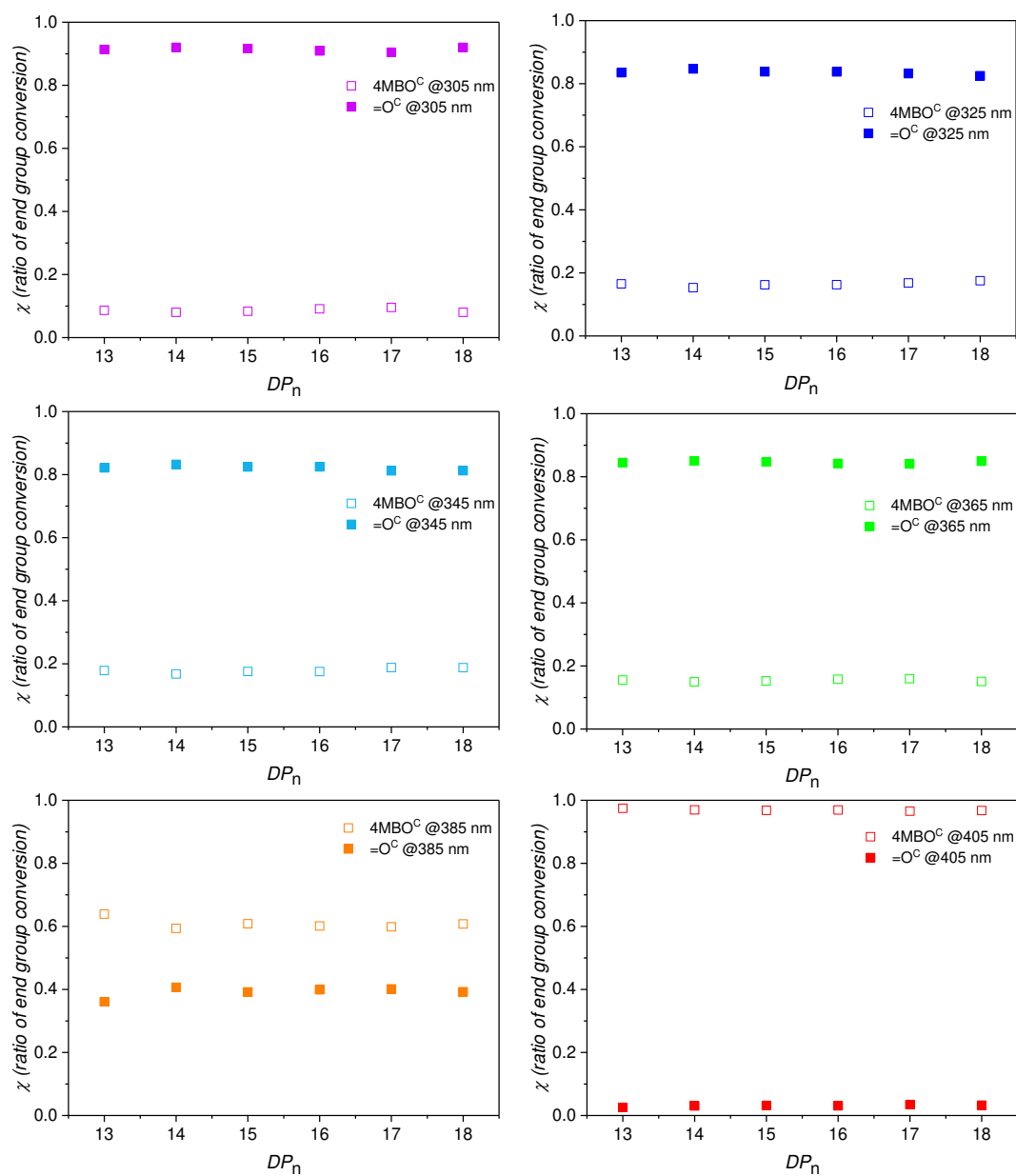
Figure 8.16.: Plot of the end group conversion ratio of the peak heights (4MBO^C and =O^C) of the polymer initiated by 4MB vs. the DP_n at 305-405 nm. Adapted with permission from reference [176]. Copyright (2017) American Chemical Society (ACS).

TriMB-pMMA
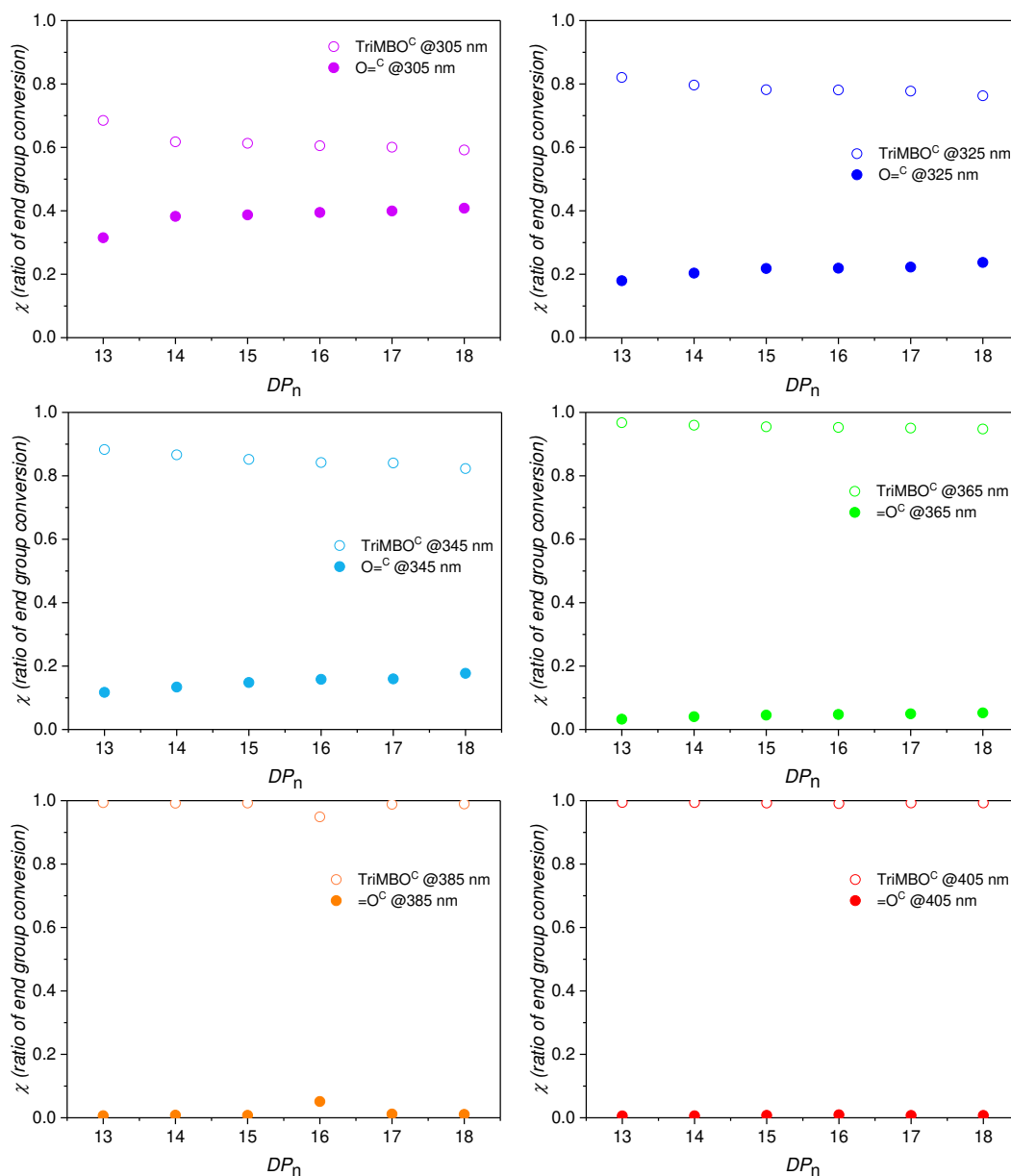
Figure 8.17.: Plot of the end group conversion ratio of the peak heights (TriMBO^C and =O^C) of the polymer initiated by TriMB vs. the DP_n at 305-405 nm. Adapted with permission from reference [176]. Copyright (2017) American Chemical Society (ACS).

2,6DMB-pMMA, TetraMB-pMMA, and PentaMB-pMMA
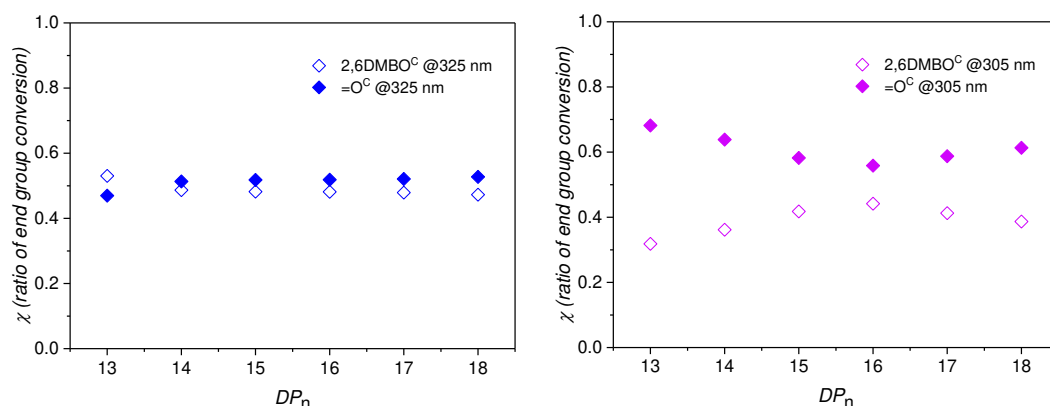
Figure 8.18.: Plot of the end group conversion ratio of the peak heights (2,6DMBO^C and =O^C) of the polymer initiated by 2,6DMB vs. the DP_n at 305 nm. Adapted with permission from reference [176]. Copyright (2017) American Chemical Society (ACS).
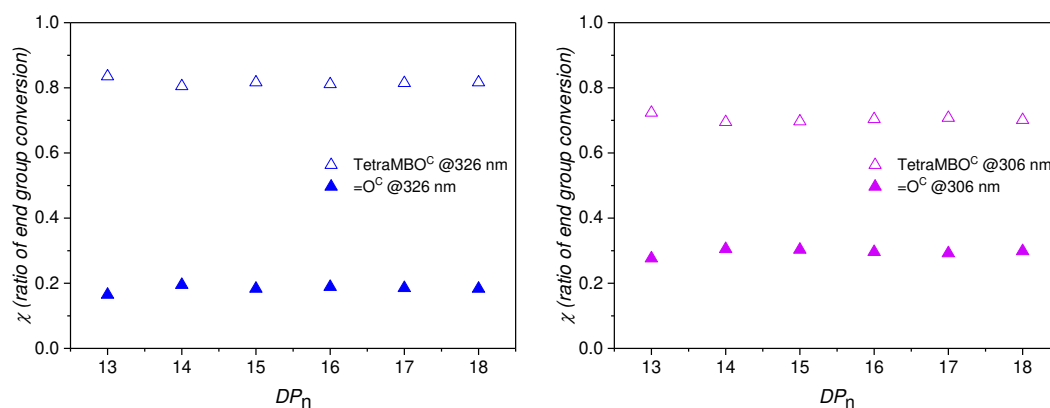
Figure 8.19.: Plot of the end group conversion ratio of the peak heights (TetraMBO^C and =O^C) of the polymer initiated by TetraMB vs. the DP_n at 326 nm. Adapted with permission from reference [176]. Copyright (2017) American Chemical Society (ACS).
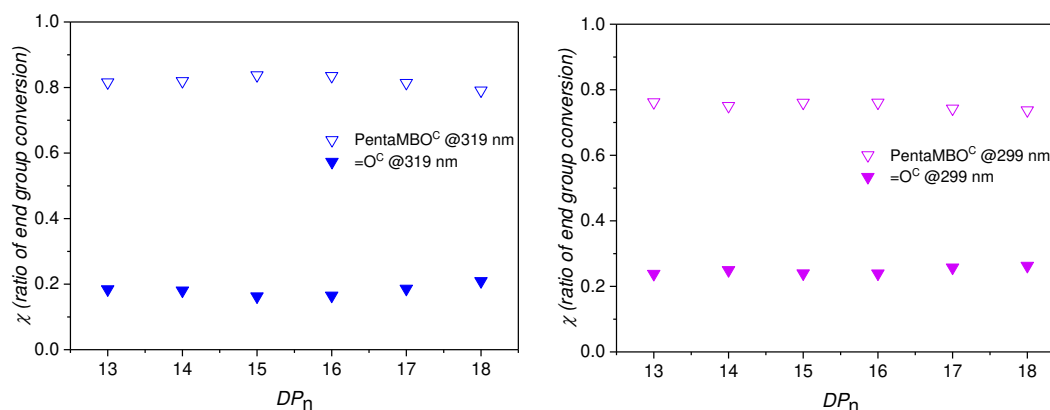
Figure 8.20.: Plot of the end group conversion ratio of the peak heights (PentaMBO^C and =O^C) of the polymer initiated by PentaMB vs. the DP_n at 319 and 299 nm. Adapted with permission from reference [176]. Copyright (2017) American Chemical Society (ACS).

8.2.3 Additional Calculations for the Quantification of the Unsaturated Species

Table 8.17.: Overview of the assigned signals of the polymers post-irradiated at high laser energies (305 to 345 nm, 100Hz) of TriMB-initiated pMMA, as well as the calculated signal intensity ratios of OH^D and $=H^D$ and the percentage deviation from $=H^D$ to OH^D, as detected by SEC-ESI-MS with a resolution of 50000. Adapted with permission from reference [176]. Copyright (2017) American Chemical Society (ACS).

Species	λ / nm	Ionization	$(m/z)^{theo}$/Da	$(m/z)^{exp}$/Da	$\Delta(m/z)$	Signal Intensity Ratio of XH^D	Percentage Deviation from $=H^D$ to OH^D / %
OH^D	305	Na^+	1631.8332	1631.8294	0.0038	0.8472	
$O=^D$	305	Na^+	1629.8175	1629.8228	0.0053		7
$=H^D$	305	Na^+	1609.8124	1609.8132	0.0008	0.9102	
$==^D$	305	Na^+	1607.7968	1607.7935	0.0033		
OH^D	325	Na^+	1631.8332	1631.8294	0.0038	0.7848	
$O=^D$	325	Na^+	1629.8175	1629.8228	0.0053		5
$=H^D$	325	Na^+	1609.8124	1609.8132	0.0008	0.8268	
$==^D$	325	Na^+	1607.7968	1607.7935	0.0033		
OH^D	345	Na^+	1631.8332	1631.8294	0.0038	0.7532	
$O=^D$	345	Na^+	1629.8175	1629.8228	0.0053		6
$=H^D$	345	Na^+	1609.8124	1609.8132	0.0008	0.8032	
$==^D$	345	Na^+	1607.7968	1607.7935	0.0033		

Table 8.18.: Overview of the assigned signals of the polymers post-irradiated at high laser energies (351 nm, 200Hz) of 2,6DMB-, TriMB-, TetraMB-, and PentaMB-initiated pMMA, as well as the calculated signal intensity ratio of $=O^C$, as detected by SEC-ESI-MS with a resolution of 50000. Adapted with permission from reference [176]. Copyright (2017) American Chemical Society (ACS).

Species	λ / nm	Ionization	$(m/z)^{theo}$/Da	$(m/z)^{exp}$/Da	$\Delta(m/z)$	Signal Intensity Ratio of $=O^C$
2,6DMBO^C	351	Na$^+$	1664.9989	1664.8562	0.0146	0.1322
$=O^C$	351	Na$^+$	1516.7528	1516.7558	0.0030	
TriMBO^C	351	Na$^+$	1678.8573	1678.8647	0.0074	0.1071
$=O^C$	351	Na$^+$	1516.7528	1516.7544	0.0048	
TetraMBO^C	351	Na$^+$	1692.8729	1692.8792	0.0063	0.0536
$=O^C$	351	Na$^+$	1516.7528	1516.7449	0.0033	
PentaMBO^C	351	Na$^+$	1706.8886	1706.8925	0.0039	0
$=O^C$	351	Na$^+$	1516.9101	-	-	

8.3 Systematic Assessment of the Role of the Benzoyl Fragment

8.3.1 SEC-ESI-MS Measurements

Table 8.19.: Overview of the signals of the PLP generated polymer (0.35 mJ/pulse), and PLI (in acetonitrile, 6 mJ/pulse) (Benzoin-initiated pMMA), as detected by SEC-ESI-MS (R = 65000).

Species	Ionization	$(m/z)^{theo}$/Da	$(m/z)^{exp}$/Da	$\Delta(m/z)$
B=^{D}	Na$^+$	1227.5922	1227.5925	0.0003
BH^D	Na$^+$	1229.6078	1229.6041	0.0037
O=^{D}	Na$^+$	1229.6078	1229.6041	0.0037
OH^D	Na$^+$	1231.6235	1231.6158	0.0077
==^{D}	Na$^+$	1209.6027	1209.6027	0.0000
=H^D	Na$^+$	1207.5871	1207.5852	0.0019

Table 8.20.: Overview of the signals of the PLP generated polymer (0.35 mJ/pulse), and PLI (6 mJ/pulse) (Fbz-initiated pMMA), as detected by SEC-ESI-MS (R = 60000).

Species	Ionization	$(m/z)^{theo}$/Da	$(m/z)^{exp}$/Da	$\Delta(m/z)$
B=^{D}	Na$^+$	1345.6352	1345.6328	0.0024
BH^D	Na$^+$	1347.6508	1347.6483	0.0025
O=^{D}	Na$^+$	1329.6602	1329.6590	0.0012
OH^D	Na$^+$	1331.6759	1331.6733	0.0026
==^{D}	Na$^+$	1307.6395	1307.6421	0.0026
=H^D	Na$^+$	1309.6552	1309.6570	0.0018
?	-	-	1299.6514	-

Table 8.21.: Overview of the signals of the PLP generated polymer (0.35 mJ/pulse), and PLI (6 mJ/pulse) (369-initiated pMMA), as detected by SEC-ESI-MS (R = 60000).

Species	Ionization	$(m/z)^{\text{theo}}$/Da	$(m/z)^{\text{exp}}$/Da	$\Delta(m/z)$
B=$^{\text{D}}$	Na$^+$	1312.6449	1312.6419	0.0030
BH$^{\text{D}}$	Na$^+$	1314.6606	1314.6571	0.0035
N=$^{\text{D}}$	Na$^+$	1298.7021	1298.7036	0.0015
NH$^{\text{D}}$	Na$^+$	1300.7177	1300.7163	0.0014
N=$^{\text{D}}$	H$^+$	1376.7725	1376.7715	0.0010
NH$^{\text{D}}$	H$^+$	1378.7882	1378.7849	0.0033
==$^{\text{D}}$	Na$^+$	1307.6395	1307.6434	0.0039
=H$^{\text{D}}$	Na$^+$	1309.6552	1309.6589	0.0037
?	-	-	1330.6584	-
?	-	-	1346.6541	-
?	-	-	1354.7293	-

Table 8.22.: Overview of the signals of the PLP generated polymer (0.35 mJ/pulse), and PLI (6 mJ/pulse) (907-initiated pMMA), as detected by SEC-ESI-MS (R = 60000).

Species	Ionization	$(m/z)^{\text{theo}}$/Da	$(m/z)^{\text{exp}}$/Da	$\Delta(m/z)$
B=$^{\text{D}}$	Na$^+$	1373.6323	1373.6331	0.0008
BH$^{\text{D}}$	Na$^+$	1375.6480	1375.6456	0.0024
Mo=$^{\text{D}}$	Na$^+$	1350.7181	1350.7174	0.0007
MoH$^{\text{D}}$	Na$^+$	1352.7337	1352.7322	0.0015
Mo=$^{\text{D}}$	H$^+$	1328.7361	1328.7385	0.0024
MoH$^{\text{D}}$	H$^+$	1330.7518	1330.7495	0.0023
==$^{\text{D}}$	Na$^+$	1307.6395	1307.6434	0.0039
=H$^{\text{D}}$	Na$^+$	1309.6552	1309.6580	0.0028

Table 8.23.: Overview of the signals of the PLP generated polymer (0.35 mJ/pulse), and PLI (6 mJ/pulse) (2959-initiated pMMA), as detected by SEC-ESI-MS (R = 60000).

Species	Ionization	$(m/z)^{\text{theo}}$/Da	$(m/z)^{\text{exp}}$/Da	$\Delta(m/z)$
B=$^{\text{D}}$	Na$^+$	1387.6657	1387.6665	0.0008
BH$^{\text{D}}$	Na$^+$	1389.6814	1389.6788	0.0026
O=$^{\text{D}}$	Na$^+$	1381.7127	1381.7165	0.0038
OH$^{\text{D}}$	Na$^+$	1383.7283	1383.7285	0.0002
==$^{\text{D}}$	Na$^+$	1307.6395	1307.6436	0.0041
=H$^{\text{D}}$	Na$^+$	1309.6552	1309.6587	0.0035

Table 8.24.: Overview of the signals of the PLP generated polymer (0.35 mJ/pulse), and PLI (6 mJ/pulse) (Benzoin-initiated pMMA), as detected by SEC-ESI-MS (R = 55000).

Species	Ionization	$(m/z)^{theo}$/Da	$(m/z)^{exp}$/Da	$\Delta(m/z)$
B=^{D}	Na$^+$	1427.6970	1427.6947	0.0023
BH^D	Na$^+$	1429.7127	1429.7114	0.0013
O=^{D}	Na$^+$	1429.7127	1429.7114	0.0013
OH^D	Na$^+$	1431.7283	1431.7200	0.0083
==^{D}	Na$^+$	1407.6919	1407.6992	0.0073
=H^D	Na$^+$	1409.7076	1409.7115	0.0061

Table 8.25.: Overview of the signals of the PLP generated polymer (0.35 mJ/pulse), and PLI (6 mJ/pulse) (Benzoin-initiated pnBMA), as detected by SEC-ESI-MS (R = 45000).

Species	Ionization	$(m/z)^{theo}$/Da	$(m/z)^{exp}$/Da	$\Delta(m/z)$
B=^{D}	Na$^+$	2116.4068	2116.4157	0.0089
BH^D	Na$^+$	2118.4224	2118.4363	0.0139
O=^{D}	Na$^+$	2118.4224	2118.4363	0.0139
OH^D	Na$^+$	2120.4381	2120.4491	0.0110
==^{D}	Na$^+$	2138.4486	2138.4679	0.0193
=H^D	Na$^+$	2140.4643	2140.4760	0.0117

Table 8.26.: Overview of the signals of the PLP generated polymer (0.35 mJ/pulse), and PLI (6 mJ/pulse) (Benzoin-initiated ptBMA), as detected by SEC-ESI-MS (R = 45000).

Species	Ionization	$(m/z)^{theo}$/Da	$(m/z)^{exp}$/Da	$\Delta(m/z)$
B=^{D}	Na$^+$	2116.4068	2116.4192	0.0124
BH^D	Na$^+$	2118.4224	2118.4290	0.066
O=^{D}	Na$^+$	2118.4224	2118.4290	0.066
OH^D	Na$^+$	2120.4381	2120.4417	0.0099
==^{D}	Na$^+$	2138.4486	2138.4639	0.0153
=H^D	Na$^+$	2140.4643	2140.4818	0.0175

Table 8.27.: Overview of the signals of the PLP generated polymer (0.35 mJ/pulse), and PLI (6 mJ/pulse) (Benzoin-initiated pBnMA), as detected by SEC-ESI-MS (R = 49000).

Species	Ionization	$(m/z)^{\text{theo}}$/Da	$(m/z)^{\text{exp}}$/Da	$\Delta(m/z)$
B=$^{\text{D}}$	Na$^+$	2063.9365	2063.9531	0.0034
BH$^{\text{D}}$	Na$^+$	2065.9521	2065.9666	0.0045
O=$^{\text{D}}$	Na$^+$	2065.9521	2065.9666	0.0045
OH$^{\text{D}}$	Na$^+$	2067.9678	2067.9722	0.0044
==$^{\text{D}}$	Na$^+$	2119.9627	2119.9800	0.0173
=H$^{\text{D}}$	Na$^+$	2121.9783	2121.9924	0.0141

Table 8.28.: Overview of the signals of the PLP generated polymer (0.35 mJ/pulse), and PLI (in solution, 6 mJ/pulse) (3MB-initiated pMMA), as detected by SEC-ESI-MS (R = 60000).

Species	Ionization	$(m/z)^{\text{theo}}$/Da	$(m/z)^{\text{exp}}$/Da	$\Delta(m/z)$
B=$^{\text{D}}$	Na$^+$	941.4505	941.4502	0.0003
BH$^{\text{D}}$	Na$^+$	943.4662	931.4648	0.0014
O=$^{\text{D}}$	Na$^+$	929.4505	929.4524	0.0019
OH$^{\text{D}}$	Na$^+$	931.4662	931.4648	0.0014
==$^{\text{D}}$	Na$^+$	907.4298	907.4292	0.0006
=H$^{\text{D}}$	Na$^+$	909.4454	909.4451	0.0003

8.4 Wavelength-Dependent Photochemistry of Oxime Esters

8.4.1 DFT Calculations

Table 8.29.: Vertical singlet excitations of OXE01, as computed by the CAM-B3LYP/6-311++G(2d,p) method in acetonitrile. Adapted with permission from reference [184]. Copyright (2017) American Chemical Society (ACS).

OXE01	S_1	S_2	S_3	S_4	S_5	S_6
eV	3.7735	3.969	4.5931	4.8807	4.961	5.0147
Nm	328.6	312.4	269.9	254.0	249.	247.2
F	0.0119	0.6301	0.0033	0.0011	0.0336	0.0975
M01	112 → 119	118 → 119	113 → 119	118 → 121	115 → 120	115 → 120
C	0.62	0.65	0.42	0.65	0.40	0.34
M02	108 → 119		116 → 119		115 → 119	108 → 119
C	0.16		0.36		0.31	0.27
M03			118 → 122		108 → 119	114 → 119
C			0.22		-0.22	0.22
M04					111 → 119	111 → 119
C					0.20	-0.22
M05						114 → 120
C						0.19

Table 8.30.: Vertical singlet excitations of OXE02, as computed by the CAM-B3LYP/6-311++G(2d,p) method in acetonitrile. Adapted with permission from reference [184]. Copyright (2017) American Chemical Society (ACS).

OXE02	S_1	S_2	S_3	S_4	S_5	S_6
eV	3.9548	4.0463	4.1575	4.5258	4.6802	4.8395
Nm	313.5	306.4	298.2	274.0	264.9	256.2
F	0.1792	0.2018	0.1878	1.0306	0.2047	0.1157
M01	109 → 110	109 → 110	109 → 111	108 → 110	109 → 112	107 → 110
C	0.42	0.37	0.46	0.44	0.51	0.42
M02	104 → 110	104 → 110	108 → 110	108 → 111	109 → 111	108 → 111
C	-0.40	0.37	-0.30	-0.37	-0.31	0.39
M03	106 → 110	109 → 112	109 → 110	109 → 111	105 → 110	108 → 110
C	0.21	-0.26	0.26	0.29	0.20	0.17
M04		106 → 110	108 → 112		109 → 110	
C		-0.19	0.19		0.17	
M05		108 → 110	109 → 112			
C		0.17	0.17			

8.4.2 Wavelength-dependent Conversion

Table 8.31.: Irradiation parameters and conversion of MMA initiated by OXE01. Adapted with permission from reference [184]. Copyright (2017) American Chemical Society (ACS).

Sample	Irradiation Wave-length λ / nm	Target Energy per Pulse E / µJ	Number of Pulses n_p / a.u.	Number of incident Photons n_{ph} / mol	Con-version p / %	Mean Conver-sion p / %	Mean Deviation d / %
1	285	700	270000	60	3.415		
2	285	700	270000	60	3.237	3.28	0.123
3	285	700	270000	60	3.178		
4	300	709	90000	60	2.172		
5	300	709	90000	60	2.319	2.21	0.095
6	300	709	90000	60	2.140		
7	315	498	90000	60	2.494		
8	315	498	90000	60	2.494	2.51	0.025
9	315	498	90000	60	2.537		
10	330	398	90000	60	1.570		
11	330	398	90000	60	2.791	2.71	0.075
12	330	398	90000	60	2.649		
13	345	371	90000	60	2.154		
14	345	371	90000	60	2.052	2.26	0.271
15	345	371	90000	60	2.565		
16	360	334	90000	60	3.060		
17	360	334	90000	60	2.600	3.044	0.436
18	360	334	90000	60	3.471		
19	375	328	90000	60	5.131		
20	375	328	90000	60	4.539	4.76	0.326
21	375	328	90000	60	4.599		
22	390	305	90000	60	7.464		
23	390	305	90000	60	7.628	6.63	0.258
24	390	305	90000	60	6.933		
25	405	286	90000	60	9.533		
26	405	286	90000	60	9.401	9.37	0.173
27	405	286	90000	60	9.190		
28	420	260	90000	60	8.836		
29	420	260	90000	60	8.673	8.70	0.127
30	420	260	90000	60	8.587		
31	435	244	90000	60	2.993		
32	435	244	90000	60	2.938	2.90	0.116
33	435	244	90000	60	2.770		

Table 8.32.: Irradiation parameters and conversion of MMA initiated by OXE02. Adapted with permission from reference [184]. Copyright (2017) American Chemical Society (ACS).

Sample	Irradiation Wave-length λ / nm	Target Energy per Pulse E / µJ	Number of Pulses n_P / a.u.	Number of incident Photons n_{ph} / µmol	Con-version p / %	Mean Con-version p / %	Mean Deviation d / %
1	285	700	270000	60	0.776		
2	285	700	270000	60	0.984	0.90	0.107
3	285	700	270000	60	0.920		
4	300	709	90000	60	0.669		
5	300	709	90000	60	0.389	0.50	0.149
6	300	709	90000	60	0.442		
7	315	498	90000	60	0.847		
8	315	498	90000	60	0.886	0.88	0.026
9	315	498	90000	60	0.895		
10	330	398	90000	60	0.869		
11	330	398	90000	60	1.151	1.035	0.148
12	330	398	90000	60	1.086		
13	345	371	90000	60	0.737		
14	345	371	90000	60	0.812	0.84	0.112
15	345	371	90000	60	0.958		
16	360	334	90000	60	1.911		
17	360	334	90000	60	1.666	1.70	0.190
18	360	334	90000	60	1.536		
19	375	328	90000	60	1.658		
20	375	328	90000	60	1.782	1.66	0.122
21	375	328	90000	60	1.538		
22	390	305	90000	60	2.278		
23	390	305	90000	60	2.110	2.16	0.099
24	390	305	90000	60	2.101		
25	405	286	90000	60	3.072		
26	405	286	90000	60	2.948	3.07	0.116
27	405	286	90000	60	3.179		
28	420	260	90000	60	1.079		
29	420	260	90000	60	1.099	0.99	0.164
30	420	260	90000	60	0.806		
31	435	244	90000	60	0.900		
32	435	244	90000	60	1.078	0.96	0.104
33	435	244	90000	60	0.894		

8.5 Photoinduced Generation of Lactone Chain Termini

8.5.1 SEC-ESI-MS Measurements
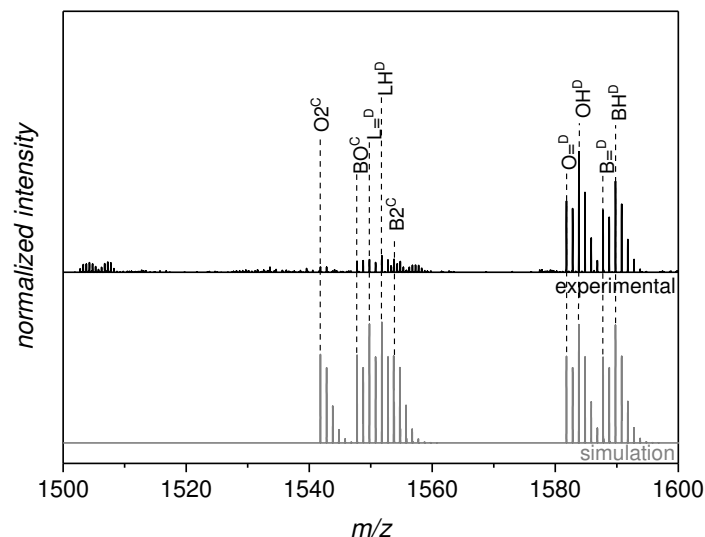
Figure 8.21.: High resolution SEC-ESI mass spectrum of p(MMA) initiated by Irgacure 2959 (zoom into one repeating unit), synthesized at low laser energies (0.35 mJ/pulse, 100 Hz, 351 nm, 18°C, black spectrum), and the associated isotopic pattern simulation (gray spectrum). Adapted from reference [193] with permission from the Royal Society of Chemistry.
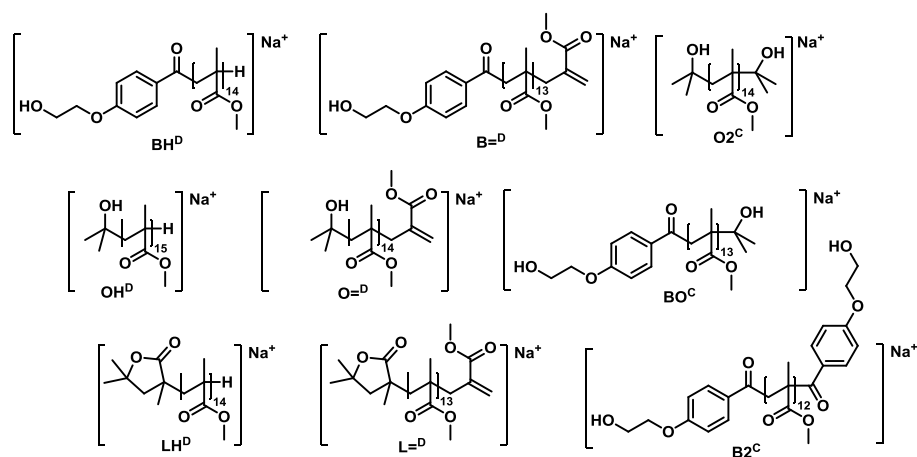
Scheme 8.7.: Disproportionation and combination products of p(MMA) initiated by Irgacure 2959, at low laser energies (0.35 mJ/pulse, 100 Hz, 351 nm, 18 °C), as detected by SEC-ESI-MS. Adapted from reference [193] with permission from the Royal Society of Chemistry.

Table 8.33.: Overview of the assigned signals of p(MMA) synthesized at low laser energies (351 nm, 0.35 mJ/pulse, 100 Hz), as detected by SEC-ESI-MS with a resolution of 50000. Adapted from reference [193] with permission from the Royal Society of Chemistry.

| Species	Ionization	$(m/z)^{theo}$/Da	$(m/z)^{exp}$/Da	$\Delta(m/z)$
BH^D	Na$^+$	1589.7862	1589.7794	0.0068
B=^{D}	Na$^+$	1587.7706	1587.7671	0.0035
OH^D	Na$^+$	1583.8332	1583.8294	0.0038
O=^{D}	Na$^+$	1581.8175	1581.8135	0.0040
LH^D	Na$^+$	1551.8070	1551.8022	0.0048
L=^{D}	Na$^+$	1549.7913	1549.7900	0.0013
B2^C	Na$^+$	1553.7287	1553.7274	0.0013
O2^C	Na$^+$	1541.8226	1541.8224	0.0002
BO^C	Na$^+$	1547.7757	1547.7774	0.0017
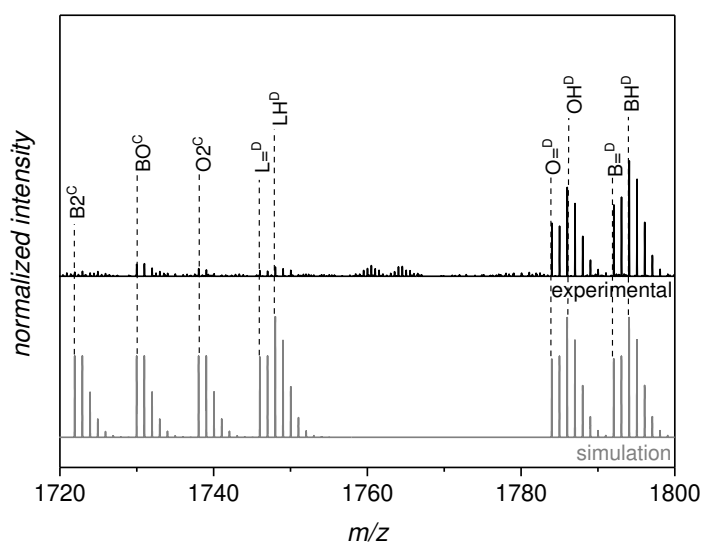
Figure 8.22.: High resolution SEC-ESI mass spectrum of p(EMA) initiated by Irgacure 2959 (zoom into one repeating unit), synthesized at low laser energies (0.35 mJ/pulse, 100 Hz, 351 nm, black spectrum), and the associated isotopic pattern simulation (gray spectrum). Adapted from reference [193] with permission from the Royal Society of Chemistry.
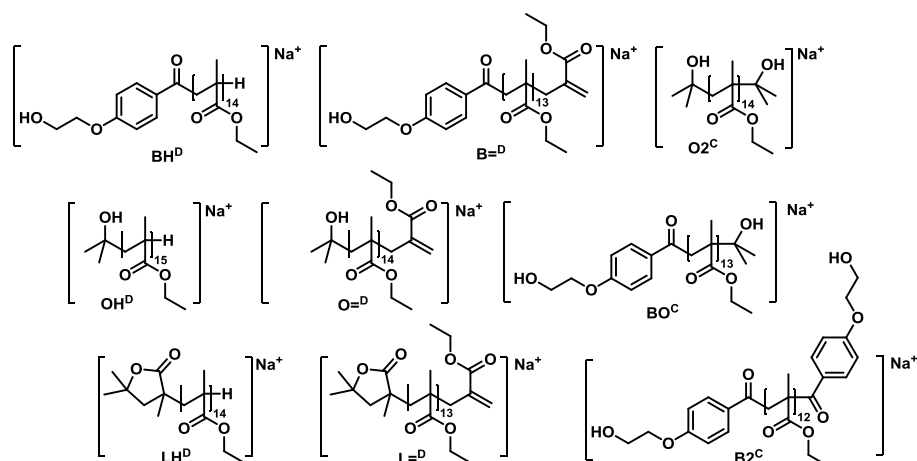
Scheme 8.8.: Disproportionation and combination products of p(EMA) initiated by Irgacure 2959, at low laser energies (0.35 mJ/pulse, 100 Hz, 351 nm), as detected by SEC-ESI-MS. Adapted from reference [193] with permission from the Royal Society of Chemistry.

Table 8.34.: Overview of the assigned signals of p(EMA) synthesized at low laser energies (351 nm, 0.35 mJ/pulse, 100 Hz), as detected by SEC-ESI-MS with a resolution of 50000. Adapted from reference [193] with permission from the Royal Society of Chemistry.

| Species	Ionization	$(m/z)^{theo}$/Da	$(m/z)^{exp}$/Da	$\Delta(m/z)$
BH^D	Na$^+$	1786.0053	1786.0138	0.0085
B=^{D}	Na$^+$	1783.9897	1784.0021	0.0124
OH^D	Na$^+$	1794.0679	1794.0765	0.0086
O=^{D}	Na$^+$	1792.0523	1792.0602	0.0079
LH^D	Na$^+$	1748.0261	1748.0363	0.0102
L=^{D}	Na$^+$	1746.0104	1746.0193	0.0089
B2^C	Na$^+$	1721.9165	1721.9320	0.0155
O2^C	Na$^+$	1738.0417	1738.0546	0.0129
BO^C	Na$^+$	1729.9791	1729.9907	0.0116
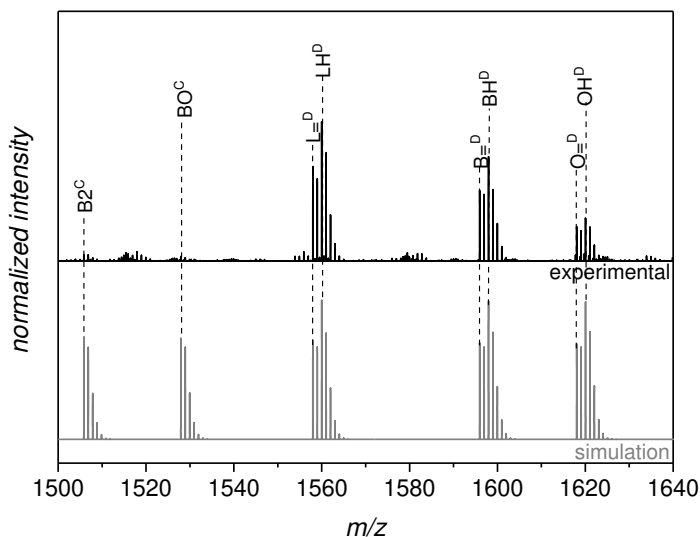
Figure 8.23.: High resolution SEC-ESI mass spectrum of p(*n*PMA) initiated by Irgacure 2959 (zoom into one repeating unit), synthesized at low laser energies (0.35 mJ/pulse, 100 Hz, 351 nm, black spectrum), and the associated isotopic pattern simulation (gray spectrum). Adapted from reference [193] with permission from the Royal Society of Chemistry.
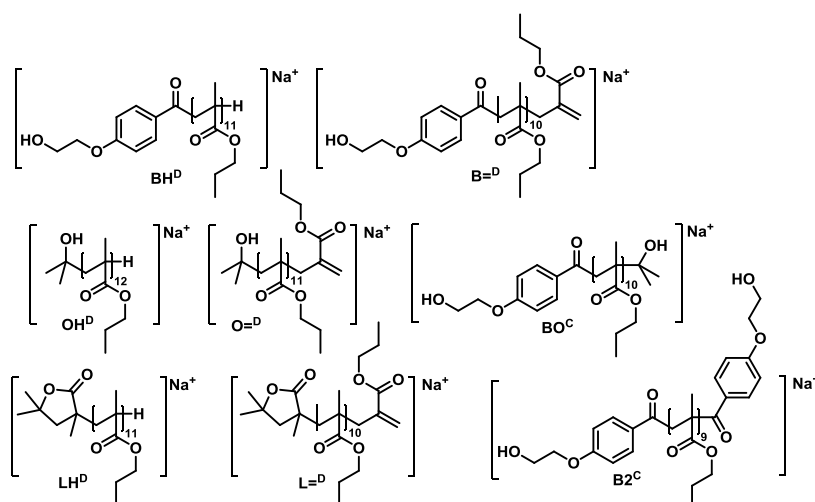
Scheme 8.9.: Disproportionation and combination products of p(*n*PMA) initiated by Irgacure 2959, at low laser energies (0.35 mJ/pulse, 100 Hz, 351 nm, 18 °C), as detected by SEC-ESI-MS. Adapted from reference [193] with permission from the Royal Society of Chemistry.

Table 8.35.: Overview of the assigned signals of p(nPMA) synthesized at low laser energies (351 nm, 0.35 mJ/pulse, 100 Hz), as detected by SEC-ESI-MS with a resolution of 50000. Adapted from reference [193] with permission from the Royal Society of Chemistry.

| Species	Ionization	$(m/z)^{theo}$/Da	$(m/z)^{exp}$/Da	$\Delta(m/z)$
BH^D	Na^+	1597.9732	1597.9718	0.0014
$B{=}^D$	Na^+	1595.9576	1595.9593	0.0017
OH^D	Na^+	1620.0515	1620.0460	0.0055
$O{=}^D$	Na^+	1618.0358	1618.0379	0.0021
LH^D	Na^+	1559.9940	1559.9948	0.0008
$L{=}^D$	Na^+	1557.9783	1557.9806	0.0023
$B2^C$	Na^+	1505.8531	1505.8507	0.0025
BO^C	Na^+	1527.9314	1527.9335	0.0021
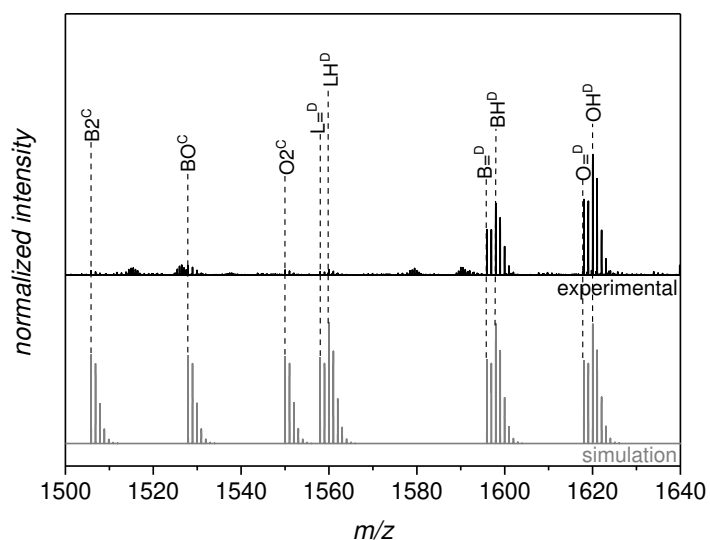
Figure 8.24.: High resolution SEC-ESI mass spectrum of p(iPMA) initiated by Irgacure 2959 (zoom into one repeating unit), synthesized at low laser energies (0.35 mJ/pulse, 100 Hz, 351 nm, black spectrum), and the associated isotopic pattern simulation (gray spectrum). Adapted from reference [193] with permission from the Royal Society of Chemistry.
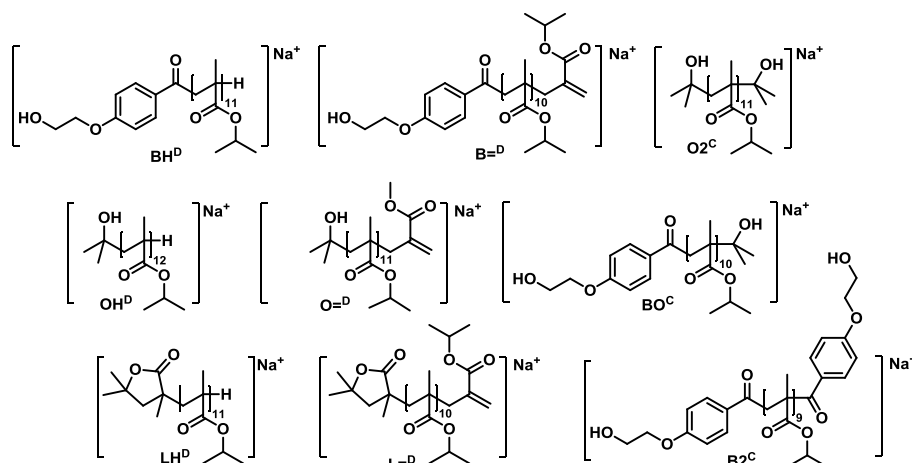
Scheme 8.10.: Disproportionation and combination products of p(iPMA) initiated by Irgacure 2959, at low laser energies (0.35 mJ/pulse, 100 Hz, 351 nm, 18 °C), as detected by SEC-ESI-MS. Adapted from reference [193] with permission from the Royal Society of Chemistry.

Table 8.36.: Overview of the assigned signals of p(iPMA) synthesized at low laser energies (351 nm, 0.35 mJ/pulse, 100 Hz), as detected by SEC-ESI-MS with a resolution of 50000. Adapted from reference [193] with permission from the Royal Society of Chemistry.

| Species	Ionization	$(m/z)^{theo}$/Da	$(m/z)^{exp}$/Da	$\Delta(m/z)$
BH^D	Na$^+$	1597.9732	1597.9677	0.0055
B=^{D}	Na$^+$	1595.9576	1595.9551	0.0025
OH^D	Na$^+$	1620.0515	1620.0493	0.0022
O=^{D}	Na$^+$	1618.0358	1618.0333	0.0025
LH^D	Na$^+$	1559.9940	1559.9902	0.0038
L=^{D}	Na$^+$	1557.9783	1557.9735	0.0048
B2^C	Na$^+$	1505.8531	1505.8550	0.0019
O2^C	Na$^+$	1550.0096	1550.0101	0.0005
BO^C	Na$^+$	1527.9314	1527.9298	0.0016
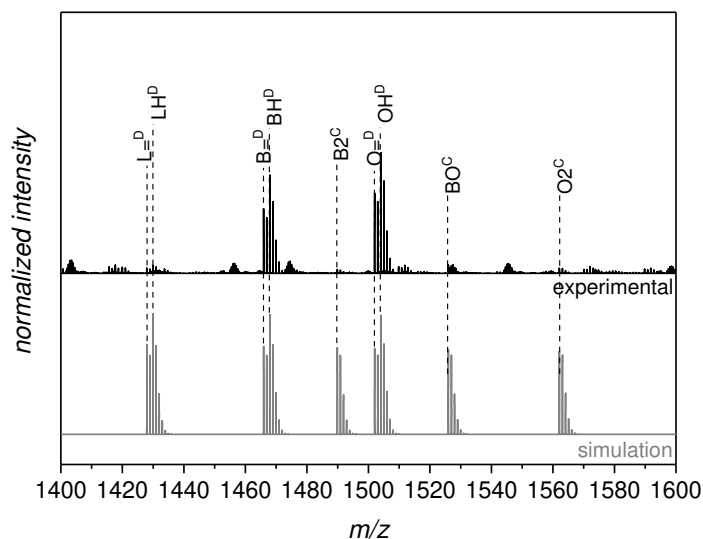
Figure 8.25.: High resolution SEC-ESI mass spectrum of p(*n*BMA) initiated by Irgacure 2959 (zoom into one repeating unit), synthesized at low laser energies (0.35 mJ/pulse, 100 Hz, 351 nm, black spectrum), and the associated isotopic pattern simulation (gray spectrum). Adapted from reference [193] with permission from the Royal Society of Chemistry.
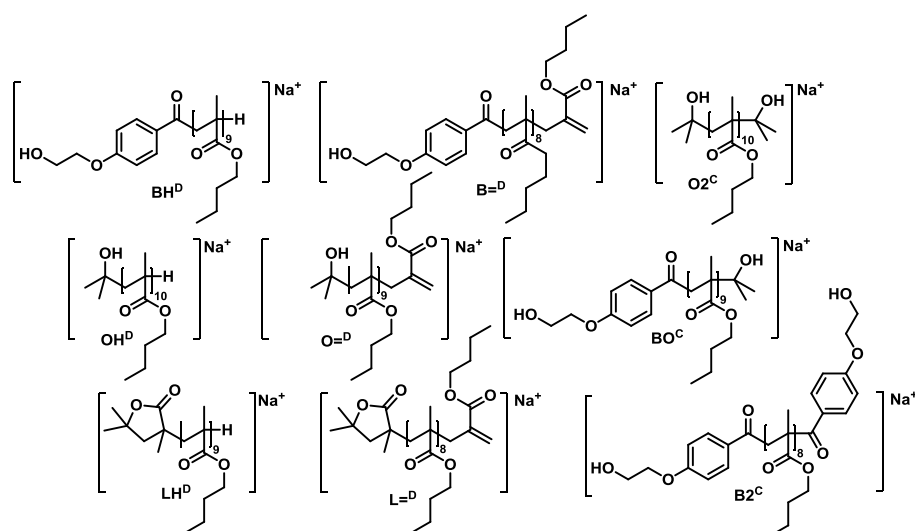
Scheme 8.11.: Disproportionation and combination products of p(*n*BMA) initiated by Irgacure 2959, at low laser energies (0.35 mJ/pulse, 100 Hz, 351 nm), as detected by SEC-ESI-MS. Adapted from reference [193] with permission from the Royal Society of Chemistry.

Table 8.37.: Overview of the assigned signals of p(*n*BMA) synthesized at low laser energies (351 nm, 0.35 mJ/pulse, 100 Hz), as detected by SEC-ESI-MS with a resolution of 50000. Adapted from reference [193] with permission from the Royal Society of Chemistry.

| Species	Ionization	$(m/z)^{theo}$/Da	$(m/z)^{exp}$/Da	$\Delta(m/z)$
BH^D	Na$^+$	1467.9466	1467.9435	0.0031
B=^{D}	Na$^+$	1465.9310	1465.9319	0.0009
OH^D	Na$^+$	1504.0405	1504.0346	0.0059
O=^{D}	Na$^+$	1502.0249	1502.0243	0.0006
LH^D	Na$^+$	1429.9674	1429.9640	0.0034
L=^{D}	Na$^+$	1427.9517	1427.9531	0.0014
B2^C	Na$^+$	1489.8946	1489.8968	0.0022
O2^C	Na$^+$	1562.0824	1562.0832	0.0008
BO^C	Na$^+$	1525.9885	1525.9855	0.0030
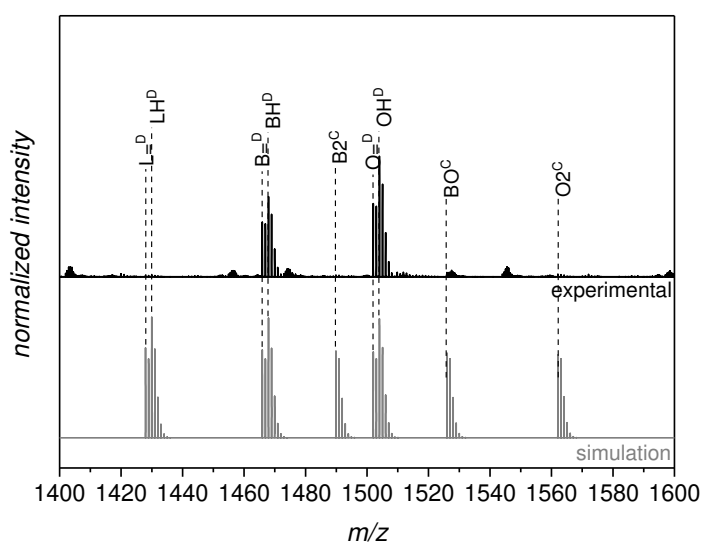
Figure 8.26.: High resolution SEC-ESI mass spectrum of p(*t*BMA) initiated by Irgacure 2959 (zoom into one repeating unit), synthesized at low laser energies (0.35 mJ/pulse, 100 Hz, 351 nm, black spectrum), and the associated isotopic pattern simulation (gray spectrum). Adapted from reference [193] with permission from the Royal Society of Chemistry.
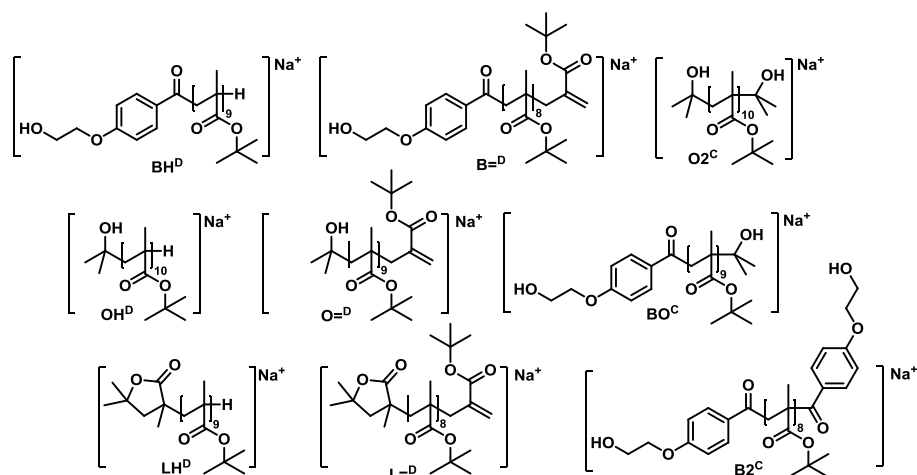
Scheme 8.12.: Disproportionation and combination products of p(*t*BMA) initiated by Irgacure 2959, at low laser energies (0.35 mJ/pulse, 100 Hz, 351 nm), as detected by SEC-ESI-MS. Adapted from reference [193] with permission from the Royal Society of Chemistry.

Table 8.38.: Overview of the assigned signals of p(*t*BMA) synthesized at low laser energies (351 nm, 0.35 mJ/pulse, 100 Hz), as detected by SEC-ESI-MS with a resolution of 50000. Adapted from reference [193] with permission from the Royal Society of Chemistry.

| Species	Ionization	$(m/z)^{theo}$/Da	$(m/z)^{exp}$/Da	$\Delta(m/z)$
BH[D]	Na$^+$	1467.9466	1467.9461	0.0005
B=[D]	Na$^+$	1465.9310	1465.9279	0.0031
OH[D]	Na$^+$	1504.0405	1504.0373	0.0032
O=[D]	Na$^+$	1502.0249	1502.0201	0.0048
LH[D]	Na$^+$	1429.9674	1429.9665	0.0009
L=[D]	Na$^+$	1427.9517	1427.9493	0.0024
B2[C]	Na$^+$	1489.8946	1489.8927	0.0019
O2[C]	Na$^+$	1562.0824	1562.0787	0.0037
BO[C]	Na$^+$	1525.9885	1525.9883	0.0002
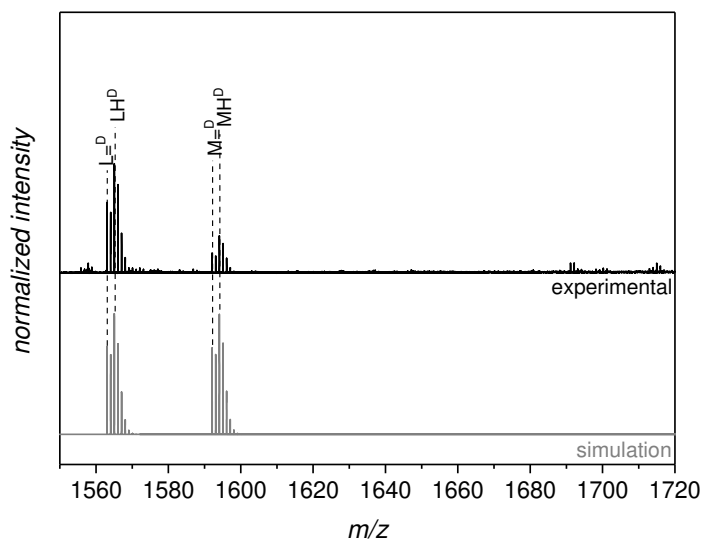
Figure 8.27.: High resolution SEC-ESI mass spectrum of p(DMAEMA) initiated by Irgacure 2959 (zoom into one repeating unit), synthesized at low laser energies (0.35 mJ/pulse, 100 Hz, 351 nm, black spectrum), and the associated isotopic pattern simulation (gray spectrum). Adapted from reference [193] with permission from the Royal Society of Chemistry.
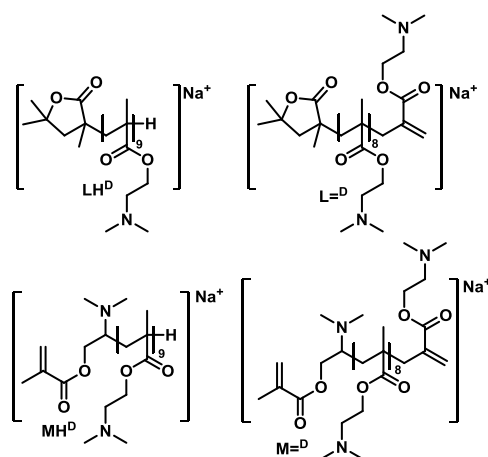
Scheme 8.13.: Disproportionation and combination products of p(DMAEMA) initiated by Irgacure 2959, at low laser energies (0.35 mJ/pulse, 100 Hz, 351 nm), as detected by SEC-ESI-MS. Adapted from reference [193] with permission from the Royal Society of Chemistry.

Table 8.39.: Overview of the assigned signals of p(DMAEMA) synthesized at low laser energies (351 nm, 0.35 mJ/pulse, 100 Hz), as detected by SEC-ESI-MS with a resolution of 50000. Adapted from reference [193] with permission from the Royal Society of Chemistry.

| Species	Ionization	$(m/z)^{theo}$/Da	$(m/z)^{exp}$/Da	$\Delta(m/z)$
BH^D	Na^+	1565.0655	1565.0603	0.0052
$B=^D$	Na^+	1563.0498	1563.0510	0.0012
MH^D	Na^+	1594.0920	1594.0923	0.0003
$M=^D$	Na^+	1592.0764	1592.0720	0.0044
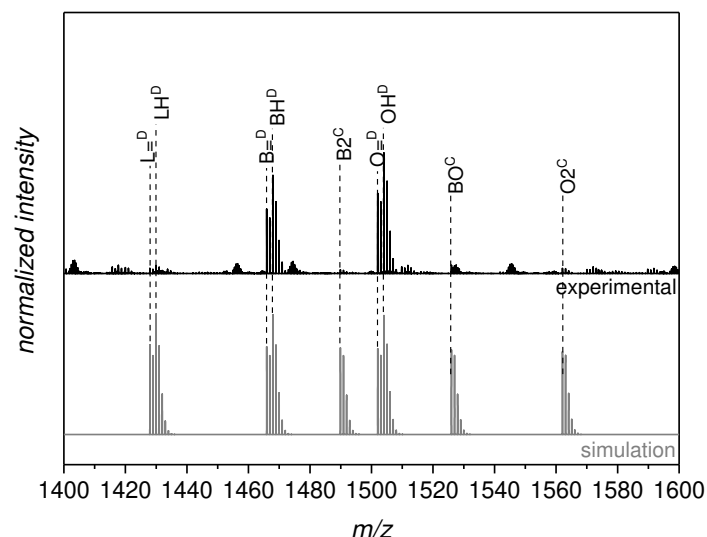
Figure 8.28.: High resolution SEC-ESI mass spectrum of p(BnMA) initiated by Irgacure 2959 (zoom into one repeating unit), synthesized at low laser energies (0.35 mJ/pulse, 100 Hz, 351 nm, black spectrum), and the associated isotopic pattern simulation (gray spectrum). Adapted from reference [193] with permission from the Royal Society of Chemistry.
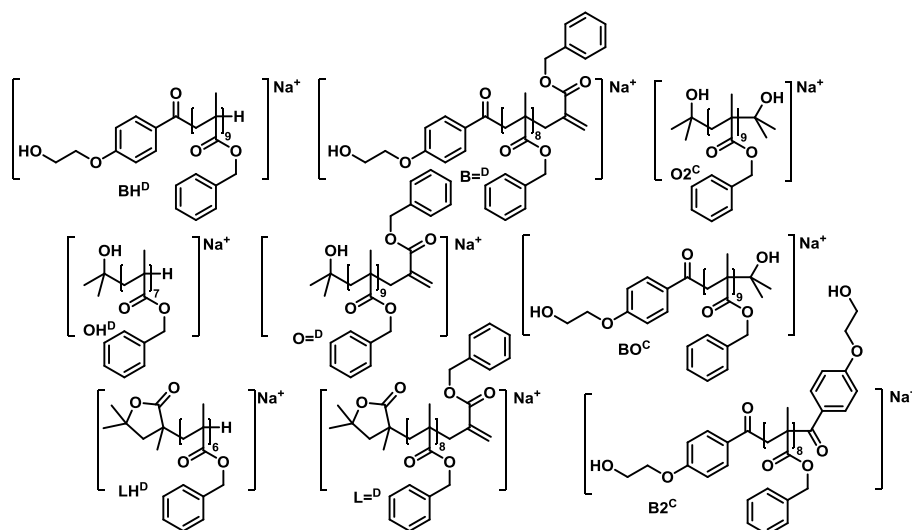
Scheme 8.14.: Disproportionation and combination products of p(BnMA) initiated by Irgacure 2959, at low laser energies (0.35 mJ/pulse, 100 Hz, 351 nm), as detected by SEC-ESI-MS. Adapted from reference [193] with permission from the Royal Society of Chemistry.

Table 8.40.: Overview of the assigned signals of p(BnMA) synthesized at low laser energies (351 nm, 0.35 mJ/pulse, 100 Hz), as detected by SEC-ESI-MS with a resolution of 50000. Adapted from reference [193] with permission from the Royal Society of Chemistry.

| Species	Ionization	$(m/z)^{theo}$/Da	$(m/z)^{exp}$/Da	$\Delta(m/z)$
BH^D	Na^+	1773.8058	1773.8182	0.0124
$B=^D$	Na^+	1771.7901	1771.8005	0.0104
OH^D	Na^+	1843.8840	1843.8930	0.0090
$O=^D$	Na^+	1841.8684	1841.8857	0.0173
LH^D	Na^+	1735.8265	1735.8332	0.0067
$L=^D$	Na^+	1733.8109	1733.8199	0.0090
$B2^C$	Na^+	1761.7694	1761.7817	0.0123
$O2^C$	Na^+	1725.8422	1725.8110	0.0312
BO^C	Na^+	1831.8476	1831.8654	0.0176
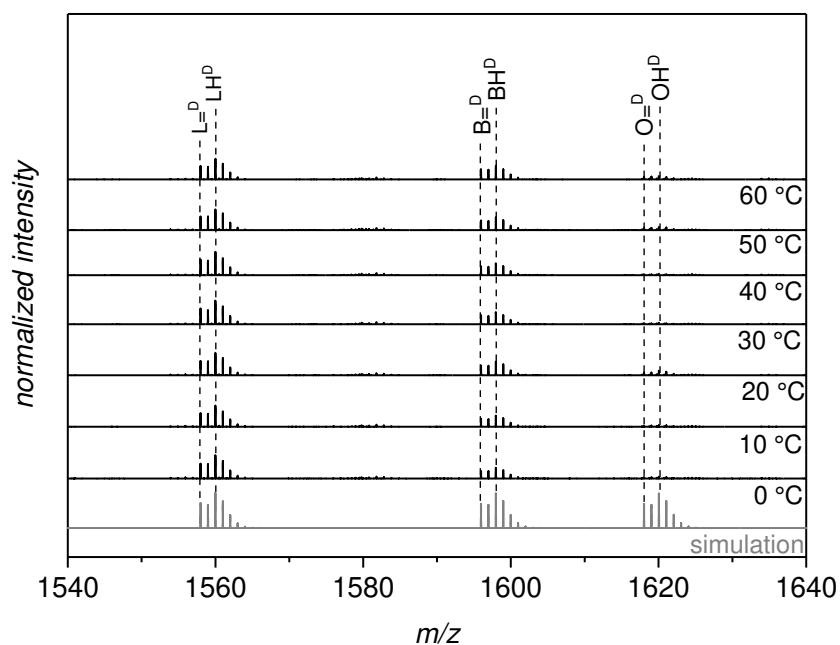
Figure 8.29.: High resolution SEC-ESI mass spectra of p(nPMA) initiated by Irgacure 2959 (zoom into one repeating unit), synthesized at low laser energies (0.35 mJ/pulse, 100 Hz, 351 nm, black spectra) at variable temperatures (0-60 °C) at a constant photon count and the associated isotopic pattern simulation (gray spectrum). Adapted from reference [193] with permission from the Royal Society of Chemistry.
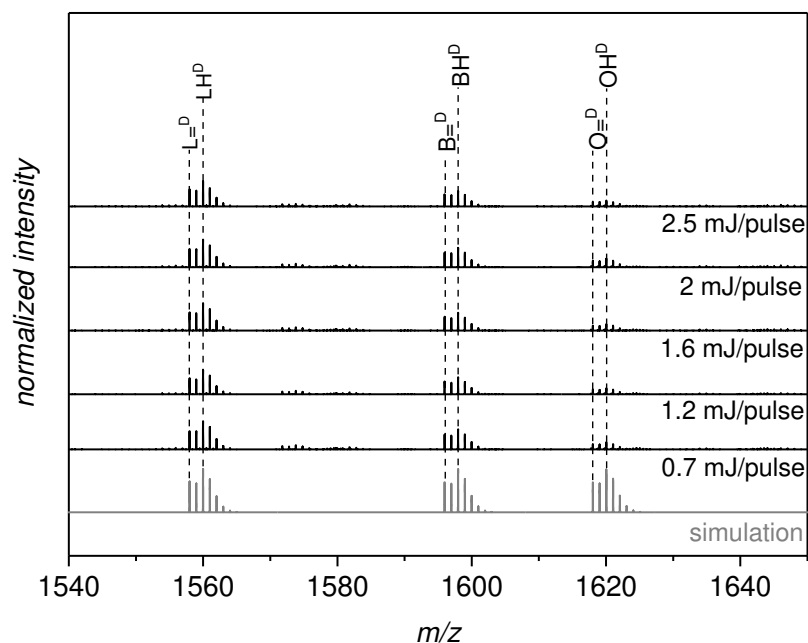
Figure 8.30.: High resolution SEC-ESI mass spectra of p(nPMA) initiated by Irgacure 2959 (zoom into one repeating unit), synthesized at low laser energies (0.35 mJ/pulse, 100 Hz, 351 nm, black spectra) at variable energies (0.7-2.5 mJ/pulse) at a constant photon count and the associated isotopic pattern simulation (gray spectrum). Adapted from reference [193] with permission from the Royal Society of Chemistry.

Figure 8.31.: High resolution SEC-ESI mass spectrum of p(*n*PMA) initiated by Irgacure 2959, synthesized at low laser energies (0.31 mJ/pulse, 100 Hz, 275 nm, pink spectrum) and the associated isotopic pattern simulation (gray spectrum). Adapted from reference [193] with permission from the Royal Society of Chemistry.
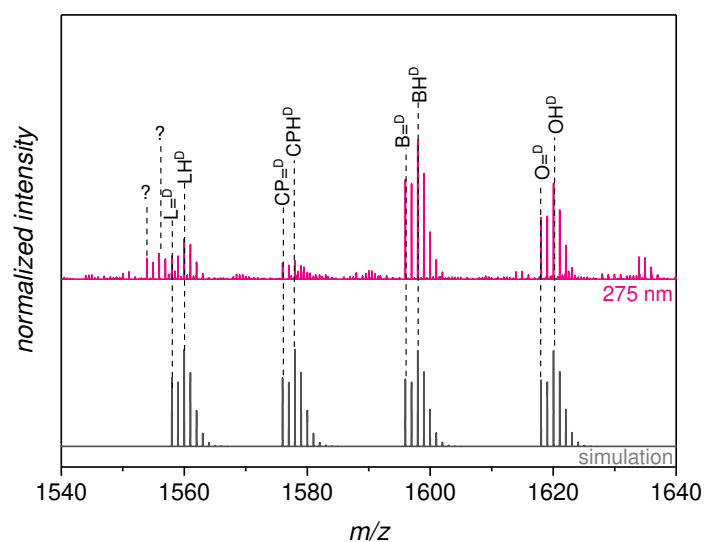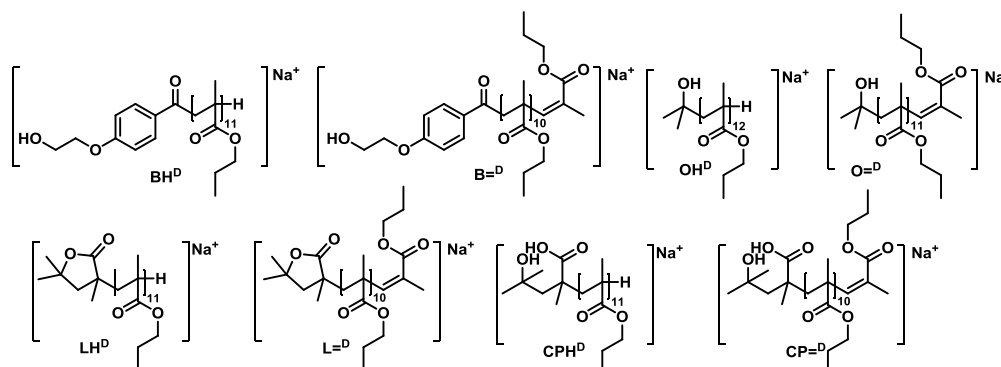
Scheme 8.15.: Disproportionation and combination products of p(nPMA) initiated by Irgacure 2959, at low laser energies (0.31 mJ/pulse, 100 Hz, 275 nm, 18 °C), as detected by SEC-ESI-MS. Adapted from reference [193] with permission from the Royal Society of Chemistry.

Table 8.41.: Overview of the assigned signals of p(nPMA) synthesized at low laser energies (275 nm, 0.35 mJ/pulse, 100 Hz), as detected by SEC-ESI-MS with a resolution of 50000. Adapted from reference [193] with permission from the Royal Society of Chemistry.

Species	Ionization	$(m/z)^{theo}$/Da	$(m/z)^{exp}$/Da	$\Delta(m/z)$
BH^D	Na$^+$	1597.9732	1597.9718	0.0014
B=^{D}	Na$^+$	1595.9576	1595.9593	0.0017
OH^D	Na$^+$	1620.0515	1620.0460	0.0055
O=^{D}	Na$^+$	1618.0358	1618.0379	0.0021
LH^D	Na$^+$	1559.9940	1559.9948	0.0008
L=^{D}	Na$^+$	1557.9783	1557.9806	0.0023
CPH^D	Na$^+$	1578.0045	1578.0080	0.0035
CP=^{D}	Na$^+$	1575.9889	1575.9926	0.0037

8.5.2 Signal Intensity Ratio

Table 8.42.: Irradiation parameters (wavelength study) and the amount of lactonization of p(PMA) initiated by Irgacure 2959, given by the signal intensity ratio of LH^D. Adapted from reference [193] with permission from the Royal Society of Chemistry.

Irradiation Wave-length	Target Energy per Pulse [*1]	Number of Pulses	Glass Trans-mission	Number of incident Photons	Signal Intensity Ratio of LH^D
λ / nm	E / μJ	n_p	%	n_{ph} / μmol	
275	314	90000	91.8	60	0.44
300	702	90000	37.7	60	0.68
320	440	90000	56.3	60	0.70
340	377	90000	61.9	60	0.73
360	331	90000	66.7	60	0.69

[*1] after deduction of the glass transmission

Table 8.43.: Irradiation parameters (monomer study) and the amount of lactonization of the polymers initiated by Irgacure 2959, given by the signal intensity ratio of LH^D. Adapted from reference [193] with permission from the Royal Society of Chemistry.

Polymers	Irradiation Wave-length	Target Energy per Pulse [*1]	Number of Pulses	Glass Transmis-sion	Number of incident Photons	Signal Intensity Ratio of LH^D
	λ / nm	E / µJ	n_p	%	n_{ph} / µmol	
p(MMA)	351	350	90000	64.6	60	0.10
p(EMA)	351	350	90000	64.6	60	0.06
p(nPMA)	351	350	90000	64.6	60	0.78
p(iPMA)	351	350	90000	64.6	60	0.04
p(nBMA)	351	350	90000	64.6	60	0.06
p(tBMA)	351	350	90000	64.6	60	0.02
p(BnMA)	351	350	90000	64.6	60	0.83
p(DMAEMA)	351	350	90000	64.6	60	1.00

[*1] after deduction of the glass transmission

Table 8.44.: Irradiation parameters (temperature study) and the amount of lactonization of p(PMA) initiated by Irgacure 2959, given by the signal intensity ratio of LH^D at 351 nm. Adapted from reference [193] with permission from the Royal Society of Chemistry.

Temperature	Target Energy per Pulse [*1]	Number of Pulses	Glass Trans-mission	Number of incident Photons	Signal Intensity Ratio of LH^D
℃	E / µJ	n_p	%	n_{ph} / µmol	
0	350	90000	64.6	60	0.93
10	350	90000	64.6	60	0.91
20	350	90000	64.6	60	0.82
30	350	90000	64.6	60	0.94
40	350	90000	64.6	60	0.94
50	350	90000	64.6	60	0.87
60	350	90000	64.6	60	0.85

[*1] after deduction of the glass transmission

Table 8.45.: Irradiation parameters (energy study) and the amount of lactonization of p(PMA) initiated by Irgacure 2959, given by the signal intensity ratio of LH^D at 351 nm. Adapted from reference [193] with permission from the Royal Society of Chemistry.

Energy [1]	Number of Pulses	Glass Transmission	Number of incident Photons	Signal Intensity Ratio of LH^D
mJ/pulse	n_p	%	n_{ph} / µmol	
0.7	90000	64.6	119	0.80
1.2	90000	64.6	205	0.79
1.6	90000	64.6	273	0.81
2.0	90000	64.6	341	0.76
2.5	90000	64.6	426	0.80

[1] after deduction of the glass transmission

Figure 8.32.: Plot of the lactonization ratio of the peak height (LH^D) of p(MMA) and p(EMA) initiated by Irgacure 2959 vs. the DP_n at 351 nm. Adapted from reference [193] with permission from the Royal Society of Chemistry.

Figure 8.33.: Plot of the lactonization ratio of the peak height (LH^D) of p(nPMA) and p(iPMA) initiated by Irgacure 2959 vs. the DP_n at 351 nm. Adapted from reference [193] with permission from the Royal Society of Chemistry.
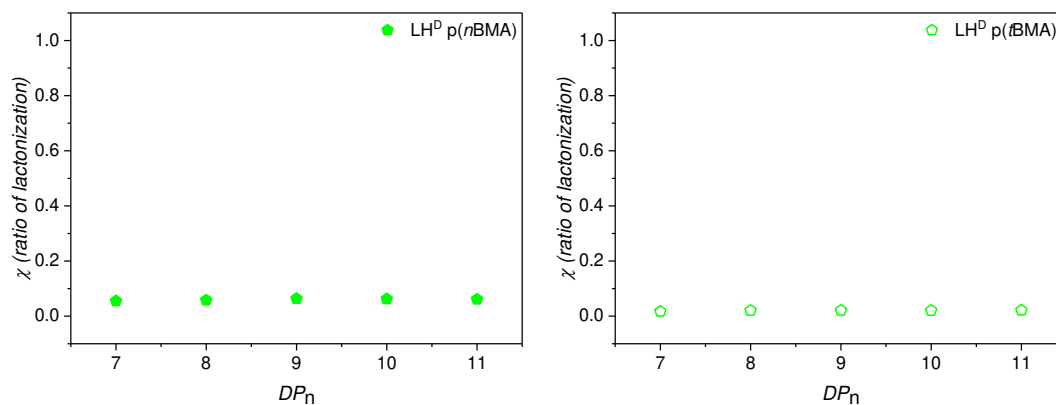
Figure 8.34.: Plot of the lactonization ratio of the peak height (LH^D) of p(nBMA) and p(tBMA) initiated by Irgacure 2959 vs. the DP_n at 351 nm. Adapted from reference [193] with permission from the Royal Society of Chemistry.
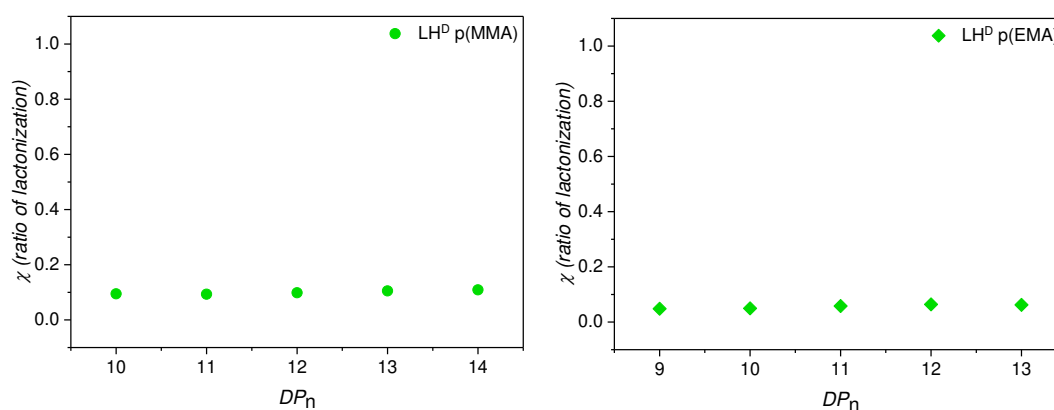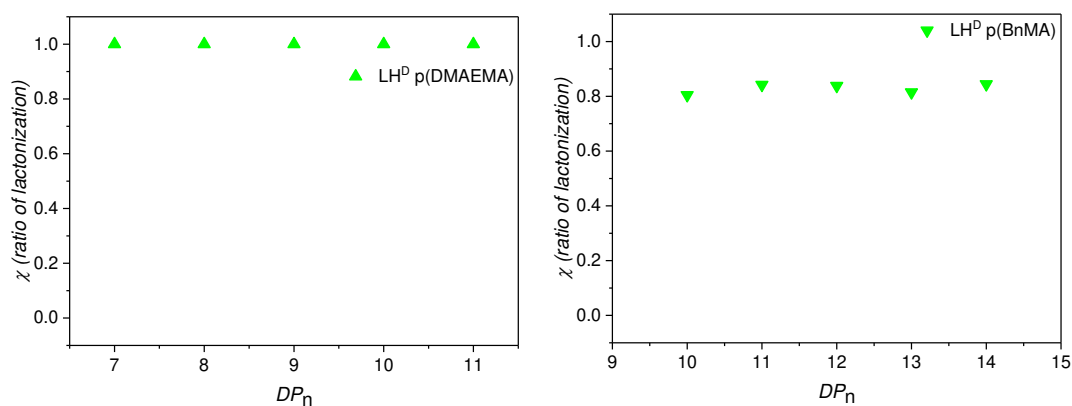

Figure 8.35.: Plot of the lactonization ratio of the peak height (LH^D) of p(BnMA) and p(DMAEMA) initiated by Irgacure 2959 vs. the DP_n at 351 nm. Adapted from reference [193] with permission from the Royal Society of Chemistry.

Figure 8.36.: Plot of the lactonization ratio of the peak height (LH^D) of p(nPMA) initiated by Irgacure 2959 vs. the DP_n between 275-360 nm. Adapted from reference [193] with permission from the Royal Society of Chemistry.
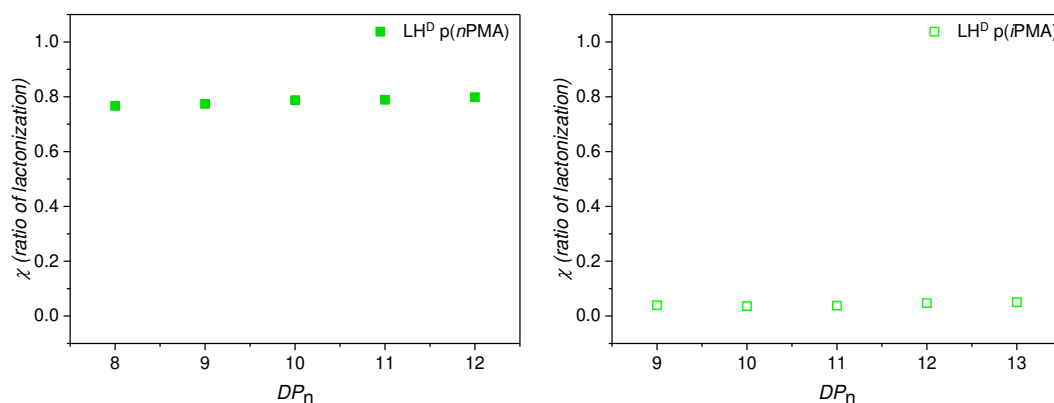
Figure 8.37.: Plot of the lactonization ratio of the peak height (LH^D) of p(nPMA) initiated by Irgacure 2959 (351 nm) vs. the DP_n between 0-60 °C. Adapted from reference [193] with permission from the Royal Society of Chemistry.

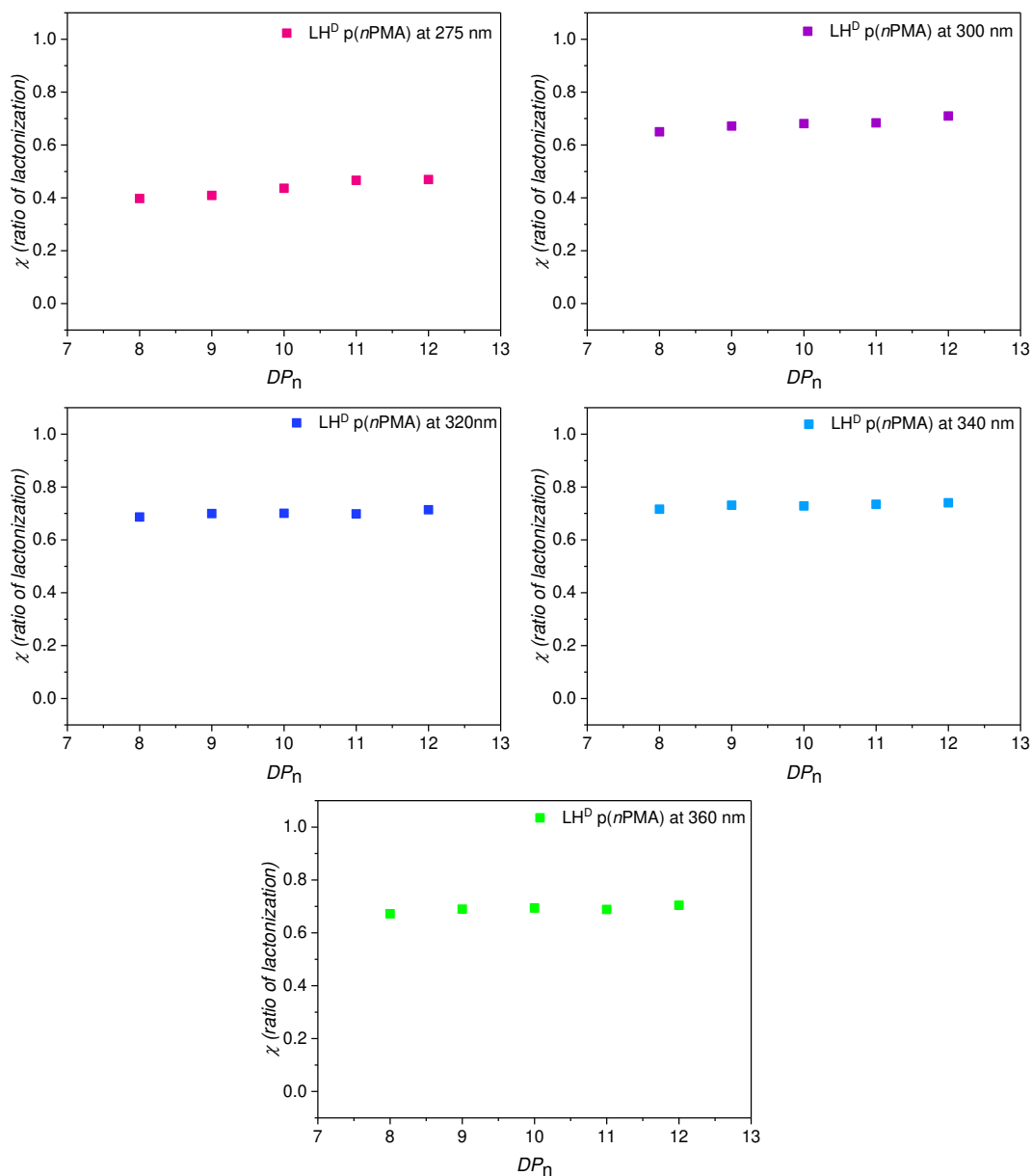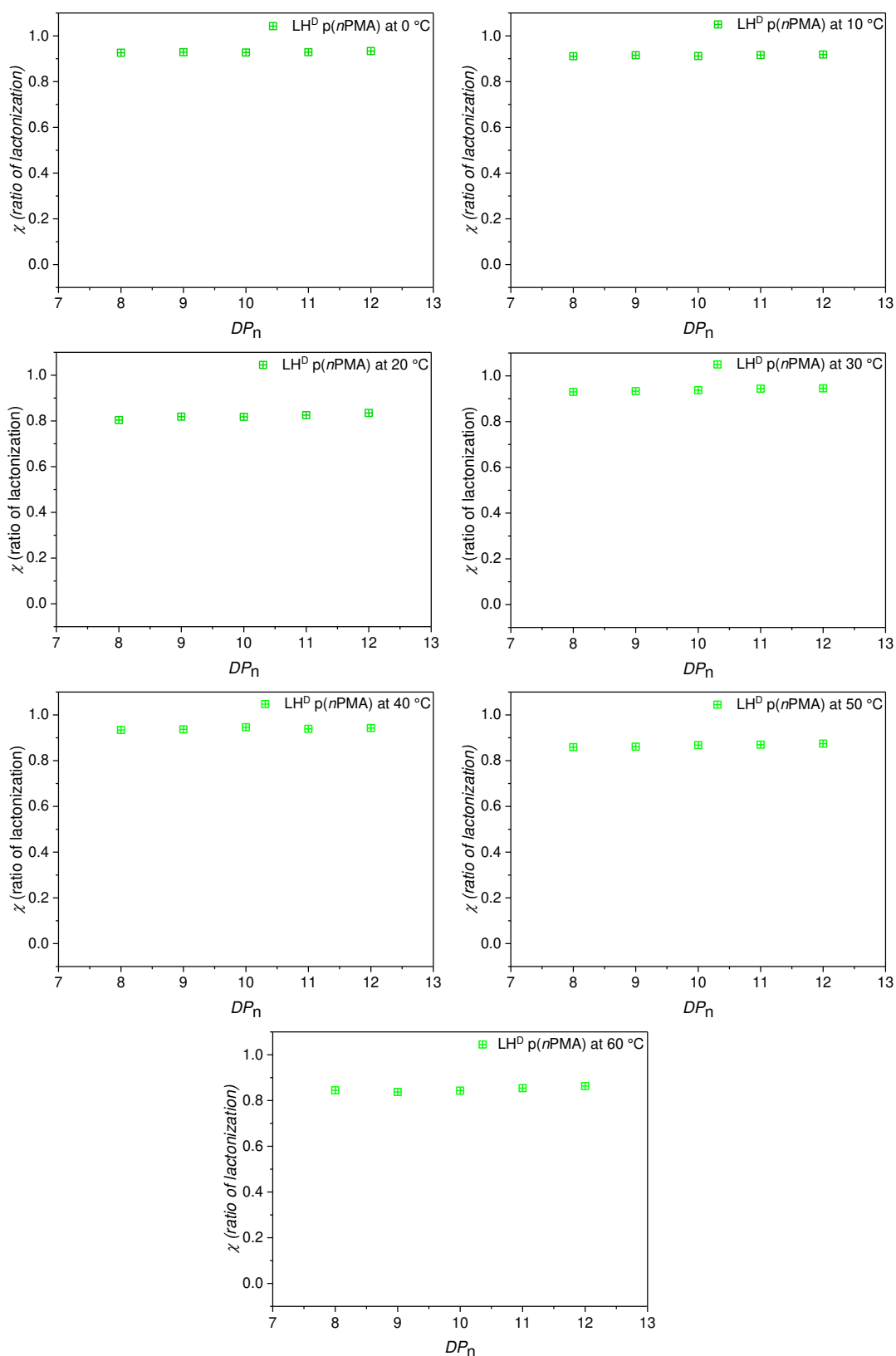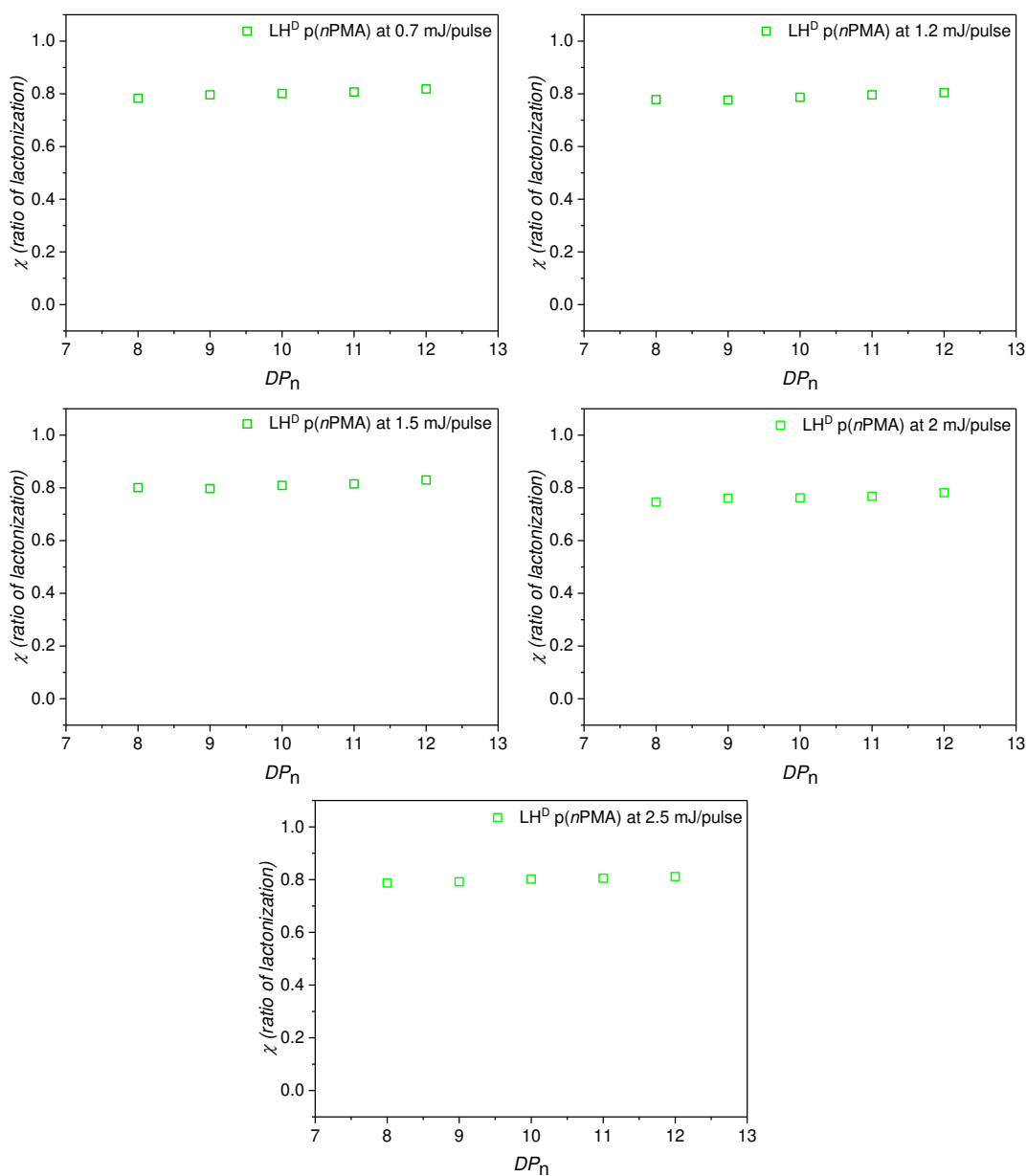**Figure 8.38.:** Plot of the lactonization ratio of the peak height (LH[D]) of p(nPMA) initiated by Irgacure 2959 (351 nm) vs. the DP_n between 0.7-2.5 mJ/pulse. Adapted from reference [193] with permission from the Royal Society of Chemistry.

8.5.3. DFT Calculations

The reaction paths of spontaneous lactonization were calculated for the substituents propyl (**R3**) and butyl (**R4**) as described in Scheme 8.16 for *si* face and *re* face attack. From the open polymer end group conformation **OH_3** and **OH_4**, the transition states of lactonization (TS$_{\text{ring closure}}$) were located transforming to stable intermediates **I_3** and **I_4** after ring closure (see Scheme 8.16). After separation of the alcohol from the intermediate, the product of the reaction was located as a complex of alcohol (**R3-OH** and **R4-OH**) and the lactone (**LH_3** and **LH_4**), respectively. For time reasons, the transition state between the intermediates and the product lactone was not computed.

The *S* enantiomer polymer is 54 kJ·mol^{-1} more stable than the *R* enantiomer (see Table 8.46), which makes only the former experimentally accessible. Therefore, the discussion of our DFT results concentrates on the reaction paths after *si* face attack (left side of Figure 8.39). The barriers of lactonization, i.e. the ring closure from open polymer end group **OH_3** and **OH_4** to the intermediates **I_3** and **I_4**, respectively, are similar for both substituents (~154 kJ·mol^{-1}) and constitute the rate-limiting step. As presented in Table 8.46, the barriers of ring closure and the stability of the intermediates are similar for **R3** and **R4** substituents. The product complex, created after release of the alcohol (propanol, butanol) from the lactone (**LH_3**, **LH_4**), respectively, is thermodynamically stabilized for **R3** (-12 kJ·mol^{-1}) whereas it is unstable for **R4** (+2 kJ·mol^{-1}).

For completeness, the lactonization intermediates and products of the unstable *R* enantiomer were also calculated. There exists a lower energy barrier (93.9 kJ·mol^{-1}) with planar conformation inducing a possible modification of *si* face to *re* face polymer (right side of Figure 8.39). Both **R3** and **R4** product complexes are thermodynamically stable (~-45 kJ·mol^{-1} for *re* phase attack).

To sum up, our DFT calculations confirm the different reactivity of the **R3** and **R4** motifs from a thermodynamic point of view, because the *S* enantiomer can create a stable lactone after spontaneous ring closure and alcohol expellation.

Table 8.46.: Relative Gibbs Free energies ΔGrel in kJ/mol for conformations after *si* face and *re* face attacks. Data are given for M06-2X/D3BJ/PCM/ aug-cc-pVDZ (aug-cc-pVTZ) method.[171,201,207–210] Adapted from reference [193] with permission from the Royal Society of Chemistry.

si face attack (R3)	ΔG_{rel} [a]	
Polymer OH_3	0.0	
TS$_{ring\ closure}$	153.7	
	(157.3)	
Intermediate I_3	22.8	
	(27.1)	
Complex of lactone LH_3 and propanol	-12.0	
	(-13.5)	
Transition State *si* ↔ *re* face attack (R3)	ΔG_{rel} [a]	
TS$_{planar}$ (*si* ↔ *re*)	93.9	
re face attack (R3)	ΔG_{rel} [a]	ΔG_{rel} [b]
Polymer OH_3	53.2	0.0
Intermediate I_3	36.9	-16.2
Complex of lactone LH_3 and propanol	8.0	-45.2
si face attack (R4)	ΔG_{rel} [c]	
Polymer OH_4	0.00	
TS$_{ring\ closure}$	155.4	
Intermediate I_4	29.4	
Complex of lactone LH_4 and butanol	2.2	
re face attack (R4)	ΔG_{rel} [c]	ΔG_{rel} [d]
Polymer OH_4	53.5	0.0
Intermediate I_4	49.7	-3.8
Complex of lactone LH_4 and butanol	7.9	-45.6

[a] relative to the lowest energy *si* polymer OH_3.

[b] relative to the *re* face polymer OH_3.

[c] relative to the lowest energy *re* polymer OH_4.

[d] relative to the *re* face polymer OH_4.
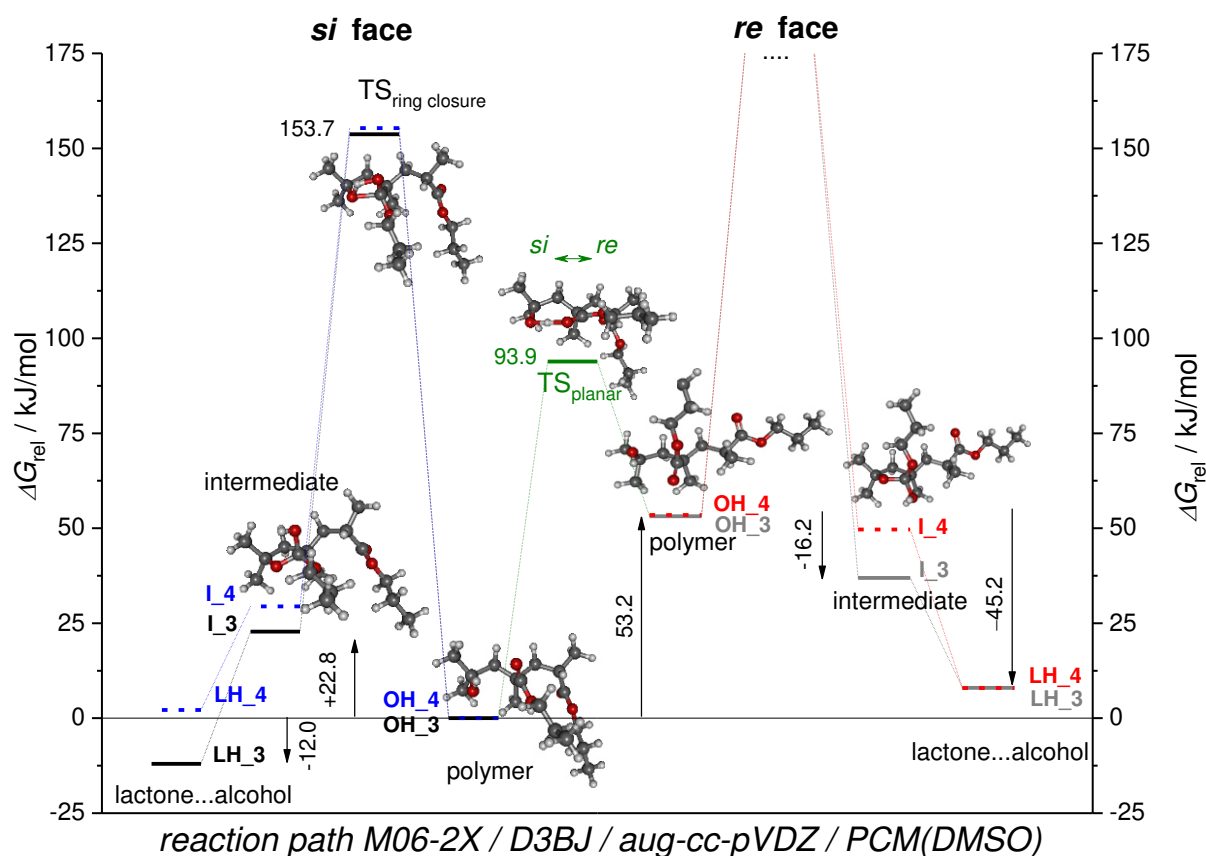
Figure 8.39.: Lactonization reaction paths after *si* face (left) and *re* face (right) attacks. Gibbs free energies are given relative to the lowest-energy polymer, respectively. Adapted from reference [193] with permission from the Royal Society of Chemistry.
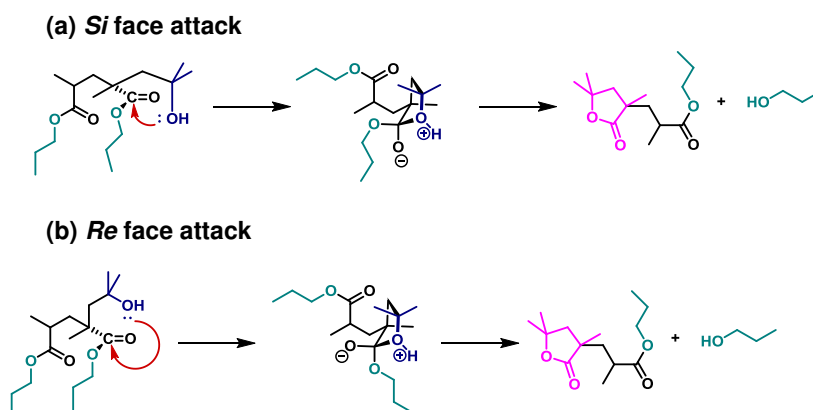
Scheme 8.16.: Reaction paths of the propyl substituted molecule via *si* face attack (a) or *re* face attack (b). Adapted from reference [193] with permission from the Royal Society of Chemistry.

Bibliography

(1) Yamago, S.; Nakamura, Y. *Polymer (Guildf).* **2013**, *54* (3), 981–994.

(2) Otsu, T. *J. Polym. Sci. Part A Polym. Chem.* **2000**, *38* (12), 2121–2136.

(3) Zhou, H.; Johnson, J. A. *Angew. Chemie Int. Ed.* **2013**, *52* (8), 2235–2238.

(4) Fors, B. P.; Hawker, C. J. *Angew. Chemie Int. Ed.* **2012**, *51* (35), 8850–8853.

(5) Adzima, B. J.; Tao, Y.; Kloxin, C. J.; DeForest, C. A.; Anseth, K. S.; Bowman, C. N. *Nat. Chem.* **2011**, *3* (3), 256–259.

(6) Hurrle, S.; Goldmann, A. S.; Gliemann, H.; Mutlu, H.; Barner-Kowollik, C. *ACS Macro Lett.* **2018**, *7* (2), 201–207.

(7) Claus, T. K.; Zhang, J.; Martin, L.; Hartlieb, M.; Mutlu, H.; Perrier, S.; Delaittre, G.; Barner-Kowollik, C. *Macromol. Rapid Commun.* **2017**, *38* (16), 1700264.

(8) Sugawara, Y.; Hiltebrandt, K.; Blasco, E.; Barner-Kowollik, C. *Macromol. Rapid Commun.* **2016**, *37* (17), 1466–1471.

(9) Scott, T. F.; Schneider, A. D.; Cook, W. D.; Bowman, C. N. *Science.* **2005**, *308* (5728), 1615–1617.

(10) Ryu, J.; D'Amato, M.; Cui, X.; Long, K. N.; Jerry Qi, H.; Dunn, M. L. *Appl. Phys. Lett.* **2012**, *100* (16), 161908.

(11) Amamoto, Y.; Kamada, J.; Otsuka, H.; Takahara, A.; Matyjaszewski, K. *Angew. Chemie* **2011**, *123* (7), 1698–1701.

(12) Fairbanks, B. D.; Singh, S. P.; Bowman, C. N.; Anseth, K. S. *Macromolecules* **2011**, *44* (8), 2444–2450.

(13) Trout, T. J.; Schmieg, J. J.; Gambogi, W. J.; Weber, A. M. *Adv. Mater.* **1998**, *10* (15), 1219–1224.

(14) Moszner, N.; Zeuner, F.; Pfeiffer, S.; Schurte, I.; Rheinberger, V.; Drache, M. *Macromol. Mater. Eng.* **2001**, *286* (4), 225–231.

(15) Fouassier, J. P.; Allonas, X.; Burget, D. *Prog. Org. coatings* **2003**, *47* (1), 16–36.

(16) Loccufier, J.; Claes, R. *Curable liquids and inks for toys and food packaging applications*, U.S. Patent No. 9,249,321, **2016**.

(17) Aparicio, J. L.; Elizalde, M. *Packag. Technol. Sci.* **2015**, *28* (3), 181–203.

(18) Crivello, J. V; Reichmanis, E. *Chem. Mater.* **2013**, *26* (1), 533–548.

(19) Baikerikar, K. K.; Scranton, A. B. *Polymer (Guildf).* **2001**, *42* (2), 431–441.

(20) Moszner, N.; Salz, U. *Prog. Polym. Sci.* **2001**, *26* (4), 535–576.

(21) Lee, K.-S.; Kim, R. H.; Yang, D.-Y.; Park, S. H. *Prog. Polym. Sci.* **2008**, *33* (6), 631–681.

(22) Cumpston, B. H.; Ananthavel, S. P.; Barlow, S.; Dyer, D. L.; Ehrlich, J. E.; Erskine, L. L.; Heikal, A. A.; Kuebler, S. M.; Lee, I.-Y. S.; McCord-Maughon, D.; et al. *Nature* **1999**, *398* (6722), 51–54.

(23) Allen, N. S. *J. Photochem. Photobiol. A Chem.* **1996**, *100* (1–3), 101–107.

(24) Anseth, K. S.; Newman, S. M.; Bowman, C. N. In *Biopolymers II*; Springer, **1995**; pp 177–217.

(25) Matyjaszewski, K.; Davis, T. P. *Handbook of radical polymerization*; John Wiley & Sons, **2003**.

(26) Iwasaki, T.; Yoshida, J. *Macromolecules* **2005**, *38* (4), 1159–1163.

(27) Odian, G. *Principles of polymerization*; John Wiley & Sons, **2004**.

(28) Hawker, C. J. *J. Am. Chem. Soc.* **1994**, *116* (24), 11185–11186.

(29) Rey, L.; Duchet, J.; Galy, J.; Sautereau, H.; Vouagner, D.; Carrion, L. *Polymer (Guildf).* **2002**, *43* (16), 4375–4384.

(30) Gruber, H. F. *Prog. Polym. Sci.* **1992**, *17* (6), 953–1044.

(31) Lagos, A.; Reyes, J. *J. Polym. Sci. Part A Polym. Chem.* **1988**, *26* (4), 985–991.

(32) Matheson, M. S.; Auer, E. E.; Bevilacqua, E. B.; Hart, E. J. *J. Am. Chem. Soc.* **1951**, *73* (4), 1700–1706.

(33) Tonge, M. P.; Kajiwara, A.; Kamachi, M.; Gilbert, R. G. *Polymer (Guildf).* **1998**, *39* (11), 2305–2313.

(34) Buback, M.; Gilbert, R. G.; Hutchinson, R. A.; Klumperman, B.; Kuchta, F.-D.; Manders, B. G.; O'Driscoll, K. F.; Russell, G. T.; Schweer, J. *Macromol. Chem. Phys.* **1995**, *196* (10), 3267–3280.

(35) Junkers, T.; Schneider-Baumann, M.; Koo, S. S. P.; Castignolles, P.; Barner-Kowollik, C. *Macromolecules* **2010**, *43* (24), 10427–10434.

(36) Haehnel, A. P.; Schneider-Baumann, M.; Arens, L.; Misske, A. M.; Fleischhaker, F.; Barner-Kowollik, C. *Macromolecules* **2014**, *47* (10), 3483–3496.

(37) Allen, P. E. M.; Patrick, C. R. *Macromol. Chem. Phys.* **1961**, *47* (1), 154–167.

(38) Krstina, J.; Moad, G.; Rizzardo, E.; Winzor, C. L.; Berge, C. T.; Fryd, M. *Macromolecules* **1995**, *28* (15), 5381–5385.

(39) Ayrey, G.; Humphrey, M. J.; Poller, R. C. *Polymer (Guildf).* **1977**, *18* (8), 840–844.

(40) Bonta, G.; Gallo, B. M.; Russo, S.; Uliana, C. *Polymer (Guildf).* **1976**, *17* (3), 217–220.

(41) Hensley, D. R.; Goodrich, S. D.; Huckstep, A. Y.; Harwood, H. J.; Rinaldi, P. L. *Macromolecules* **1995**, *28* (5), 1586–1591.

(42) Barner-Kowollik, C.; Russell, G. T. *Prog. Polym. Sci.* **2009**, *34* (11), 1211–1259.

(43) Mayo, F. R. *J. Am. Chem. Soc.* **1943**, *65* (12), 2324–2329.

(44) Boissel, J. *J. Appl. Polym. Sci.* **1977**, *21* (3), 855–857.

(45) Suddaby, K. G.; Maloney, D. R.; Haddleton, D. M. *Macromolecules* **1997**, *30* (4), 702–713.

(46) Szablan, Z.; Junkers, T.; Koo, S. P. S.; Lovestead, T. M.; Davis, T. P.; Stenzel, M. H.; Barner-Kowollik, C. *Macromolecules* **2007**, *40* (19), 6820–6833.

(47) Ahmad, N. M.; Heatley, F.; Lovell, P. A. *Macromolecules* **1998**, *31* (9), 2822–2827.

(48) Cramer, N. B.; Stansbury, J. W.; Bowman, C. N. *J. Dent. Res.* **2011**, *90* (4), 402–416.

(49) Fouassier, J.-P. *Photoinitiation, photopolymerization, and photocuring: fundamentals and applications*; Hanser, **1995**.

(50) Davidson, R. S. *Exploring the science, technology and applications of UV and EB curing*; Sita Technology Limited, **1999**.

(51) Roffey, C. G. *Photogeneration of reactive species for UV curing*; John Wiley & Sons, **1997**.

(52) Kloosterboer, J. G. In *Electronic applications*; Springer, **1988**; pp 1–61.

(53) Bunning, T. J.; Natarajan, L. V; Tondiglia, V. P.; Sutherland, R. L. *Annu. Rev. Mater. Sci.* **2000**, *30* (1), 83–115.

(54) Sun, H.-B.; Kawata, S. *Two-photon photopolymerization and 3D lithographic microfabrication*; Springer, **2004**.

(55) Kagami, M.; Yamashita, T.; Ito, H. *Appl. Phys. Lett.* **2001**, *79* (8), 1079–1081.

(56) Gatlik, I.; Rzadek, P.; Gescheidt, G.; Rist, G.; Hellrung, B.; Wirz, J.; Dietliker, K.; Hug, G.; Kunz, M.; Wolf, J.-P. *J. Am. Chem. Soc.* **1999**, *121* (36), 8332–8336.

(57) Sluggett, G. W.; McGarry, P. F.; Koptyug, I. V; Turro, N. J. *J. Am. Chem. Soc.* **1996**, *118* (31), 7367–7372.

(58) Wolf, T. J. A.; Voll, D.; Barner-Kowollik, C.; Unterreiner, A.-N. *Macromolecules* **2012**, *45* (5), 2257–2266.

(59) Wolf, T. J. A.; Fischer, J.; Wegener, M.; Unterreiner, A.-N. *Opt. Lett.* **2011**, *36* (16), 3188–3190.

(60) Criqui, A.; Lalevée, J.; Allonas, X.; Fouassier, J.-P. *Macromol. Chem. Phys.* **2008**, *209* (21), 2223–2231.

(61) Rist, G.; Borer, A.; Dietliker, K.; Desobry, V.; Fouassier, J. P.; Ruhlmann, D. *Macromolecules* **1992**, *25* (16), 4182–4193.

(62) Dietliker, K.; Broillet, S.; Hellrung, B.; Rzadek, P.; Rist, G.; Wirz, J.; Neshchadin, D.; Gescheidt, G. *Helv. Chim. Acta* **2006**, *89* (10), 2211–2225.

(63) Fast, D. E.; Zalibera, M.; Lauer, A.; Eibel, A.; Schweigert, C.; Kelterer, A.-M.; Spichty, M.; Neshchadin, D.; Voll, D.; Ernst, H.; Liang, Y.; Dietliker, K.; Unterreiner, A.-N.; Barner-Kowollik, C.; Grützmacher, H.; Gescheidt, G. *Chem. Commun.* **2016**, *52* (64), 9917–9920.

(64) Wenn, B.; Conradi, M.; Carreiras, A. D.; Haddleton, D. M.; Junkers, T. *Polym. Chem.* **2014**, *5* (8), 3053–3060.

(65) Genkin, V. N.; Sokolov, V. V. *Dokl. Akad. Nauk SSSR* **1977**, *234* (1), 94–96.

(66) Aleksandrov, A. P.; Genkin, V. N.; Kitai, M. S.; Sokolov, I. M. S. V. V. *J. Quant. Electron.* **1977**, *7* (5), 547–550.

(67) Olaj, O. F.; Bitai, I.; Hinkelmann, F. *Makromol. Chem.* **1987**, *188* (7), 1689–1702.

(68) Olaj, O. F.; Schnöll-Bitai, I. *Eur. Polym. J.* **1989**, *25* (7–8), 635–641.

(69) Kockler, K. B.; Fleischhaker, F.; Barner-Kowollik, C. *Polym. Chem.* **2016**, *7* (26), 4342–4351.

(70) Haehnel, A. P.; Wenn, B.; Kockler, K.; Bantle, T.; Misske, A. M.; Fleischhaker, F.; Junkers, T.; Barner-Kowollik, C. *Macromol. Rapid Commun.* **2014**, *35* (23), 2029–2037.

(71) Kockler, K. B.; Fleischhaker, F.; Barner-Kowollik, C. *Macromolecules* **2016**, *49* (22), 8572–8580.

(72) Kockler, K. B.; Haehnel, A. P.; Fleischhaker, F.; Schneider-Baumann, M.; Misske, A. M.; Barner-Kowollik, C. *Macromol. Chem. Phys.* **2015**, *216* (14), 1573–1582.

(73) Dervaux, B.; Junkers, T.; Schneider-Baumann, M.; Du Prez, F. E.; Barner-Kowollik, C. *J. Polym. Sci. Part A Polym. Chem.* **2009**, *47* (23), 6641–6654.

(74) Bouguer, P. *Essai d'optique sur la gradation de la lumière*; chez Claude Jombert, ruë S. Jacques, au coin de la ruë des Mathurins, à l'Image Notre-Dame, **1729**.

(75) Lambert, J. H. *Photometria sive de mensura et gradibus luminis, colorum et umbrae*; Klett, **1760**.

(76) Beer. *Ann. der Phys. und Chemie* **1852**, *162* (5), 78–88.

(77) Balzani, V.; Ceroni, P.; Juris, A. *Photochemistry and photophysics: concepts, research, applications*; John Wiley & Sons, **2014**.

(78) El-Sayed, M. A. *J. Chem. Phys.* **1963**, *38* (12), 2834–2838.

(79) Franck, J.; Dymond, E. G. *Trans. Faraday Soc.* **1926**, *21*, 536–542.

(80) Condon, E. *Phys. Rev.* **1926**, *28* (6), 1182.

(81) Fouassier, J.-P.; Lalevée, J. *Photoinitiators for Polymer Synthesis: Scope, Reactivity, and Efficiency*; John Wiley & Sons, **2012**.

(82) Wedler, G.; Freund, H.-J. *Lehrbuch der physikalischen Chemie*; John Wiley & Sons, **2012**; Vol. 1.

(83) Franck, J.; Rabinowitsch, E. *Trans. Faraday Soc.* **1934**, *30*, 120–130.

(84) Denisov, E. T. *Macromol. Chem. Phys.* **1984**, *8* (S19841), 63–78.

(85) Norrish, R. G. W.; Bamford, C. H. *Nature* **1936**, *138* (3502), 1016.

(86) Norrish, R. G. W.; Bamford, C. H. *Nature* **1937**, *140* (3535), 195.

(87) Wang, H. *Comprehensive Organic Name Reactions*; John Wiley & Sons, **2010**.

(88) Ramamurthy, V.; Corbin, D. R.; Johnston, L. J. *J. Am. Chem. Soc.* **1992**, *114* (10), 3870–3882.

(89) Wagner, P. J. *Acc. Chem. Res.* **1971**, *4* (5), 168–177.

(90) Davidson, R. S.; Goodwin, D.; de Violet, P. F. *Tetrahedron Lett.* **1981**, *22* (26), 2485–2486.

(91) Scaiano, J. C.; Lissi, E. A.; Encina, M. V. *Rev. Chem. Intermed.* **1978**, *2* (2), 139–196.

(92) Yang, N. C.; Yang, D.-D. H. *J. Am. Chem. Soc.* **1958**, *80* (11), 2913–2914.

(93) Kuhlmann, R.; Schnabel, W. *Macromol. Mater. Eng.* **1978**, *70* (1), 145–157.

(94) Yagci, Y.; Onen, A.; Schnabel, W. *Macromolecules* **1991**, *24* (16), 4620–4623.

(95) Esen, D. S.; Arsu, N.; Da Silva, J. P.; Jockusch, S.; Turro, N. J. *J. Polym. Sci. Part A Polym. Chem.* **2013**, *51* (8), 1865–1871.

(96) Frick, E.; Schweigert, C.; Noble, B. B.; Ernst, H. A.; Lauer, A.; Liang, Y.; Voll, D.; Coote, M. L.; Unterreiner, A.-N.; Barner-Kowollik, C. *Macromolecules* **2016**, *49* (1), 80–89.

(97) Fischer, H.; Radom, L. *Angew. Chemie Int. Ed.* **2001**, *40* (8), 1340–1371.

(98) Hurrle, S.; Lauer, A.; Gliemann, H.; Mutlu, H.; Wöll, C.; Goldmann, A. S.; Barner-Kowollik, C. *Macromol. Rapid Commun.* **2017**, *38* (13), 1600598.

(99)   Eibel, A.; Fast, D. E.; Sattelkow, J.; Zalibera, M.; Wang, J.; Huber, A.; Müller, G.; Neshchadin, D.; Dietliker, K.; Plank, H.; Grützmacher, H.; Gescheidt, G. *Angew. Chemie - Int. Ed.* **2017**, *56* (45), 14306–14309.

(100)   Segurola, J.; Allen, N. S.; Edge, M.; McMahon, A.; Wilson, S. *Polym. Degrad. Stab.* **1999**, *64* (1), 39–48.

(101)   Tehfe, M.-A.; Blanchard, N.; Fries, C.; Lalevée, J.; Allonas, X.; Fouassier, J. P. *Macromol. Rapid Commun.* **2010**, *31* (5), 473–478.

(102)   Günersel, E. D.; Hepuzer, Y.; Yagci, Y. *Die Angew. Makromol. Chemie* **1999**, *264* (1), 88–91.

(103)   Fouassier, J. P.; Burr, D. *Macromolecules* **1990**, *23* (15), 3615–3619.

(104)   Liska, R.; Seidl, B. *J. Polym. Sci. Part A Polym. Chem.* **2005**, *43* (1), 101–111.

(105)   Seidl, B.; Kalinyaprak-Icten, K.; Fuß, N.; Hoefer, M.; Liska, R. *J. Polym. Sci. Part A Polym. Chem.* **2008**, *46* (1), 289–301.

(106)   Dadashi-Silab, S.; Doran, S.; Yagci, Y. *Chem. Rev.* **2016**, *116* (17), 10212–10275.

(107)   Sagratini, G.; Caprioli, G.; Cristalli, G.; Giardiná, D.; Ricciutelli, M.; Volpini, R.; Zuo, Y.; Vittori, S. *J. Chromatogr. A* **2008**, *1194* (2), 213–220.

(108)   Keskin, S.; Jockusch, S.; Turro, N. J.; Arsu, N. *Macromolecules* **2008**, *41* (13), 4631–4634.

(109)   Liska, R. *J. Polym. Sci. Part A Polym. Chem.* **2004**, *42* (9), 2285–2301.

(110)   Jakubiak, J.; Allonas, X.; Fouassier, J. P.; Sionkowska, A.; Andrzejewska, E.; Linden LÅand Rabek, J. F. *Polymer (Guildf).* **2003**, *44* (18), 5219–5226.

(111)   Yamaoka, T.; Nakamura, Y.; Koseki, K.; Shirosaki, T. *Polym. Adv. Technol.* **1990**, *1* (5–6), 287–295.

(112)   Gordon, J. P.; Zeiger, H. J.; Townes, C. H. *Phys. Rev.* **1955**, *99* (4), 1264.

(113)   Schawlow, A. L.; Townes, C. H. *Phys. Rev.* **1958**, *112* (6), 1940.

(114)   Maiman, T. H. *Nature* **1960**, *187*, 493-494.

(115)   Williams, D. *Anaesth. Intensive Care Med.* **2008**, *9* (12), 550–552.

(116)   Bose, S. N. *Plancks gesetz und lichtquantenhypothese*; Springer, **1924**.

(117)   Duarte, F. J.; Kelley, P.; Hillman, L. W.; Liao, P. F. *Dye laser principles: with applications*; Academic Press, **1990**.

(118)   Harris, S. E. *Proc. IEEE* **1969**, *57* (12), 2096–2113.

(119)   Closs, G. L. In *Advances in Magnetic and Optical Resonance*; Elsevier, **1974**; Vol. 7, pp 157–229.

(120)   Adrian, F. J. In *Chemically Induced Magnetic Polarization*; Springer, **1977**; pp 77–105.

(121)   Goez, M. *Concepts Magn. Reson. Part A* **1995**, *7* (1), 69–86.

(122)   Pine, S. H. *J. Chem. Educ.* **1972**, *49* (10), 664-668.

(123)   Neshchadin, D. *Quantitative applications of ^{1}H and ^{31}P chemically induced dynamic nuclear polarization*, dissertation, University of Basel, **2003**.

(124)   Goudsmit, G. H.; Paul, H.; Shushin, A. I. *J. Phys. Chem.* **1993**, *97* (50), 13243–13249.

(125)   Hore, P. J.; Joslin, C. G.; McLauchlan, K. A. *Chem. Soc. Rev.* **1979**, *8* (1), 29–61.

(126)   Atkins, P. W. In *Chemically Induced Magnetic Polarization*; Springer, **1977**; pp 191–203.

(127)   Kaptein, R. *J. Chem. Soc. D: Chem. Commun.* **1971**, (14), 732–733.

(128)   Yamashita, M.; Fenn, J. B. *J. Phys. Chem.* **1984**, *88* (20), 4451–4459.

(129)   Fenn, J. B.; Mann, M.; Meng, C. K.; Wong, S. F.; Whitehouse, C. M. *Mass Spectrom. Rev.* **1990**, *9* (1), 37–70.

(130)   Steinkoenig, J.; Cecchini, M. M.; Reale, S.; Goldmann, A. S.; Barner-Kowollik, C. *Macromolecules* **2017**, *50* (20), 8033–8041.

(131)   Wilm, M. S.; Mann, M. *Int. J. Mass Spectrom. Ion Process.* **1994**, *136* (2–3), 167–180.

(132)   Peschke, M.; Verkerk, U. H.; Kebarle, P. *J. Am. Soc. Mass Spectrom.* **2004**, *15* (10), 1424–1434.

(133)   Banerjee, S.; Mazumdar, S. *Int. J. Anal. Chem.* **2012**, *2012*, 1-40.

(134)   Karas, M.; Bachmann, D.; Hillenkamp, F. *Anal. Chem.* **1985**, *57* (14), 2935–2939.

(135)   Tanaka, K.; Waki, H.; Ido, Y.; Akita, S.; Yoshida, Y.; Yoshida, T.; Matsuo, T. *Rapid Commun. mass Spectrom.* **1988**, *2* (8), 151–153.

(136) Hanton, S. D. *Chem. Rev.* **2001**, *101* (2), 527–570.

(137) Wolff, M. M.; Stephens, W. E. *Rev. Sci. Instrum.* **1953**, *24* (8), 616–617.

(138) Gross, J. H. *Mass spectrometry: a textbook*; Springer, **2006**.

(139) Chughtai, K.; Heeren, R. M. A. *Chem. Rev.* **2010**, *110* (5), 3237–3277.

(140) Glish, G. L.; Vachet, R. W. *Nat. Rev. Drug Discov.* **2003**, *2* (2), 140–150.

(141) Barner-Kowollik, C.; Gruendling, T.; Falkenhagen, J.; Weidner, S. *Mass spectrometry in polymer chemistry*; John Wiley & Sons, **2012**.

(142) Makarov, A. *Anal. Chem.* **2000**, *72* (6), 1156–1162.

(143) Hu, Q.; Noll, R. J.; Li, H.; Makarov, A.; Hardman, M.; Graham Cooks, R. *J. mass Spectrom.* **2005**, *40* (4), 430–443.

(144) Papayannopoulos, I. A. *Mass Spectrom. Rev.* **1995**, *14* (1), 49–73.

(145) Frese, C. K.; Altelaar, A. F. M.; van den Toorn, H.; Nolting, D.; Griep-Raming, J.; Heck, A. J. R.; Mohammed, S. *Anal. Chem.* **2012**, *84* (22), 9668–9673.

(146) Singh, C.; Zampronio, C. G.; Creese, A. J.; Cooper, H. J. *J. Proteome Res.* **2012**, *11* (9), 4517–4525.

(147) Prokai, L.; Simonsick, W. J. *Rapid Commun. mass Spectrom.* **1993**, *7* (9), 853–856.

(148) Simonsick, W. J.; Prokai, L. In *Chromatographic Characterization of Polymers*; ACS Publications, **1995**; pp 41–56.

(149) Gruendling, T.; Guilhaus, M.; Barner-Kowollik, C. *Anal. Chem.* **2008**, *80* (18), 6915–6927.

(150) Gruendling, T.; Guilhaus, M.; Barner-Kowollik, C. *Macromolecules* **2009**, *42* (17), 6366–6374.

(151) Beesley, R. M.; Ingold, C. K.; Thorpe, J. F. *J. Chem Soc* **1915**, *107*, 1080-1106.

(152) Jung, M. E.; Piizzi, G. *Chem. Rev.* **2005**, *105* (5), 1735–1766.

(153) Bruice, T. C.; Pandit, U. K. *J. Am. Chem. Soc.* **1960**, *82* (22), 5858–5865.

(154) Allinger, N. L.; Zalkow, V. *J. Org. Chem.* **1960**, *25* (5), 701–704.

(155) von Ragué Schleyer, P. *J. Am. Chem. Soc.* **1961**, *83* (6), 1368–1373.

(156) Milstien, S.; Cohen, L. A. *J. Am. Chem. Soc.* **1972**, *94* (26), 9158–9165.

(157) Günzler, F.; Wong, E. H. H.; Koo, S. P. S.; Junkers, T.; Barner-Kowollik, C. *Macromolecules* **2009**, *42* (5), 1488–1493.

(158) Voll, D.; Hufendiek, A.; Junkers, T.; Barner-Kowollik, C. *Macromol. Rapid Commun.* **2012**, *33* (1), 47–53.

(159) Jöckle, P.; Schweigert, C.; Lamparth, I.; Moszner, N.; Unterreiner, A.-N.; Barner-Kowollik, C. *Macromolecules* **2017**, *50* (22), 8894–8906.

(160) Frick, E.; Anastasaki, A.; Haddleton, D. M.; Barner-Kowollik, C. *J. Am. Chem. Soc.* **2015**, *137* (21), 6889–6896.

(161) Gruendling, T.; Voll, D.; Guilhaus, M.; Barner-Kowollik, C. *Macromol. Chem. Phys.* **2010**, *211* (1), 80–90.

(162) Voll, D.; Junkers, T.; Barner-Kowollik, C. *Macromolecules* **2011**, *44* (8), 2542–2551.

(163) Voll, D.; Neshchadin, D.; Hiltebrandt, K.; Gescheidt, G.; Barner-Kowollik, C. *Macromolecules* **2012**, *45* (15), 5850–5858.

(164) Frick, E.; Ernst, H. A.; Voll, D.; Wolf, T. J. A.; Unterreiner, A.-N.; Barner-Kowollik, C. *Polym. Chem.* **2014**, *5* (17), 5053–5068.

(165) Lauer, A.; Fast, D. E.; Kelterer, A. M.; Frick, E.; Neshchadin, D.; Voll, D.; Gescheidt, G.; Barner-Kowollik, C. *Macromolecules* **2015**, *48* (23), 8451–8460.

(166) Voll, D.; Junkers, T.; Barner-Kowollik, C. *J. Polym. Sci. Part A Polym. Chem.* **2012**, *50*, (14), 2739–2757.

(167) Becke, A. D. *J. Chem. Phys* **1993**, *98* (7), 5648–5652.

(168) Lee, C.; Yang, W.; Parr, R. G. *Phys. Rev. B* **1988**, *37* (2), 785.

(169) Stephens, P. J.; Devlin, F. J.; Chabalowski, Cf.; Frisch, M. J. *J. Phys. Chem.* **1994**, *98* (45), 11623–11627.

(170) Vosko, S. H.; Wilk, L.; Nusair, M. *Can. J. Phys.* **1980**, *58* (8), 1200–1211.

(171) Grimme, S.; Antony, J.; Ehrlich, S.; Krieg, H. *J. Chem. Phys.* **2010**, *132* (15), 154104.

(172) Schäfer, A.; Horn, H.; Ahlrichs, R. *J. Chem. Phys.* **1992**, *97* (4), 2571–2577.

(173) Jacquemin, D.; Perp, E. A. **2009**, *5* (9), 2420–2435.

(174) Schäfer, A.; Huber, C.; Ahlrichs, R. *J. Chem. Phys.* **1994**, *100* (8), 5829–5835.

(175) Yanai, T.; Tew, D. P.; Handy, N. C. *Chem. Phys. Lett.* **2004**, *393* (1), 51–57.

(176) Lauer, A.; Fast, D. E.; Steinkoenig, J.; Kelterer, A. M.; Gescheidt, G.; Barner-Kowollik, C. *ACS Macro Lett.* **2017**, *6* (9), 952–958.

(177) Dietliker, K.; Hüsler, R.; Birbaum, J.-L.; Ilg, S.; Villeneuve, S.; Studer, K.; Jung, T.; Benkhoff, J.; Kura, H.; Matsumoto, A.; et al. *Prog. Org. coatings* **2007**, *58* (2), 146–157.

(178) Baas, P.; Cerfontain, H. *J. Chem. Soc., Perkin Trans. 2* **1979**, (2) 156–162.

(179) Baas, P; Cerfontain, H. *J. Chem. Soc., Perkin Trans. 2* **1979**, (12), 1653–1660.

(180) Amat-Guerri, F.; Mallavia, R.; Sastre, R. *J. Photopolym. Sci. Technol.* **1995**, *8* (1), 205–232.

(181) Groenenboom, C. J.; Hageman, H. J.; Oosterhoff, P.; Overeem, T.; Verbeek, J. *J. Photochem. Photobiol. A Chem.* **1997**, *107* (1–3), 261–269.

(182) Mallavia, R.; Sastre, R.; Amat-Guerri, F. *J. Photochem. Photobiol. A Chem* **2001**, *138* (3), 193–201.

(183) Miyake, Y.; Takahashi, H.; Akai, N.; Shibuya, K.; Kawai, A. *Chem. Lett.* **2014**, *43* (8), 1275–1277.

(184) Fast, D. E.; Lauer, A.; Menzel, J. P.; Kelterer, A. M.; Gescheidt, G.; Barner-Kowollik, C. *Macromolecules* **2017**, *50* (5), 1815–1823.

(185) Kolczak, U.; Rist, G.; Dietliker, K.; Wirz, J. *J. Am. Chem. Soc.* **1996**, *118* (27), 6477–6489.

(186) Buback, M.; Frauendorf, H.; Günzler, F.; Vana, P. *Polymer (Guildf).* **2007**, *48* (19), 5590–5598.

(187) Muramatsu, Y.; Kaji, M.; Unno, A.; Hirai, O. *J. Photopolym. Sci. Technol.* **2010**, *23* (3), 447–450.

(188) Menzel, J. P.; Noble, B. B.; Lauer, A.; Coote, M. L.; Blinco, J. P.; Barner-Kowollik, C. *J. Am. Chem. Soc.* **2017**, *139* (44), 15812–15820.

(189) Neshchadin, D.; Rosspeintner, A.; Griesser, M.; Lang, B.; Mosquera-Vazquez, S.; Vauthey, E.; Gorelik, V.; Liska, R.; Hametner, C.; Ganster, B.; Saf, R.; Moszner, N.; Gescheidt, G. *J. Am. Chem. Soc.* **2013**, *135* (46), 17314–17321.

(190) Zivic, N.; Zhang, J.; Bardelang, D.; Dumur, F.; Xiao, P.; Jet, T.; Versace, D.-L.; Dietlin, C.; Morlet-Savary, F.; Graff, B.; Fouassier, J. P.; Gigmes, D.; Lalevée, J. *Polym. Chem.* **2016**, *7* (2), 418–429.

(191) Mokbel, H.; Poriel, C.; Rault-Berthelot, J.; Dumur, F.; Gigmes, D.; Toufaily, J.; Hamieh, T.; Cordella, D.; Detrembleur, C.; Fouassier, J. P.; Lalevée, J. *J. Appl. Polym. Sci.* **2016**, *133* (12), 1–9.

(192) Song, H. B.; Baranek, A.; Bowman, C. N. *Polym. Chem.* **2016**, *7* (3), 603–612.

(193) Lauer, A.; Steinkoenig, J.; Jöckle, P.; Kelterer, A.-M.; Unterreiner, A. N.; Barner-Kowollik, C. *Polym. Chem.* **2018**, *9* (24), 3336–3341.

(194) George, G. A. *J. Appl. Polym. Sci.* **1974**, *18* (1), 117–124.

(195) Yang, H.; Zhu, S.; Pan, N. *J. Appl. Polym. Sci.* **2004**, *92* (5), 3201–3210.

(196) Heiler, C.; Bastian, S.; Lederhose, P.; Blinco, J. P.; Blasco, E.; Barner-Kowollik, C. *Chem. Commun.* **2018**, *54* (28), 3476–3479.

(197) Becke, A. D. *J. Chem. Phys.* **1993**, *98* (7), 5648–5652.

(198) Neese, F. *Wiley Interdiscip. Rev. Comput. Mol. Sci.* **2012**, *2* (1), 73–78.

(199) Allouche, A.-R. *J. Comput. Chem.* **2011**, *32* (1), 174–182.

(200) Adamo, C.; Barone, V. *J. Chem. Phys.* **1999**, *110* (13), 6158–6170.

(201) Grimme, S.; Ehrlich, S.; Goerigk, L. *J. Comput. Chem.* **2011**, *32* (7), 1456–1465.

(202) Hehre, W. J.; Ditchfield, R.; Pople, J. A. *J. Chem. Phys.* **1972**, *56* (5), 2257–2261.

(203) Clark, T.; Chandrasekhar, J.; Spitznagel, G. W.; Schleyer, P. V. R. *J. Comput. Chem.* **1983**, *4* (3), 294–301.

(204) Krishnan, R.; Binkley, J. S.; Seeger, R.; Pople, J. A. *J. Chem. Phys.* **1980**, *72* (1), 650–654.

(205) Cances, E.; Mennucci, B.; Tomasi, J. *J. Chem. Phys.* **1997**, *107* (8), 3032–3041.

(206)   Frisch, M. J.; Trucks, G. W.; Schlegel, H. B.; Scuseria, G. E.; Robb, M. A.; Cheeseman, J. R.; Scalmani, G.; Barone, V.; Mennucci, B.; Petersson, G. A.; et al. Gaussian 09, Revision D. 01, Gaussian Inc., Wallingford, CT, **2009**.

(207)   Zhao, Y.; Truhlar, D. G. *Theor. Chem. Acc.* **2008**, *120* (1–3), 215–241.

(208)   Dunning Jr, T. H. *J. Chem. Phys.* **1989**, *90* (2), 1007–1023.

(209)   Kendall, R. A.; Dunning Jr, T. H.; Harrison, R. J. *J. Chem. Phys.* **1992**, *96* (9), 6796–6806.

(210)   Mennucci, B.; Cammi, R.; Tomasi, J. *J. Chem. Phys.* **1998**, *109* (7), 2798–2807.

List of Abbreviations

2MB	2-methyl benzoin
2,4DMB	2,4-dimethyl benzoin
2,6DMB	2,6-dimethyl benzoin
3D	3-dimensional
3MB	3-methyl benzoin
4MB	4-methyl benzoin
A	absorption
AIBN	azobisisobutyronitrile
AlGaAs	aluminium gallium arsenide
APCI	atmospheric pressure chemical ionization
Ar	argon
ArF	argon monofluoride
a.t.	ambient temperature
BEE	benzoin ethyl ether
BMA	butyl methacrylate
BnMA	benzyl methacrylate
δ	chemical shift
CBG	p-cyanobenzoyltrimethylgermane
CI	chemical ionization
CID	collision-induced decay
CIDNP	chemically induced dynamic nuclear
CO_2	carbon dioxide
Đ	dispersity
Da	dalton
°C	degree celsius
dc	direct current
DCM	dichloromethane
DFT	density functional theory
DMPA	2,2-Dimethoxy-2-phenylacetophenone
DMSO	dimethyl sulfoxide
DP_n	degree of polymerization
E	emission
EI	electron ionization
EMA	ethyl methacrylate
eq	equivalent
ESI	electrospray ionization
ESI-MS	electrospray ionization-mass spectrometry
ESR	electron spin resonance
eV	electronvolt
FBG	p-fluorobenzoyltrimethylgermane

F₂Bz	1,2-bis(4-fluorophenyl)-2-hydroxyethan-1-one
F₂Benzil	1,2-bis(4-fluorophenyl)ethane-1,2-dione
FAB	fast atom bombardment
FBz	1-(4-fluorophenyl)-2-hydroxy-2-phenylethan-1-one
FBz Iso	2-(4-fluorophenyl)-2-hydroxy-1-phenylethan-1-one
FI	field ionization
FNMe₂Bz	2-(4-(dimethylamino)phenyl)-1-(4-fluorophenyl)-2-hydroxyethan-1-one
FRP	free radical polymerization
FT-ICR	fourier transform ion cyclotron resonance
HCD	higher energy C-trap dissociation
He-Ne	helium-neon
HOMO	highest occupied molecular orbital
h	peak height
HBG	benzoyltrimethylgermane
$h\nu$	photon energy
Hz	hertz
IC	internal conversion
INADEQUATE	incredible natural abundance double quantum transfer experiments
ISC	intersystem crossing
J	coupling constant
kV	kilovoltage
KrF	krypton monofluoride
L	liter
λ_{exc}	excitation wavelength
laser	light amplification by stimulated emission of radiation
LUMO	lowest unoccupied molecular orbital
χ	molar ratio
M	monomer
MALDI	matrix-assisted laser desorption/ionization
MBG	p-methoxybenzoyltrimethylgermane
MeCN	acetonitrile
MIB	methyl isobutyrate
min	minute
mJ	millijoule
MMMP	2-methyl-4′-(methylthio)-2-morpholinopropiophenone
μL	microliter
μM	micromolar
MMA	methyl methacrylate
MO	molecular orbital
mol	molar
MS	mass spectrometry
m/z-ratio	mass-to-charge ratio
N₂	nitrogen
NBG	p-nitrobenzoyltrimethylgermane
Nd:YAG	Neodym³⁺ ions Yttrium Aluminium Granat

nm	nanometer
NMe₂Bz	1-(4-(dimethylamino)phenyl)-2-hydroxy-2-phenylethan-1-one
NMe₂Bz Iso	2-(4-(dimethylamino)phenyl)-2-hydroxy-1-phenylethan-1-one
NMR	nuclear magnetic resonance
ns	nanosecond
OPO	optical parametric oscillator
p(BMA)	poly(butyl methacrylate)
p(BnMA)	poly(benzyl methacrylate)
p(DMAEMA)	poly(dimethyl amino ethyl methacrylate)
p(EMA)	poly(ethyl methacrylate)
PentaMB	penta-methyl benzoin
PI	photoinitiator
PLI	pulsed-laser irradiation
PLP	pulsed-laser polymerization
PLP-SEC-ESI-MS	pulsed-laser polymerization and subsequent product analysis by SEC-ESI-MS
PMA	propyl methacrylate
p(MMA)	poly(methyl methacrylate)
ppm	parts per million
p(PMA)	poly(propyl methacrylate)
ps	picosecond
R	resolution
RDRP	reversible-deactivation radical polymerization
Rf	radio frequency
s	second
S	singlet state
SEC	size-exclusion chromatography
SFG	frequency-mixing
SHG	frequency-doubling
SOMO	singly occupied molecular orbital
T	triplet state
t	time constant
TD-DFT	time-dependent density functional theory
TetraMB	tetra-methyl benzoin
THF	tetrahydrofuran
Ti	titan
ToF	time of flight
TriMB	tri-methyl benzoin
TS	transition state
U	voltage
UV-Vis	ultraviolet and visible light
V	voltage
Xe₂	xenon
XeCl	xenon monochloride
XeF	xenon monofluoride

Acknowledgements

First of all, I want to thank Prof. Dr. Christopher Barner-Kowollik for giving me this opportunity to work on such an exciting project and to pursue my own ideas in a self-directed manner. Your support and guidance throughout the course of my doctoral research as well as your inexhaustible energy, enthusiasm, and optimism created an excellent and very motivating working environment. I am also very thankful for your support during my 6 months studies abroad at the Queensland University of Technology in Brisbane, Australia.

Furthermore, I would like to thank Dr. Anja Goldmann for her help to solve so many organisational problems. Thanks for always having an open door for me!

I am grateful to Dr. David Fast and Prof. Dr. Georg Gescheidt from the University of Graz for scientific discussions and friendly as well as fruitful collaboration within the joint DFG project. Especially, I would like to say thank you to David. I have learnt so much from you in the ways of presentation of data and scientific thinking.

The DFG is acknowledged for the funding of my PhD studies for three years.

I am also very thankful to my Hiwi-students Nadine Kalverkamp, Melissa Reith and Larissa Hammer. You all did a great job!

Furthermore, I very much appreciate working in the old and new mass spec team (Michi, Astrid, Kai, Janin, Waldemar and Charlotte).

Many thanks go to the entire macroarc team for the friendly working atmosphere, good team spirit, and after-work activities. Special thanks to Caro, Jan, Charlotte, and Elena.

Caro, I really enjoyed our adventures, driving through the Rocky Mountains in a Mustang GT. It was amazing! Jan was the best flatmate in Brisbane. We had super much fun and I will miss that time! I will never forget our jump into the pool! Charlotte, thanks for your support during the late evenings in the office. I really enjoyed our Sushi and Indian food dinners and it was fun to work with you on the doctor hats. I think we did a super creative job! Elena, I would like to thank you for helpful discussions and support in the beginning of my doctoral thesis.

Evelyn Stühring, Dr. Maria Schneider, Vincent Schüler and Katharina Elies are thanked for 'the many things that need to be done' in and outside of the laboratory.

Many thanks go to Dr. Eva Blasco, Dr. Anja Goldmann, Dr. Charlotte Petit, Dr. Hatice Mutlu, Dr. Dominik Voll, Dr. David Fast and Matthias Eing for proofreading of this thesis.

Besides the working group, I would like to thank my three girls: Betty, Caro, and Franzi. I really enjoyed our girl's nights.

Finally, I am very thankful to my parents and sisters for their continues support and encouragement. My special gratitude is for Chris. Your support has always been my source of strength and inspiration and I am really looking forward to our future, wherever this may be!